Late time response analysis in UWB Radar for Concealed Weapon Detection: feasibility study by

Averkios Vasalos

A thesis submitted to
The University of Birmingham
for the degree of
DOCTOR OF PHILOSOPHY

Department of Electronic, Electrical
& Computer Engineering
The University of Birmingham
September 2010

UNIVERSITY OF
BIRMINGHAM

University of Birmingham Research Archive

e-theses repository

This unpublished thesis/dissertation is copyright of the author and/or third parties. The intellectual property rights of the author or third parties in respect of this work are as defined by The Copyright Designs and Patents Act 1988 or as modified by any successor legislation.

Any use made of information contained in this thesis/dissertation must be in accordance with that legislation and must be properly acknowledged. Further distribution or reproduction in any format is prohibited without the permission of the copyright holder.

Acknowledgments

Firstly I would like to express my gratitude to my main supervisor Professor Mike Cherniakov, who gave me the opportunity to pursue this research, provided me with all the required experimental equipment and supervised the Thesis corrections. Such help was fundamental in order to reach the goals set at the beginning of the project.

Secondly I would like to thank my family, who without their financial and psychological help I would not be able to work in England for the PhD. They always gave me faith to believe in my ability to work and always keep trying to achieve my goals

Abstract

Remote detection of body-worn concealed weapons or explosives (CWE) is a field of ongoing research in order to provide security against terrorist attacks that can potentially cause a threat to the security of the society. So far there is a gap on detection systems able to function at extended stand-off distances and which operate robustly under harsh environmental conditions. In this Thesis the feasibility of CWE detection via the usage of UWB radar is explored as a system able to fulfil such requirements.

The hypothesis that the CWE detection is realised is based on the processing and analysis of the Late Time Response (LTR) of the human body which has been illuminated by the UWB transmitted signal. A specific set of LTR parameters characterizes the unique signature of the target. Therefore the existence of a CWE attached on the human body will influence the LTR characteristics and give the composite object i.e. human-CWE a different signature than the simple object i.e. human.

The CWE detection methodology is verified by theoretical analysis, modelling and extensive laboratory experimentation. The aim of the research is to demonstrate the methodology of the approach and its ability to extract and characterise the LTR parameters-signature of simple object i.e. human or composite object i.e. human-CWE. In this research the grenade is considered as the CWE as it is a weapon that could be easily used during a terrorist attack. Throughout the thesis, the grenade is approximated as a conducting sphere of 0.0325 m radius since the sphere and the grenade have similar shapes, and since the reflected field of sphere is theoretically known. Most importantly experiments are performed with the sphere appended at the front, the back and the side of the human.

Investigation of the way the LTR parameters are influenced by the existence of the CWE signifies the differences of the LTR signature between the human and human-CWE. So the resolution of the differences in the LTR of a human with and without a sphere as the main objective of the research, are presented in the Thesis. The results verify that CWE detection with the use of LTR is feasible under the experimental conditions presented. However a generalisation about CWE detection concerning all possible detection scenarios cannot yet be made. At this early stage of research, the identification of a specific CWE on the human and the robustness of the method to the human movement were out of scope of this Thesis and are considered for further research.

Table of Contents

List of Figures

Chapter 1

Chapter 2

Chapter 3

Chapter 4

Chapter 5

Chapter 6

APPENDIX chapter 5 and chapter 6

Figure 5.e.7: Comparison of human LTR poles. (page 293)
(.) average of 120 measurements
(×) 2nd and 3rd measured responses
(◊) 2nd and 4rth measured responses
(□) 3rd and 4rth measured responses

Figure 5.e.8: Amplitudes of the human LTR poles. (page 291)
(.) average of 120 measurements
(×)1st and 2nd measured responses
(◊) 1st and 3rd measured responses
(□)1st and 4rth measured responses

Figure 5.e.9: Amplitudes of the human LTR poles.
(.) average of 120 measurements
(×) 2nd and 3rd measured responses
(◊) 2nd and 4rth measured responses
(□) 3rd and 4rth measured responses

Abbreviations

C

CWE: Concealed Weapon and Explosive

D

DARPA: Defence Advanced Research Projects Agency

DFT: Discrete Fourier Transform

E

EMP: Electromagnetic Pulse

ETR: Early Time Response

F

FM: Frequency Modulation

FT: Fourier Transform

G

GMD: Gradiometer Metal Detectors

GPR: Ground-Penetrating Radar

I

IFFT: Inverse Fast Fourier Transform

IFT: Inverse Fourier Transform

IIR: Infinite Impulse Response

IR: Impulse Response

L

LoS: Line of Sight

LSI: Linear Shift Invariant

LT: Laplace Transform

LTI: Linear Time-Invariant

LTR: Late Time Response

M

MDL: Minimum Description Length

MUSIC: MUltiple SIgnal Classification

P

PM: Phase Modulation

PO: Physical Optics

PRF: Pulse Repetition Frequency

PSD: Power Spectral Density

R

RCS: Radar Cross Section

RTLS: Real Time Locating Systems

S

SAR: Synthetic Aperture Radar

SEM: Singularity Expansion Method

SNR: Signal-to-Noise Ratio

SVD: Singular Value Decomposition

T

THz: Teraherz

U

UWB: Ultra WideBand

V

VNA: Vector Network Analyser

Chapter 1

INTRODUCTION

1.1 Introduction

Ultra-Wideband (UWB) systems emerged from the work, which begun in 1962 in time-domain electromagnetics [1]. Time-domain electromagnetics were used to describe and characterize a specific type of microwave networks through their characteristic impulse response. Since then UWB systems have experienced almost 50 years of research and technological progress. In the initial investigation, as presented in [1], the electromagnetic wave propagation was studied from a time domain rather than a frequency domain point of view, although the frequency domain viewpoint was more widely used. In general UWB systems are also referred as short pulse systems, since they utilise short bursts of microwave energy, which means that the transmission bandwidths of these systems are large and often exceed 1 GHz [2]. Nowadays UWB systems have a vast area of applications. Some of these applications are, Real Time Locating Systems (RTLS), wireless communication networks and Radar.

RTLS systems are used for real time tracking and identification of the location of objects. RTLS systems use nodes which are appended in objects and devices that receive the transmitted signals from the objects so that the location of the objects is determined. Therefore the term RTLS refers to passive systems which collect information on the location of objects.

Considering wireless communication networks, UWB technology is used since it provides high data rates. UWB radio has been proposed as a physical layer for high bit rate, short or long range communication networks. Hence UWB communication systems are optimised for applications such as video distribution, or video teleconferencing.

These applications require a very high level of quality of service, since they are real time, high bandwidth applications that cause large bursts of data packets [3].

In this thesis, UWB technology is used on the concept of Late Time Response (LTR) analysis related to UWB radar for remote detection of human body-attached Concealed Weapons and Explosives (CWEs). The UWB radar is also referred as impulse radar; this means that if the received signal is considered in the time domain, the outcome is equivalent to the impulse response (IR) [1] of the illuminated system, which in this case is the human-CWE composite object. The fundamental idea of the research methodology is that the LTR, which is a component of the IR of this complex object should provide a unique CWE signature, which will make the CWE detection feasible. The next section describes the motivating conditions that encouraged the research for the detection of CWE and the various existing ways for the accomplishment of detection.

1.2 Motivation for the Present Work - CWE Detection

Nowadays the danger posed by the presence of terrorist attacks is experienced in many areas of our society. Since there is the need to respond to the potential threats of life loss, destruction and economic devastation which terrorism creates, currently many security issues have arisen. One of the most important security issues is the remote detection and identification of CWE, which are carried by terrorists.

From airports, military installations, border check points and correctional facilities to places of large public gatherings like public buildings, courthouses, transportation hubs, schools, banks and other financial institutions, high-value manufacturing plants, amusements parks, and other areas, society aims to meet the needs

for increased security. Consequently, there is the requirement to search individuals for concealed weapons and explosives so as to prevent terrorist attacks, ensure protection of secure facilities, and guarantee public safety. Such searches must be effective and precise. However, it should be made certain that the searches involve minimal inconvenience, and that they do not pose problems for the individuals being searched.

The most traditional method of concealed weapons and explosives search that is currently used, involves a more hand–on approach, which is also known as frisking. Although frisking might provide an efficient search technique, it is not acceptable in terms of not maintaining and assaulting the privacy of the individual. Also it can be extremely time consuming when searches need to be performed on an increased number of individuals. Therefore there is the need to develop special sensors which will perform the search and will essentially detect the concealed weapons.

The concealed weapons and explosives detection issue is visualized in three different scenarios:

Portal: People entering increased security areas should pass through a portal or gateway, as shown in Figure 1.1. The gateway sensors will scan or screen the people in order to search for weapons, plastic explosives and other illegal imports hidden under layers of clothing of people. In this way a direct physical search will not be needed.

Figure 1.1: Portal scenario.

Security checkpoints: People passing through an outdoor checkpoint or a border crossing will be scanned by sensors, as shown in Figure 1.2, so as to be searched from a safe standoff distance for concealed weapons and explosives. The scanning of people will ensure the protection of secure facilities.

Crowd Scanning: This scenario involves scanning people as they pass by the sensor, at various ranges on the street.

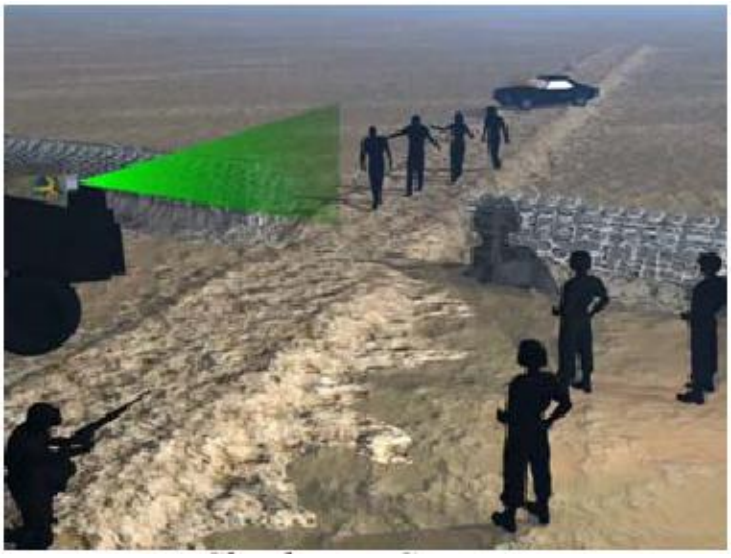

Figure 1.2: Checkpoint scenario.

Overview of existing systems

The motivation for concealed object recognition in different scenarios as mentioned above, has led the research community and industry into development of such systems. In the following paragraphs a review of these systems is presented along with their advantages and disadvantages.

Sensors

Conventional systems for the detection of concealed weapons and explosives at high security checkpoints include X-ray systems and magnetometers.

X -ray systems

Currently, one of the methods for weapon and explosive detection is the use of X-ray devices. These devices provide an X-ray image, which is more revealing than a metal detector. X-rays can provide an efficient search of luggage and other items. X-ray systems can provide detection of plastic ceramic or metal weapons; additionally X-ray systems can detect solid plastic explosives or liquid explosives. However health risks that have been observed make the X-ray search method unsuitable for weapons concealed on a person. These health issues are associated with the ionizing radiation emitted from X-ray systems [4, 5].

Magnetometers (Metal Detectors)

Metal detectors, or magnetometers, are common devices used to search for weapons and explosives with metal components. Magnetometers are devices that emit a

magnetic pulse, which if it encounters a metallic object it is reflected back to the source. Magnetometers are limited by many factors. Initially these detectors are limited to detecting metal objects, allowing dangerous items such as non-metal guns, ceramic weapons, and plastic explosives to go undetected. Furthermore another metal detector weakness is that, detection capabilities are directly related and depend on the level of the magnetometer sensitivity. Hence, if the sensitivity level is set too low, small dangerous metal weapons, such as box-cutters, could pass undetected. On the contrary, when the sensitivity level is too high, non-hazardous metallic objects cause false alarms. Therefore the high rate of false alarms limits the effectiveness of metal detectors [4] and the magnetometer sensitivity must always be examined.

However existing magnetometer sensors will have a new application in the concealed weapon detection via a technique, which is based on the distortion of the earth's magnetic field. These devices are called Gradiometer Metal Detectors (GMD) [6, 7]. The Idaho National Laboratory portal [5] where the gradiometer sensing technique is applied is shown in Figure 1.3 in this application the scanned person must pass through the portal. Gradiometers use a combination of sensors in order to improve the sensitivity of the field measurements. Thus the magnetic field difference between sensors is obtained. In general magnetometers have applications where the scanned person has an operating range which is limited to 3 m.

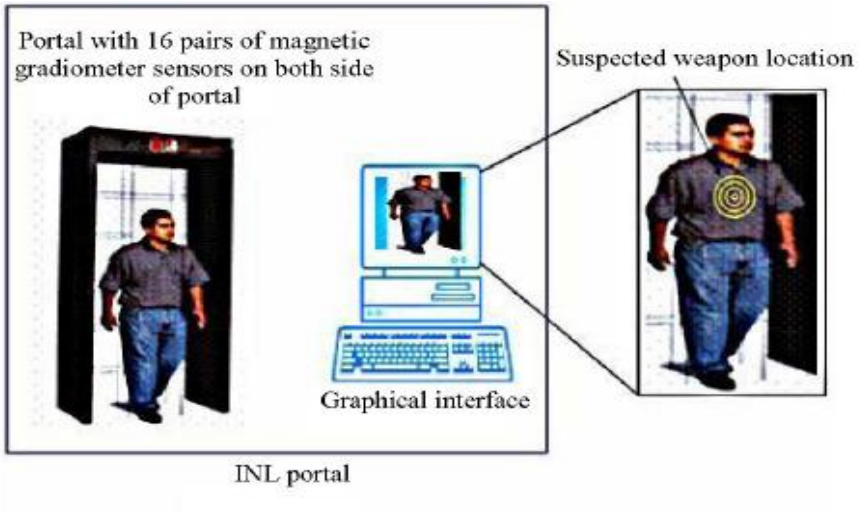

Figure 1.3: The Gradiometer Metal Detector [5]

Imaging Sensors

The weaknesses that the previous detection methods demonstrate increase the possibility for certain hazardous items to pass through security checkpoints without being detected. For example, as explained in [4], a body attached gun made out of composite plastic, would pass through current screening devices undetectable. Additionally, the previously presented systems are suitable for limited operating range, or certain proximity. So for the elimination of such problems special imaging sensors have been developed, these are Millimetre wave, Terahertz (THz) or Infrared imaging sensors. The scanning time required for weapon detection is always an issue. In practical weapon detection systems for airport or other high-throughput applications require high-speed scanning in the order of 3 to 10 s [4].

Millimetre Wave imaging

Millimetre wave screening systems or sensors used for concealed weapon detection operate in the frequency band between 30 GHz and 300 GHz and their wavelengths vary between 10 and 1.0 mm. Millimetre wave sensors measure the apparent temperature through the energy that is emitted or reflected by the complex human-concealed weapon object of the scene. Therefore Millimetre wave imaging is essentially based on the measurement of power received from the considered scene object via means of radiometers which are thermal radiation detectors. The received power from the object is a combination of the power that is emitted by the object and the power that is reflected by the object provided that the object is illuminated by the environment. The object illumination can be due to a natural or man-made source. The output of the sensors is a function of the reflectivity and the emissivity of the complex objects in the Millimetre wave spectrum as measured by the receiver. The output appears as the quantity of power that can be assigned a level within a gray scale to generate the image [8].

Millimetre wave sensors are classified in two types: passive and active. Passive sensors operate without Millimetre wave illumination and they observe whatever objects exist in the scene. Passive systems as presented in [8] rely on the fact that in the radio frequency spectrum natural surfaces like the human body naturally emit different amounts of Millimetre wave radiation depending on parameters such as surface brightness temperature and emissivity. Additionally the metallic hazardous objects like weapons or explosives, for which the sensor searches, are mainly reflective in the frequency spectrum, which means that the metal surface emissivity is reduced. In essence metal surfaces produce reflections due to illuminations from natural sources of the scene

of which, as explained in [5], the most significant source is the sky. Additionally the feasibility of non-metal weapon detection via Millimetre wave sensors is affected by parameters like emissivity and surface brightness temperature of the non-metal weapon. Passive sensors have the advantage of operating without transmitting any electromagnetic radiation on the human.

Normally active sensors work via emitting signals. Therefore, the active sensors excite the objects screened via transmitting a signal. The illumination signal is a Millimetre wave signal which is also called Millimetre wave light. The transmitted signal is incident to the objects of interest and interacts with them causing a reflected signal from the object back to the sensor.

In general as it is stated in [5] the Millimetre wave systems used for concealed weapon detection employ lower power levels than X-ray systems. Hence issues associated with the ionizing radiation which are often encountered in X-ray systems, are not present in Millimetre wave systems [9-11].

One issue for consideration of passive Millimetre wave sensors is the comparatively long time intervals of the individuals scanning that are required, so as to get a good image on the scanner screen. The long scanning time period is due to the fact that the human body emits very light millimetre -wave radiation while most of it comes at visible and infrared bands of spectrum. The focal-plane array sensor [12] was one of the first generation Millimetre wave sensors. First generation sensors needed 90 minutes in order to generate one image [12]. Advances in MMW technology of sensors have led to video-rate (30 frames/s) MMW cameras. However the quality of MMW images must be improved [12].

A different drawback of the Millimetre wave sensors is that they operate in relatively short distances from the scanned objects, since the scanned object must be within the focal plane of the sensor. These distances must be less than 7.62 m [5]. Additionally another weakness of the Millimetre -Wave sensors is the fact that millimetre -waves do not encircle the human body. Therefore the object must be in the line of sight of the sensor in order to achieve concealed weapon detection. Consequently it is crucial to scan the individual from several angles so as to perform a full search for concealed weapons and explosives [4]. Moreover Millimetre waves are attenuated by water, so the Millimetre wave screening systems may be affected by the humidity of the atmosphere and are vulnerable to environmental or bad weather conditions.

Terahertz (THz) imaging

The THz sensors used for concealed weapon detection, are active systems that transmit electromagnetic waves in the THz frequency band between 300 GHz and 300 THz and identify the weapon through the spectrum of the weapon reflected signal. Metal weapons or guns entirely reflect the incident THz wave, while ceramic or non metal weapons partially reflect the THz wave, also known as THz light. The skin almost absorbs the THz light since the skin has high water content [13]. Consequently in a THz image the human's skin would emerge essentially dark. However the reflected signal of a weapon would be visible.

The utilisation of THz sensors presents some advantages which are: THz radiation is harmless to human, while due to the frequency bandwidth considered this class of transmitted signals offers some spatial resolution. However there are some issues for

consideration which are: medium or low penetrability of THz waves through some kinds of clothes, and low penetrability of THz waves through atmosphere for the case of stand-off detection. In general THz waves are attenuated by the atmosphere and by the existence of water. Hence THz sensors are vulnerable to environmental conditions and operate at small distances. Additionally, as noted in [5], the THz rates of capturing an image have been improving. Originally THz imaging systems required several minutes in order to capture an image.

Infrared imaging

Infrared imager is another class of sensors used for concealed weapon detection. Infrared sensors operate in the frequency band between 200 THz and 400 THz. Infrared imagers, as presented in [5], are passive sensors that use the information on the temperature distribution of the object to form an image. Therefore different objects have different wavelengths according to their individual temperature. The infrared radiation power emitted by the object also depends on the size and the emissivity of the object [5]. Infrared imagers are used for many night vision applications such as observing vehicles.

However infrared imaging for concealed weapon detection has some considerable drawbacks. Infrared waves emitted by the human body do not penetrate through the clothes. Additionally the radiation emitted by the human body is absorbed by the clothes and re-emitted. Consequently infrared radiation cannot show the image of a weapon unless the person is wearing tight clothes. When the person wears loose clothes the emitted infrared radiation is distributed on the loose clothes so it is spread over a widened

area. In this case the ability of the infrared sensors to produce the image of a weapon is decreased since the weapon temperature cannot be retrieved [12].

Hybrid imaging sensors

The considered significant drawbacks of infrared imaging have lead to the creation of sensors that deploy both millimetre waves and infrared or optical imaging methods. The images from millimetre wave method and infrared or optical method are assembled by means of algorithms and this process is called fusion. Before the assemblage each image is pre-processed in order to boost some image features and reduce any noisy data that is contained in the image [12]. Figure 1.4 shows the result of image fusion. The image on the left is the optical one and the central image is the Millimetre wave image. On the right the result of the fusion process can be seen.

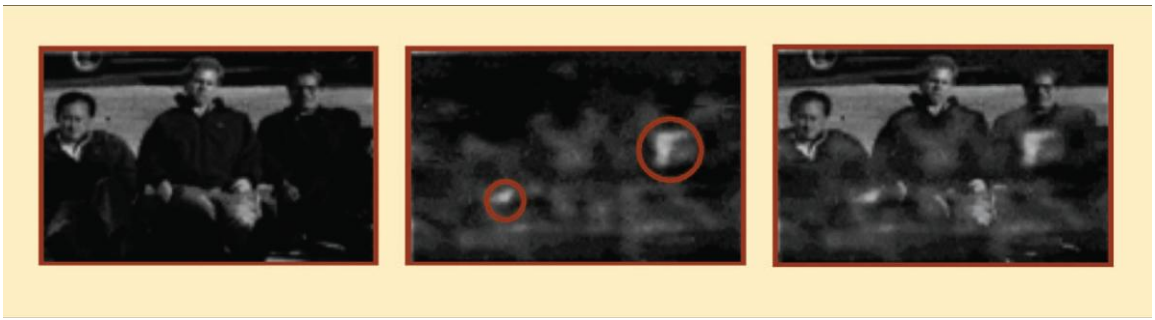

Figure 1.4: Concealed weapon detection via image fusion [12].

This section presented the various sensors used for concealed weapon detection and their relative advantages and drawbacks. The most critical drawbacks that these sensors have are: the relatively short standoff distances in which some sensors operate, the long scanning time period needed for some sensors and the vulnerability of the sensors to weather or environmental conditions. For the elimination of such problems

special sensors need to be developed, which will have improved capabilities of CWE remote detection and will be robust to environmental conditions. These sensors must execute the individual's scanning and they should have the ability to "see through" most clothing materials. Such sensors should also provide some information on the shape and the material of the CWE or other hazardous objects and thus being able to present their identity.

In this thesis the UWB radar, which has been effectively applied in many cases for target-object recognition, is considered for the remote detection and identification of CWE. The major advantage of UWB radar is that it can operate in extended standoff distances and that it is robust to harsh environmental conditions. Hence it is considered as a complimentary sensor for further data fusion or alternative technological solution to the systems described above. In brief, an optimised sensor will aid in the CWE detection and in determining what kind of threat a CWE poses. In this way public security would be increased and inconveniences such as time consuming - privacy disturbing individual searches would be minimised. In the next section the aim of the thesis is stated along with the methodology that will be followed.

1.3 Problem Statement, Original Contributions and Methodology

The research in this Thesis is targeted to the remote body –worn CWE detection via LTR analysis in UWB radar. Therefore the Thesis explores the issues and investigates the essential problems related to the detection of the CWE. Fundamentally any target (object) illuminated via a UWB sensor produces a reflected field, which if it is

transformed in the time domain, it gives rise to the object's IR. Within the IR, the LTR [14] of the object is included, so considering the time domain representation; the LTR is part of the IR. The LTR has the form of a series of damped sinusoids and if it is extracted it provides a unique electromagnetic signature or a unique spectrum for that specific object. This electromagnetic signature consists of the complex natural resonant frequencies of the object or poles of the object's transfer function. The LTR and the resonant frequencies depend on the shape, dimensions and electrical properties of the object of interest

In the case of CWE detection via UWB radar, the specular reflection from the human is much higher than the reflection from the CWE for which the sensor searches, due to the bigger dimensions of the human. Consequently, the reflected field from an individual with a CWE is very similar in magnitude to the reflected field from an individual without one. However the LTR from the human-CWE composite object could provide both the resonant frequencies of the human and the resonant frequencies of the CWE. Hence, if a method is found in order to obtain the CWE complex natural resonant frequencies through LTR analysis, detection of the CWE will be possible.

On the fundamental concept, as presented above, this Thesis lays the framework in order to examine the feasibility of distinguishing the resonant frequencies of the CWE from the overall resonant frequencies of the human-CWE composite object. In order to achieve this original contribution the following methodology is considered:

- The first stage in any radar design is the selection of the suitable waveform, since the performance of radar critically depends upon the transmitted waveform. Therefore the appropriate UWB waveform that will lead to the excitation of the

resonant frequencies of the weapon or explosive is synthesized. The waveform is designed by means of frequency stepped pulse compression, and on the basis of the band of resonant frequencies of the weapon or explosive that will be detected.

- The next stage is the presentation of the concept of resonant frequencies, and the appreciation of how these frequencies are involved in the LTR of the object. The role of the resonant frequencies can be understood by transformation of the reflected field of the object in the time domain i.e. by obtaining the object's IR, from which the LTR is selected and it is analysed.
- Furthermore, the objective is to extract the resonant frequencies from the LTR of the studied object, as an essential process for the object's detection. In order to find an algorithm to extract the resonant frequencies of any object, the sphere is considered as the object whose backscattered field is described from scattering theory. Thus the conducting sphere IR is derived and consequently it is generated via a computer simulation algorithm. For the obtained IR, techniques for signal modelling are applied on the LTR in order to numerically extract the poles of the sphere simulated LTR and their residues. When the numerically extracted poles coincide with the precise analytical solution for the sphere poles, the algorithms for pole extraction will be considered reliable. Therefore these algorithms will be applied as the basis for pole extraction of experimental LTRs of different composite objects as presented later in the Thesis.
- The next issue is to experimentally obtain the sphere IR and confirm that the experimental LTR corresponds to the theoretically obtained one. Once the experimental LTR of the sphere is obtained its poles and residues are extracted.

These poles and residues are compared with the ones extracted from theoretical LTR. In this way the accuracy of the experimental data for this experimental set-up is tested and conclusions are drawn on the different parameters that are used for the processing of the experimental measurements.

- The most important stage of the thesis is to carry out an experiment with the human and CWE as a complex target. In this way it is possible to examine the human-CWE poles and residues as the position of the CWE on the human body changes, and compare them with the human poles and residues. Research on CWE detection in this Thesis is focused on the grenade as it is the smallest one among all possible CWEs (grenade, pistol, Uzi, small machine guns). Therefore its detection will be the most difficult as it has the smallest reflected field amplitude. Hence grenade detection, although more difficult, will naturally indicate that detection of bigger CWEs is also feasible. Additionally the grenade is the most probable weapon to be carried by a terrorist due to its small size and destruction capabilities. For the grenade detection its resonant frequencies must be estimated, so the conducting sphere of radius $\alpha = 0.0325$ m is used to approximate the grenade as an object whose theoretical resonant frequencies are previously evaluated. So throughout the Thesis the sphere will be used as the object that must be detected. This experiment will be carried out initially with a flat reflector as the target approximating the human and most importantly with a human as the target.
- The final issue is to draw conclusions as to whether there is a difference in the observed resonant frequencies or poles (human poles and human-sphere poles), or

difference in the amplitudes of the respective poles, i.e. amplitude modulation at the specific poles of interest, when the sphere is present. Any difference in the clustering of the poles at natural resonant frequencies of sphere or any amplitude (residue) modulation due to the existence of sphere will signify that the detection of the sphere or the approximated CWE attached to the body is feasible.

This section presented all the essential issues that will be addressed and resolved for efficient detection of concealed weapons and explosives via UWB radar at a stand-off distance.

1.4 Thesis Outline

According to the problem statement and methodology of the research, as presented in the previous section, this thesis is organised in seven chapters.

Chapter 2, overviews the essential issues related to the transmission of a UWB waveform as a signal which is incident on the object and outlines the aspects in relation to the reflected wave from the illuminated object. The general description of radar systems is followed by the definition and analysis of pulse radar. Furthermore pulse compression techniques are investigated. This chapter also describes the reflected wave via the Radar Cross Section (RCS) and presents the resonant frequencies bands of the possible CWE that may be detected. Finally the transmitting signal power for detection of a grenade is estimated for a stand-off distance of 30 m.

Chapter 3 reviews the fundamental theoretical principles, which allow the detection of an object via UWB radar. These principles are utilised to analyse the transient reflected field from an object and thus represent the reflected wave in the time

domain. Therefore the analysis of the transient signals leads to the formation of the object's IR. The IR of the object involves the LTR which consists of poles or complex natural resonant frequencies and residues.

The original contribution of this Thesis starts in chapter 4, which presents the theoretical backscattered far field of the sphere and in this way the theoretical poles, IR and LTR of the sphere are obtained via simulation. Furthermore, this chapter analyses the signal processing algorithm for pole extraction. These algorithms are used to exponentially model the theoretical LTR of sphere and numerically extract its poles and residues. Since the theoretical sphere poles coincide with the numerically extracted ones, these algorithms can be used as the basis for processing of experimental LTRs, as studied in the following chapters.

Chapter 5 analyses the experimental configuration, methodology and results for detection of a grenade appended on the human. For this stage the conducting sphere of radius $\alpha = 0.0325$ m is used to approximate the grenade. Additionally a flat reflector is used to approximate the human. In chapter 6 the same experiment as in chapter 5 is repeated, however the approximated grenade or sphere is attached to the human. Conclusions for the detection of the sphere are drawn as the position of the sphere on the human body changes. Finally chapter 7 concludes with a discussion of the results of investigations completed. Useful conclusions are drawn about all essential observations.

1.5 Publications arising from this Research

1. Vasalos, A., Vasalos, I., Ryu, H. G., Fotinea S. E., "LTR Analysis and Signal Processing for Concealed Explosive Detection ", IEEE GEMIC 2010 International conference, Berlin, Germany , 2010 pp. 166-169.
2. Gashinova, M., Cherniakov, M., Vasalos, A., "UWB signature analysis for detection of body-worn weapons", IEEE Radar 2006 International conference, Shanghai, China, 2006 pp. 1-4.
3. Cherniakov, M., Vasalos, A., "Pedestrian Recognition via Ultra wideband (UWB) Radar ", International Workshop on Intelligent Transportation – WIT 2005, Hamburg, Germany, Proceedings pp 95-99, 2005.
4. Cherniakov, M., Vasalos, A., "Ultra Wideband Radar for Pedestrian Recognition", First International Conference VehCom-2003, Birmingham, UK, June 2003, Proceeding pp. 61-66.
5. Vasalos, A., Ryu, H. G., Vasalos, I., Fotinea, S. E., "Fast Concealed Weapon Detection via LTR Analysis", IEEE RadarCon 2011 International Conference, Kansas City , USA , 2011, pp. 979-984 .
6. Vasalos, A., Vasalos, I., Ryu, H. G., Fotinea, S. E., "LTR Analysis for Fast Concealed Weapon Detection ", IEEE GEMIC 2011 International Conference, Darmstadt , Germany , March 2011.

Chapter 2

ULTRA WIDEBAND RADAR OVERVIEW

2.1 Introduction

This chapter overviews the fundamental aspects associated with the illumination of an object with an incident Ultra-Wideband (UWB) waveform, and the reflected wave from the illuminated object. Initially a general description of radar systems is presented and it is followed by the definition and analysis of pulse radar. In addition, methods of compression of the transmitted pulse waveforms, like phase, frequency modulation, and frequency stepping are analysed. Furthermore the evolution of conventional radar to the UWB radar is considered, and the UWB radar is defined. Moreover there is an overview of the applications of UWB radar.

The consideration of the reflected wave from the illuminated object starts by the definition of Radar Cross Section (RCS). Furthermore the deployment of the RCS in the radar equation is shown, and the dependence of RCS on parameters like angle of incidence, angle of scattering, incident field polarisation and frequency is described.

The overall goal of the thesis is the investigation of the feasibility of concealed weapon detection via Late Time Response (LTR) analysis in UWB radar at a stand-off distance. In section 1.3 it was presented that the technique for the detection is the acquirement and the study of the complex natural resonant frequencies of the weapon. The range or band of resonant frequencies of the weapon may be obtained via consideration of the RCS of the weapon. Therefore the description of the reflected wave from the weapon starts with the weapon RCS.

Amongst all probable CWEs the grenade is the object that must be detected, and therefore as explained in Section1.3 the sphere of radius 0.0325 m is used to approximate the grenade. In this way the RCS plot and the natural resonant frequencies band of the

particular sphere are obtained. Therefore an estimation of the grenade RCS and resonant frequencies band is discussed. Other weapons, whose resonant frequencies bands are considered, are the machine gun AK-105, the M1911A1 and Uzis since these could be potential concealed weapons that should be detected.

2.2 Radar Signals

2.2.1 Generic Radar

One of the aims of current technology is the consideration and the solution of problems related to the remote sensing and detection of various objects. The deployment of radar systems is one method of resolving these problems. Section 2.2 describes the general issues associated with processing of the radar signals. Figure 2.1 shows a generic system block diagram of a radar system [14].

Radar systems involve the utilisation of a device that generates the transmitted signal and analyses the received signal, as it will be discussed later, in our experimental procedure this device is a vector network analyser. Additionally, transmitting and receiving antennas are deployed as the interface that manages the coaxial cable to free space interference. The antennas radiate electromagnetic waves or receive the reflected electromagnetic waves from the target, in order to detect, locate and identify the target (object).

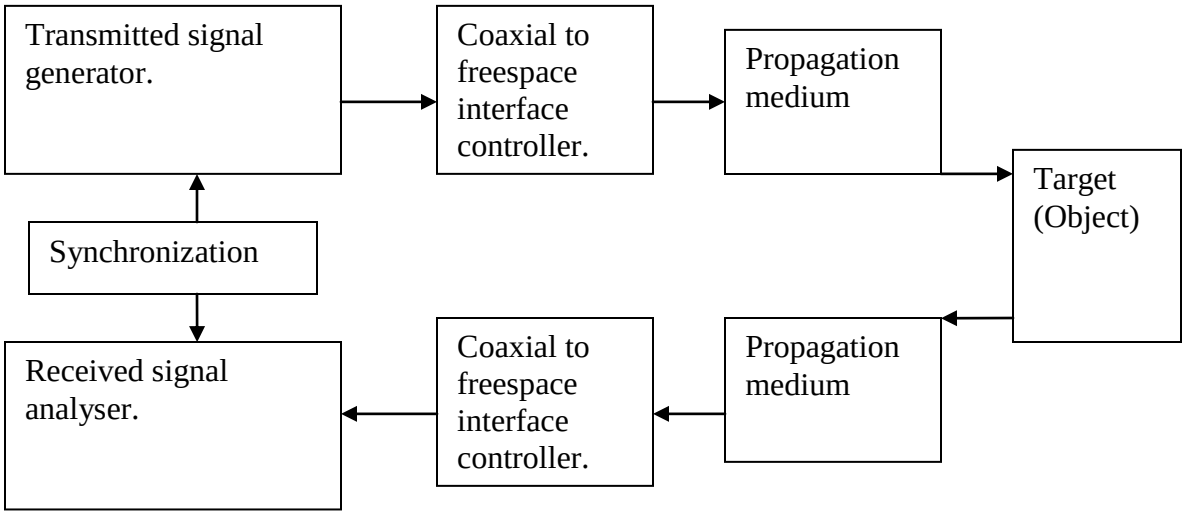

Figure 2.1: Block diagram of a radar system [14].

2.2.2 Monostatic and Bistatic Radar

Depending on the relative positions of transmitter and receiver, the radar system can be characterised as monostatic or bistatic. Since bistatic radar is beyond the scope of this research, this will not be discussed further. The term monostatic refers to the cases where, there is either one common antenna, as shown in Figure 2.2.a, which switches mode and is used for both transmitting and receiving, or there are two antennas used as the transmitter and receiver, as shown in Figure 2.2.b, which are close to each other or collocated.

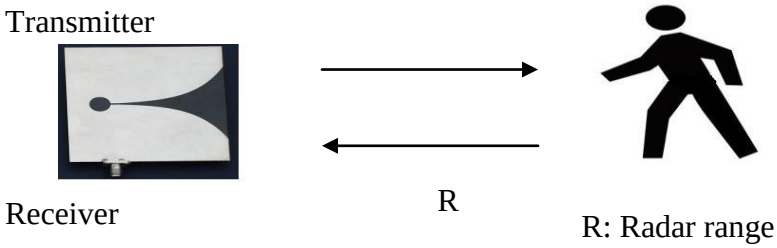

Figure 2.2.a: Monostatic radar with one Vivaldi antenna configuration (Conditionally Vivaldi broadband antenna is shown).

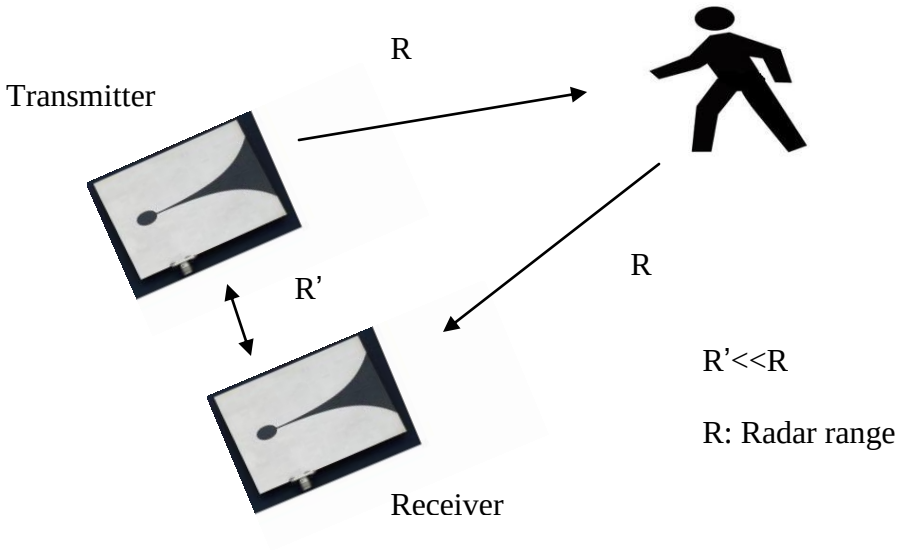

Figure 2.2.b: Monostatic radar with two Vivaldi antennas configuration (Conditionally Vivaldi broadband antennas are shown).

In this project, the utilisation of monostatic (two antennas configuration) ultra wideband (UWB) pulse radar for concealed weapons detection is addressed as the object of research. The term pulse radar refers to the case where the transmitted signal resembles to the shape of a pulse. Additionally, for reasons of radar performance improvement, the transmitted waveform is modulated using procedures described by pulse compression at the reception side, as analysed in the following subsections.

2.2.3 Pulse radar

The pulse radar system transmits a series of electromagnetic pulses. After each pulse is transmitted it propagates at the speed of light c. When the pulse is incident on a target, it is backscattered and a portion of the reflected energy is received at the radar where it is analysed.

The pulse radar transmits the train of pulses at a specific Pulse Repetition Frequency (*PRF*). This pulse train is the overall transmitted signal while each transmitted pulse is referred as the sub-signal. If the reflected wave from a previous pulse is received after a subsequent pulse is transmitted, then the reflected wave would be considered to originate from a target at a much shorter distance or range. This would generate an ambiguity with respect to the range of the target. Since the existence of the pulse radar is primarily related to the definition of the target range and the target coordinates, ambiguities related to the target range should be eliminated.

The maximum unambiguous range which the pulse radar can measure, is related to *PRF* with [14, 15]

$$PRF = \frac{c}{2R_{max}} \tag{2.1}$$

where R_{max} is the maximum unambiguous range of the radar.

The *PRF* is the inverse of the inter-pulse interval or pulse repetition period τ_T which is equal to the duration of the transmitted sub-signal or, to the length of period of the overall signal, and it is defined by

$$\tau_T = \frac{1}{PRF} \tag{2.2}$$

From equations (2.1) and (2.2)

$$R_{max} = \frac{c}{2}\tau_T \tag{2.3}$$

The individual pulse length (or pulse width), is given by [15, 16]

$$\tau = \frac{1}{B} \tag{2.4}$$

where *B* is the total bandwidth of the transmitted signal. Therefore the pulse length is inversely proportional to the transmitted signal bandwidth, assuming matched filtering [15].

An illustration of the transmitted pulse $Pu(t)$ and its associated parameters, pulse length τ and inter-pulse interval τ_T, are shown in Figures 2.3 and 2.4 respectively. Accordingly the magnitude of the frequency spectrum $Pu(e^{j\omega})$ of the pulse is shown in Figure 2.5 and is obtained via Fourier Transform (FT) of $Pu(t)$.

The ratio of the pulse length τ to inter-pulse interval τ_T, determines the radar's duty cycle as

$$DT = \frac{\tau}{\tau_T} \tag{2.5}$$

A study of Figures 2.3, 2.4 and 2.5, shows that the bandwidth of the pulse is *B* = 0.05 GHz while the pulse width is equal to τ = 20 ns. The inter-pulse interval τ_T is equal to 200 ns. The pulse $Pu(t)$ is the outcome of the modulation of a rectangular time domain pulse with the carrier signal $cos(\omega_{ca} n\Delta t)$ of frequency $f_{ca} = 1$GHz. As a result in Figure 2.5 the real part of the spectrum $Pu(e^{j\omega})$ is symmetric around the frequency of 1 GHz. For this pulse the radar's duty cycle is $DT = 0.1$. As it is shown in section 2.a of the appendix, a periodic signal such as the pulse of Figure 2.4 yields a discrete frequency spectrum. The frequency increment or step of the spectrum of Figure 2.5 is equal to $\frac{1}{\tau_T}$.

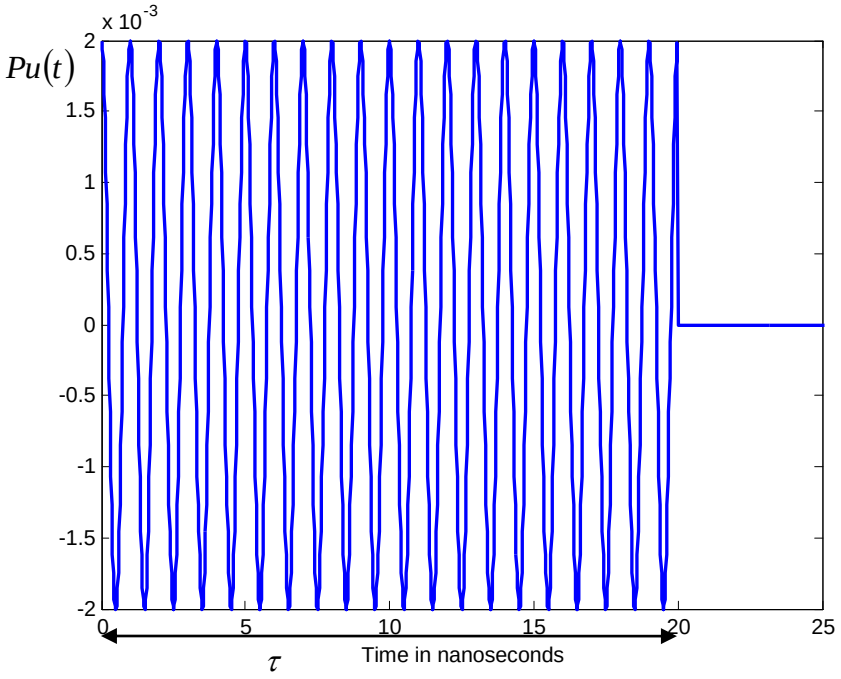

Figure 2.3: The transmitted pulse and parameter τ .

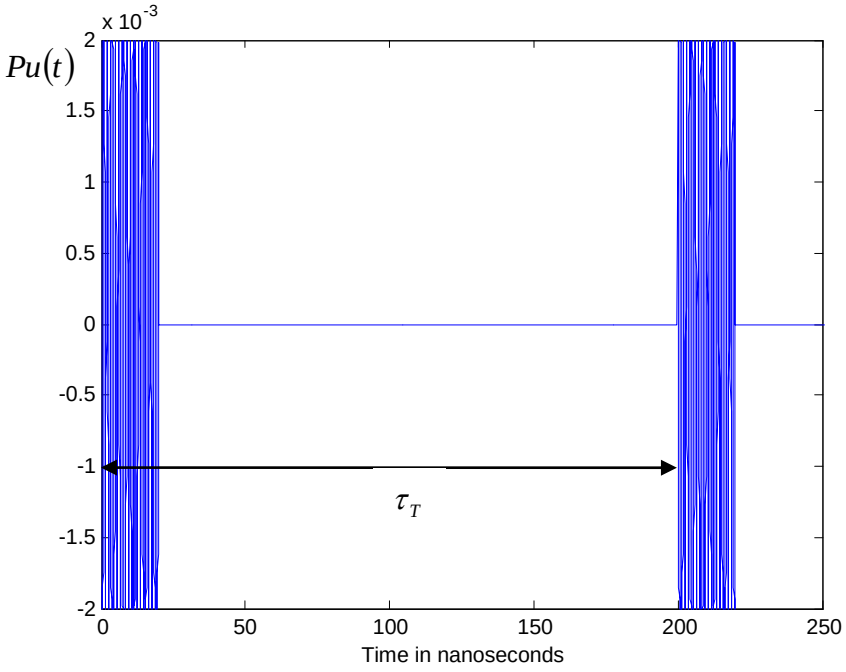

Figure 2.4: The transmitted pulse and parameter τ_T .

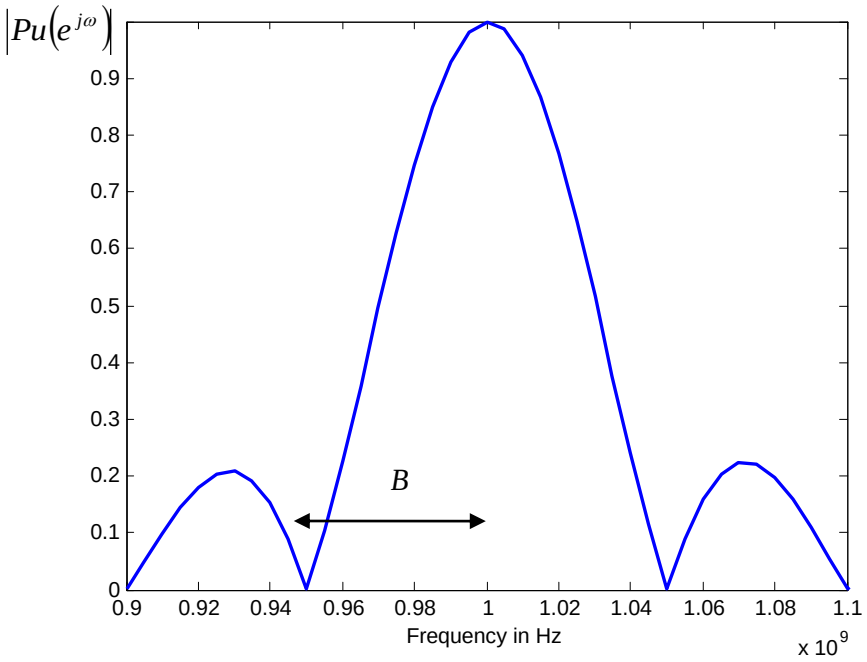

Figure 2.5: Frequency spectrum of the transmitted pulse and the bandwidth B .

Since the pulse radar is primarily used for the definition of the range of the target, it is essential to consider its range or spatial resolution. The range resolution implies the increment of range between any two neighbouring discrete range positions. In [15, 16] the range resolution is defined as a function of pulse width τ and is given by

$$\Delta R = \frac{c\tau}{2} \tag{2.6}$$

Combining (2.6) with (2.4) yields

$$\Delta R = \frac{c}{2B} \tag{2.7}$$

Considering equation (2.6) and equation (2.7), it can be seen that the range resolution is proportional to the pulse width or inversely proportional to the transmitted pulse bandwidth. Consequently, shorter pulses result in increased range resolution.

Enhanced range resolution is significant when the target range or position must be known with increased accuracy in the determination of the range.

The principle of target detection via radar at a specific range fundamentally depends on the transmitted signal energy, since it is required that the level of the received signal exceeds the receiver noise level. Receiver noise includes the receiver thermal noise depending on the considered bandwidth, the radar clutter and interference signals from other radar sets like jammers or communication transmitters. Therefore an adequate Signal-to-Noise Ratio (SNR) at the receiver is needed and this SNR depends on the energy of the transmitted signal.

The energy of the transmitted signal depends on the pulse peak power and on the pulse length. As was stated above shorter pulses are suitable for range or spatial resolution. However, for a particular peak power P_t, shorter pulses result in lower average power $\overline{P}_t$ and lower overall energy during the time required for detection which is called the integration time. Consequently the receiver (SNR) is also low. This means that the detection of the target with the presence of high level of receiver noise at the specific range is not feasible, or that the range of detection is limited.

The average power is given in terms of the peak power and the duty cycle as

$$\overline{P}_t = P_t \frac{\tau}{\tau_T} \tag{2.8}$$

$$\text{or} \quad \overline{P}_t = P_t \tau (PRF) \tag{2.9}$$

The deployment of a transmitter that will radiate a time domain pulse of high peak power will result in long range detection and sufficient range resolution. However, high power transmitters are generally more complex and they face reliability problems.

An alternative approach of maintaining a high average power and thus achieving extended range detection and adequate range resolution without increasing the output peak power of the transmitter, are either the coding i.e. modulation of the transmitted pulse or the technique of frequency stepping. The most well known schemes of coding are the Phase Modulation (PM) and the Frequency Modulation (FM). FM can be either linear (chirp waveform) or non-linear. The methods used for pulse modulation and the technique of frequency stepping are generally called pulse compression [17]. In order to detect the signal and distinguish it from noise in radar receivers, pulse compression techniques are used to improve the SNR.

Phase modulated pulse

Phase modulated pulse, is the case of coding in which the long pulse is subdivided into a number of equal length sub-pulses. Each one of the sub-pulses has its own phase modulation; therefore each sub-pulse is transmitted with a particular phase. The phase of each sub-pulse is adjusted according to a particular "phase code". This code is a binary sequence that consists of the values 1 and -1 and these values correspond to the phases of the sub-pulses which are either 0 or π, according to each binary value in the phase code. Hence the transmitted long pulse is in essence a sequence of binary phase coded sub-pulses. There are many ways of selecting the codes. For example, one of the schemes is the Barker codes [15], which are also called optimum codes since they provide low ambiguity function sidelobes. For example, a seven bit phase coded radar pulse contains 7 times the energy of a non-coded pulse of the same range resolution or the range resolution is seven times finer than a non-coded pulse of the same length or duration and

overall energy. Transmission of a phase modulated pulse provides a reflected field, which can be uniquely identified by the receiver. In this way the receiver discriminates between the signals and rejects the unwanted ones. As an example, Figure 2.6 shows the seven bit Barker baseband pulse of sequence [1,1,1,-1-1,1,-1].

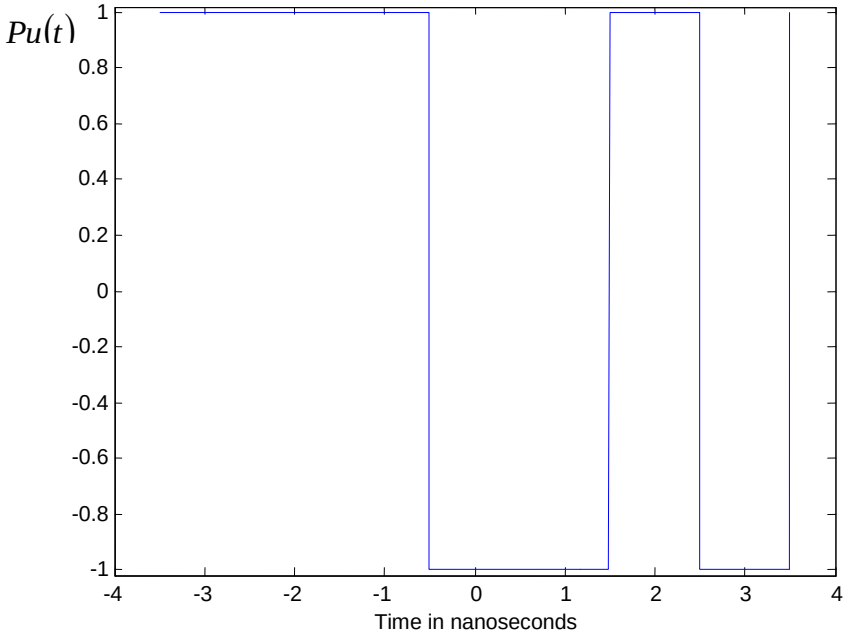

Figure 2.6: Seven bit Barker baseband pulse.

Figure 2.7 shows a seven bit Barker phase coded pulse of sequence [1,1,1,-1-1,1,-1], while Figure 2.8 the non-modulated pulse. Apparently the pulse of Figures 2.7 has 7 times better range resolution than the pulse of Figure 2.8. Figure 2.9 shows a slice or cut through the ambiguity function diagram [15] at zero Doppler, with respect to time displacement or shift. The plot of Figure 2.9 is created via the autocorrelation of the pulse in Figure 2.7, zero displacement means that the pulse or code and its copy are

aligned. The ambiguity function squared in terms of Doppler frequency f_D and time displacement τ_D is given by the integral $\left|X_{AF}(\tau_D, f_D)\right|^2 = \left|\int_{-\infty}^{\infty} Pu(t)Pu^*(t-\tau_D)e^{2\pi j f_D t}\,dt\right|^2$

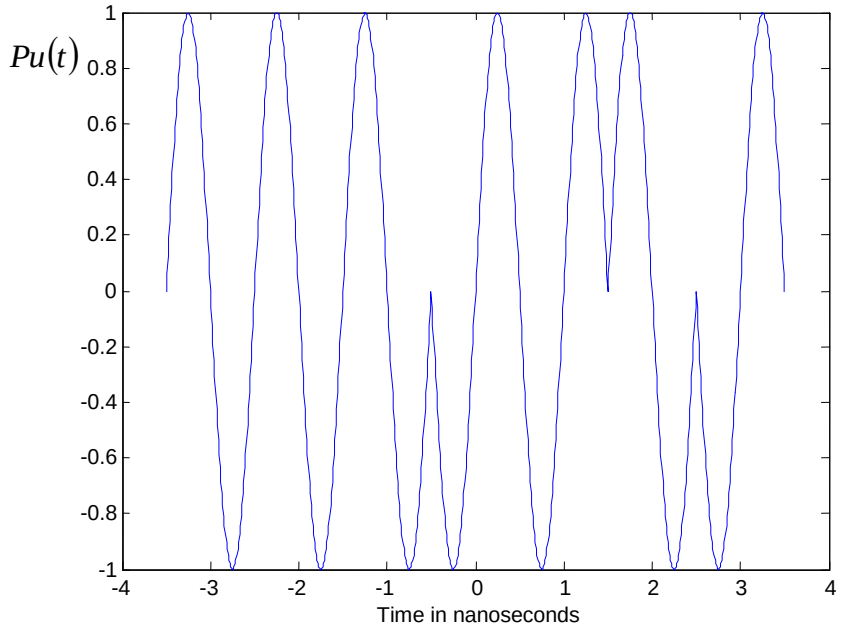

Figure 2.7: Seven bit Barker coded pulse.

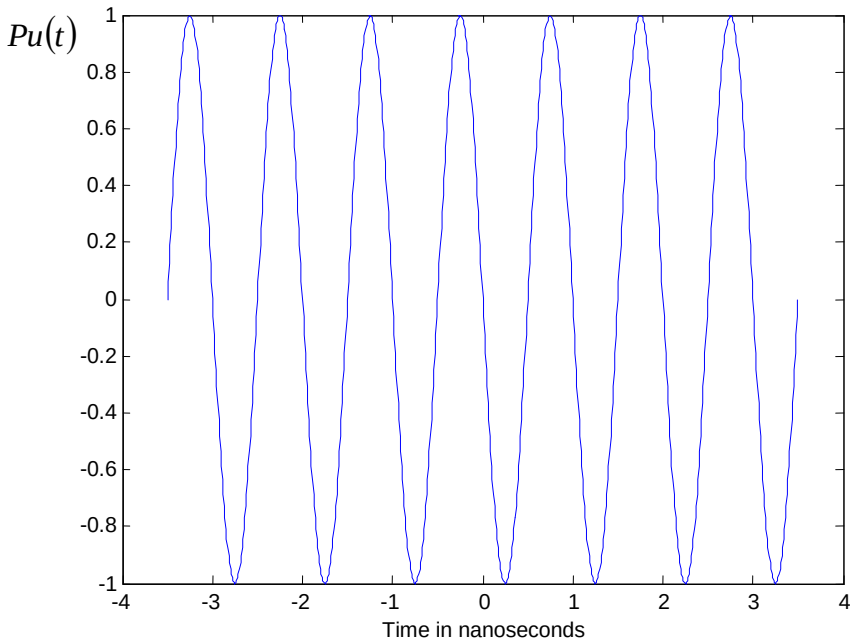

Figure 2.8: Non-coded pulse.

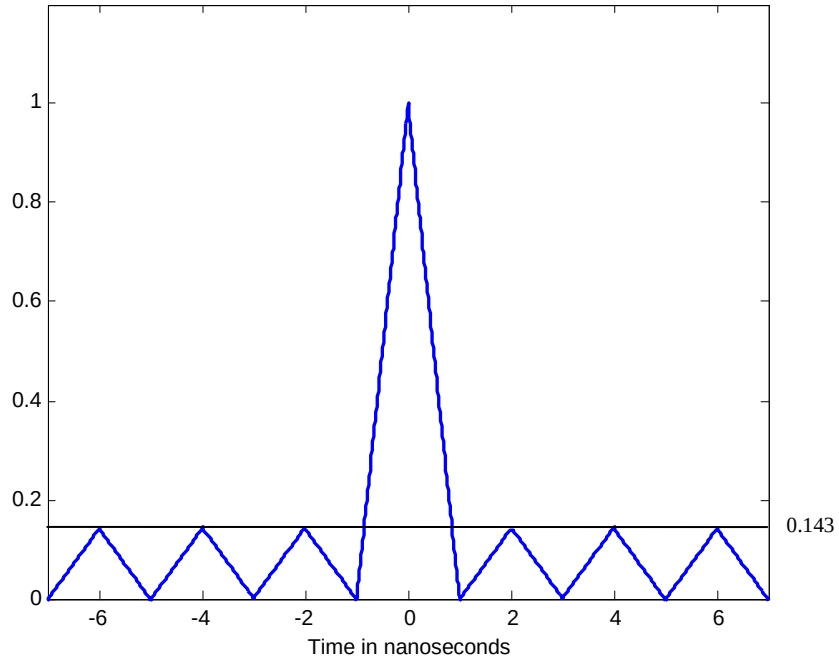

Figure 2.9: Slice through ambiguity function at zero Doppler against time displacement.

Linear frequency modulated pulse (chirp)

A linear frequency modulated pulse or chirp pulse, is the signal in which the frequency increases or decreases with time. A continuous chirp pulse is defined in [15], [16] by

$$Ch(t) = exp\left(j\pi k_2 t^2\right) \tag{2.10}$$

In this pulse, the instantaneous frequency is estimated by differentiation of the phase of the pulse and therefore is given by

$$\omega(t) = \frac{d}{dt}\left(\pi k_2 t^2\right) = 2\pi k_2 t \tag{2.11}$$

$\omega(t)$ changes linearly versus time t, while the phase of $Ch(t)$ varies quadratically versus t. If τ is the length of the two sided chirp pulse [15], for the one sided chirp pulse the

variable t takes values in the range $\left[-\frac{\tau}{2},0\right]$. So $\omega(t)$ for the one sided chirp pulse, sweeps in the range $\left[-\frac{2\pi k_2\tau}{2},0\right]$. Therefore the total frequency deviation or frequency sweep during the pulse is $\pi k_2\tau$ or $k_2\frac{\tau}{2}$ in Hz . Thus the bandwidth of the one sided chirp pulse is given by $k_2\frac{\tau}{2}$.

The parameter k_2 is also expressed as $k_2=\frac{B_{Ch}}{\tau}$ where B_{Ch} is the swept bandwidth of the two sided pulse in Hz. So the angular frequency $\omega(t)$ of the one sided chirp signal sweeps in the range $\left[-\frac{2\pi B_{Ch}}{2},0\right]$. Figure 2.10 shows a one sided chirp pulse and Figure 2.11 shows the instantaneous frequency of chirp pulse as a function of time t . Figure 2.12 shows a slice or cut through the ambiguity function diagram of the chirp pulse, at zero Doppler, with respect to time displacement or shift. The plot of Figure 2.12 is created via the autocorrelation of the pulse in Figure 2.10, zero displacement means that the pulse and its copy are aligned.

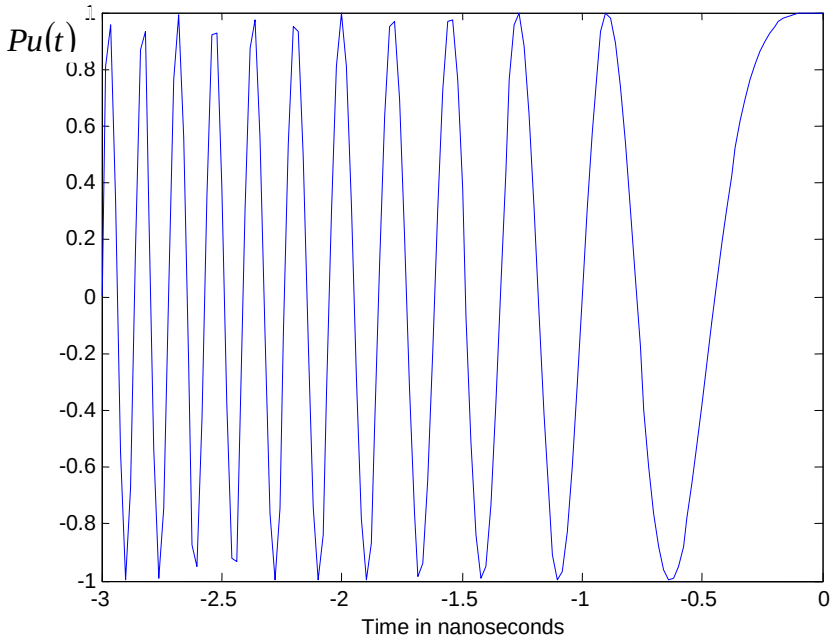

Figure 2.10: Chirp pulse.

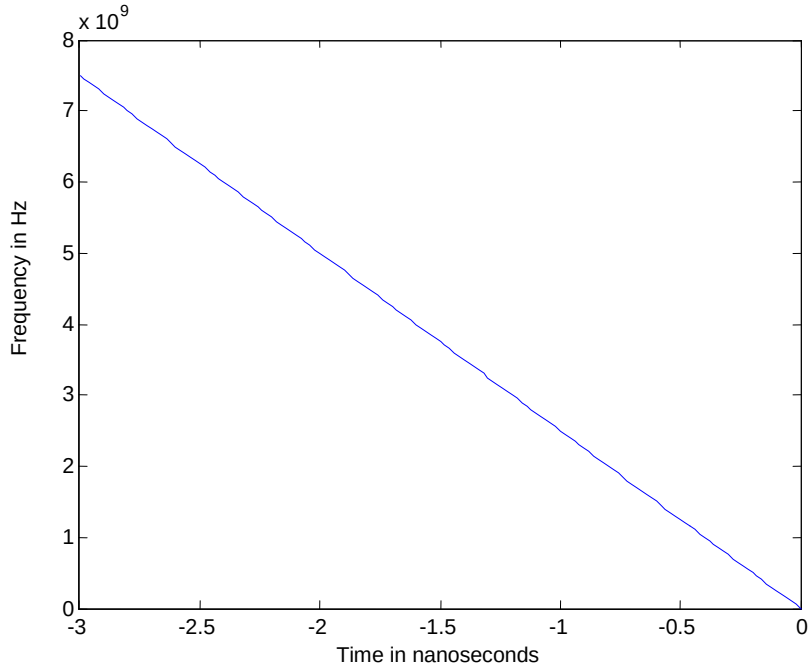

Figure 2.11: Instantaneous frequency of chirp pulse of Figure 2.10 as a function of time.

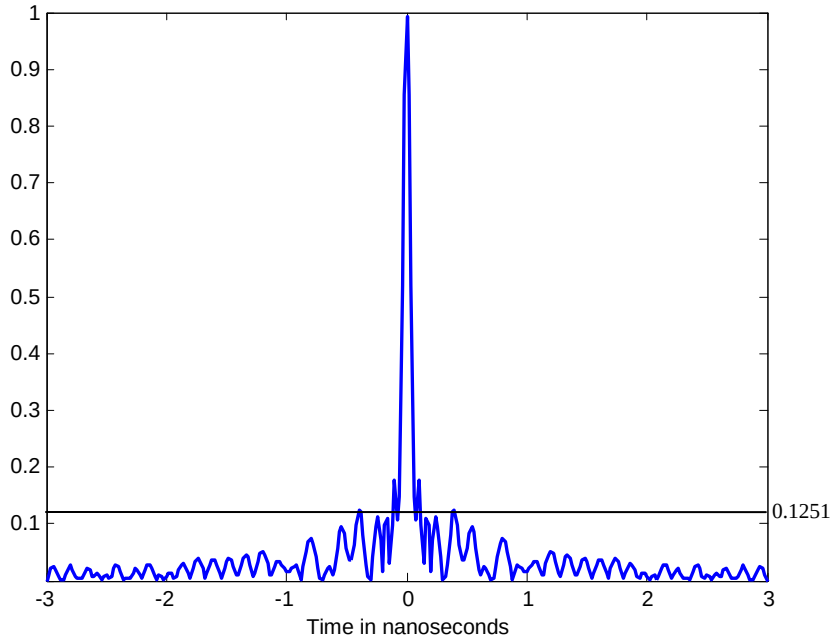

Figure 2.12: Slice through the ambiguity function at zero Doppler against time displacement.

The design of a frequency modulation system involves the consideration of two parameters. The first parameter to be selected is the pulse length, for a particular peak transmitter power. This parameter will influence the transmitted signal energy and therefore it will determine the possibility of detection of a target by the radar at a particular range. The second parameter is the required resolution. This parameter will determine the bandwidth of the transmitted signal.

Frequency Stepped Pulse Compression

Frequency stepping is a pulse compression technique in which discrete frequency steps are deployed in the transmitted signal. Additionally, the received waveform from the target is received and recorded in the frequency domain and it is transformed into time domain via Inverse Fourier Transform (IFT). In this way the data can be obtained

over a wide bandwidth. Hence pulse compression is achieved by increasing the signal bandwidth.

Frequency stepping may accomplish a better SNR by converting long-duration low-power received signals into short-duration high-power signals as explained in [17]. In this way the received signal power increases above the level of the noise power.

Theoretical background

Fundamentally frequency stepped pulse compression refers to a method used to increase the bandwidth and the power or energy of the transmitted time domain pulse [17]. In this method discrete frequency steps are applied to the transmitted signal in the frequency domain starting from the frequency f_0, so in essence there is a number of frequency stepped transmitted signals with increasing frequencies that are incident onto the target. Furthermore the reflected signal from the target is received and stored in these frequency domain steps. Considering the number of frequency steps is equal to N_1, and the total bandwidth of the transmitted signal is equal to *B*, then the relation between the frequency step Δf and B is

$$B = (N_1 - 1)\Delta f \tag{2.12}$$

Therefore the highest frequency of the transmitted signal as shown in Figure 2.13 is equal to $f_h = f_0 + (N_1 - 1)\Delta f$.

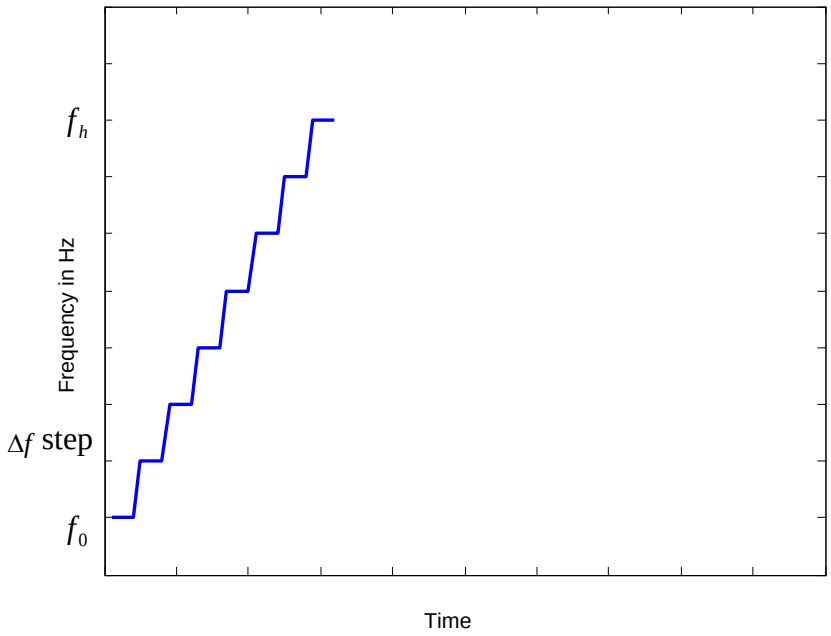

Figure 2.13: The frequency steps with respect to time

By means of applying an IFT on the frequency domain measurement, the transmitted signal can be represented in the time domain. Before the use of IFT the frequency domain signal is *zero padded*, or it is extended with zeros. This is a method of interpolation, which allows the selection of the sampling frequency of the time domain signal. Consequently the frequency domain signal is extended with $N - N_1$ zeros and the sampling frequency selected is equal to $f_s = (N-1)\Delta f$, which yields $\Delta f = \frac{f_s}{N-1}$.

As it is shown in Figure 2.14, and theoretically proved in section 2.a of the appendix, frequency domain sampling or stepping represented via the discrete spectrum $K_p\left(e^{j\omega}\right)$ yields a time domain signal $k_p(n\Delta t)$ which is periodic. The description of the frequency step in equation (2.a.7) of the appendix, is also $\Delta f = \frac{f_s}{N-1}$

Due to the periodicity, the inter-pulse interval τ_T of $k_p(n\Delta t)$, which is equal to the length of period of the overall signal, is defined by considering equation (2.a.7) of the appendix, therefore

$$\tau_T = (N-1)\Delta t = \frac{N-1}{f_s} = \frac{1}{\Delta f} \tag{2.13}$$

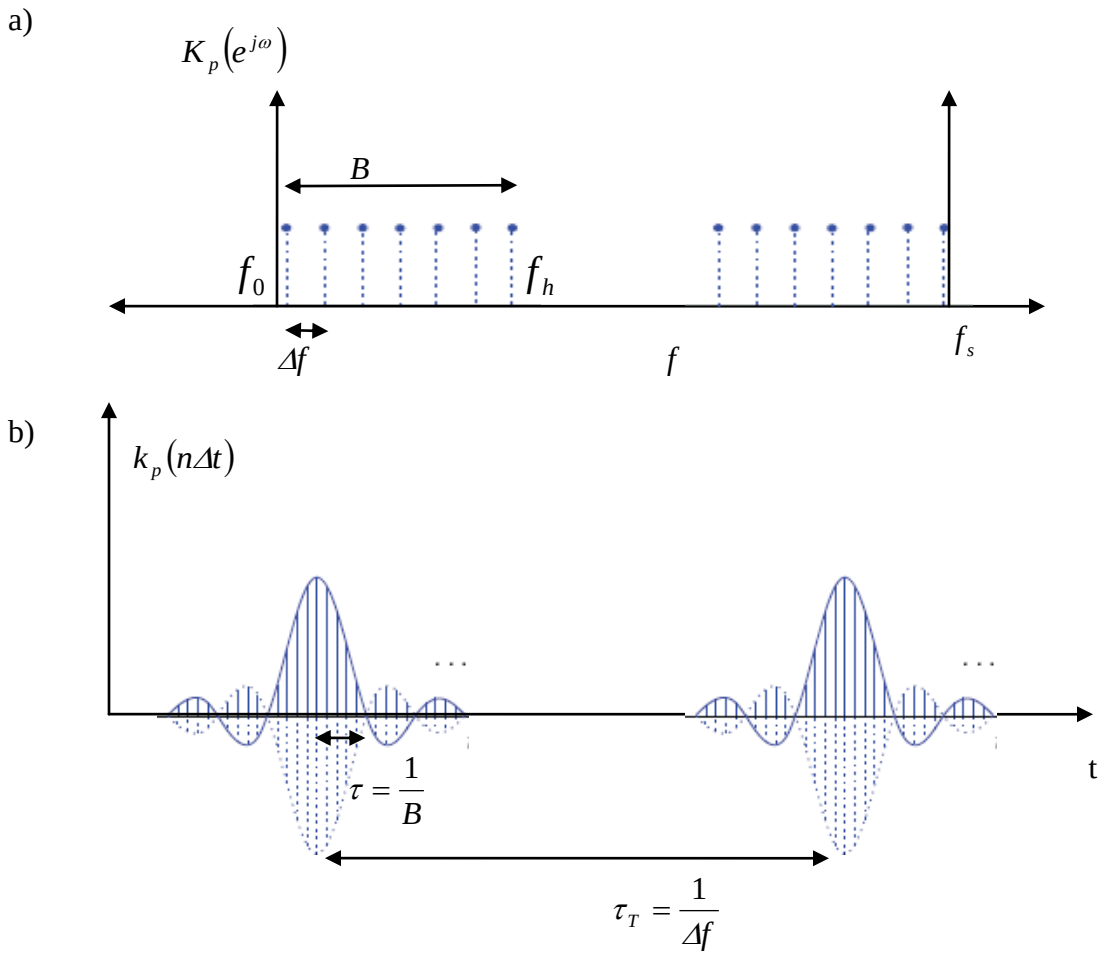

Figure 2.14: Frequency stepped pulse compression in (a) frequency and (b) time domain.

Considering equations (2.3) and (2.13) the maximum unambiguous range of the radar is equal to

$$R_{max} = \frac{c}{2\Delta f} \tag{2.14}$$

Since for the total bandwidth B there are N_1 frequency steps or samples, in the time domain there will be N_1 sub-signals or pulses of which the overall transmitted signal consists, therefore the duration T of the overall transmitted signal equals

$$T = N_1 \tau_T \tag{2.15}$$

The transmitted or compressed pulse length by means of equations: (2.4), (2.12) and (2.13) is defined as

$$\tau = \frac{1}{B} = \frac{1}{(N_1 - 1)\Delta f} = \frac{\tau_T}{N_1 - 1} \tag{2.16}$$

The pulse compression ratio is defined as in [4] by means of equations (2.15) and (2.16)

$$CR = \frac{T}{\tau} = \frac{N_1 \tau_T}{\frac{\tau_T}{N_1 - 1}} = N_1 (N_1 - 1) \tag{2.17}$$

Considering the spectrum $K_p(e^{j\omega})$, as it is proved in section 2.b of the appendix, if $K_p(e^{j\omega})$ is shifted in the frequency domain by a frequency ω_{ca} then the pulse $k_p[n\Delta t]$ is modulated with the carrier signal $cos(\omega_{ca} n\Delta t)$.

Frequency stepped pulse compression and synthetic range profile

Frequency Stepped Pulse Compression also contributes to the description of the synthetic range profile of the target. The range profile is defined as the backscattered field of the target as a function of range positions along the radar Line of Sight (LOS). Supposing that a simple target consists of various isolated scattering centres along the

LOS of the radar, the target range profile will constitute of a range of distinct peaks which will be spatially associated with the scattering centres of the target. As it is explained in [18] the synthetic range profile for a point target at initial range R when time is zero, which has a motion along the radar LOS and is illuminated by N_1 frequency stepped signals is given by

$$Hrp_{l_{rp}} = \frac{1}{N_1}\left[\exp\left(-j2\pi f_0 \frac{2R}{c}\right)\right]\frac{\sin(\pi y)}{\sin\left(\frac{\pi y}{N_1}\right)}\exp\left(j\frac{N_1-1}{2}\frac{2\pi y}{N_1}\right) \tag{2.18}$$

where the argument y is

$$y = \frac{-2N_1 R\Delta f}{c} + l_{rp} \tag{2.19}$$

The range index l_{rp} is used to indicate the range position in the synthetic range profile at which the backscattered wave is measured. Since there are N_1 frequency stepped incident fields onto the target per inter-pulse interval τ_T, as shown in equation (2.16), there will also be N_1 range-delay measurements of target reflected field. So l_{rp} depends on the number of frequency steps (N_1) contained by the range profile function. Since in this case there are N_1 range–delay reflections, l_{rp} takes the values from $l_{rp} = 0$ to $l_{rp} = N_1 - 1$.

Considering equation (2.18) the magnitude of the range profile can be given as

$$\left|Hrp_{l_{rp}}\right| = \left|\frac{sin(\pi y)}{sin\left(\frac{\pi y}{N_1}\right)}\right| \tag{2.20}$$

From equation (2.20) the magnitude of the range profile will be maximum at $y = 0$, $y = \mp N_1, y = \mp 2N_1, \ldots$; by substitution of these values of y in equation (2.19) the relation between the range position l_{rp} and the range R can be found

For $y = 0$ giving $0 = \frac{-2N_1 R_1 \Delta f}{c} + l_{rp}$ or $R_1 = \frac{c l_{rp}}{2N_1 \Delta f}$ (2.21)

For $y = \mp N_1$ giving $\mp N_1 = \frac{-2N_1 R_2 \Delta f}{c} + l_{rp}$ or $R_2 = \frac{c\left(l_{rp} \mp N_1\right)}{2N_1 \Delta f}$ (2.22)

For $y = \mp 2N_1$ giving $\mp 2N_1 = \frac{-2N_1 R_3 \Delta f}{c} + l_{rp}$ or $R_3 = \frac{c\left(l_{rp} \mp 2N_1\right)}{2N_1 \Delta f}$ (2.23)

Considering (2.21), (2.22) and (2.23), the difference or length between two different adjacent range R values for maximum range profile is given by $\frac{c}{2\Delta f}$. The length $\frac{c}{2\Delta f}$ is equal to the maximum unambiguous range of the radar which was given by equation (2.14).

Since the index l_{rp} showing the range position in the range profile, takes the values $l_{rp} = 0$ to $l_{rp} = N_1 - 1$, this means that there will be N_1 equally spaced range positions or increments within the unambiguous range $R_{max} = \frac{c}{2\Delta f}$. Therefore each increment will have the length of $\frac{c}{2\Delta f\left(N_1 - 1\right)}$. $\frac{c}{2\Delta f\left(N_1 - 1\right)}$ is equivalent to $\frac{c}{2B}$, which is equal to the range resolution of the radar, as given by equation (2.6).

This section analysed the fundamental principles associated with pulse radar. The methods for maintaining a high average power and adequate range resolution for a certain transmitter output peak power were also presented. These methods that are also referred

to as pulse compression are phase modulation of pulse, frequency modulation of pulse and frequency stepped pulse compression. The range resolution associated with frequency stepping depends on the number of frequency steps considered and is equal to $\frac{c}{2\Delta f\left(N_1-1\right)}$. Therefore frequency stepping will be used in this thesis, since it enables the selection of the appropriate range resolution for the specific radar application. Additionally frequency stepping is easily deployed via the use of Vector Network Analyser for experimental purposes. So frequency stepping is a suitable waveform.

Under certain conditions the frequency stepped pulse compression or the spreading of the spectrum can create an Ultra-Wideband pulse. The appropriate conditions to create an UWB pulse are described in the next section.

2.3 UWB Radar Definition Classification and Application

2.3.1 Evolution of UWB radar from Conventional Systems

The amount of information carried by the electromagnetic waves is determined by the frequency band used. Considering the illumination of an object via radar, the quantity of information reflected from the object is proportional to the frequency band. In order to increase the capacity of the system to carry information, the frequency band must be widened [14]. Section 2.3 consists of the definition of UWB radar, the potential applications of UWB radar and finally the different classes of UWB waveforms.

The UWB term refers to radar systems that use wide relative proportional bandwidth signals [14]. Conventional radars are narrow band systems, that provide target detection and coordinates measurement. However the transmission of UWB signals onto

an object results in the object reflecting a field that carries a large amount of information, which provides sensing ability further than the simple object's detection. In particular, as it was shown in [14, 19], UWB backscattered signals fields may also provide object identification, which means that the object can be recognised among the other targets. Thus the UWB signals may lead to the formation of an object's radar image. This special characteristic of UWB radar is due to the fact that the reflected field from the object includes information about the object that depends on the object's particular geometry, dimensions, shape and its electrical properties, making the identification of the object feasible.

Comparing conventional radar with UWB radar systems, it can be stated that conventional radars are similar to a pedestrian with weak eyes, the pedestrian can realize being blocked by an object but cannot recognize the kind of obstacle. The object recognition can be achieved only by the use of UWB radar.

2.3.2 UWB Radar Definition

In this subsection a brief outline along with the definition of the UWB radar is given. For the UWB definition the main publications referred to are [2, 14, 20]. According to the definition presented in [14], the UWB waveform merges or combines the baseband or information and carrier signal. The UWB waveform may appear as a non sinusoidal signal. Hence it can occur as a square, triangular or chirp waveform. Occasionally it can be assumed that the UWB signal is carrierless, since the baseband signal is not always modulated with another much higher frequency carrier signal. As stated in [14] the UWB sensor in some applications like the one studied in this Thesis can

be called impulse radar; this means that the transmitted signal may be replicating an impulse (very short) waveform and that the backscattered field is the impulse response of the system, which in our case, is the target (object). Additionally, the UWB term refers to the electromagnetic signal waveforms with instantaneous fractional or proportional bandwidth greater than 0.25 with respect to a centre frequency. Signals that have fractional bandwidths less that 1% are classified as narrowband, while signals with fractional bandwidths from 0.01 to 0.25 are classified as wideband [14]. Fractional bandwidth is defined in [14, 17] as

$$\text{Fractional bandwidth} = \frac{2(f_h - f_l)}{f_h + f_l} \tag{2.24}$$

where f_h and f_l are the higher and lower frequency band limits or edges respectively.

The term fractional bandwidth is also referred as "percentage bandwidth" when the fractional bandwidth is converted to percent. When conventional narrowband radar signals are considered, the term band limit or edge is defined as the point in frequency at which the power spectral density is 3 dB below what it is at the centre of the spectrum. Therefore the band limit is a -3dB emission point. In conventional narrowband signals, greater than 90% of the spectral energy lies in the part of the spectrum between the band limits (-3dB emission frequency points) [14].

Considering UWB signals, the same definition on frequency band limits may be used [14]. Depending on the utilised UWB signal waveform, the power spectral density may be usually symmetrical about a centre frequency, but sometimes it is not, as mentioned in [14], like in the case where the antenna response is measured.

Another definition for UWB that was accepted by the Federal Communications Commission is the following [2]: "A UWB device is any device where the fractional

bandwidth (shown in eq.2.21), is greater than 0.25 or occupies 1.5 GHz or more of spectrum." Subsequently the 1.5 GHz minimum bandwidth limit was reduced to a limit of 0.5 GHz for UWB devices. In this case the band limits are the -10 dB emission points. Therefore the bandwidth occupied by the frequency spectrum must be $B = 0.5$ GHz

Finally a complementary definition given in [20], is that the UWB term refers to the electromagnetic signal waveforms where the centre frequency defined as f_o and the signal bandwidth B defined as $B=df= f_h - f_l$ are comparable which means

$$\frac{df}{f_o} \cong 1 \tag{2.25}$$

Since the centre frequency is defined as $f_o = \frac{(f_h + f_l)}{2}$ then the equation $\frac{df}{f_o} = 1$ becomes $\frac{2(f_h - f_l)}{f_h + f_l} = 1$, which means that the instantaneous fractional or proportional bandwidth with respect to a centre frequency must be around 1. In this case the band limits are the -20 dB emission points.

In this Thesis research, UWB signals are considered, whose fractional bandwidth is greater than 1. Taking into account the large fractional bandwidth of the signal it can be assumed that the incident field onto an object consists of components with different frequencies. Therefore, the backscattered field from the object, which is the object's response, will be investigated over a wide frequency range. This wide frequency range (wide bandwidth) will provide a high range resolution. The high range resolution is the crucial advantage of the UWB Radar for object recognition, since the backscattered fields from the local scattering centers of the object can be measured. Thus the influence of the local scattering centers responses towards the overall reflected field from the object could

be investigated. In this way the dependence of the reflected field of the object from the object's particular geometry, dimensions, and shape will be examined.

2.3.3 Historical Background and Applications of UWB Radar

The origin of UWB radar concept and technology originated from radar applications that required larger fractional bandwidth. One of these applications was the detection of buried objects like mines. The army requirement for such application has existed since 1960. For this application, large bandwidth is required for satisfactory resolution of the measured depth of the buried object and a long wavelength is required for penetrating the earth's surface [14].

Another research activity that contributed into the formation of UWB radar technology is the high power/short pulse radiation. Radiating systems for such pulses were created for the simulation of nuclear Electromagnetic Pulse (EMP) effects on electronic components and circuits, so as to determine the vulnerability of the systems on EMP pulse [14].

A third research area from which UWB radar emerged is the work in time-domain electromagnetics, which begun in 1962. Time-domain electromagnetics were used to describe a type of microwave networks through their characteristic impulse response. Until then microwave networks which are linear time-invariant (LTI) systems, were characterised by conventional radar through swept frequency response, which includes amplitude and phase measurements versus frequency [1]. Afterwards the LTI systems could otherwise be entirely characterized by their response to an impulse waveform excitation, which is also called impulse response (IR) $h(t)$. The output signal of an LTI

system to any random input signal $i(t)$ could be distinctively determined by the convolution integral in terms of continuous functions

$$y(t) = \int_{-\infty}^{\infty} h(u)i(t-u)du\,. \tag{2.26}$$

Nowadays the UWB radar has a multiplicity of applications. As was discussed in [21], UWB radars are one of the most promising approaches to build radar systems with significantly improved capabilities for target identification and classification, with direct applications to civil uses and environmental monitoring. Fundamentally, as it is explained in the review papers [21] and [22], the applications of UWB radars can be separated into three main categories depending on the radar range and distance from the target. These are short range, mid range and long range applications.

Short range UWB radars are mainly operated when the target is located in an extremely dense and impenetrable environment. One of the most prominent applications is Ground-Penetrating Radar (GPR), with a variety of uses as explained in [23], for terrain profiling, earth penetration and inspection of condition of foundations in various building constructions. Such capabilities are used for trapped victim detection as presented in paper [24] where a detection method through UWB radar is proposed to recognise periodic motion, such as respiratory motion, in very low signal-to-noise-and-clutter ratio conditions. Another significant utilisation of the UWB radar, explained in [25], is for security and military purposes, such as "through-wall motion detection radar" that utilizes the UWB's very fine resolution and low frequency of operation in order to be placed on the wall and detect motion on the other side of the wall area. Through wall imaging applications may operate below 960 MHz, or in the 1.99-10.6 GHz range as indicated in [26]. The latest advances in this research area include systems performing a

variety of applications. Namely [27, 28] present optimised algorithms for through-the-wall UWB radar imaging of moving targets, while [29] presents the methodology for the mapping of a large area building, utilizing UWB radar imaging.

Medical imaging can be achieved through UWB radar approach, especially for the detection and monitoring of malignant tumours. Tumour detection is investigated in [30], via the classification of the salient features of a dielectric target, using multichannel microwave backscattered signal in the 1-11 GHz band [31]. Additional work on the subject [32] demonstrated a classification method of the shape and size characteristics of the tumour directly from its UWB backscatter. Other medical sensing includes the detection of internal head injuries like intracranial haematoma detection and the monitoring of cardiac or respiratory functions [24, 26]. In this case handheld micro-power impulse radar was developed which has a centre frequency of 2 GHz, a 200 psec (0.2 nsec) pulse width and a 2 MHz Pulse Repetition Frequency.

Mid range UWB radar applications, mainly concern surveillance and security tasks. As an example, the concept "UWB Radar Sensor Network" [25] can be used for terrain surveillance such as an airfield. In this case the sensor network functions in monostatic, bistatic or multistatic modes for the purpose of creating an electronic fence. In [25] a bistatic radar experiment is shown which was performed using a 2 GHz UWB transmitter. Furthermore for a variety of distance ranges, UWB vehicular radar sensors can be used for collision avoidance, blind spot monitoring and short/long range cruise control as suggested in [33, 34], in order to improve transportation safety and reduce the number of road accidents. UWB vehicular radar systems operate in the spectrum between 22–29 GHz. The sensor described in [33] produces pulses with carrier frequency of 24

GHz. Further advances on vehicular UWB radar applications include research work in [34] where a new quadrature pulse generator for use in UWB vehicular radar is presented that offers increased pulse compression, detection and interference mitigation characteristics.

Finally, long range applications mainly include Synthetic Aperture Radar (SAR) detection and imaging. Specifically, SAR systems that use longer wavelength UWB signals have the ability of foliage and camouflage penetration [35]. Such systems are used from the air or the ground to provide images for hidden, buried or concealed objects. Therefore they are increasingly utilized from the army for detection of weapons like buried 155-mm shells, mine fields or long range missiles [35, 36]. In [35] an experimental time domain SAR system was developed which operates in the 50-1200 MHz band. Furthermore, as it was discussed in the paper [37] by "Defence Advanced Research Projects Agency" (DARPA): "Both wideband and ultra-wideband radars can offer foliage penetration applications, however ultra-wideband radars may have an advantage in implementation in terms of cost, size and weight". In this research the UWB radar will be utilized for CWE detection at a standoff distance.

2.3.4 Cases of UWB Waveforms

In order to demonstrate the generic shape and properties of the UWB pulse, the "sinc" waveform and the "Gaussian monocycle" waveform are considered.

Sinc Waveform

The UWB sinc signal generally appears in time domain as non sinusoidal, carrier-free, short duration waveform that resembles the impulse waveform. The transmitted

signal can be mathematically described by means of the $sinc(\omega_c t)$ function, as shown in [38], where

$$sinc(\omega_c t) = \frac{sin(\omega_c t)}{\omega_c t} \tag{2.27}$$

or

$$sinc(\omega_c n\Delta t) = \frac{sin(\omega_c n\Delta t)}{\omega_c n\Delta t} \quad -\infty < n < \infty \tag{2.28}$$

if the transmitted signal is considered as a discrete function. In theory the *sinc* waveform is not restricted with respect to time [38]. However as it is shown in Figure 2.15 the waveform can be restricted to the point where the sequence approaches zero.

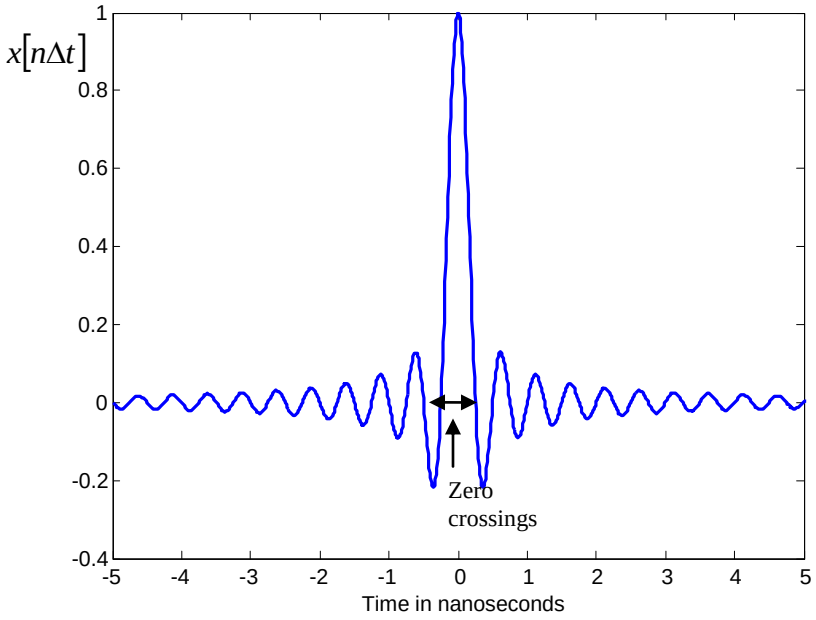

Figure 2.15: The *sinc* pulse in time domain.

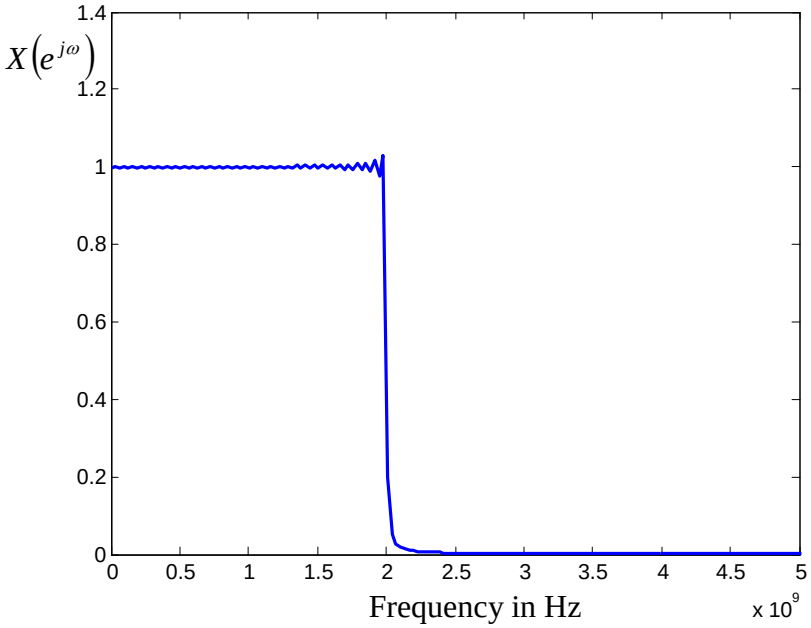

Figure 2.16: The *sinc* pulse in frequency domain.

The $sinc$ shaped pulse in the time domain is a window in the frequency domain so a signal which has a flat frequency spectrum with cut-off frequency $\omega_c = 2\pi f_c$ is considered

$$X\left(e^{j\omega}\right) = \begin{cases} 1, & |\omega| < \omega_c \\ 0, & \omega_c, |\omega| < \pi \end{cases} \tag{2.29}$$

It needs to be mentioned that the kind of signals shown in equations 2.28 and 2.29 are not causal therefore they cannot be generated or processed in the time domain; they are just referred as the general theoretical waveforms.

If $X\left(e^{j\omega}\right)$ is periodic with periodicity 2π and the Fourier synthesis equation [38] is considered

$$x[n\Delta t] = \frac{1}{2\pi}\int_{-\omega_c}^{\omega_c} e^{j\omega n\Delta t}\, d\omega = \frac{1}{2\pi jn\Delta t}\left[e^{j\omega n\Delta t}\right]_{-\omega_c}^{\omega_c} = \frac{1}{2\pi jn\Delta t}\left(e^{j\omega n\Delta t} - e^{-j\omega n\Delta t}\right) = \frac{sin\left(\omega_c n\Delta t\right)}{\pi n\Delta t}$$

$$\text{or } x[n\Delta t] = 2f_c \frac{\sin(\omega_c n\Delta t)}{\omega_c n\Delta t} = 2f\ sinc(\omega_c n\Delta t) \text{ for } -\infty < n < \infty \qquad (2.30)$$

Therefore

$$x[n\Delta t] = \frac{1}{2\pi}\int_{-\omega_c}^{\omega_c} e^{j\omega n\Delta t} d\omega = 2f\ sinc(\omega_c n\Delta t).$$

If $\omega_c = \pi$ then

$$\frac{1}{2\pi}\int_{-\omega_c}^{\omega_c} e^{j\omega n\Delta t} d\omega = \frac{1}{2\pi}\int_{-\pi}^{\pi} e^{j\omega n\Delta t} d\omega = \delta[n\Delta t]$$

where $\delta[n\Delta t]$ is the impulse or Dirac waveform. Consequently, if the frequency spectrum of $x[n\Delta t]$ is widened, it will theoretically reach the frequency spectrum of an impulse. Therefore in this case the UWB transmitted pulse tends to become impulse and considering the FT of $x[n\Delta t] = \frac{\sin(\omega_c n\Delta t)}{\pi n\Delta t}$, it yields

$$\sum_{n=-\infty}^{\infty} x[n\Delta t] e^{-jn\omega\Delta t} = \sum_{n=-\infty}^{\infty} \frac{\sin(\omega_c n\Delta t)}{\pi n\Delta t} e^{-jn\omega\Delta t} \qquad (2.31)$$

Because of the existence of $\sin(\omega_c n\Delta t)$, the infinite sum $\sum_{n=-\infty}^{\infty} \frac{\sin(\omega_c n\Delta t)}{\pi n\Delta t} e^{-jn\omega\Delta t}$ does not have a uniform convergence for all values of ω as n increases. This in the frequency domain is shown as an oscillatory behaviour at $\omega = \omega_c$ or $f = f_c$, which is called Gibbs phenomenon [20]. However as n increases the effect of Gibbs phenomenon is reduced.

A demonstration of the *sinc* function in time domain and frequency domain are shown in Figure 2.15 and Figure 2.16 respectively. The graph in Figure 2.16 is the FT of the function in Figure 2.15. The cut-off frequency f_c which is equivalent to bandwidth B for this pulse is 2 GHz. By observation of the frequency domain plot the ripples at 2 GHz

are due to the Gibbs phenomenon. By observation of the time domain plot it can be seen that the duration or length between the first two zero crossings is τ =0.5 ns and this is in accordance with equation (2.16). This is because of the existence of the sinusoidal function $sin(\omega_c n\Delta t)$ in $\frac{sin(\omega_c n\Delta t)}{\pi n\Delta t}$. The first zero crossings happen when

$$\sin(\omega_c n\Delta t) = 0 \text{ or } \omega_c n\Delta t = \pi \quad \text{or } n\Delta t = 1/2f_c = 0.25\,\text{ns}$$

$$\text{and } \omega_c n\Delta t = -\pi \text{ or } n\Delta t = -1/2f_c = -0.25\,\text{ns}$$

In general waveforms with flat or horizontal frequency spectrums resemble to the sinc pulse in the time domain.

Gaussian Monocycle Waveform

The UWB monocycle pulse [14] is considered carrier-based with the centre frequency and the bandwidth dependent upon the duration of the monocycle. The centre frequency f_{c2} of a monocycle is the reciprocal of the duration or length τ_{c2} of the monocycle, as shown in Figure 2.17. The time domain representation of the monocycle pulse is given by

$$x(t) = \frac{t}{\tau_{c2}} e^{-\left(\frac{t}{\tau_{c2}}\right)^2} \tag{2.32}$$

Figure 2.17 and Figure 2.18 illustrate the monocycle function in the time domain and frequency domain, respectively. The graph in Figure 2.18 is the FT of the function in Figure 2.17. For the signal in Figure 2.18 the centre frequency is 2 GHz, consequently the pulse length in Figure 2.17 should be 0.5 ns. In Figure 2.17 it can be seen that the monocycle pulse tends asymptotically to zero at points $0.25\,\text{ns}$ and $-0.25\,\text{ns}$.

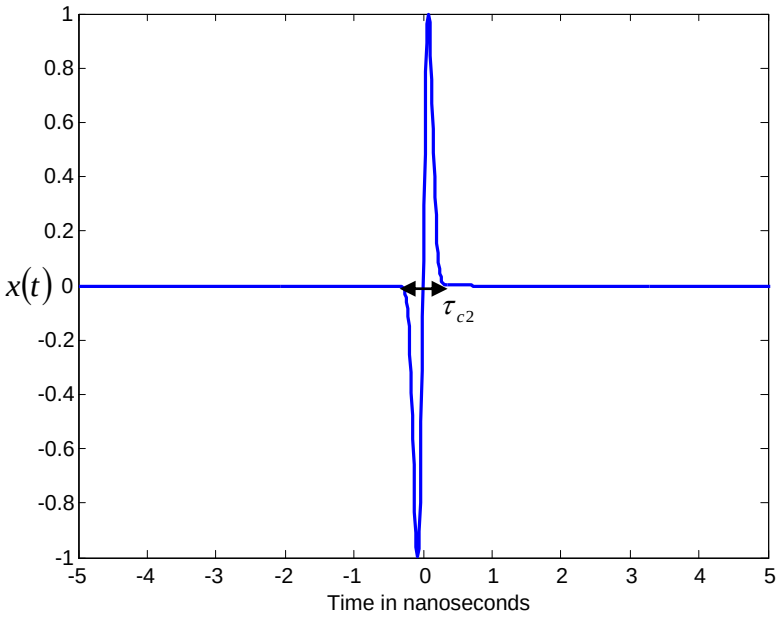

Figure 2.17: The Gaussian monocycle pulse in time domain.

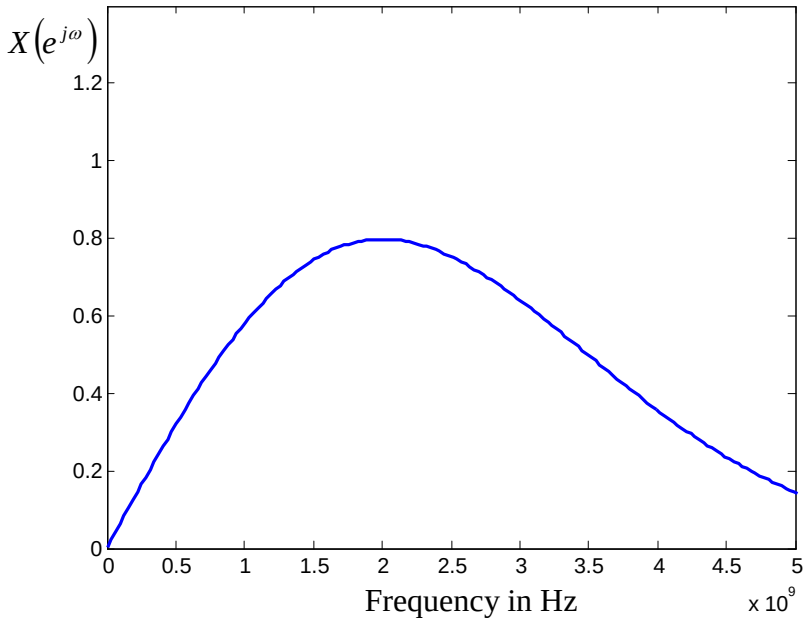

Figure 2.18: The Gaussian monocycle pulse in frequency domain.

This section analysed the fundamental UWB radar theory and its applications. Initially, a definition of UWB radar in terms of fractional bandwidth is given, in this Thesis the UWB signals considered will have a fractional bandwidth greater than 1. Furthermore, an outline of the major applications of UWB radar is presented. These are medical sensing; security and surveillance; ground penetrating radar; camouflage penetration and detection of various concealed or buried objects. Finally, there was an overview of the theoretical waveforms that are usually transmitted in UWB radar systems. As it was explained these waveforms are not causal since they do not have a uniform convergence with respect to time, therefore they cannot be generated or processed in the time domain; in the next section a frequency domain window will be used to tackle this issue.

2.4 UWB Signal Reflection from Targets

The illumination of an object via an electromagnetic wave results in the backscattering of a wave from the object. The creation of a reflected wave happens when the incident wave encounters a discontinuity in the characteristic impedance of the propagation medium (air), namely when an incident wave meets a target-object in free space. At the specific point of characteristic impedance discontinuity, an electric field which is opposite to the incident electric field is created, so that the boundary conditions are met. At the interface between propagation medium (dielectric) and conducting target the total tangential electric field is zero. At the interface between propagation medium (dielectric) and dielectric target the total tangential electric field is continuous. Additionally due to boundary conditions local currents are produced on the object. These generated currents result in the object getting charged, and a wave to be reflected or re-radiated from the object. One of the ways of characterising the reflected wave is the RCS. The induced currents and the reflected wave are a function of many parameters such as angle of incidence, angle of scattering, incident field polarisation, polarisation of scattered field (co- or cross- polar RCS), frequency and material, etc. Consequently the RCS also depends on those parameters.

2.4.1 Radar Cross Section (RCS)

As defined from [14, 39], the RCS is a measure of the power that is scattered per unit solid angle (power density) by a target (object), in a particular direction, normalised with respect to the power density of the incident field. If the scattered electromagnetic wave is spherically spread along the range *R,* from the radar to the target, the scattered

wave decays and its amplitude reduces with respect to distance. By means of the normalisation, the effect of the decay of the electromagnetic wave due to distance is removed. Consequently this description of RCS is independent of the distance between the radar and the target, as long as the target is in the far field. The far field criterion is expressed as $R > \frac{2D^2}{\lambda}$, where R is the range, λ is the considered wavelength and D is the transverse antenna aperture extent for antennas or the target extent facing the radar for radar targets [16]. The RCS varies with respect to the range in near field, as may be the case in several UWB applications. The RCS is effectively the surface area of the target that the radar sees and is also referred to as echo area. For this definition of RCS it must be assumed that the target is in the far field of the transmitter so that the incident field is essentially a plane wave and that the target is in free space. The RCS is defined as

$$\sigma_{RCS} = 4\pi_R \lim_{\to\infty} R^2 \frac{\left|E^S\right|^2}{\left|E^I\right|^2} = 4\pi_R \lim_{\to\infty} R^2 \frac{\left|H^S\right|^2}{\left|H^I\right|^2} \tag{2.33}$$

where E^S is the scattered electric field, E^I is the incident electric field, R is the distance between radar and target, H^S is the scattered magnetic field and H^I is the incident magnetic field.

The total electric field E^T at the boundary between free space and target (object) is equal to incident plus scattered field

$$E^T = E^S + E^I \tag{2.34}$$

The RCS of a target (object) is engaged in the radar equation.

2.4.2 Radar Equation

The radar equation expresses the power of the signal received at the radar as a function of various parameters like the transmitting and receiving systems, the target's RCS and propagation and polarization effects. For the monostatic case, where the two antennas used as the transmitter and receiver are collocated, the range from the transmitter to the target is similar to the range from the target to the receiver. The radar equation is given by [14]

$$P_r = \frac{P_t G_t G_r \sigma_{RCS} \lambda^2}{(4\pi)^3 R^4} \tag{2.35}$$

where P_r is the received power in watts, P_t is the transmitting antenna field power in watts, σ_{RCS} is the target's RCS in square meters, G_t is the transmitting antenna directive gain and G_r is the receiving antenna directive gain, R is the range from the target to the transmitter or receiver in meters and λ is the wavelength at the specific frequency of interest in meters.

As it is shown in [15] the radar equation can also include the parameter L_{system} which is the system's loss factor. This factor introduces all the inevitable inefficiencies of the radar system. Consequently the monostatic radar equation becomes

$$P_r = \frac{P_t G_t G_r \sigma_{RCS} \lambda^2 L_{system}}{(4\pi)^3 R^4} \tag{2.36}$$

In case that identical antennas are used as transmitter and receiver, then $G_t = G_r = G$. The radar equation along with the RCS of the target, the average noise power present in the system, and a specific Signal-to-Noise ratio (SNR) could define the limits on the range at which the radar can detect the target. Thus these parameters are

very important in the design of the system. The understanding of how the RCS depends on parameters like angle of incidence, angle of scattering, incident field polarisation and frequency is also significant.

2.4.3 Monostatic Radar Cross Section of Target

2.4.3.1 Dependence of RCS on Incident Angle and Scattering Angle

The incident and scattering angles for a target (object) are represented in the spherical coordinate system as shown in Figure 2.19 [14].

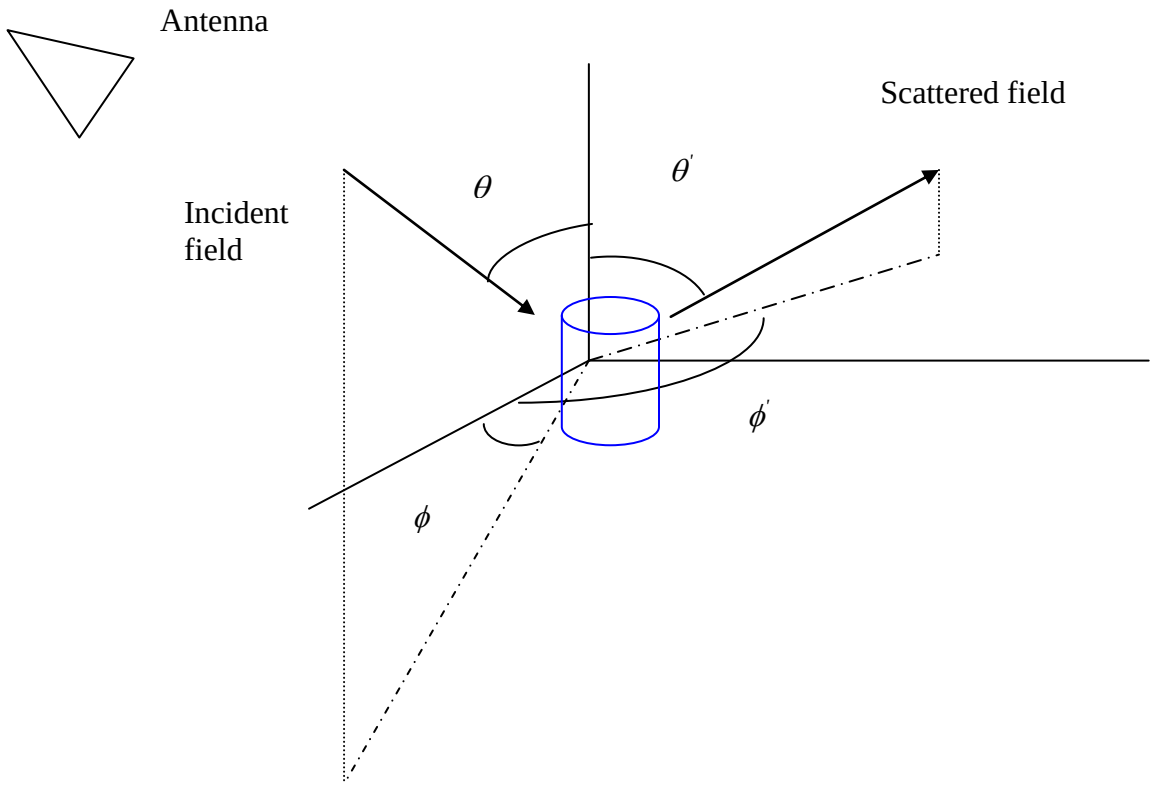

Figure 2.19 [1]: Coordinate system that shows incident and scattering angles.

The direction of propagation of the incident field is defined by the angles θ and ϕ while the direction of propagation of the scattered field is defined by the angles θ' and ϕ'. For a monostatic radar RCS the scattering and incident angles are the same, therefore $\theta = \theta'$ and $\phi = \phi'$. Consequently for monostatic radar the incident and scattered fields propagate on the same axis with different directions. By considering these angles the RCS can be expressed as

$$\sigma_{RCS}\left(\theta,\phi;\theta',\phi'\right) = 4\pi_R \lim_{\to\infty} R^2 \frac{\left|E^S\left(\theta',\phi'\right)\right|^2}{\left|E^I\left(\theta,\phi\right)\right|^2} \tag{2.37}$$

2.4.3.2 Dependence of RCS on Polarisation

One of the methods of quantifying the RCS, is by use of a transfer function, which relates the incident field to the scattered field. The relationship between the incident (E^I) and scattered (E^S) fields, is represented by the scattering matrix (S) which consists of the various scattering coefficients (a_{ij}). Using this representation, the relationship between the polarisations of the incident and scattered fields can be investigated.

The relationship between the incident E^I and scattered E^S fields is

$$\begin{aligned} E^S{}_1 &= a_{11}E^I{}_1 + a_{12}E^I{}_2 \\ E^S{}_2 &= a_{21}E^I{}_1 + a_{22}E^I{}_2 \end{aligned} \tag{2.38}$$

The subscripts i and j of the coefficients a_{ij} refer to the polarizations of the scattered and incident waves and the subscripts 1 *and* 2 represent any two general orthogonal polarization components. The a_{12} and a_{21} coefficients are referred to as cross-

polarisation coefficients. The cross-polarisation coefficient is associated with the scattered field in one polarisation when the object is illuminated with an incident field with orthogonal polarisation. For monostatic radar the cross-polarisation coefficients are equal and $a_{12} = a_{21.}$ The previous equation can be written in terms of matrices as

$$\begin{bmatrix} E^{S}{}_{1} \\ E^{S}{}_{2} \end{bmatrix} = \left[\underline{S_{sc}}\right] \begin{bmatrix} E^{I}{}_{1} \\ E^{I}{}_{2} \end{bmatrix} \tag{2.39}$$

and therefore the scattering matrix is equal to

$$\begin{bmatrix} a_{11} a_{12} \\ a_{21} a_{22} \end{bmatrix} = \left[\underline{S_{sc}}\right] \tag{2.40}$$

Each scattering coefficient is a complex number and therefore it can be represented in terms of magnitude and phase

$$a_{ij} = \left|a_{ij}\right| e^{j\kappa_{ij}} \tag{2.41}$$

Since the RCS depends on frequency and incident and scattering angles, in addition to the dependence on polarisation, the scattering coefficient can be expressed as

$$a_{ij}\left(\theta,\phi;\theta',\phi';f\right) = \left|a_{ij}\left(\theta,\phi;\theta',\phi';f\right)\right| e^{jk_{ij}\left(\theta,\phi;\theta',\phi';f\right)} \tag{2.42}$$

The scattering matrix coefficients are related to the RCS as

$$\sigma_{RCS_{ij}} = 4\pi R^2 \left|a_{ij}\right|^2 \tag{2.43}$$

The equation (2.43) is valid for specific orthogonal polarisations.

2.4.3.3 Dependence of RCS on Frequency

The dependence of RCS on frequency can be separated into three categories in terms of how the wavelength λ of the incident field compares with the maximum object

dimension L_{dim}. These three categories are the Rayleigh region, the resonance region and the optical region. These three regions are defined as:

- Rayleigh region or low frequency region is the region where the wavelength λ is large compared to the object dimension L_{dim}: $L_{dim}/\lambda << 1$.
- Resonance region is the region where the wavelength λ is on the same order as the object dimension L_{dim}: $0.5 < L_{dim}/\lambda < 10$.
- Optical region or high frequency region is the region where the wavelength λ is small compared to the object dimension L_{dim}: $L_{dim}/\lambda > 10$.

Considering spherical objects especially, as the sphere and grenade studied in the Thesis, the dimension that controls the scattering performance with respect to frequency is the sphere circumference. If the impulse response of a system is the continuous function $h(t)$, the Laplace Transform (LT) of $h(t)$ is the transfer function $H(s)$ of the system and is defined as

$$H(s) = \int_0^\infty h(t) e^{-st} dt \tag{2.44}$$

where $s = \sigma + j\omega$ the scattering matrix $\underline{S_{sc}}$ of equation (2.39) and (2.40), represents the scattering transfer function of the object. If in equation (2.39) the dependence on polarisation and the dependence on angle of incidence are suppressed, then equation (2.39) can be written in terms of complex frequency $s = \sigma + j\omega$. Hence the scattering transfer function of the object will be $\underline{S_{sc}}(s)$ and it will be related to the incident and reflected fields as

$$E^S(s) = \underline{S_{sc}}(s) E^I(s) \tag{2.45}$$

In this case the scattering transfer function of the object is $H(s) = \underline{S_{sc}}(s)$. Therefore from equation (2.33) the RCS can be written as

$$\sigma_{RCS}(s) = 4\pi_R \lim_{\to\infty} R^2 \frac{\left|E^S(s)\right|^2}{\left|E^I(s)\right|^2} = 4\pi_R \lim_{\to\infty} R^2 \left[\underline{S_{sc}}(s)\right]^2 = 4\pi_R \lim_{\to\infty} R^2 \left[H(s)\right]^2 \quad (2.46)$$

and for the representation of RCS of the object as a function of frequency

$$\sigma_{RCS}(j\omega) = 4\pi_R \lim_{\to\infty} R^2 \frac{\left|E^S(j\omega)\right|^2}{\left|E^I(j\omega)\right|^2} = 4\pi_R \lim_{\to\infty} R^2 \left[\underline{S_{sc}}(j\omega)\right]^2 = 4\pi_R \lim_{\to\infty} R^2 \left[H(j\omega)\right]^2 \quad (2.47)$$

2.4.4 New features due to UWB Radar

Due to the reduction in transmitted pulse duration some new features and improvements are provided by the UWB radar as described in [14] and [19]:

- Enhanced precision in the target-object's range measurement.
- Improved radar immunity to extraneous or irrelevant to the radar system signals like electromagnetic radiation or noise that interferes with the radar signals.
- Object recognition and detectability, which leads to the creation of the object's radar image via the formation of the object's RCS. When a UWB pulse is transmitted onto a complex object, the overall reflected signal and therefore the RCS, are unique since they depend on many factors like:
    1. Particular geometry and electrical dimensions (size), relative to the incident signal wavelength, of the object, or all the individual reflectors of which the complex object consists.

2. Spatial relationship or distance among all reflectors.
3. Electrical properties of the object.
4. Angle of incidence of the transmitted signal and the scattering angle of the reflected signal.
5. Incident signal polarization.

- Radar robustness to passive interference created by bad weather conditions (snow, mist, hail, and rain), clutter, aerosols or metallized strips.
- Increase in target tracking reliability
- Increase in radar operation security.

2.4.5 Radar Cross Section of Weapon

The grenade is the target that will be detected via radar and it is the smallest one of all CWEs. Other CWEs could be considered and are shown in Figure 2.20 and Figure 2.21. These are the Uzi pistol with 0.24 m length, the folded Micro Uzi small machine gun with length 0.282 m, the M1911A1 0.45 calibre pistol with 0.219 m length or the folded AK-105 small size assault rifle with length 0.586 m. These weapons are reported, since they are adequately compact and could be hidden between a person's clothes hence they are potential CWEs. Nevertheless since the research is focused on the grenade their detection is out of the scope of the Thesis.

Figure 2.20: Other possible concealed weapons.

Figure 2.21: Other possible concealed weapons.

In order to estimate the grenade RCS and resonant frequencies, the conducting sphere of radius $\alpha = 0.0325$ m is used to approximate the grenade. Hence the RCS [39] of the conducting sphere of radius 0.0325 m is considered and shown in Figure 2.22. In this figure the RCS is plotted against the frequency.

The resonance region of the sphere RCS has peaks that correspond to the natural resonant frequencies of the sphere. In the optical region, the resonant frequencies peaks still exist but converge asymptotically to the physical cross section, which is the area of the sphere $\pi\alpha^2 = 0.0033$ m^2. As it can be seen from the figure, the first resonant frequency occurs at 1.46 GHz, this frequency corresponds to $\frac{\omega\alpha}{c} = 1$ or $\frac{2\pi\alpha}{\lambda} = 1$, which means that the first resonant peak corresponds to the frequency point where the circumference equals

one wavelength. Therefore the resonant frequencies depend on the circumference of the sphere. For the sphere, the resonance region is the region where the wavelength λ is of the same order as the sphere dimension $0.5 < 2\pi\alpha / \lambda < 10$.

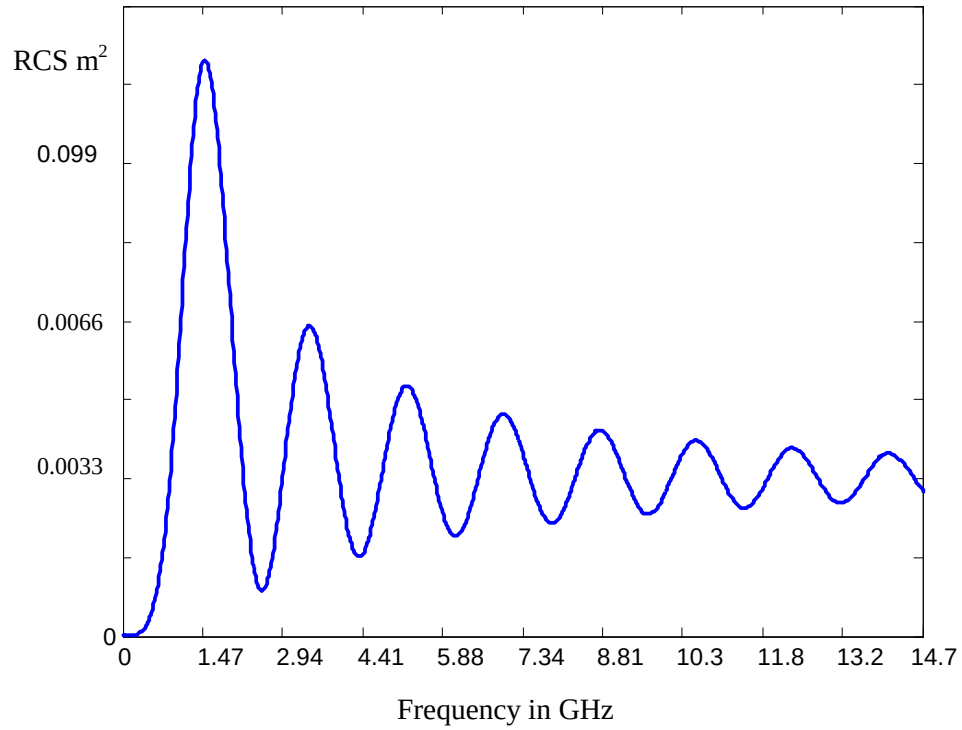

Figure 2.22: The RCS of sphere (the scale is in multiples of the first resonant frequency).

Since the grenade is approximated by the conducting sphere of radius 0.0325 m, from Figure 2.22, the resonance region and therefore the frequency response (spectrum) of the sphere and the grenade can be estimated to start from 0.73 GHz. Hence the first resonant frequency, which also has the highest contribution into the formation of the reflected field from the sphere or the grenade, can be seen at around 1.4 GHz. The subsequent resonant frequencies can be estimated to occur at frequencies which are around integer multiples of 1.4 GHz. For the grenade detection the first three or four resonant frequencies will be considered, therefore the reflected wave from the grenade

will be obtained in the 0.7-4.5 GHz band or 0.7-6.7 GHz band depending on the number of resonant frequencies that are considered . Considering Figure 2.22, it can be deduced that the RCS of the grenade oscillates and converges for higher frequencies around the value of the physical cross section which is the area $\pi(0.0325)^2 = 0.0033\text{m}^2$.

Considering the Uzis, pistol, and AK-105 these targets could be approximated as cylinders of radius varying from 0.025m to 0.1 m and length varying from 0.2m to 0.6 m. From the RCS of cylinder [40] a general idea can be figured of the resonant frequencies of the weapons.

The principle that the first resonant peak corresponds to the frequency point where the circumference equals one wavelength applies for any object. So, when the polarisation of the incident wave on the cylinder or pistol or machine gun is parallel to the axis of the weapon, the wavelength corresponding to the first resonant frequency will approximately be equal to twice the biggest dimension of the illuminated weapon. For the considered M1911A1 or Uzis, this significant wavelength is around 0.5m. Therefore the first resonant frequency of these weapons can be estimated to be at 0.6 GHz. For the AK-105 the wavelength is around 1.172 m therefore the first resonant frequency of the gun can be estimated to be at 0.25 GHz. Additionally, by consideration of these resonant frequencies the band can be defined at which the measurement of the reflected field from the weapon of interest will be made. This band is 0.125-1 GHz for AK-105 and 0.3-2.4 GHz for M1911A1 or Uzis. In table 2.1 the first and fourth resonant frequencies of each weapon are shown. So according to the weapon under consideration the appropriate band should be selected.

Table 2.1: Type of weapon and first and fourth resonant frequency.

Type	1st Resonance around	4th Resonance around
Grenade	1.4 GHz	5.6 GHz
Uzi pistol	0.6 GHz	2.4 GHZ
Micro Uzi SMG	0.6 GHz	2.4 GHZ
M1911A1 0.45	0.6 GHz	2.4 GHZ
AK-105	0.25 GHz	1 GHz

2.4.6 Power Level Analysis for Reliable Detection of Weapon

The existence of the radar equation enables us to approximately estimate the required transmitting power P_t for reliable target detection at a specific range R. For this estimation the transmitting antenna G_t gain and receiving antenna G_r gain must be known.

For the experimental procedure and for the concealed object detection two Vivaldi broadband antennas are going to be used, as shown in Figure 2.23. In order to estimate the gains G_t and G_r, the antennas were set to face each other at distance $R_d = 3.2$ m. So the insertion loss (S_{21}) due to separation between the antennas was measured using the network analyzer, assuming no polarization loss. The S_{21} is shown in Figure 2.24. The gain of both antennas can be estimated by means of the Friis equation [15]

$$G_t G_r = \frac{P_r}{P_t}\left(\frac{4\pi R_1}{\lambda}\right)^2 \tag{2.48}$$

Where P_t is the power of the transmitting antenna , P_r is the power of the receiving antenna and the power ratio $\frac{P_r}{P_t}$ is the measured S_{21} squared. Since transmitting and

receiving antenna are the same $G_t G_r = G^2$ and λ is the wavelength at the specific frequency.

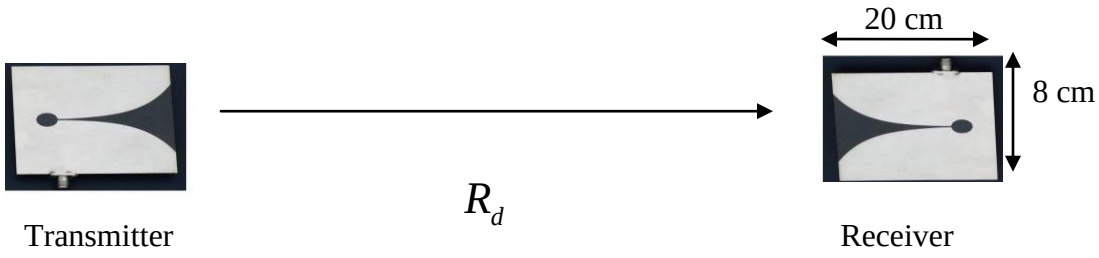

Figure 2.23: Experimental configuration with two Vivaldi antennas facing each other at distance $R_d = 3.2$m.

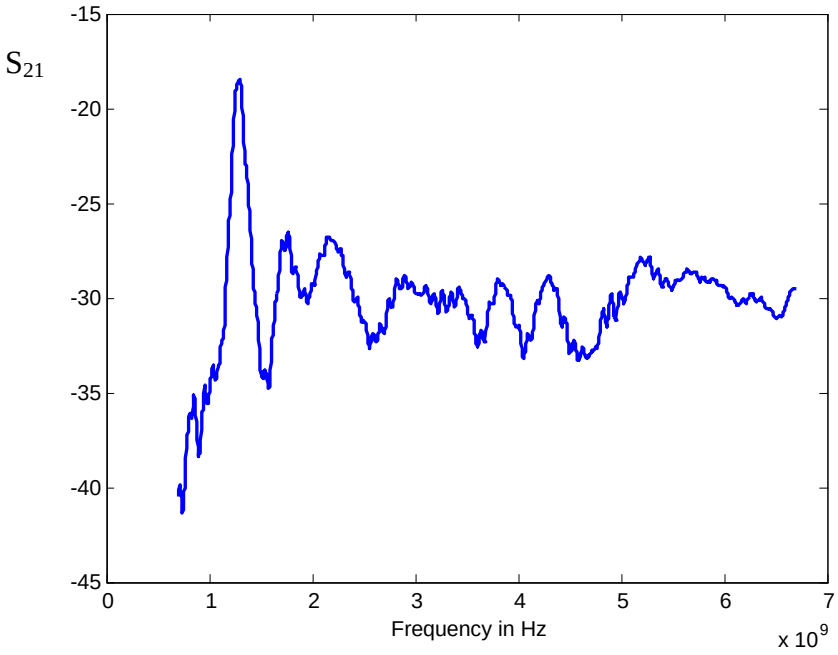

Figure 2.24: Measured S_{21} parameter in *dB* of two antennas facing each other.

From Figure 2.24, it is shown that the measured averaged S_{21} parameter at frequency 3 GHz is S_{21}= 0.0308 or -30.2 *dB*. For higher frequencies than 3 GHz the S_{21} is more or

less stable. Consequently the gain of both antennas at frequency 3 GHz can be estimated as

$$G_t G_r = G^2 = (0.0308)^2 \left(\frac{4\pi \times 3.2}{0.1} \right)^2 = 153 \tag{2.49}$$

Therefore the gain of each antenna is $G = \sqrt{153} = 12.365$ or $G = 11dB$.

Having calculated the antennas gain, the required transmitting antenna power for reliable target detection can be computed by means of the radar equation. The power received by the radar from the target is given by

$$P_r = \frac{P_t G_t G_r \sigma_{RCS} \lambda^2 L_{system}}{(4\pi)^3 R^4} \tag{2.50}$$

where σ_{RCS} is the RCS of the target and L_{system} is the system's loss factor. The power received by the target can be compared with the power of noise via the Signal-to-Noise ratio (SNR)

$$SNR = \frac{P_r}{P_N} = \frac{P_t G_t G_r \sigma_{RCS} \lambda^2 L_{system}}{(4\pi)^3 R^4 P_N} \tag{2.51}$$

As it is known the noise power is given by [15]

$$P_N = kT_0 FB \tag{2.52}$$

where k is the Boltzmanns's constant $k = 1.38 \times 10^{-23}$ JK^{-1} and $T_0 = 300$ K and F is the noise figure of the receiver which can be estimated to take the value $F = 10$ or $10dB$. Equation (2.51) can be modified to include the average power given by $\overline{P_t} = P_t \frac{\tau}{\tau_T}$ and the integration gain [15] of several pulses added together by involving the factor $n_p L_{n_p}$. n_p is

the number of added pulses and L_{n_p} is the loss over perfect integration. Assuming that in contemporary radar systems $L_{n_p} \cong 0.9$ [15] is used. Also if the average power is $\overline{P}_t = P_t \frac{\tau}{\tau_T}$ then $P_t = \overline{P} \frac{\tau_T}{\tau}$. Thus the factor $n_p L_{n_p}$ and $\overline{P}_t$ are included in equation (2.51). Consequently SNR becomes

$$SNR = \frac{P_r}{P_N} = \frac{\overline{P}_t \left(\frac{\tau_T}{\tau} \right) G_t G_r \sigma_{RCS} \lambda^2 n_p L_{n_p} L_{system}}{(4\pi)^3 R^4 P_N} \tag{2.53}$$

Equation (2.51) can be written in terms of $\overline{P}_t$ as

$$\overline{P}_t = \frac{SNR(4\pi)^3 R^4 P_N \left(\frac{\tau}{\tau_T} \right) \left(\frac{1}{n_p L_{n_p}} \right)}{G_t G_r \sigma_{RCS} \lambda^2 L_{system}} \tag{2.54}$$

By means of the noise equation (2.52), equation (2.54) can be written as

$$\overline{P}_t = \frac{SNR(4\pi)^3 R^4 k T_0 F B \left(\frac{\tau}{\tau_T} \right) \left(\frac{1}{n_p L_{n_p}} \right)}{G_t G_r \sigma_{RCS} \lambda^2 L_{system}} \tag{2.55}$$

and using equation (2.4) $\tau = \frac{1}{B}$, $\overline{P}_t$ will become

$$\overline{P}_t = \frac{SNR(4\pi)^3 R^4 k T_0 F \left(\frac{1}{\tau_T} \right) \left(\frac{1}{n_p L_{n_p}} \right)}{G_t G_r \sigma_{RCS} \lambda^2 L_{system}} \tag{2.56}$$

The product $n_p \tau_T$ is called the integration time of n_p pulses required for target detection.

Supposing the specific SNR which is required for target detection is at least $30dB$, which means that the received power is 1000 times the noise power and the system's loss

factor is $L_{system} = -10dB$. The assumption that the SNR is $30dB$ is applicable only in a noise-limited environment. Also it is assumed that the radar tracks the target which is a moving person over 1 m range and the person has the speed of 5 m/sec, therefore the integration time is 1/5=0.2 sec so $n_p \tau_T = 0.2$ sec.

By means of the equation (2.51) for $\overline{P}_t$, the required level of the transmitting antenna power is estimated for effective detection of a sphere with RCS equal to the value $\pi\alpha^2 = \pi(0.0325)^2 = 0.0033m^2$ at distance $R = 30$m at frequency 3 GHz. The frequency 3 GHz is chosen since for this value and for higher frequencies the sphere RCS converges to $0.0033m^2$. $\overline{P}_t$ is calculated as

$$\overline{P}_t = \frac{SNR(4\pi)^3 R^4 k T_0 F\left(\frac{1}{\tau_T}\right)\left(\frac{1}{n_p L_{n_p}}\right)}{G_t G_r \sigma_{RCS} \lambda^2 L_{system}} =$$

$$\overline{P}_t = \frac{1000 \times (4\pi)^3 \times (30)^4 \times 1.38 \times 10^{-23} \times 300 \times 10 \times \frac{1}{0.2} \times \frac{1}{0.9}}{(12.356)^2 \times \pi (0.0325)^2 \times (0.1)^2 \times 0.1} = \frac{3.6969 \times 10^{-7}}{0.0005735}$$

$$\overline{P}_t = 7.2868 \times 10^{-4} \text{ Watts}$$

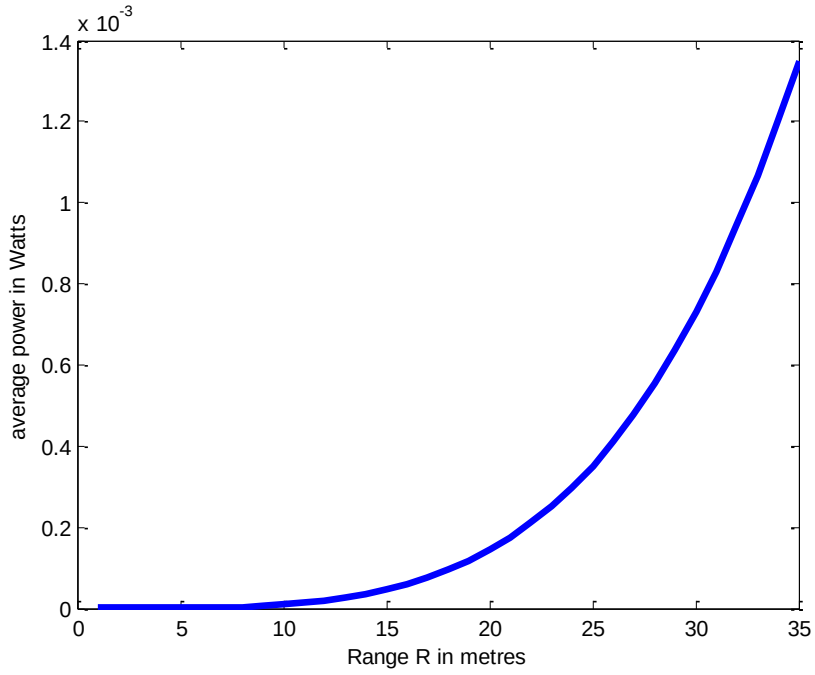

Figure 2.25: Average power against distance.

The estimated power $\overline{P_t}$ for effective weapon detection is the average power and is plotted in Figure 2.25 as the distance or range *R* increases. So for the same integration time and noise, the range of detection is affected by the average power $\overline{P_t}$. Pulse compression will not affect the range for the same integration time. However pulse compression increases the range resolution.

Therefore, in this project frequency stepped pulse compression is used, via utilization of the vector network analyser as the instrument that performs the frequency stepping. Hence the flat frequency spectrum is obtained in steps in order to create a UWB *sinc* pulse which is periodic with period $\tau_T = \frac{1}{\Delta f}$. Supposing the reflected field of the smallest target which is the grenade is considered, the bandwidth of the synthesized *sinc*

pulse should start from 0.7 GHz since it will be used for obtaining the response of the 0.0325 sphere or grenade whose resonance region starts from 0.7 GHz.

2.4.7 *Sinc* Pulse via Frequency Stepping

Considering that a *sinc* pulse is transmitted between 2 antennas which are facing each other and located 3.2m apart; and that for the signal transmission the method of frequency sampling of the flat spectrum (or window) i.e. frequency stepping is used. These pulses are shown in Figures 2.26, 2.27 and 2.28 respectively. The frequency band of the pulse in Figure 2.26 is 0.7-1.45 GHz and its fractional bandwidth is 0.7. The frequency bands of the pulses in Figures 2.27 and 2.28 are 0.7-2.7 GHz and 0.7-6.7 GHz respectively, while their fractional bandwidths are 1.18 and 1.62 respectively. For all pulses $\tau_T = 267$ nanoseconds (*ns*). Figure 2.29 shows the magnitude of the frequency spectrum of the pulse of Figure 2.28. In these pulses the starting frequency of the window was 0.7 GHz, the frequency spectrum delay, or shift causes modulation with a carrier frequency signal which is observed in the pulse signal of Figures 2.26, 2.27 and 2.28. Additionally in Figure 2.28 the sidelobes show ripples of high frequency and this is due to the fact that the spectrum of this specific pulse extends to the frequency of 6.7 GHz.

By observation of Figure 2.26, it can be seen that the pulse level is only marginally higher than the sidelobes level. This is due to the fact that the fractional bandwidth of the signal is not large enough. According to [20] this signal is not classified as UWB. However for Figures 2.27 and 2.28 as the fractional bandwidth becomes larger, and the frequency spectrum of the waveform becomes wider, the pulse level (main lobe) is getting more distinctive than the sidelobes level and thus a *sinc* pulse is created.

Additionally the time domain extent of the *sinc* waveform becomes shorter; this has been predicted by equation (2.16). For Figures 2.27 and 2.28 the duration between the first two zero crossings is τ =0.5 *ns* and τ =0.166 *ns* respectively and this is in accordance with equation (2.16), however this duration is critically influenced by the modulation with respect to the carrier signal $cos(\omega_{ca} n\Delta t)$. By observation of Figure 2.29, the spectrum in frequency domain is shifted and starts from 0.7 GHz, and $K_{mp}(e^{j\omega})$ is symmetric around the frequency of 3.7 GHz. For the pulse of Figure 2.28 the carrier frequency signal was $f_{ca} = 3.7\,\text{GHz}$.

Observation of Figure 2.28 shows the existence of sidelobes. The sidelobes are present since the *sinc* pulse is not causal. If the pulse, as illustrated in Figure 2.28, was incident onto an object, the sidelobes would create a lot of reflections, which would critically affect the processing of the received signal. To eliminate sidelobes a frequency domain window [23], can be applied as in the case of Figure 2.30. Figure 2.30 shows the pulse of Figure 2.28 (0.7-6.7 GHz bandwidth) after a Gaussian window has been applied. In Figure 2.30 the absence of sidelobes is observed. The selection of the parameters of the window or frequency tapper is a complex process as sometimes a frequency tapper may introduce a processing loss.

While the considered fractional bandwidth increases, the frequency spectrum of the pulse waveform becomes wider until it theoretically reaches the frequency spectrum of an impulse. This is the critical benefit offered by frequency stepped pulse compression.

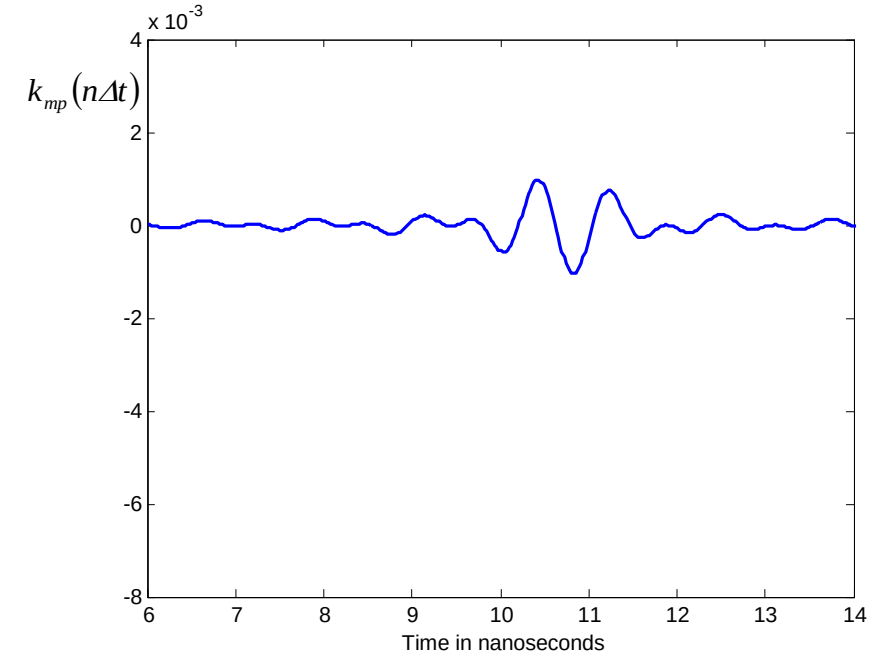

Figure 2.26: The *sinc* pulse in time domain in the 0.7-1.45 GHz band.

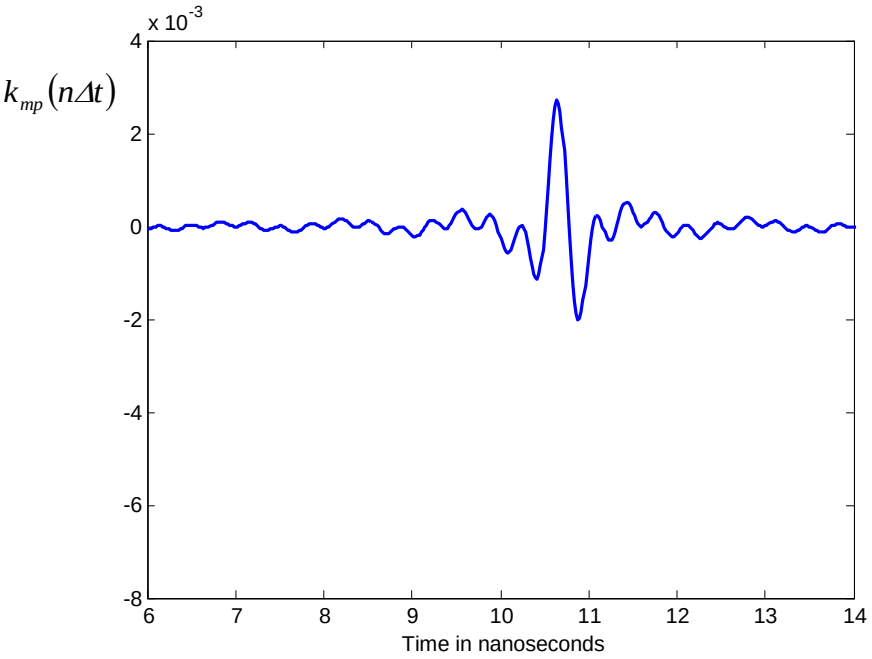

Figure 2.27: The *sinc* pulse in time domain in the 0.7-2.7 GHz band.

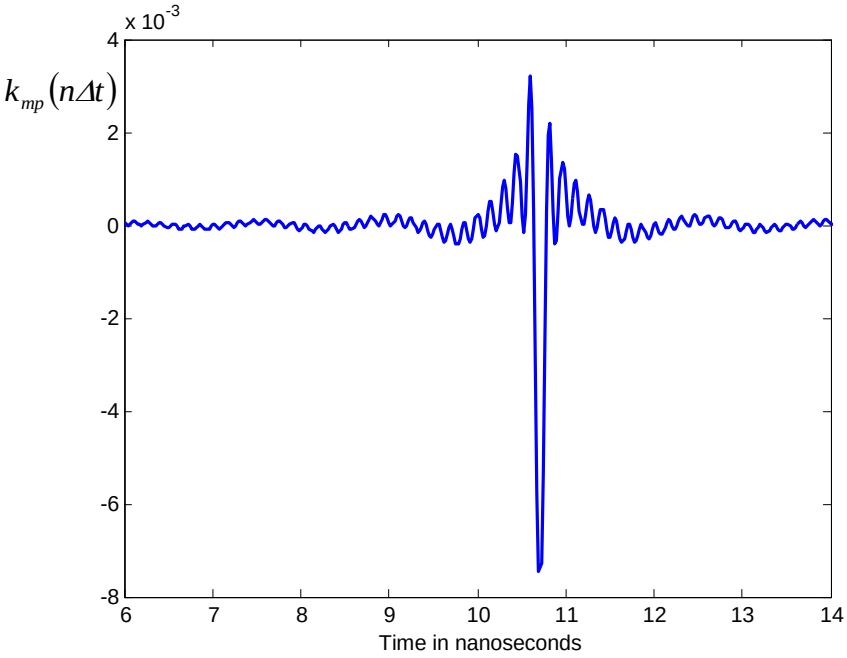

Figure 2.28: The *sinc* pulse in time domain in the 0.7-6.7 GHz band.

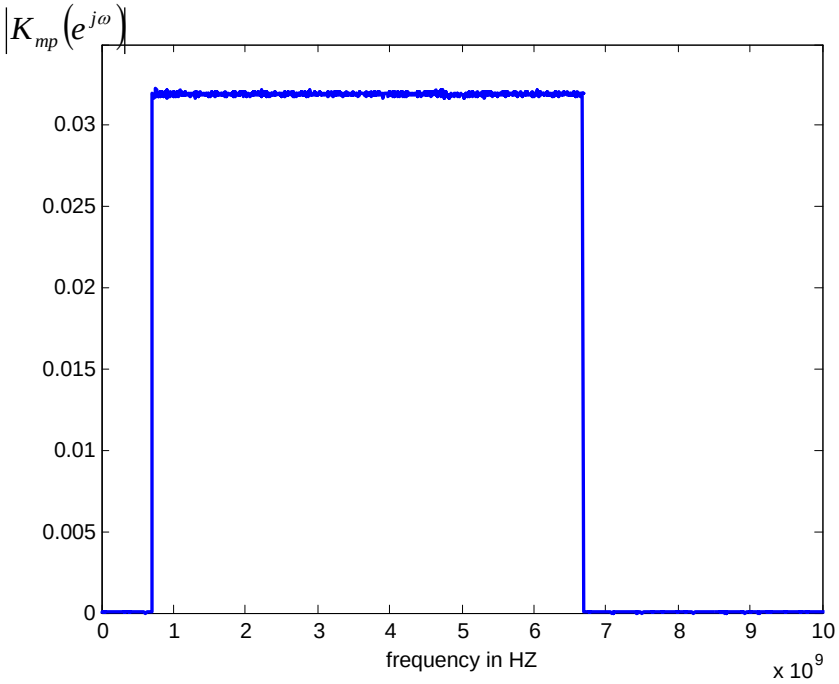

Figure 2.29: The magnitude of frequency spectrum of Figure 2.28.

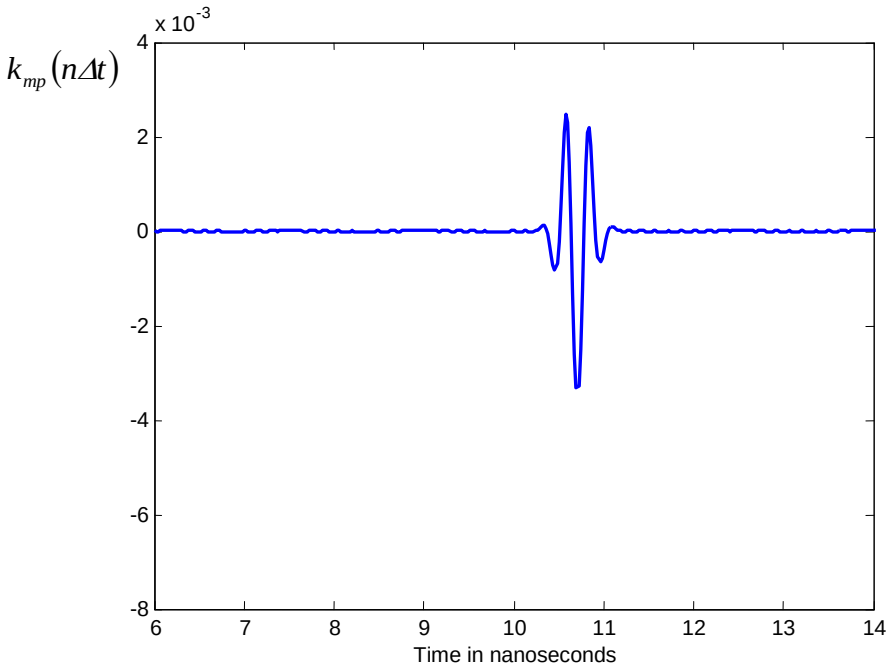

Figure 2.30: The *sinc* pulse in time domain in the 0.7-6.7 GHz band after a Gaussian window has been applied.

2.4.8 Conclusions

In this chapter a general analysis is presented of the main elements of the Ultra-Wideband Radar theory. After the introduction, sections 2.2 and 2.3 gave a general idea of the radar concept and analysed the fundamental UWB radar theory and its applications. Studying the applications of the UWB radar, in their majority include ground, foliage, camouflage penetration and detection of hidden objects in various distance ranges. Therefore it is apparent that for our research objective of "concealed weapon detection", the use of UWB radar is most preferable.

In section 2.4, an attempt is made to derive the resonant frequency bands of the radar operation for the possible weapons for detection. The AK-105 is considered as the biggest weapon with first resonant frequency at 0.25 GHz or wavelength 1.172 and bandwidth of reflected signal measurement 0.125-0.8 GHz. The grenade is the smallest

weapon that will be detected with first resonant frequency at 1.46 GHz or wavelength 0.2 m and bandwidth of reflected signal measurement 0.7-6.7 GHz. By means of the radar equation and its dependence on the RCS of the smallest target, which in this case is the grenade approximated as a sphere, it was calculated that at the standoff distance of 30 m a UWB radar should be used with transmitting average power of about $\overline{P_t} = 6.5581 \times 10^{-4}$ depending on the antenna gain. This level of average power was estimated via the assumption that the SNR is $30dB$. However this assumption is applicable only in a noise-limited environment. In a different environment there are large clutter returns, hence tracking the clutter power or other forms of CFAR [15] could be used.

The antennas that will be used should have a flat frequency response from frequency limits f_l to f_h. These frequency limits are involved in the fractional bandwidth equation given by (2.24). Thus by means of these antennas and the technique of pulse compression the waveform of Figure 2.30 will be used as the transmitted pulse for grenade detection.

Chapter 2 and the description of the radar and UWB concepts lay the framework in order to explain the detection of the hidden target (weapon). Hence the following chapters build upon the radar equation, the target's RCS, so as to explain how the reflected signal will be analysed in order to perform target detection. These are explained in chapters 3 and 4 with experimental results shown in chapters 5, 6 and 7.

Chapter 3

LATE TIME RESPONSE PHENOMENON and its EXPLOITATION

3.1 Introduction

This chapter presents the concept of the Late Time Response (LTR) as the fundamental principle that enables the detection of an object via UWB radar. The LTR is related to the techniques the UWB radar utilises to analyse the transient reflected signals from various targets (objects). The analysis of transient signals leads to the formation of the object's signature. This signature can be used for object recognition and classification.

Fundamentally, when an impulsive field is incident on an object, a transient field is backscattered from the target. The term transient is used to depict the short duration oscillation caused by the excitation of the object or system. Transient scattering which is a temporary phenomenon is investigated by the Singularity Expansion Method (SEM). The analysis of the transient field via SEM leads to the creation of the impulse response of the object. After the impulse response is formulated, the natural resonant frequencies of each object can be obtained and these frequencies contribute to the development of the object's signature.

Initially this chapter presents the mathematical principles that constitute the foundation of SEM. Consequently the theoretical aspects of SEM are analysed; this includes the study of transient reflected fields and how they are considered in the time domain. Eventually the concepts of Early Time Response (ETR) and the LTR are shown and the connection between the LTR and its resonant frequencies (poles) is described.

3.2 Singularity Expansion of Meromorphic Functions

3.2.1 Meromorphic Functions

This section presents the Mittag-Leffler theorem, which from a pure theoretical point of view is the concept that lays the framework for the singularity or pole expansion of meromorphic functions, as explained in [42] and [43]. The term "meromorphic function", defines the analytic function $f(s)$ that has only isolated poles as singularities. For the description of meromorphic functions, it is assumed that these poles are located at finite $s = s_i$, with $0 < |s_1| < |s_2| < |s_3| < ...$ (where i is the poles index) and that these poles are all simple. Additionally the number of finite s-plane poles may be infinite. The residues of the poles are denoted as q_i. A meromorphic function has no essential singularities in the finite plane. The term essential singularity describes poles of infinite order [44].

3.2.2 Mittag-Leffler Theorem

Consider a series of concentric circles C_i about the origin so that C_i includes $s_1, s_2, s_3, ..., s_i$ but no other poles. Also C_i does not pass through any other poles. The radius of C_i which is $R_i \to \infty$ as $i \to \infty$. In order to guarantee convergence, it is assumed that $|f(s)| < \varepsilon R_i$ for all values of s on C_i and for any small positive constant ε. Under these circumstances the Mittag-Leffler singularity expansion theorem [42, 43] states that the series in the right of equation (3.1) converges to $f(s)$

$$f(s) = f(0) + \sum_{i=1}^{\infty} q_i \left[\frac{1}{s - s_i} + \frac{1}{s_i} \right] \tag{3.1}$$

If $p_{in}+1$is an arbitrary positive integer then a different singularity expansion exists if $|f(s)|<\varepsilon R_i^{p_{in}+1}$ as $R_i \to \infty$ and $i \to \infty$. In this case $f(s)$can be represented by

$$f(s)= f(0)+ f'(0)s+\frac{s^2 f''(0)}{2!}+....+\frac{s^{p_{in}} f^{(p_{in})}(0)}{p_{in}!}+\sum_{i=1}^{\infty}\frac{q_i}{s-s_i}\left[\frac{s^{p_{in}+1}}{s_i^{p_{in}+1}}\right] \qquad (3.2)$$

The function $f(0)+ f'(0)s+\frac{s^2 f''(0)}{2!}+....+\frac{s^{p_{in}} f^{(p_{in})}(0)}{p_{in}!}$ is a polynomial that represents an *entire function*. This polynomial is similar to the Laplacian of a differential of order $p_{in}+1$. The term "entire" defines a function which is analytic at points of the finite s-plane. Therefore an entire function has no singularities in the finite s-plane.

3.3 Singularity Expansion Method

3.3.1 Theoretical Background

This section establishes the theoretical foundation concerning the backscattered field of an object by means of the singularity expansion method (SEM) as analysed in [14, 45]. The backscattered field of the object is considered both in the *s* domain (Laplace Transform plane) via the transfer function of the object-system and in the time domain via the object's transient field, which is the object's Impulse Response (IR). In chapter-two as it is explained in sub-section 2.4.3.3, equation (2.46-2.47), the transfer function was involved in the definition of the Radar Cross Section (RCS); therefore it is fundamental for the reflected field description.

The normalised transfer function $\overline{H}(\bar{r},s)$for a finite-sized object that has only pole singularities in free space is given in [14] as

$$\overline{H}(\bar{r},s)=\sum_{i=1}^{\infty}\frac{\eta_i(s,\bar{p})M_i(\bar{r})}{(s-s_i)^{m_i}}+\overline{W}(\bar{r},s,\bar{p}) \qquad (3.3)$$

The parameters of equation (3.3) are

- s_i is the pole, singularity, or natural resonant frequency and it has a complex value. It is the pole of the transfer function after an impulse signal has been applied on the system. The poles of the transfer function appear in complex conjugate pairs if the IR is a real function of time. If the studied system is considered as stable i.e. the IR of the system converges or the IR is a series of damped exponentials, then the poles lie in the negative half of the *s* domain.
- $\bar{p}$ is the polarisation of the incident wave.
- $\bar{r}$ is the position vector. It is the position on the structure and the components of the object at which the transient response is being obtained.
- m_i is the multiplicity of the s_i pole.
- $M_i(\bar{r})$ is referred to as natural mode. This is the strength of the response of the system at complex frequency s_i and it depends on the position vector $\bar{r}$ on the structure of the object.
- $H_i(s,\bar{p})$ is referred to as the coupling coefficient. This is the strength of the response of the system at complex frequency s_i and it is independent of the position vector. However it depends on the incident wave polarisation.
- $\overline{W}(\bar{r},s,\bar{p})$ is an entire function and is explained by the Mittag-Leffler theorem which is associated with meromorphic functions as explained in section 3.2.2. This entire function ensures the convergence of the infinite series.

The coupling coefficients $H_i(s,\bar{p})$ can be a function of complex frequency *s*, or they can be constant with respect to *s* i.e. $H_i(\bar{p})$. In [14], $H_i(s,\bar{p})$ are referred to as class-two coupling coefficients and $H_i(\bar{p})$ are referred to as class-one coupling coefficients.

Considering the inverse Laplace Transform (LT) of the transfer function in equation (3.3), it yields the time domain IR [14]

$$\bar{h}(\bar{r},t)=\sum_{i=1}^{\infty}\eta_i(t,\bar{p})M_i(\bar{r})e^{s_i t}+\bar{w}(\bar{r},t,\bar{p}) \tag{3.4}$$

Since in equation (3.3) class-two coefficients are used, the IR representation in equation (3.4) should have the time dependent coefficients $\eta_i(t,\bar{p})$.

As it is explained in [14], the IR can also be represented in terms of time independent coefficients $\eta_i(\bar{p})$, which combine with $M_i(\bar{r})$ to form the coefficients $A_i(\bar{r})$. Therefore $A_i(\bar{r})=M_i(\bar{r})\,\eta_i(\bar{p})$.

In this case the IR from (3.4) is represented as

$$\bar{h}(\bar{r},t)=[u(t-T_L)]\sum_{i=1}^{\infty}A_i(\bar{r})e^{s_i t}+[u(t)-u(t-T_L)]\bar{w}_2(\bar{r},t,\bar{p}) \tag{3.5}$$

Where $[u(t)]$ is the unit step function and

$$u(t-T_L)=\begin{cases}1 & t>T_L\\ 0 & t<T_L\end{cases} \tag{3.6}$$

T_L is twice the time the transmitted field takes to pass over the object.

If *L* is the Line of Sight (LoS) extent of the object and *c* is the velocity of light

$$T_L=\frac{2L}{c} \tag{3.7}$$

In equation (3.5) the response of the class-two coefficients $\eta_i(t,\bar{p})$ and their sum of exponentials of resonant frequencies are included in $\overline{w}_2(\bar{r},t,\bar{p})$.

3.3.2 Formulation of IR of Target-Object from Transient Scattering

This section describes the reflected field of the illuminated object in terms of the currents that are induced on the object and on the waves that are created on the surface of the object as the result of these currents. The interaction of an incident wave with obstacles in the wave path gives rise to diffraction. The term diffraction refers to the phenomena that occur when propagating waves encounter obstacles in their paths; the effects of diffraction are generally most pronounced for waves where the wavelength is on the order of the size of the diffracting objects [39]. As stated in the formation of the reflected wave in chapter-two, section 2.4 , when an impulse field is incident on an object, local impulsive currents are excited due to the generated electric field which is opposite to the incident electric field so that the total tangential electric field is zero (boundary condition theorem). These currents are called Physical Optics (PO) currents as explained in [45-48] where the physical interpretation and need of entire function in equation (3.2) and (3.3) is described. Therefore as the incident field passes over the object, impulsive PO currents are excited.

PO currents are the cause for the generation of travelling waves of current on the object, which propagate in all directions on the body. These waves travel all the way around the body until they reach the limit of the object, which is the specular point (object's front surface limit, or nearest vertex point to the transmitter). When the travelling waves reach the specular point they create a backscattered field. The

backscattered field due to travelling waves, is combined with the specularly reflected field both constructively and destructively as shown in Figure 3.1 to create a standing wave. Therefore the moment the travelling waves reach the specular point, standing waves are generated on the surface and are reflected. The standing waves involve the sum of exponentials of resonant frequencies of the object's response.

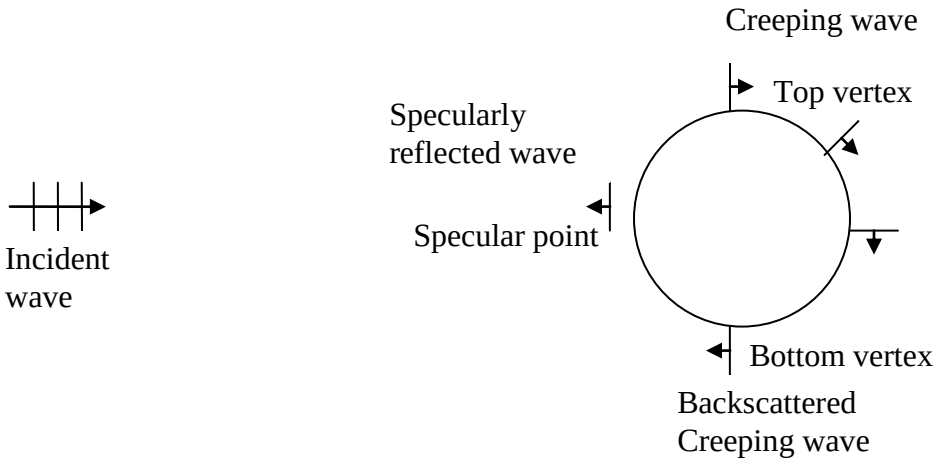

Figure 3.1: Specularly reflected and creeping waves

Consider the overall response of the object, PO currents and travelling waves last while the incident wave passes over the object i.e. $t < T_L$. Consequently this part of the response is also referred to as the driven or forced response. Standing waves exist after the illumination of the object by the incident wave ceases i.e. $t > T_L$. In general the waves existing on the surface of the illuminated object are also called creeping waves. As it is explained in [39] the characterization creeping waves are the waves which are launched at the shadow boundary which in Figure 3.1 is the top vertex of the sphere. Consequently these waves propagate along the body surface in the shadow region. Then

they re-emerge in the opposite shadow boundary which is the bottom vertex of sphere of Figure 3.1. Creeping waves are directly associated to the object surface-diffracted rays, that are described by the geometrical theory of diffraction [39]. Additionally creeping waves are also related to the high frequency approximation of the scattered field of specific shapes. In the case of conducting objects, as there are no fields inside a perfect conductor the creeping waves revolve in the exterior of the dimensions of the object. However for dielectric objects as the electric and magnetic field exist in the dielectric, there are creeping waves revolving both in the exterior and in the interior of the object [49]. The interior creeping waves revolve around particular volumes inside the object.

In equation (3.5), the response during the early time interval that the travelling waves propagate along the extent of the body, or $t < T_L$ is described by $\overline{w}_2(\bar{r}, t, \bar{p})$. In this way the response consists of a sum of exponentials that have time varying coupling coefficients or class two coupling coefficients. After the travelling waves become standing waves or $t > T_L$ the coupling coefficients are independent of time or class one.

The relation between creeping or surface, waves and natural resonant frequencies has been extensively studied in references [50-59] for multiple objects like conducting and dielectric spheres and cylinders via initial consideration of the object's backscattered frequency domain field. Consider the case of sphere or cylinder with circumference $2\pi\alpha$ in Figure 3.1. If the creeping wave starts at the object's top vertex, travels to the bottom vertex, and continues, then as stated in [52] after one circumnavigation it will reach again the bottom vertex where the creeping wave will have the same phase as the first time it reached the bottom vertex. Therefore each circumnavigation causes a match of the creeping wave's phase with itself. This is the phenomenon of phase matching.

Considering the travelling path from top to bottom vertex after one complete circumnavigation, it shows that 1+1/2 wavelengths span the circumference of the object (1/2 wavelength is due to a phase jump [52]), and after *n* circumnavigations *n*+1/2 wavelengths. In fact in [58] the object circumference is related to the creeping wave's wavelength λ via

$$2\pi\alpha = \left(n + \frac{1}{2}\right)\lambda \tag{3.8}$$

The conclusive point is that the wavelength λ of the creeping wave equals one circumference of the object or $2\pi\alpha$. At this specific wavelength the first natural resonant frequency will be observed. The subsequent resonant frequencies can be estimated to occur at frequencies which are around integer multiples of the first resonance. This syllogism refers to objects like cylinders or spheres. Considering the case of sphere, the creeping waves revolve in a path around the circumference of sphere.

The same conclusion can be drawn if the backscattered field of the conducting sphere via the RCS is considered, as it was shown in chapter two, sub-section 2.4.5. The first resonant peak of the RCS corresponds to the frequency point where the circumference equals one wavelength. At this specific frequency a wave travelling entirely around the spherical surface will constructively add to a wave that is reflected from the specular point at the surface of the sphere as shown in Figure 3.1. Thus surface standing waves or resonance fields are created, which are the resulting reflections, when there is no incident wave influencing the object.

The consideration of the PO backscattered electric field, PO currents, and creeping waves, which were described in this section is very important since these

features constitute the backscattered field from the object, after this object is illuminated with an impulsive field. The backscattered field represents the IR of the object and is of transient nature since it is the response of the system-object to a change from equilibrium.

3.4 Description of IR Components ETR and LTR

This section analyses the IR of the object by means of the ETR and LTR [14, 19, 39]. The ETR and LTR are described in terms of PO currents, travelling waves and standing waves. Initially the time domain backscattered field or IR from the illuminated object via a UWB pulse is given in [45] as

$$\bar{h}(t) = \left[u(t) - u(t - T_L)\right]\left[E^{PO}(t) + E^{NRE}(t)\right] + u(t - T_L)\sum_{i=1}^{I} A_i e^{S_i t} \qquad (3.9)$$

In equation (3.9) the description of the response in terms of a sum of exponential of complex frequencies s_i and their coefficients A_i, is similar to the response in equation (3.5) and is based on SEM. In this representation the sum of exponentials is not a function of the position vector $\bar{r}$, or class-two coefficients $\eta_i(t, \bar{p})$ and associated *entire function* $\bar{w}_2(\bar{r}, t, \bar{p})$. T_L is the time the transmitted signal interacts with the object and $u(t)$ is the unit step function .

The IR of an aircraft target model and the IR of a sphere of radius a, as can be seen in Figure 3.2 [19] and Figure 3.3 respectively, consist of the ETR and LTR of the reflected signal.

3.4.1 ETR Description

In relation to $\bar{h}(t)$ from equation (3.9), the ETR consists of:

- E^{PO}, which is the backscattered field (IR) component due to the PO currents contribution. The E^{PO} contribution results from the PO currents, which are induced to match the boundary conditions that exist when the transmitting signal interacts with the object. Consequently E^{PO} exists for $t < T_L$.

- E^{NRE} is the backscattered field (IR) component due to the contribution of the travelling waves, which disseminate in all directions and which occur due to the forced PO currents. E^{NRE} stands for natural resonance entire function and it lasts during the existence of PO currents; therefore it lasts for $t < T_L$. As it has been stated for equation (3.5) E^{NRE} is a sum of exponentials, which have complex frequencies and time varying exponential coupling coefficients or residues.

Since E^{PO} and E^{NRE} are limited to $t < T_L$, these fields are usually a small part of the total backscattered signal, and constitute the ETR. The ETR does not carry specific information for the object and it can be used mainly for the object's detection. Considering Figure 3.3 the general sphere IR is represented in terms of normalised amplitude as $V\left(\frac{r}{\alpha}\right)$ and is plotted against time in the scale $t' = t/(\alpha / c)$. Where V is the un-normalised amplitude; r is the distance from the centre of the sphere, at the point of backscattered field consideration and α is the sphere radius. The black line denotes the ETR and the red line of the plot denotes the LTR.

The sphere ETR starts when the backscattered field from the front vertex or specular point of the sphere is received, and it lasts for a time interval equal to T_L. In this case T_L is equal to twice the time the incident field takes to pass over the line of sight extent or diameter (2α) of the body i.e. $T_L = 4\left(\frac{\alpha}{c}\right)$. It is observed that at the end of ETR, beginning of LTR there is a discontinuity. This is due to the limitation of the model with respect to the number of resonant frequencies considered.

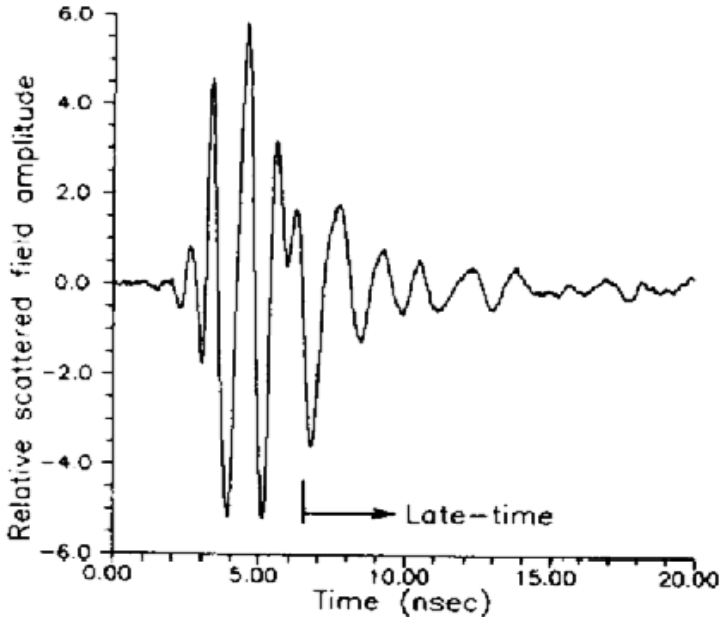

Figure 3.2: IR of an F15 aircraft target model [19].

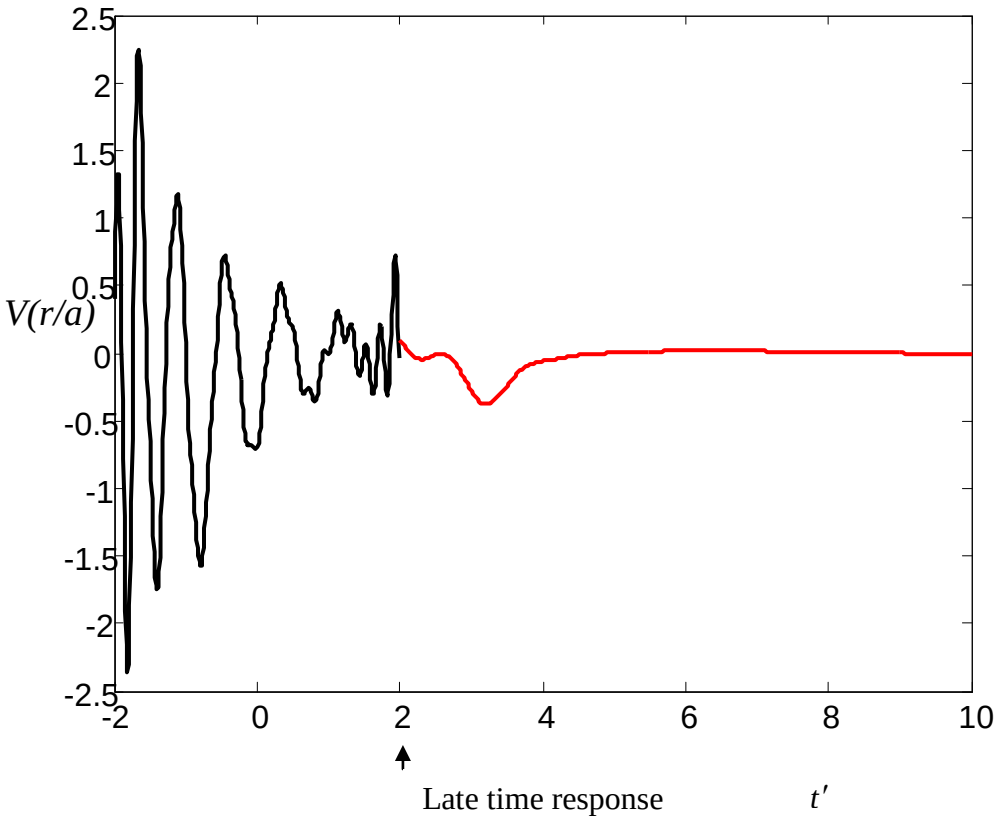

Figure 3.3: The IR i.e. ETR (black) and LTR (red) of a sphere of radius α .

3.4.2 LTR Description

In relation to the UWB backscattered field (or IR), after the forced PO currents cease to exist and the travelling waves become surface standing waves, the IR can be represented as a sum of exponentials, which have complex frequencies and constant exponential coupling coefficients. This representation is the LTR. The LTR of the object has a duration in the order of ten nanoseconds [19] depending on the dimensions of the object, and in general the LTR signal carries unique information for every object. The LTR is a series of damped exponentials as represented in equation (3.10) and it exists for $t > T_L$

$$\bar{h}_{LTR}(t) = \quad u(t - T_L)\sum_{i=1}^{I} A_i e^{S_i t} \tag{3.10}$$

After the LTR of the object is obtained; the complex frequencies of the exponentials are extracted. Sometimes the frequencies exist in complex conjugate pairs $S_i = \sigma_i + j\omega_i$ and $S_i^{\,*} = \sigma_i - j\omega_i$ for $\sigma_i < 0$, where σ_i is the damping coefficient and ω_i is the radian frequency of the exponential. Furthermore the coupling coefficient A_i could be complex, so A_i and their complex conjugates may be represented with amplitudes $R_i / 2$ and phases ϕ_i i.e. $A_i = \frac{R_i}{2} e^{j\phi_i}$ and $A_i^{\,*} = \frac{R_i}{2} e^{-j\phi_i}$. Consequently by means of the complex conjugate pairs the LTR becomes

$$\bar{h}_{LTR}(t) = \quad u(t - T_L)\sum_{i=1}^{I} A_i e^{s_i t}$$

$$\bar{h}_{LTR}(t) = u(t - T_L)\sum_{i=1}^{\frac{I}{2}} \frac{R_i}{2}\left[e^{s_i t} e^{j\phi_i} + e^{s_i^{\,*} t} e^{-j\phi_i}\right] \tag{3.11}$$

$$\bar{h}_{LTR}(t) = u(t - T_L)\sum_{i=1}^{\frac{I}{2}} \frac{R_i}{2}\left[e^{(\sigma_i t + j\omega_i t)} e^{j\phi_i} + e^{(\sigma_i t - j\omega_i t)} e^{-j\phi_i}\right] \tag{3.12}$$

$$\bar{h}_{LTR}(t) = u(t - T_L)\sum_{i=1}^{\frac{I}{2}} \frac{R_i}{2} e^{\sigma_i t}\left[e^{j(\omega_i t + \phi_i)} + e^{-j(\omega_i t + \phi_i)}\right] \tag{3.13}$$

$$\bar{h}_{LTR}(t) = u(t - T_L)\sum_{n=1}^{\frac{I}{2}} R_i e^{\sigma_i t}\,\frac{e^{j(\omega_i t + \phi_i)} + e^{-j(\omega_i t + \phi_i)}}{2} \tag{3.14}$$

$$\text{or} \quad \bar{h}_{LTR}(t) = u(t - T_L)\sum_{i=1}^{\frac{I}{2}} R_i e^{\sigma_i t}\cos(\omega_i t + \phi_i) \tag{3.15}$$

In equation (3.11), if the S_i frequencies are obtained in complex conjugate pairs the LTR $\bar{h}(t)$ is obtained as a real function of time. The S_i frequencies of the LTR, which are also referred to as the complex natural resonant frequencies of the system, are a distinctive signature for the object, since they depend on the object's particular geometry,

dimensions, and its electrical properties. Considering two objects of similar dimensions but different shape, these objects could have similar resonant frequencies due to their similar dimensions. However they would presumably have different amplitudes associated with their resonant frequencies due to different shape. Therefore the information related to the resonant frequencies must be distinguishing for every object, and the resonant frequencies are presumably a unique signature for the considered object. However the presumption about the information related to the amplitudes of the LTRs of objects of similar dimensions should in general be proved experimentally. The dependence of the resonant frequencies to angle of incidence and polarisation is considered later in the Thesis.

The LTR could also be represented in the frequency domain by means of the Laplace Transform (LT) of the LTR. By means of equation (3.11) this yields

$$\overline{H}_{LTR}(s) = \mathrm{LT}\left[\overline{h}_{LTR}(t)\right] = \int_0^{\infty}\left[u(t-T_L)\sum_{i=1}^{\frac{I}{2}}\frac{R_i}{2}\left[e^{s_i t}e^{j\phi_i} + e^{s_i^* t}e^{-j\phi_i}\right]\right]e^{-st}dt \qquad (3.16)$$

$$\overline{H}_{LTR}(s) = e^{-(s-s_i)(T_L)}\sum_{i=1}^{\frac{I}{2}}\frac{R_i}{2}e^{j\phi_i}\frac{1}{s-s_i} + e^{-(s-s_i^*)(T_L)}\sum_{i=1}^{\frac{I}{2}}\frac{R_i}{2}e^{-j\phi_i}\frac{1}{s-s_i^*} \qquad (3.17)$$

The derivation for equation (3.17) is shown in the appendix section 3.a

In equation (3.17), where the function is in terms of s, it can be realised that $\frac{R_i}{2}$ and the $e^{j\phi_i}$ terms and $\frac{R_i}{2}$ and the $e^{-j\phi_i}$ terms combine as residues of the poles S_i and S_i^* respectively while $e^{-(s-s_i)(T_L)}$ and $e^{-(s-s_i^*)(T_L)}$ reveal a phase shift.

3.4.3 Time Variance of an Object

In relation to the illumination of an object via UWB radar, it must be taken into account whether the object is a time variant system. Time variance of an object implies that, if the orientation of the object constantly changes, the incident wave polarisation and the angle of incidence, which is the angle between the sensor and the object, i.e. aspect angle, will also change depending on the object's orientation. Consequently for a time variant system, the incident wave properties, aspect angle and wave polarisation are also time variant.

Suppose that the object is a time variant system, as the incident wave parameters-aspect angle and the wave polarisation vary, some factors of the IR change accordingly, but some factors remain unchanged. As it has been stated in [60-65] the poles S_i and S_i^* of the LTR are independent of the incident wave parameters and therefore they are time invariant. Nevertheless the ETR and the residues of the LTR of the object depend on those parameters and consequently they are time variant.

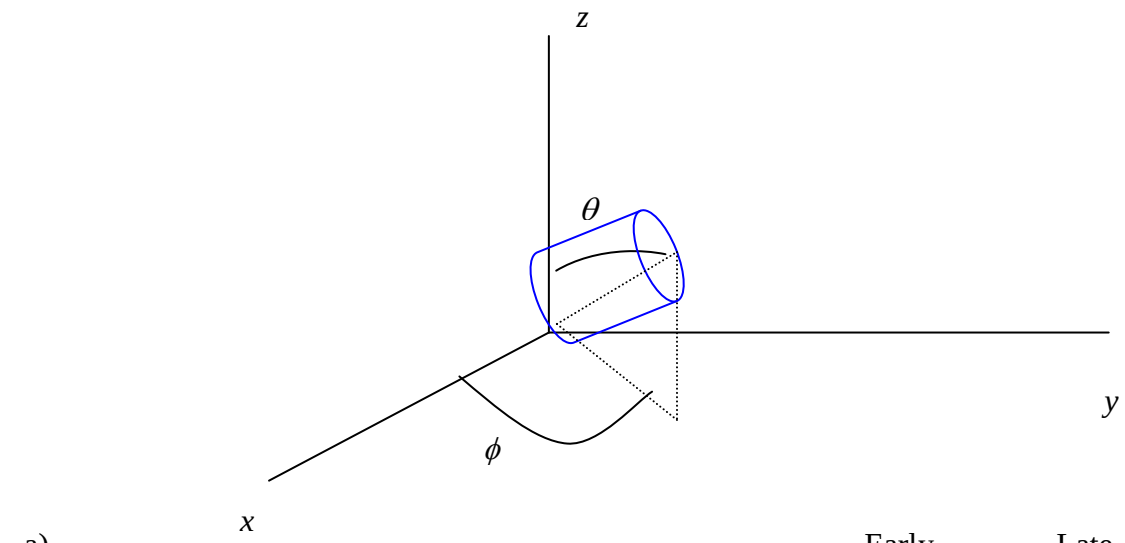

a)

Early response

Late response

E^I

H^I

Excitation pulse

$\theta = 0^o$

b)

Early response

Late response

E^I

H^I

Excitation pulse

$\theta = 90^o$

$\phi = 0^o$ or $\phi = 180^o$

c)

Early response

Late response

E^I

H^I

Excitation pulse

$\theta = 45^o$

$\phi = 90^o$

E^I is the electric field

H^I is the magnetic field

Figure 3.4: Effects of orientation on IR.

In view of the residues of the LTR, as explained in [66], a preset incident polarisation and aspect angle excite only certain selected poles. Consequently although the poles of the LTR are independent of incident field parameters, they are excited depending on the illuminated object dimension that will be encircled by the surface wave. For every dimension, a unique wavelength of surface wave will be created and unique natural resonance frequencies will be excited.

As an example Figure 3.4 shows the excitation of resonant frequencies for an object whose polarisation and aspect angle vary. In the figure E^I is the electric field and H^I is the magnetic field. The system is in spherical coordinates and θ is the angle from the positive *z*-axis to the top of the cylinder, while ϕ is the angle between the positive *x*-axis to the projection of the top of the cylinder in the *x*-*y* plane. The variations of θ and ϕ are in reference to the polarisation of the E^I field. The E^I field vector has the same direction as the z -axis. For $\theta = 0^o$ and any angle ϕ, in Figure 3.4.a the E^I field polarisation is parallel to the cylinder axis. The first resonant frequency occurs at the frequency point where the perimeter equals one wavelength. So, for this E^I field polarisation, it is assumed that the wavelength corresponding to the first resonant frequency will primarily depend on the length of the cylinder. In this case the length of cylinder is approximately equal to $\lambda / 2$. Similarly for $\theta = 90^o$ and $\phi = 0^o$ or $\phi = 180^o$ in Figure 3.4.b, where the E^I field polarisation is perpendicular to the cylinder axis, it can be assumed that the wavelength corresponding to the first resonant frequency will approximately be equal to the cylinder circumference. Therefore in these two cases of different polarisation incidence, the creeping waves encircle different dimensions so different resonant frequencies are excited, which do not appear at the orthogonal

polarisation case. Furthermore as it is explained in [40] the E^I field polarisation parallel to the cylinder axis creates a higher in magnitude RCS than the RCS of polarisation perpendicular to the axis, therefore the same assumption can exist for the IRs as shown in Figures 3.4.a and 3.4.b. Considering the two previous cases of E^I field polarisation, it is concluded that resonance can occur at any value depending on the orientation of cylinder with respect to plane of polarisation. This would lead to an ambiguity in resolving the cylinder orientation. Further investigation on the cylinder reflected field, must show how the amplitudes of resonances depend on E^I field polarisation and affect the overall magnitude of LTR. This would lead to the resolution of cylinder orientation. Also the effect of circular polarisation must be considered since circular polarisation breaks down into two orthogonal planes of polarisation.

In the case of Figure 3.4.c for $\theta = 45^o$ and $\phi = 90^o$, and equation (3.7), the line of sight extent *L* is greater than the *L* of the case of Figure 3.4.a where $\theta = 0$. T_L will also be greater and the ETR will last longer.

Therefore a variation of the angle θ $(0^o\text{-}90^o)$ for $\phi = 0^o$ or $\phi = 180^o$ has the consequence that the cylinder impulse response experiences effects due to E^I field polarisation. While a variation of the angle θ $(0^o\text{-}90^o)$ for $\phi = 90^o$ causes the cylinder IR to be affected from the E^I field angle of incidence or aspect angle. Depending on variations of θ and ϕ, sometimes both the incident wave aspect angle and polarisation influence the IR.

This section analysed the IR of the object through the ETR and LTR and their parameters, and referred to the parameters like angle of incidence and incident wave polarisation that can affect the IR.

3.5 Conclusions

This chapter presented a selective analysis of all the crucial elements that lead to the description of the IR of the object. After the introduction, sections 3.2 and 3.3 gave a general idea of the basic theoretical background, which is required for the consideration of the backscattered field in the time domain. In this section the important conclusion is that propagating surface or creeping waves are generated during the excitation process, and the natural resonant frequencies are caused by the phase matching of such creeping waves as they encircle the object's respective dimension multiple times. In section 3.4 the ETR and LTR and their various components that constitute the IR of the object are described.

The time invariant parameters of LTR, which are the natural resonant frequencies, can be used to extract a unique signature. If these frequencies are obtained for many cases of aspect angles and incident wave polarisations, they can be considered as the signature of the object. Therefore the object detection and recognition is feasible.

However if the levels of the ETR and LTR are compared from Figure 3.3, it can be seen that the level of LTR is sufficiently lower than the level of ETR. Additionally although the ETR can be used for detection of the object, the LTR will be used to obtain the poles for the object's recognition. Thus for effective use of LTR during the

recognition of the object, the transmitter power should be increased beyond the level required for simple detection.

For the detection of CWE appended on the human, the duration and magnitude of the LTR of the human and the LTR of the CWE must be considered. The duration and magnitude of the Late Time Response (LTR) depend on the shape, dimensions and electrical properties of the object of interest. So an important issue must be resolved. Whether the human LTR overwhelms the CWE LTR, or the LTR from the human-CWE complex object presumably provides information on both the resonant frequencies of the human and the resonant frequencies of the CWE. This is considered later in the Thesis.

Another crucial point for consideration of CWE detection is the existence of multiple scattering objects attached to the human. These scattering objects could be two CWEs. In that case there would be multiple specular reflections from all the scattering objects and standing waves would be set up in the space between the scattering objects. So the effect of multiple scattering objects attached to the human on the overall complex object LTR must also be examined. In this Thesis the core objective is to resolve the differences in the LTR of a human with and without a sphere so the effect of multiple scattering objects attached to the human on the overall reflection is considered for further research.

Chapter 4

LATE TIME RESPONSE PARAMETERS EXTRACTION from the RECEIVED SIGNAL

4.1 Introduction

This chapter examines the acquisition of the parameters of the Late Time Response (LTR). The parameter acquisition can be realised via signal modelling. Signal modelling is an important issue that occurs in many applications such as signal reconstruction, signal prediction or signal interpolation. In these cases a signal is known over an interval of time and the aim is to determine the signal over a different time interval. As it is explained in [67], a signal can be modelled as the response of a Linear Shift Invariant (LSI) filter to a unit sample or impulse $\delta(n)$ input, provided that the signal satisfies the shift invariance property i.e. the general properties of the signal do not change with time.

Examination of the impulse response (IR) of the object in chapter 3 showed that for the specific incident wave parameters of aspect angle and wave polarisation, the object's ETR is a sum of exponentials with time varying coefficients. Additionally the LTR of the object is a sum of exponentials with constant coefficients. In [14] it is mentioned that when any resonance extraction method is used, the exponential coefficients are required to be constant. Therefore once the LTR of the considered object is obtained via theory, simulation or experiments, it will be modelled as an LSI filter, in order to extract the poles of the LTR and their residues. Obtaining the LTR poles and residues will lead to effective target-object recognition.

The remaining of the chapter is organised as follows. Section 4.2 presents the mathematical principles that constitute the foundation of signal modelling via an LSI filter. In section 4.3 the theoretical IR of the conducting sphere is derived and generated via the computer simulation algorithm, thus the ETR and LTR of sphere are obtained.

Furthermore the conducting sphere simulated LTR is processed and its poles and residues are extracted. Additionally the numerically extracted poles of the simulated LTR are compared with the exact analytical solution for the poles given by the application of the Mie scattering theory [39] for the sphere. In this way the effectiveness of the algorithms for signal modelling is assessed. Finally section 4.4 concludes the chapter.

4.2 Pole-Residue Extraction via Signal Modelling

4.2.1 LTR as IIR filter

This section presents the essential principles for modelling the LTR $\bar{h}_{LTR}(t)$ of the reflected wave via an LSI filter. In this way $h_e(n)$ is considered as the sampled or discrete function of the LTR $\bar{h}_{LTR}(t)$, therefore $h_e(n)$ is modelled as the filter unit sample ($\delta(n)$) response. Since $h_e(n)$ is the discrete LTR (as described in subsection 3.4.2), it is a collection of damped sinusoids and has the form

$$h_e(n) = \sum_{i=1}^{\frac{I}{2}} R_i e^{\sigma_i n\Delta t} \cos(\omega_i n\Delta t + \phi_i) \text{ for } n = 0,1,..,N \qquad (4.1)$$

Where Δt is the sampling time interval, ω_i is the oscillating radian resonant frequency while $\sigma_i < 0$ is the damping coefficient, R_i is the amplitude and ϕ_i is the phase of each sinusoid. Since $h_e(n)$ is a discrete function the pole of each sinusoid is mapped in the Z-transform domain as $Z_i = e^{S_i \Delta t}$, where $S_i = \sigma_i + j\omega_i$ is the pole of the sinusoid in the Laplace Transform (LT) domain.

Given the set of data $h_e(0), h_e(1), ..., h_e(N)$, that represents the damped sinusoids about to be modelled, an algorithm must be applied in order to extract the poles and the residue of each pole of the exponential. The pole-residue extraction can be achieved by means of an algorithm, which calculates the coefficients of an Infinite Impulse Response (IIR) LSI filter with a predescribed time domain impulse response $h_e(n)$, which is the LTR of the reflected waveform. The most widely acknowledged of these algorithms are *Prony's* method [67-74]; *Covariance method of linear prediction* [67, 69, 74, 75, 76, 77]; *Autocorrelation method of linear prediction* [67, 78]; *Pade method* [68, 79]. Another method for pole-residue extraction is *Matrix pencil method* [74, 80].

In [74] the accuracy of the poles extraction procedure was evaluated for the *Matrix pencil*, *Prony's* and the *Covariance* methods. *The Covariance method* was proved to give the most accurate results. Due to their accuracy *Prony's* method and *Covariance* method have a multiplicity of applications in filter design, exponential signal modelling, and parametric modelling.

Assume $h(k)$ as the impulse response of the IIR filter which models $h_e(n)$, the z- Transform of $h(k)$, which is $H(z)$, can be expressed as the ratio of two polynomials $B_q(z)$ and $A_p(z)$ of variable z^{-1} with coefficients $b_q(k)$ and $a_p(k)$ respectively, which are the parameters of the filter or model. Therefore $H(z)$can also be expressed as

$$H(z) = \sum_{k=0}^{\infty} h(k) z^{-k} = \frac{B_q(z)}{A_p(z)} = \frac{\sum_{k=0}^{q} b_q(k) z^{-k}}{\sum_{k=0}^{p} a_p(k) z^{-k}} = \frac{\sum_{k=0}^{q} b_q(k) z^{-k}}{1 + \sum_{k=1}^{p} a_p(k) z^{-k}}, \text{ since } a_p(0) = 1. \quad (4.2)$$

Additionally $H(z)$ can be expressed as

$$H(z) = b_q(0)\frac{\prod_{k=1}^{q}\left(1 - z_k z^{-1}\right)}{\prod_{k=1}^{p}\left(1 - p_k z^{-1}\right)} \tag{4.3}$$

z_k are the roots of the numerator polynomial and consequently they are the zeros of $H(z)$, while p_k are the roots of the denominator polynomial and they are the poles of $H(z)$. If $q = 0$ and the order of the numerator polynomial is zero, then $B_q(z) = b_q(0)$ and equation (2) and (3) become

$$H(z) = \frac{b_q(0)}{1 + \sum_{k=1}^{p} a_p(k) z^{-k}} = \frac{b_q(0)}{\prod_{k=1}^{p}\left(1 - p_k z^{-1}\right)} \tag{4.4}$$

In this case $H(z)$ is an all-pole filter. The relation between $h_e(n)$ and $h(k)$ is stated with the error $e'(n) = h_e(n) - h(k)$ or equivalently $E'(z) = H_e(z) - \frac{B_q(z)}{A_p(z)}$ in the frequency domain. This error must be ideally minimum so that $h(k)$ matches $h_e(n)$.

The *Covariance method* of *linear prediction* is a least squares method and it is associated with all-pole signal modelling of $h_e(n)$, in this way $A_p(z)$ is evaluated. However, although the *Covariance method* can evaluate the poles of $h_e(n)$ through the polynomial $A_p(z)$ with coefficients $a_p(k)$, it cannot be used for the reconstruction of $h_e(n)$ since only $b_q(0)$ is available and more $b_q(k)$ coefficients are needed for reliable determination of the poles residues. Therefore it is not possible to reconstruct $h_e(n)$ through the parameters $a_p(k)$ and $b_q(0)$.

Prony's method which is also a least squares method may be used to analyse $h_e(n)$ in terms of a technique commencing as all-pole signal modelling of $h_e(n)$, therefore $A_p(z)$ is evaluated. Subsequently the polynomial $B_q(z)$ with coefficients $b_q(k)$ is evaluated and $h_e(n)$ is reconstructed.

As it was stated earlier since the *Covariance method* is more accurate than *Prony's method*, the *Covariance method* will be used for the pole extraction through parameters $a_p(k)$ and once $a_p(k)$parameters are estimated they will be fed into the algorithm of *Prony's method* which evaluates $b_q(k)$ parameters for the residues extraction. *Prony's method* and the *Covariance method* are described in the following subsections.

4.2.2 Prony's *Method*

Suppose that $h_e(n)$ is a collection of damped sinusoids for $n = 0,1,...,N$ and $h_e(n)$=0 for $n < 0$, due to the causality principle, the filter coefficients $a_p(k)$and $b_q(k)$ of the filter $H(z) = \frac{B_q(z)}{A_p(z)}$ should be calculated, so that the error $e'(n) = h_e(n) - h(k)$or equivalently

$$E'(z) = H_e(z) - \frac{B_q(z)}{A_p(z)} \tag{4.5}$$

is minimised and that the unit sample response $h(k)$of the filter is as identical as possible to $h_e(n)$.

The minimisation of $e'(n)$ or $E'(z)$ in the least squares sense results in a set of nonlinear equations for the coefficients $a_p(k)$and $b_q(k)$[67]. However considering the new error $E(z)$, which is the outcome of multiplication of $E'(z)$ in equation (4.5) with $A_p(z)$

$$E(z) = E'(z)A_p(z) = H_e(z)A_p(z) - B_q(z) \tag{4.6}$$

The least squares minimisation of $E(z)$ results in a set of linear equations for the coefficients $a_p(k)$and $b_q(k)$[68]. Equation (4.6) in the time domain is expressed as

$$e(n) = a_p(n) * h_e(n) - \sum_{k=0}^{q} b_q(k)\delta(n-k) \tag{4.7}$$

$$\text{or} \qquad e(n) = \sum_{k=0}^{p} a_p(k)h_e(n-k) - \sum_{k=0}^{q} b_q(k)\delta(n-k) \tag{4.8}$$

Equation (4.8) is represented in Figure 4.1 and depending on n it can be written as

$$e(n) = \sum_{k=0}^{p} a_p(k)h_e(n-k) - b_q(n), \text{ for } n \le q \tag{4.9}$$

$$\text{and } e(n) = \sum_{k=0}^{p} a_p(k)h_e(n-k), \text{ for } n > q \tag{4.10}$$

Consequently, $h_e(n)$ for $n > q$ is the input into the all-zero filter of equation (4.4) $A_p(z) = \sum_{k=0}^{p} a_p(k)z^{-k} = 1 + \sum_{k=1}^{p} a_p(k)z^{-k}$. This filter is also referred as an inverse filter [69]. The output of the filter $e(n)$ is expressed by equation (4.10) and since $a_p(0) = 1$, $e(n)$can also be written as

$$e(n) = h_e(n) + \sum_{k=1}^{p} a_p(k)h_e(n-k) \tag{4.11}$$

In *Prony's method* the coefficients $a_p(k)$ for $k = 1,..., p$ can be found by minimising the squared error

$$E_p = \sum_{n=q+1}^{N} [e(n)]^2 = \sum_{n=q+1}^{N} \left[h_e(n) + \sum_{k=1}^{p} a_p(k) h_e(n-k) \right]^2 \tag{4.12}$$

where $n \geq q+1$ and $N >> p$. If $h_e(n)$ is complex the squared error becomes

$$E_p = \sum_{n=q+1}^{N} |e(n)|^2 = e(n)e^*(n) = \sum_{n=q+1}^{N} \left| h_e(n) + \sum_{k=1}^{p} a_p(k) h_e(n-k) \right|^2 =$$

$$\sum_{n=q+1}^{N} \left[h_e(n) + \sum_{k=1}^{p} a_p(k) h_e(n-k) \right] \left[h_e(n) + \sum_{k=1}^{p} a_p(k) h_e(n-k) \right]^* \tag{4.13}$$

which is this way the filter coefficients $a_p(k)$ are defined.

After defining the coefficients $a_p(k)$ of the poles of the signal $h_e(n)$ through the squared error minimisation, the coefficients $b_q(k)$ can be also determined by solving

$$b_q(n) = h_e(n) + \sum_{1}^{p} \tilde{a}_k \, h_e(n-k), \text{ for } 0 \leq n \leq q \tag{4.14}$$

The $\tilde{a}_p(k)$ is the solution in the equation (14) of the coefficients $a_p(k)$ of the poles of the signal $h_e(n)$.

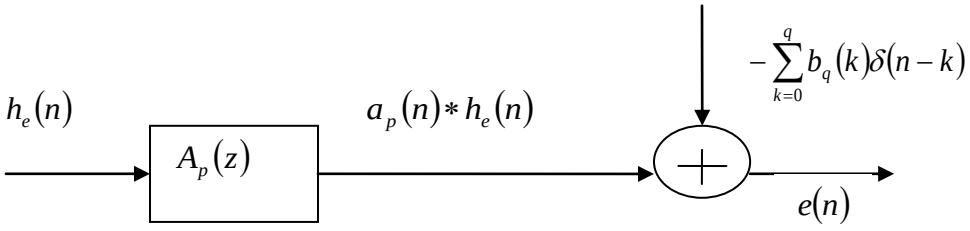

Figure: 4.1 System representation of *Prony's method.*

4.2.3 Covariance Method

The *Covariance method* of *linear prediction* is associated with the all-pole signal modelling of $h_e(n)$, therefore for this method equation (4.6) that describes the $E(z)$ (since $B_q(z) = b_q(0)$) becomes

$$E(z) = H_e(z)A_p(z) - b_q(0) \tag{4.15}$$

In time domain equation (4.15) can be written as

$$e(n) = \sum_{k=0}^{p} a_p(k)h_e(n-k) - b_q(0)\delta(n) \tag{4.16}$$

Depending on n, equation (4.16) can be written as

$$e(n) = \sum_{k=0}^{p} a_p(k)h_e(n-k) - b_q(0), \text{ for } n = 0 \tag{4.17}$$

$$e(n) = \sum_{k=0}^{p} a_p(k)h_e(n-k) = h_e(n) + \sum_{k=1}^{p} a_p(k)h_e(n-k) \text{ , since } a_p(0) = 1 \text{ for } n > 0 \tag{4.18}$$

Provided that the error $e(n)$ is replaced with white noise, equation (4.16) is similar to equations characterising an autoregressive process [69].

Equation (4.18) means that for $n = 1,..., N$, $h_e(n)$ is the input into the all-zero filter $A_p(z) = \sum_{k=0}^{p} a_p(k)z^{-k} = 1 + \sum_{k=1}^{p} a_p(k)z^{-k}$ of equation (4.4), which is the inverse filter, while $e(n)$ is the output of the filter.

$$\text{If } \tilde{h_e}(n) = -\sum_{k=1}^{p} a_p(k)h_e(n-k) \text{ then } e(n) = h_e(n) - \tilde{h_e}(n) \tag{4.19}$$

In *linear prediction* the function $e(n)$is called the *prediction error* between the actual data $h_e(n)$ and the predicted data $\tilde{h_e}(n)$while the terms $a_p(k)$for $k = 1,..., p$ are the

linear predictor coefficients that will be found, while $A_p(z)$ is described as the *prediction error filter*.

In $e(n)=h_e(n)+\sum_{k=1}^{p}a_p(k)h_e(n-k)$, in order to estimate the $e(n)$ at time n the values of $h_e(n)$ at times $n-p,n-p+1,..,n-1,n$ need to be known. Suppose that $h_e(n)$ is known for $n=0,1,..,N$, then the earliest time in which $e(n)$ can be evaluated is $n=p$. Consequently $e(n)$ is estimated for values of n in the interval $n=p,..,N$.

For the *covariance method* the all pole model coefficients $a_p(k)$ for $k=1,...,p$ are found by minimising the squared error E_p. E_p is expressed as

$$E_p=\sum_{n=p}^{N}[e(n)]^2=\sum_{n=p}^{N}\left[h_e(n)-\tilde{h}_e(n)\right]^2=\sum_{n=p}^{N}\left[h_e(n)+\sum_{k=1}^{p}a_p(k)h_e(n-k)\right]^2=$$

$$\sum_{n=p}^{N}\left[\sum_{k=0}^{p}a_p(k)h_e(n-k)\right]^2,\ \text{since}\ a_p(0)=1 \qquad (4.20)$$

where $n>p$ and $N>>p$. If $h_e(n)$ is complex, the squared error becomes

$$E_p=\sum_{n=p}^{N}|e(n)|^2=e(n)e^*(n)=\sum_{n=p}^{N}\left|h_e(n)+\sum_{k=1}^{p}a_p(k)h_e(n-k)\right|^2=$$

$$\sum_{n=p}^{N}\left[h_e(n)+\sum_{k=1}^{p}a_p(k)h_e(n-k)\right]\left[h_e(n)+\sum_{k=1}^{p}a_p(k)h_e(n-k)\right]^*$$

$$\sum_{n=p}^{N}\left[\sum_{k=0}^{p}a_p(k)h_e(n-k)\right]\left[\sum_{k=0}^{p}a_p(k)h_e(n-k)\right]^* \qquad (4.21)$$

In [75] for real $h_e(n)$, the squared error is expressed as

$$E_p=\sum_{n=p}^{N}\left[\sum_{k=0}^{p}a_p(k)h_e(n-k)\right]^2=\sum_{n=p}^{N}\left[\left[\sum_{k=0}^{p}a_p(k)h_e(n-k)\right]\left[\sum_{l=0}^{p}a_p(l)h_e(n-l)\right]\right]=$$

$$\sum_{n=p}^{N}\sum_{k=0}^{p}\sum_{l=0}^{p} a_p(k)h_e(n-k)a_p(l)h_e(n-l) \tag{4.22}$$

Comparing equation (4.20) and (4.21) with (4.12) and (4.13) respectively, it can be realised that the difference between the *covariance method* and *Prony's method* is the limits on the sum of the squared error E_p. However as the *covariance method* has been proved more accurate [74] for the same signal to noise ratio (SNR), the minimisation of E_p of equations (4.20) and (4.21) will be utilised for the estimation of coefficients $a_p(k)$. Nevertheless as the *Covariance method* is associated with the all-pole signal modelling it does not provide the means of determining the coefficients $b_q(k)$ which are useful in order to establish the impulse response of the IIR filter which models $h_e(n)$. So after estimating the coefficients $a_p(k)$ via the *Covariance method*, the *Prony's method* is used in order to determine the coefficients $b_q(k)$. The minimisation of E_p is described in the next subsection.

4.2.4 Squared Error Minimisation

This section describes how the minimisation of the squared error E_p leads into the definition of the coefficients $a_p(k)$. In equation (4.20) for real $h_e(n)$ the squared error E_p was expressed as

$$E_p = \sum_{n=p}^{N}[e(n)]^2 = \sum_{n=p}^{N}\left[h_e(n)+\sum_{k=1}^{p}a_p(k)h_e(n-k)\right]^2$$

The minimisation of E_p can be realised by setting the partial derivatives of E_p with respect to $a_p(i)$ equal to zero, this can be accomplished by solving $\frac{\partial E_p}{\partial a_p(i)} = 0$ for $i = 1,...,p$, which will yield the coefficients $a_p(i)$ of the poles of the signal $h_e(n)$. Therefore

$$\frac{\partial E_p}{\partial a_p(i)} = \frac{\partial [e(n)]^2}{\partial a_p(i)} = \frac{\partial \sum_{n=p}^{N} \left[h_e(n) + \sum_{k=1}^{p} a_p(k) h_e(n-k) \right]^2}{\partial a_p(i)} = 0 \qquad (4.23)$$

As it is shown in the appendix section 4.a, equation (4.23) becomes

$$\sum_{k=1}^{p} a_p(k) \left[\sum_{n=p}^{N} [h_e(n-k) h_e(n-i)] \right] = -\sum_{n=p}^{N} [h_e(n) h_e(n-i)], \text{ for } i = 1,...,p \qquad (4.24)$$

If $h_e(n)$ is complex, in equation (4.21) the squared error E_p was expressed as

$$E_p = \sum_{n=p}^{N} |e(n)|^2 = \sum_{n=p}^{N} \left| h_e(n) + \sum_{k=1}^{p} a_p(k) h_e(n-k) \right|^2 .$$

In this case the solution of $\frac{\partial E_p}{\partial a_p^*(i)} = 0$ results in the minimisation of E_p, so taking the partial derivative of E_p with respect to $a^*{}_p(i)$ and setting the derivative equal to zero yields

$$\frac{\partial E_p}{\partial a_p^*(i)} = \frac{\partial |e(n)|^2}{\partial a_p^*(i)} = \frac{\partial \sum_{n=p}^{N} \left| h_e(n) + \sum_{k=1}^{p} a_p(k) h_e(n-k) \right|^2}{\partial a_p^*(i)} = 0 \qquad (4.25)$$

As it is shown in the appendix section 4.a from the squared error minimisation equation (4.25) becomes

$$\sum_{k=1}^{p} a_p(k)\left[\sum_{n=p}^{N}\left[h_e(n-k)h_e^*(n-i)\right]\right] = -\sum_{n=p}^{N}\left[h_e(n)h_e^*(n-i)\right], \text{ for } i=1,...,p \qquad (4.26)$$

If the definition is made for real $h_e(n)$

$$r_{h_e h_e}(i,k) = \sum_{n=p}^{N} h_e(n-k)h_e(n-i) \qquad (4.27)$$

and for complex $h_e(n)$

$$r_{h_e h_e}(i,k) = \sum_{n=p}^{N} h_e(n-k)h_e^*(n-i) \qquad (4.28)$$

Considering equations (4.27) and (4.28), equations (4.24) and (4.26) will become

$$\sum_{k=1}^{p} a_p(k) r_{h_e h_e}(i,k) = -r_{h_e h_e}(i,0), \text{ for } i=1,...,p \qquad (4.29)$$

Where $r_{h_e h_e}(i,k)$ is defined as the deterministic autocorrelation sequence of $h_e(n)$, since $h_e(n)$ can be characterised as deterministic signal. Signals are generally classified into one of two kinds deterministic and random. A deterministic signal is one that after repeated measurements the occurring signals are replicas of the original one, so the deterministic signal is reproduced. A random signal or random process alternatively, is a signal that is not repeated in a predictable way. Discrete time random processes represent a sequence of random variables therefore they are described probabilistically.

Equation (4.29) represents a group of *p* linear equations with *p* unknowns $a_p(1),\ldots,a_p(p)$, which are also referred as the *covariance normal equations*. Equation (4.29) can be written in terms of matrices as

$$\begin{bmatrix} r_{h_eh_e}(1,1) & r_{h_eh_e}(1,2) & r_{h_eh_e}(1,3) & \cdots & r_{h_eh_e}(1,p-1) & r_{h_eh_e}(1,p) \\ r_{h_eh_e}(2,1) & r_{h_eh_e}(2,2) & r_{h_eh_e}(2,3) & \cdots & r_{h_eh_e}(2,p-1) & r_{h_eh_e}(2,p) \\ r_{h_eh_e}(3,1) & r_{h_eh_e}(3,2) & r_{h_eh_e}(3,3) & \cdots & r_{h_eh_e}(3,p-1) & r_{h_eh_e}(3,p) \\ \vdots & \vdots & \vdots & & \vdots & \vdots \\ r_{h_eh_e}(p-1,1) & r_{h_eh_e}(p-1,2) & r_{h_eh_e}(p-1,3) & \cdots & r_{h_eh_e}(p-1,p-1) & r_{h_eh_e}(p-1,p) \\ r_{h_eh_e}(p,1) & r_{h_eh_e}(p,2) & r_{h_eh_e}(p,3) & \cdots & r_{h_eh_e}(p,p-1) & r_{h_eh_e}(p,p) \end{bmatrix} \begin{bmatrix} a_p(1) \\ a_p(2) \\ a_p(3) \\ \vdots \\ a_p(p-1) \\ a_p(p) \end{bmatrix} = -\begin{bmatrix} r_{h_eh_e}(1,0) \\ r_{h_eh_e}(2,0) \\ r_{h_eh_e}(3,0) \\ \vdots \\ r_{h_eh_e}(p-1,0) \\ r_{h_eh_e}(p,0) \end{bmatrix} \quad (4.30)$$

which, since $a_p(0)=1$ is equivalent to

$$\begin{bmatrix} r_{h_eh_e}(1,0) & r_{h_eh_e}(1,1) & r_{h_eh_e}(1,2) & r_{h_eh_e}(1,3) & . & r_{h_eh_e}(1,p-1) & r_{h_eh_e}(1,p) \\ r_{h_eh_e}(2,0) & r_{h_eh_e}(2,1) & r_{h_eh_e}(2,2) & r_{h_eh_e}(2,3) & . & r_{h_eh_e}(2,p-1) & r_{h_eh_e}(2,p) \\ r_{h_eh_e}(3,0) & r_{h_eh_e}(3,1) & r_{h_eh_e}(3,2) & r_{h_eh_e}(3,3) & . & r_{h_eh_e}(3,p-1) & r_{h_eh_e}(3,p) \\ \vdots & \vdots & \vdots & \vdots & & \vdots & \vdots \\ r_{h_eh_e}(p-1,0) & r_{h_eh_e}(p-1,1) & r_{h_eh_e}(p-1,2) & r_{h_eh_e}(p-1,3) & . & r_{h_eh_e}(p-1,p-1) & r_{h_eh_e}(p-1,p) \\ r_{h_eh_e}(p,0) & r_{h_eh_e}(p,1) & r_{h_eh_e}(p,2) & r_{h_eh_e}(p,3) & . & r_{h_eh_e}(p,p-1) & r_{h_eh_e}(p,p) \end{bmatrix} \begin{bmatrix} 1 \\ a_p(1) \\ a_p(2) \\ a_p(3) \\ \vdots \\ a_p(p-1) \\ a_p(p) \end{bmatrix} = \begin{bmatrix} 0 \\ 0 \\ 0 \\ 0 \\ 0 \\ 0 \\ 0 \end{bmatrix} \quad (4.31)$$

If the autocorrelation matrix is expressed as

$$\mathbf{R}_{h_eh_e} = \begin{bmatrix} r_{h_eh_e}(1,1) & r_{h_eh_e}(1,2) & r_{h_eh_e}(1,3) & \cdots & r_{h_eh_e}(1,p-1) & r_{h_eh_e}(1,p) \\ r_{h_eh_e}(2,1) & r_{h_eh_e}(2,2) & r_{h_eh_e}(2,3) & \cdots & r_{h_eh_e}(2,p-1) & r_{h_eh_e}(2,p) \\ r_{h_eh_e}(3,1) & r_{h_eh_e}(3,2) & r_{h_eh_e}(3,3) & \cdots & r_{h_eh_e}(3,p-1) & r_{h_eh_e}(3,p) \\ \vdots & \vdots & \vdots & & \vdots & \vdots \\ r_{h_eh_e}(p-1,1) & r_{h_eh_e}(p-1,2) & r_{h_eh_e}(p-1,3) & \cdots & r_{h_eh_e}(p-1,p-1) & r_{h_eh_e}(p-1,p) \\ r_{h_eh_e}(p,1) & r_{h_eh_e}(p,2) & r_{h_eh_e}(p,3) & \cdots & r_{h_eh_e}(p,p-1) & r_{h_eh_e}(p,p) \end{bmatrix} \quad (4.32)$$

and the column vectors are equal to

$$\mathbf{r}_{h_eh_e} = \begin{bmatrix} r_{h_eh_e}(1,0) & r_{h_eh_e}(2,0) & r_{h_eh_e}(3,0) & . & . & r_{h_eh_e}(p-1,0) & r_{h_eh_e}(p,0) \end{bmatrix}^T \quad (4.33)$$

$$\mathbf{a}_p = \begin{bmatrix} a_p(1) & a_p(2) & a_p(3) & . & . & a_p(p-1) & a_p(p) \end{bmatrix}^T \quad (4.34)$$

then equation (4.31) can be written as

$$\begin{bmatrix}\mathbf{r}_{h_e h_e} & \mathbf{R}_{h_e h_e}\end{bmatrix}\begin{bmatrix}1\\ \mathbf{a}_p\end{bmatrix} = 0 \tag{4.35}$$

and equation (4.30) can be expressed as

$$\mathbf{R}_{h_e h_e}\mathbf{a}_p = -\mathbf{r}_{h_e h_e} \tag{4.36}$$

The autocorrelation matrix $\mathbf{R}_{h_e h_e}$ can be written in terms of the data matrix $\mathbf{X}_p$ as

$$\mathbf{R}_{h_e h_e} = \mathbf{X}_p^H \mathbf{X}_p \tag{4.37}$$

where

$$\mathbf{X}_p = \begin{bmatrix} h_e(p-1) & h_e(p-2) & \cdots & h_e(1) & h_e(0) \\ h_e(p) & h_e(p-1) & \cdots & h_e(2) & h_e(1) \\ h_e(p+1) & h_e(p) & \cdots & h_e(3) & h_e(2) \\ h_e(p+2) & h_e(p+1) & \cdots & h_e(4) & h_e(3) \\ \vdots & \vdots & & \vdots & \vdots \\ h_e(N-2) & h_e(N-3) & \cdots & h_e(N-p) & h_e(N-p-1) \\ h_e(N-1) & h_e(N-2) & \cdots & h_e(N-p+1) & h_e(N-p) \end{bmatrix} \tag{4.38}$$

and $\mathbf{r}_{h_e h_e}$ in terms of the data matrix $\mathbf{X}_p$ in equation (4.38) can be expressed as

$$\mathbf{r}_{h_e h_e} = \mathbf{X}_p^H \mathbf{x}_p \tag{4.39}$$

where

$$\mathbf{x}_p = \begin{bmatrix} h_e(p) & h_e(p+1) & . & . & . & h_e(N-1) & h_e(N) \end{bmatrix}^T \tag{4.40}$$

Therefore $\mathbf{R}_{h_e h_e}\mathbf{a}_p = -\mathbf{r}_{h_e h_e}$ in terms of equations (4.38) and (4.40) can be expressed as

$$\mathbf{X}_p^H \mathbf{X}_p \mathbf{a}_p = -\mathbf{X}_p^H \mathbf{x}_p \tag{4.41}$$

If $\mathbf{R}_{h_e h_e}$ has full rank and therefore is non-singular and invertible then equation (4.36) becomes

$$\mathbf{a}_p = -\left(\mathbf{R}_{h_e h_e}\right)^{-1}\mathbf{r}_{h_e h_e} \tag{4.42}$$

or**,** in terms of equations (4.38) and (4.40), equation (4.42) can be written as

$$\mathbf{a}_p = -\left(\mathbf{X}_p^H \mathbf{X}_p\right)^{-1}\mathbf{X}_p^H \mathbf{x}_p \tag{4.43}$$

The vector $\mathbf{a}_p$ contains the coefficients $a_p(k)$. After $a_p(k)$ are estimated the minimum modelling squared error can be evaluated, as shown in the appendix in pages 242-244. Since autoregressive models are pole-number dependent, they require a large number of poles thus they possibly lead to large-order models. The methodology to determine the number of poles or model order is given in [74].

4.3 Modelling the IR of Conducting Sphere

In this section the efficiency of the algorithms for signal modelling that are described in the previous sections is assessed. Hence the theoretical IR [81] of the conducting sphere of radius $\alpha = 0.0325\,\mathrm{m}$ is produced via obtaining its ETR and LTR. Furthermore the conducting sphere LTR is modelled, and it is reconstructed while its poles and residues are extracted. Consequently the numerically extracted poles are compared with the exact theoretically obtained poles of the sphere.

Assume a plane electromagnetic wave is incident along the z-axis of a conducting sphere. The propagation constant in the ambient vacuum is $k_0 = \dfrac{\omega}{c}$ and c is the velocity of light in the vacuum. The wave is expressed as

$$\vec{E}^{INC} = E_0 \hat{\varepsilon} \exp\left(ik_0 z - i\omega t\right) \tag{4.44}$$

The scattered far field is given in [39, 58] in terms of spherical coordinates (r,θ,ϕ). For the case of backscattering the field is equal to

$$\vec{E}^{BSC} = E_0\left(\frac{\hat{\varepsilon}}{kr}\right)F(0)exp(ik_0 r - i\omega t) \tag{4.45}$$

where

$$F(0) = -i\sum_{n=1}^{\infty}(-1)^{n_{MIE}}\left(n_{MIE}+\frac{1}{2}\right)\left(a_{n_{MIE}} - b_{n_{MIE}}\right) \tag{4.46}$$

The MIE series coefficients $a_{n_{MIE}}$ and $b_{n_{MIE}}$ are given in [39] and are equal to

$$a_{n_{MIE}} = -\frac{j_{n_{MIE}}(k_0\alpha)}{h^1_{n_{MIE}}(k_0\alpha)} \tag{4.47}$$

$$b_{n_{MIE}} = -\frac{\left[k_0\alpha j_{n_{MIE}}(k_0\alpha)\right]'}{\left[k_0\alpha h^1_{n_{MIE}}(k_0\alpha)\right]'} \tag{4.48}$$

where $j_{n_{MIE}}(k_0\alpha)$ is the spherical Bessel function of the first kind of order n_{MIE} and $h^1_{n_{MIE}}(k_0\alpha)$ is the spherical Hankel function of the first kind of order n_{MIE}.

In section 2.4.5, it was stated that the reflected wave from the grenade or the sphere of radius $\alpha = 0.0325\,\text{m}$, which is the object approximating the grenade, will be obtained in the 0.7-6.7 GHz band. Considering the denominators $h^1_{n_{MIE}}(k_0\alpha)$ and $\left[k_0\alpha h^1_{n_{MIE}}(k_0\alpha)\right]'$ in equations (4.47) and (4.48), for $1 \le n_{MIE} \le 4$ the poles of sphere that correspond to the first four resonant frequencies can be analytically evaluated. These poles are shown in Figure 4.2. Additionally for $1 \le n_{MIE} \le 8$ the poles of the sphere that correspond to the first 8 resonant frequencies can be analytically estimated. These poles are shown in Figure 4.3

By means of the poles of Figures 4.2 and 4.3 and singularity expansion methods and of equations (4.45)-(4.48), that describe the reflected wave of a sphere, the IR of a sphere of radius 0.0325 m can be theoretically derived. For $1 \le n_{MIE} \le 4$ and $1 \le n_{MIE} \le 8$ the IR is produced and is shown in Figures 4.4 and 4.5 respectively. In section 3.4.1 it was stated that the ETR of the sphere lasts for time interval

$$T_L = 4\left(\frac{\alpha}{c}\right) \tag{4.49}$$

In this case $T_L = 0.433\,ns.$ In Figure 4.4 it is observed that at the end of ETR, beginning of LTR there is a discontinuity. This is due to the limitation of the model to the four resonant frequencies, since the inclusion of additional resonant frequencies fills in the discontinuity as it is also observed in Figure 4.5.

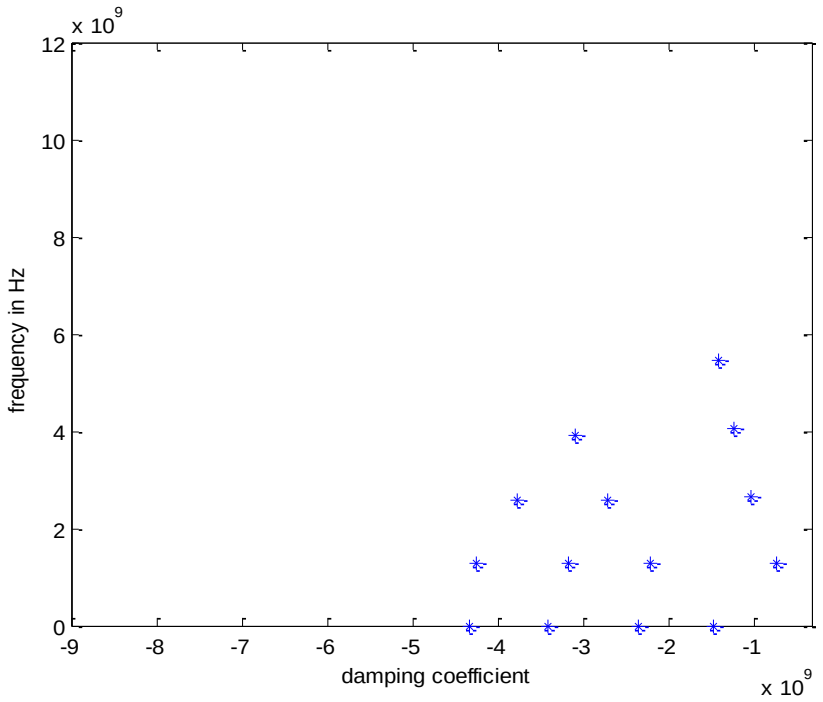

Figure 4.2: Theoretical poles for 0.0325 m radius sphere for $1 \le n_{MIE} \le 4$, or four resonant frequencies.

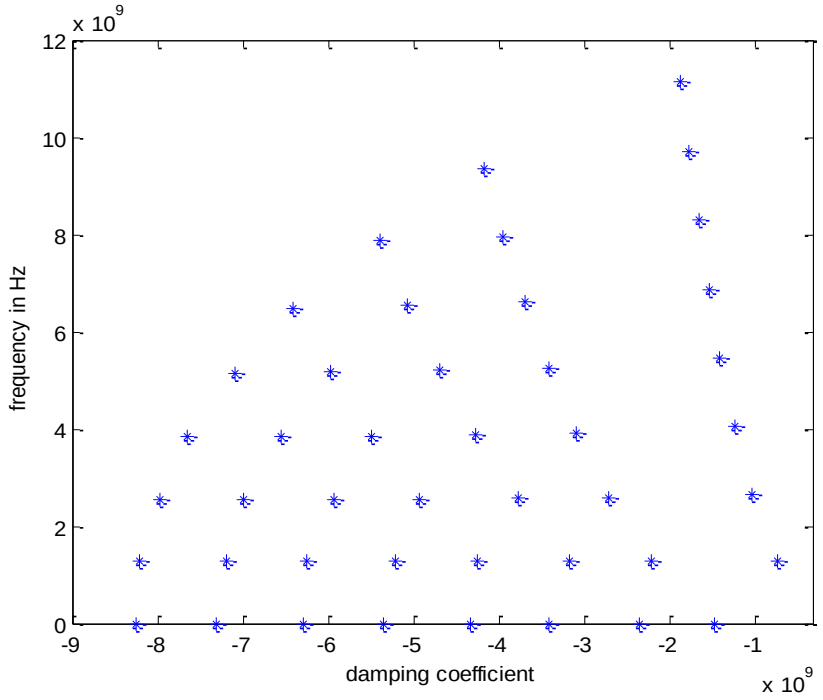

Figure 4.3: Theoretical poles for 0.0325 m radius sphere for $1 \le n_{MIE} \le 8$ or eight resonant frequencies.

.

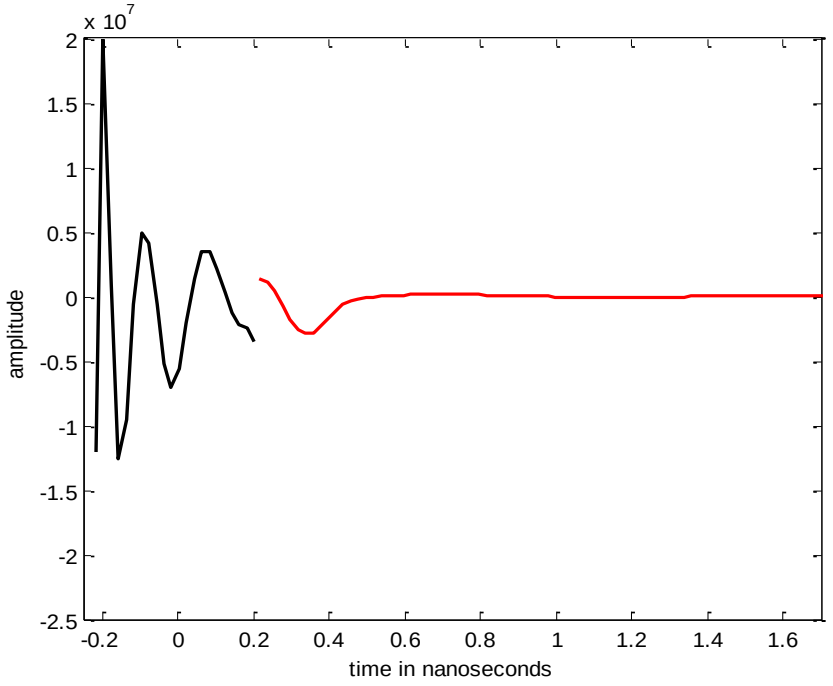

Figure 4.4: The theoretical IR of a sphere of radius 0.0325 m for $1 \le n_{MIE} \le 4$.

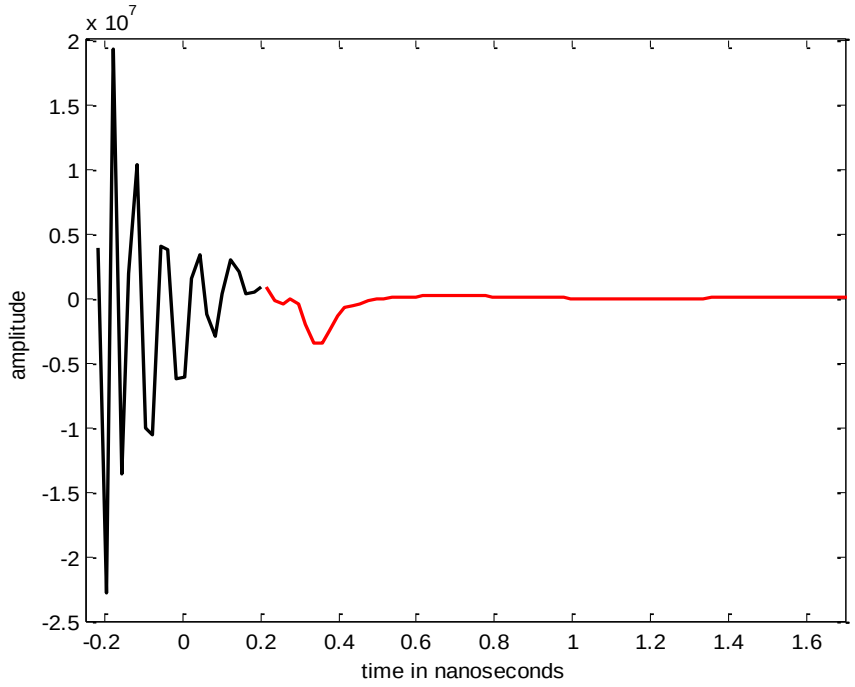

Figure 4.5: The theoretical IR of a sphere of radius 0.0325 m for $1 \le n_{MIE} \le 8$.

In order to test the modelling algorithms, the *Covariance method* on the LTR ($h_e(n)$) of the sphere is applied, which yields coefficients $a_p(k)$ of $A_p(z)$. Once $a_p(k)$ are evaluated they are fed into the algorithm of *Prony's method*, which evaluates $b_q(k)$coefficients of $B_q(z)$. $a_p(k)$ coefficients lead to LTR poles extraction. After the $a_p(k)$ and $B_q(z)$ coefficients are determined then transfer function $H_e(z)$ is established and can be expanded in poles and residues. In this way $h_e(n)$ is reconstructed and the sphere LTR is modelled. This procedure is shown in the block diagram of Fig. 4.6. The LTR reconstruction and the comparison of extracted poles with the theoretically obtained ones, examines the modelling procedure for errors.

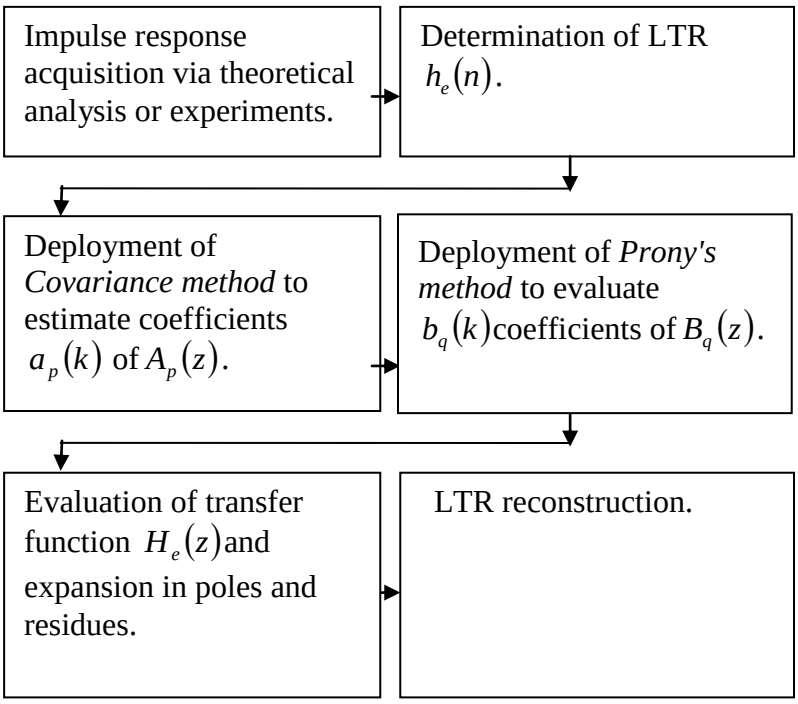

Figure 4.6: Procedure for poles and amplitudes extraction.

The poles of the reconstructed LTR have been mapped in the *s*-domain via $Z_i = e^{S_i \Delta t}$ where Δt is the sampling interval. Since the LTR is a series of damped sinusoids the poles have a negative real part. Figures 4.7 and 4.8 show the theoretical and reconstructed LTRs of a 0.0325 radius sphere for $1 \le n_{MIE} \le 4$ and for $1 \le n_{MIE} \le 8$ respectively.

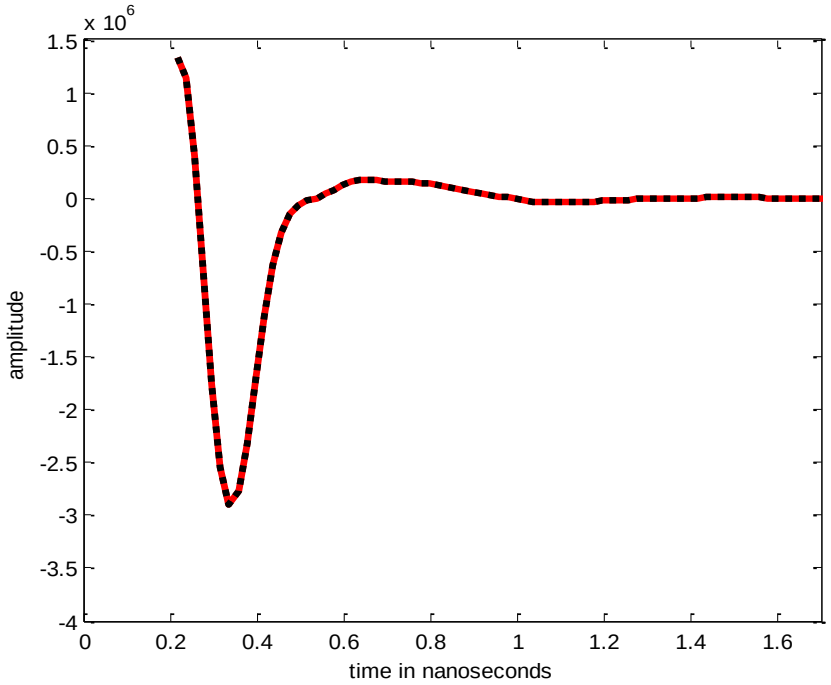

Figure 4.7: The theoretical (red) and reconstructed (black) LTRs for $1 \le n_{MIE} \le 4$.

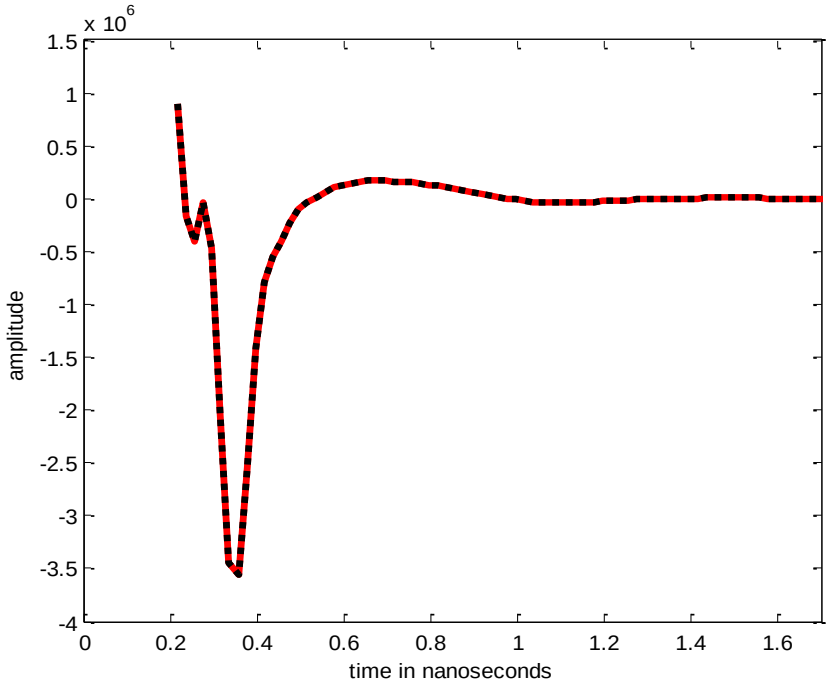

Figure 4.8: The theoretical (red) and reconstructed (black) LTRs for $1 \le n_{MIE} \le 8$.

Figures 4.9 and 4.10 show the numerically extracted poles from the reconstructed LTRs of Figures 4.7 and 4.8 respectively for a model of 42 poles.

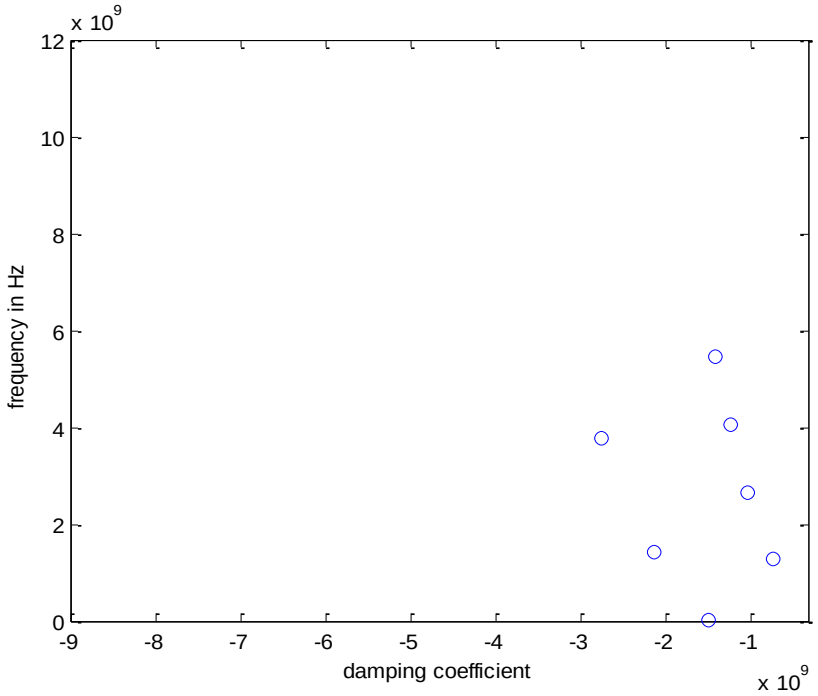

Figure 4.9: Numerically extracted poles for 0.0325 m radius sphere for $1 \le n_{MIE} \le 4$.

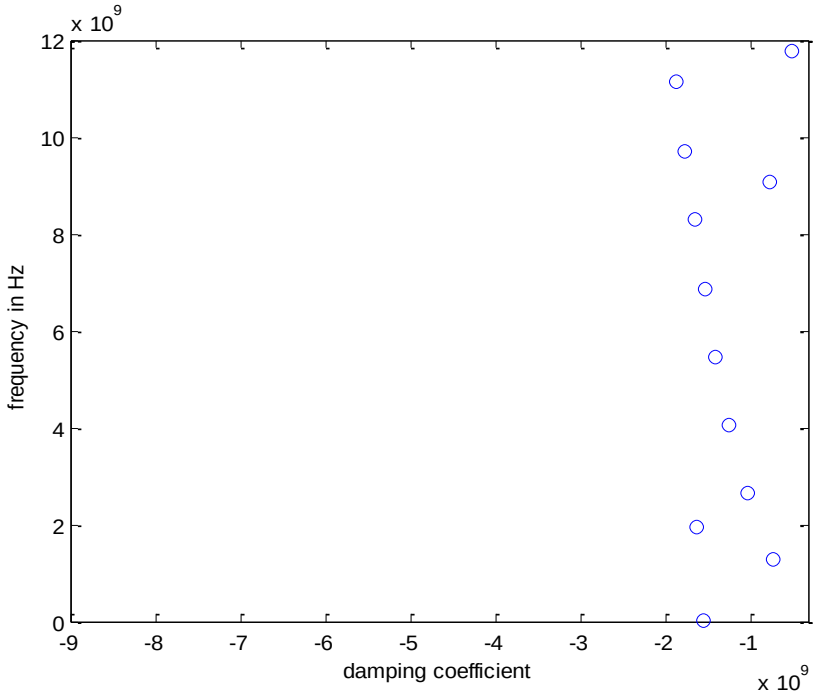

Figure 4.10: Numerically extracted poles for 0.0325 m radius sphere for $1 \le n_{MIE} \le 8$.

Figures 4.11 and 4.12 show the amplitudes of the poles of Figures 4.9 and 4.10 respectively.

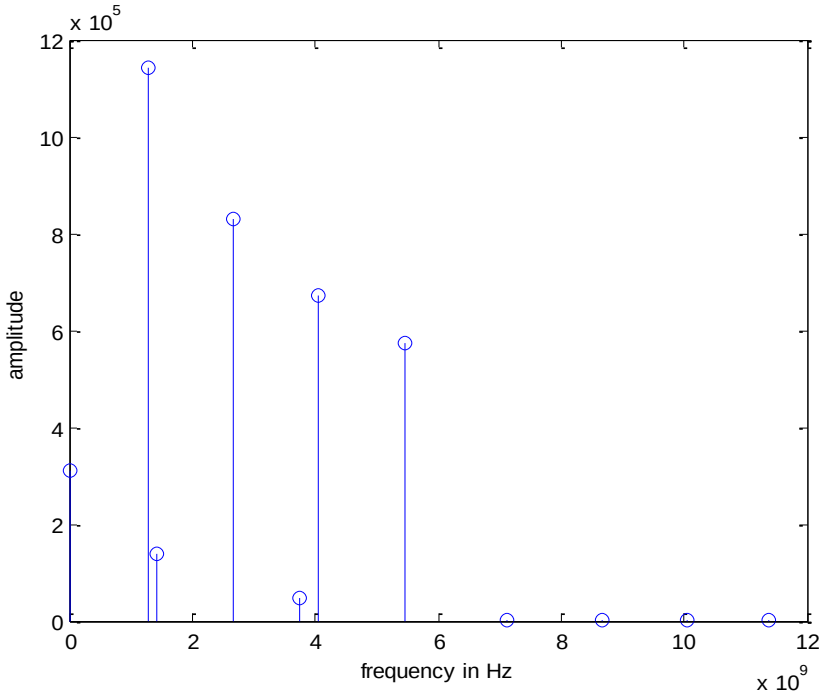

Figure 4.11: Amplitudes for 0.0325 m radius sphere for $1 \le n_{MIE} \le 4$.

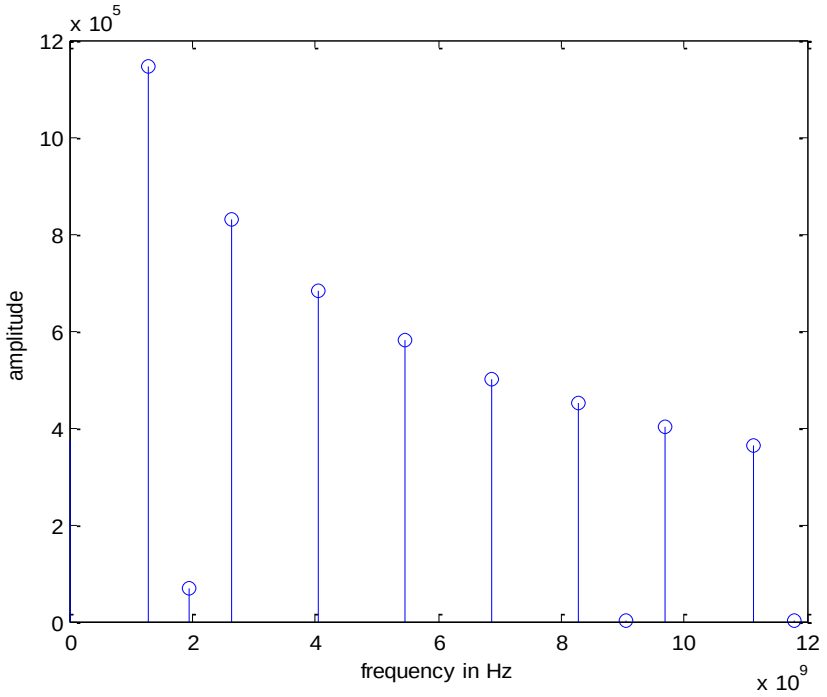

Figure 4.12: Amplitudes for 0.0325 m radius sphere for $1 \le n_{MIE} \le 8$.

Figures 4.13 and 4.14 show the theoretical poles and numerically extracted poles of the 0.0325 radius sphere for $1 \le n_{MIE} \le 4$ and $1 \le n_{MIE} \le 8$ respectively.

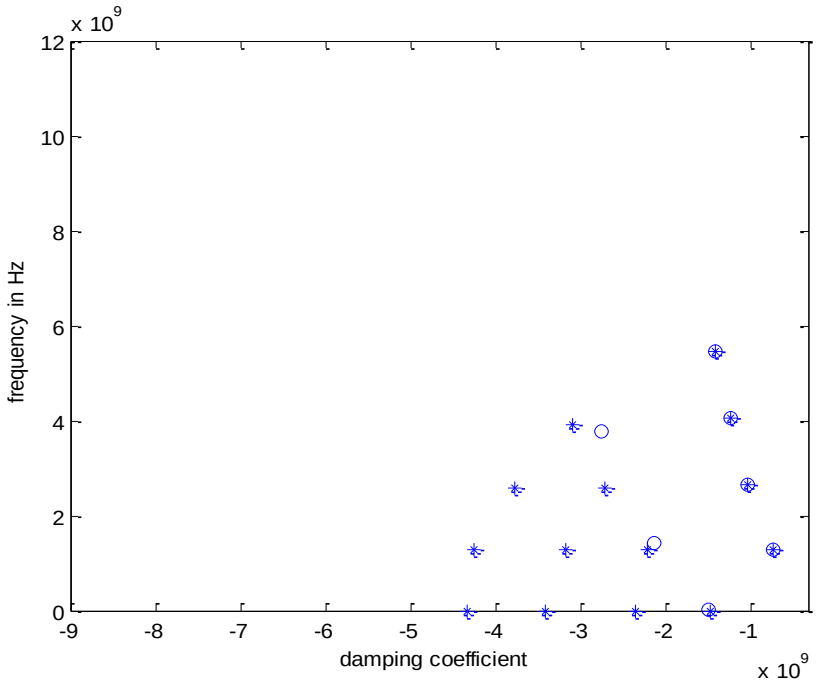

Figure 4.13: Theoretical (*) and numerically extracted (o) poles for 0.0325 m radius sphere for $1 \le n_{MIE} \le 4$.

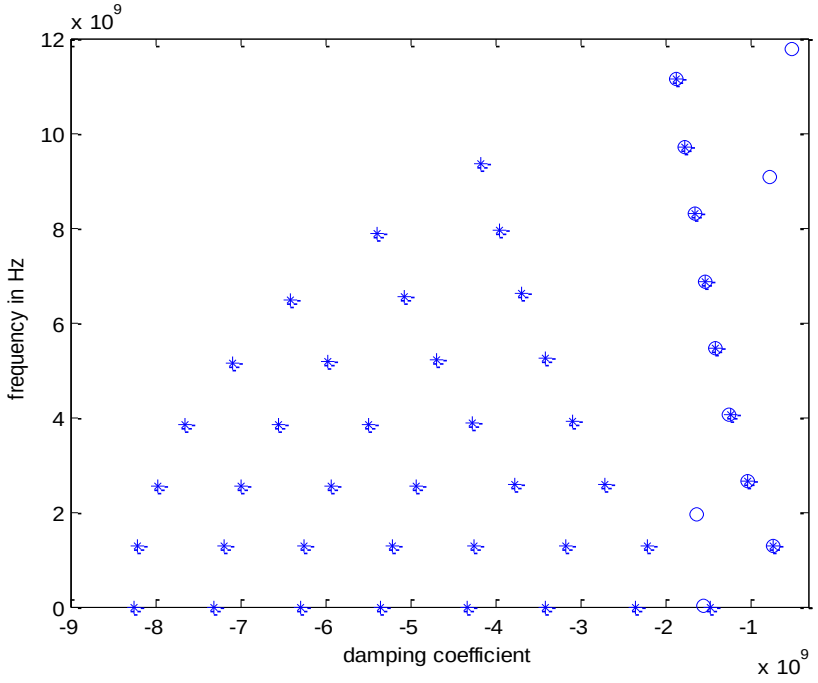

Figure 4.14: Theoretical (*) and numerically extracted (o) poles for 0.0325 m radius sphere for $1 \le n_{MIE} \le 8$.

4.4 Discussion of Results

This chapter presented the theoretical framework that describes the signal modelling in the case of noiseless signals. According to the methodology the signals are modelled as the impulse response of an LSI IIR filter. In this way the algorithms that enable us to achieve signal modelling, which are the *covariance method of linear prediction* and *Prony's method* were described.

Furthermore the theoretical IR of the conducting sphere of radius $\alpha = 0.0325\,\text{m}$ was produced in terms of the ETR and LTR of the sphere for two cases of MIE coefficients i.e. $1 \le n_{MIE} \le 4$ and $1 \le n_{MIE} \le 8$. Figure 4.2 shows that consideration of the MIE coefficients for $1 \le n_{MIE} \le 4$, means that only the first four resonant frequencies for the sphere reflected wave IR are taken into account, or that the considered band is 0.7-6.7 GHz. If the MIE coefficients for $1 \le n_{MIE} \le 8$ are considered as in Figure 4.3, then the first eight resonant frequencies are taken into account, so the considered band is 0.7-12.0 GHz.

Figure 4.4 shows the sphere IR for four resonant frequencies, while Figure 4.5 shows the sphere IR for eight resonant frequencies. Comparison of the two IRs yields that even though the two IRs involve different number of resonant frequencies, small difference can be observed between the two IRs, therefore only the first 4 resonant frequencies essentially contribute in the creation of the reflected wave of the sphere. In this way, considering the sphere IR, the conclusion can be deduced that the 0.7-6.7 GHz band is sufficient for concealed sphere or concealed grenade detection. This assumption was made in chapter 2 after the sphere Radar Cross Section (RCS) was considered.

Figure 4.7 and Figure 4.8 show the modelling of the conducting sphere LTR of radius 0.0325m, as it is shown the theoretical LTRs coincide with the reconstructed LTRs. Figure 4.9

and Figure 4.11 show the poles and amplitudes respectively that are extracted from the reconstructed LTR of Figure 4.7 for $1 \le n_{MIE} \le 4$, while Figure 4.10 and Figure 4.12 show the poles and amplitudes respectively that are extracted from the reconstructed LTR of Figure 4.8 for $1 \le n_{MIE} \le 8$. From these figures it can be seen that as the frequency of the pole increases the amplitude of the poles or the contribution of the pole to the formulation of the IR decreases. This encourages us to restrict the considered band for the reflected wave of the sphere to 0.7-6.7 GHz, i.e. to include only the first four resonant frequencies, for effective concealed sphere or concealed grenade detection.

In Figure 4.13 the numerically extracted poles are plotted with the exact theoretically obtained poles of the sphere for $1 \le n_{MIE} \le 4$. In Figure 4.14 the numerically extracted poles are plotted with the exact theoretically obtained poles of the sphere for $1 \le n_{MIE} \le 8$. Comparing the extracted poles with the theoretical poles for these two cases it is observed that the extracted poles perfectly match with the theoretical poles of the first branch with the lowest damping coefficient. Therefore from the sphere LTR only the poles belonging to the first branch with the lowest damping coefficient were extracted. This means that only these poles essentially contribute in the formulation of the LTR. The rest of the poles do not contribute since they have a relatively high damping coefficient, and the sinusoids that consist from these poles quickly converge to zero.

4.5 Conclusions

In this chapter, a particular algorithm for signal modeling was utilized in order to extract the resonant frequencies of the LTR of the sphere. Furthermore from the comparison of theoretical and reconstructed LTRs and theoretical and numerically extracted poles, it is concluded that the respective poles are in accordance. Thus the algorithm for pole-amplitude extraction is efficient. So this algorithm will be used in the next chapters for signal modelling and extraction of the resonant frequencies of the LTRs.

Chapter 5

REFLECTOR - ATTACHED

SPHERE DETECTION

5.1 Introduction

This chapter presents the experimental configuration and the methodology for the processing of the experimental measurements in order to examine the feasibility of remote detection of a grenade appended on the human body.

In the case of a concealed weapon or explosive (CWE) detection via UWB radar, the specular reflection from the human is much higher than the reflection from the CWE for which the sensor searches, due to the bigger dimensions of the human, hence the human's reflection will mask the reflection of the CWE. Consequently, the reflected field from an individual with a CWE is very similar in magnitude to the reflected field from an individual without one. Therefore a valid conclusion cannot be made on the existence of the body-worn CWE by simple observation of the overall reflection.

The magnitude and duration of the Late Time Response (LTR) also depend on the shape, dimensions and electrical properties of the object. So there is an important issue to resolve. Whether the human LTR overwhelms the CWE LTR, or the LTR from the human-CWE composite object presumably provides information on both the resonant frequencies of the human and the resonant frequencies of the CWE. Therefore by analysing the reflected LTR of the complex human-CWE object and the LTR of the human, their resonant frequencies can be obtained. Investigation of the respective LTR dissimilarities in terms of complex natural resonant frequencies can draw a conclusion on the existence of the CWE so that CWE detection is feasible.

The fundamental objective of the experiment is the identification of a grenade appended on the human body. In this stage of the research the human is approximated as a 50 cm x 40 cm conducting metal sheet used as reflector and the explosive is

approximated as a 0.0325 m radius conducting sphere or as a 0.024 m radius conducting sphere. Therefore the metal sheet and each one of the spheres were used as the UWB radar targets for the experimental procedure and these objects were considered as the components that constitute the composite human-concealed grenade object. Thus an attempt is made to detect the grenade approximated as a sphere as they have similar shapes, attached on the background of a human roughly approximated as a conducting sheet. The basic means of characterising the reflection from targets is the Radar Cross Section (RCS). The human RCS is approximately 1 m^2 [15] . The RCS of flat conducting sheet at normal incidence is expressed as $\sigma_{refl} = \frac{4\pi A_{refl}^2}{\lambda^2}$, [15] where λ is the considered wavelength, which at 1.4 GHz frequency $\lambda = 0.214\,\text{m}$ and A_{refl} is the area of the reflector which is $A_{refl} = 0.2\,\text{m}^2$. So the reflector RCS is approximately 11 m^2. Therefore the reflection from the reflector is higher than the human reflection. So the retrieval of the sphere resonant frequencies from the complex reflector-sphere object is a challenging task and it is a very strict test on the feasibility of CWE detection. In this chapter the LTR poles and residues of the object are obtained via the Singular Value decomposition (SVD)-Prony [82-89] method. The use of SVD [86] provides a robust method for extracting damped sinusoids in the presence of noise.

In the following sections a detailed analysis is presented on the various aspects involved in the experimental procedure. Initially in section 5.2 the transmission of the incident UWB pulse is described. Then the various steps are described, in order to reach the main objective of the experiment. This is the analysis of the LTR of the various illuminated objects from the UWB pulse. So the remaining of the chapter is organised as

follows, section 5.3 presents the acquired fields in terms of the objects' frequency responses while section 5.4 presents the sphere Impulse Response (IR), and section 5.5 presents the reflector IR and reflector-sphere IR. Finally section 5.6 concludes the chapter.

5.2 Transmission of the UWB Pulse

In this section the pulse compression technique of frequency stepping is applied for the transmission of a UWB pulse by means of a system consisting of two Vivaldi antennas and a Vector Network Analyser (VNA). Therefore the effect of the system of antennas-VNA on the shape of the UWB pulse is investigated at the considered frequency band of 0.7-6.7 GHz. Additionally the necessary process in order to correct the transmitted pulse and succeed in the transmission of the ideal UWB pulse is presented. Consequently an experiment is conducted where two wideband Vivaldi antennas are set to face each other as shown in the configuration of Figure 5.1. The distance between the antennas was 3.2m. The two antennas are connected to a VNA which generates the frequency stepped signal.

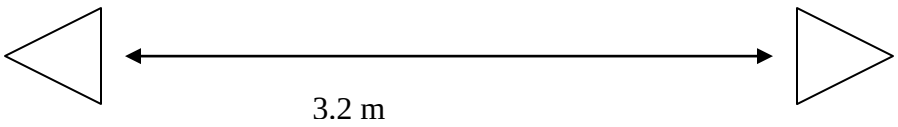

Figure 5.1: Experimental configuration with two Vivaldi antennas facing each other.

In this experiment the VNA is used to drive the transmitting antenna which has a frequency response $H_{tr}(f)$ and collect the radiated pulse wave from the receiving antenna with frequency response $H_{re}(f)$. As a result the radiated electric field between

the two antennas is measured in the frequency domain via the S_{21} parameter. So this S_{21} measurement essentially represents $H_{tr}(f)\times H_{re}(f)$.

The frequency domain measurement was made for the 0.7 GHz to 6.7 GHz band. Therefore the total bandwidth of the transmitted pulse is equal to B=6 GHz and as it has been stated in section 2.4.7 the fractional bandwidth of this signal for lower frequency band limit f_l =0.7 GHz and higher frequency band limit f_h =6.7 GHz is

$$\text{Fractional Bandwidth}=\frac{2(f_h - f_l)}{f_h + f_l}=1.62 \tag{5.1}$$

a value that classifies the signal as UWB. The measurement was made by taking N_1=1601 frequency steps and since $B=(N_1-1)\Delta f$, the frequency step is equal to $\Delta f = 3750000$Hz. The amplitude of the S_{21} parameter measurement which is shown in Figure 5.2 is $|H_{tr}(f)\times H_{re}(f)|$. This also includes a scaling of $1/(4\pi R_d)$ where $R_d = 3.2$ m

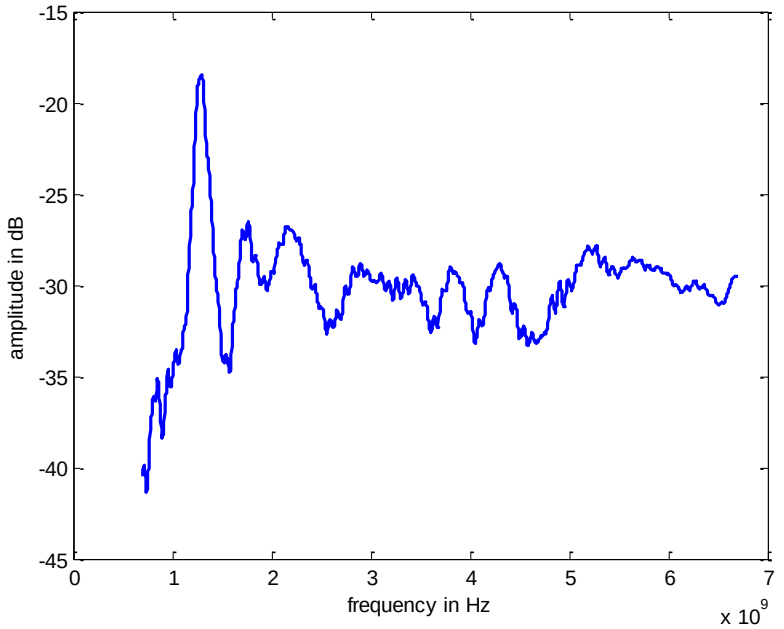

Figure 5.2: $|H_{tr}(f)\times H_{re}(f)|$ response via S21 measurement when two antennas are facing each other.

Applying an Inverse Fourier Transform (IFT) on the $H_{tr}(f)\times H_{re}(f)$ measurement as shown in Figure 5.2, the received field can be represented in the time domain. Before the use of IFT the frequency domain signal is *zero padded*, or it is extended with zeros. This interpolation technique allows us to select the sampling frequency of the time domain field. For this application the sampling frequency is selected to be $f_s = 50$ GHz, so the data series of N_1=1601 frequency steps (frequency step $\Delta f = 3750000$Hz), is padded with the appropriate number of zeros until the frequency of f_s = 50 GHz. As it was shown in section 2.3.4, the inter-pulse interval, or duration of the transmitted sub-signal was equal to $\tau_T = \frac{N}{f_s} = \frac{1}{\Delta f} = 267$ nanoseconds (*ns*). Consequently the UWB pulse length or width is equal to $\tau = \frac{1}{B} = \frac{1}{N_1 \Delta f} = \frac{\tau_T}{N_1} = 0.16667 ns$.

Therefore the received pulse wave $p_{t-r}(t)$=IFT[$H_{tr}(f)\times H_{re}(f)$] has the shape of the waveform, which is shown in Figure 5.3. As it is observed at the main peak which is at 10.67 *ns* since the distance between the antennas was 3.2m, the duration between the first two zero crossings is about 0.167 ns.

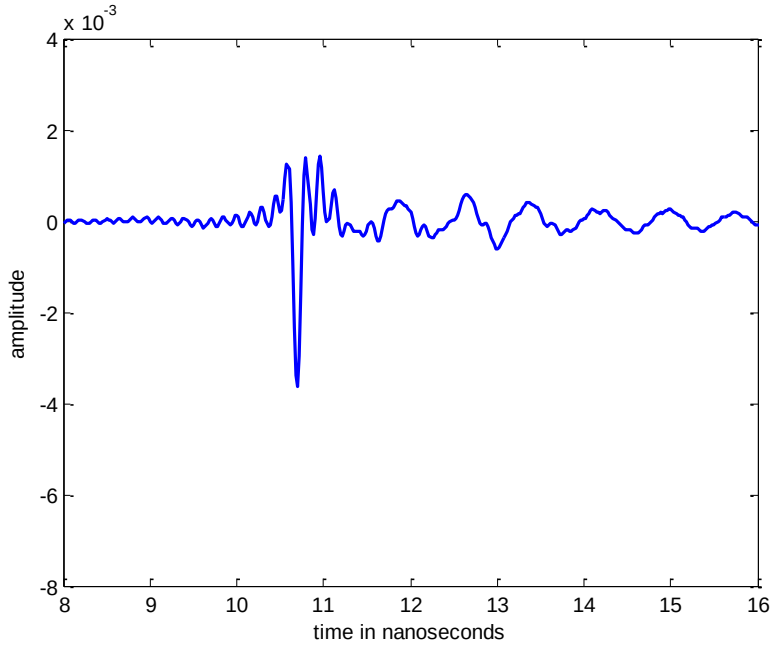

Figure 5.3: Received UWB pulse $p_{t-r}(t)$ when two antennas are facing each other.

The UWB pulse p_{t-r} of Figure 5.3 is essentially the time domain response or received field between the two antennas configuration. If this UWB pulse is incident onto an object, the antennas time domain field will affect the overall reflected field from the object due to convolution between the object's impulse response and the antennas response. Moreover if this pulse is considered as the incident field, the lobes that can be observed after the main peak would create a lot of reflected fields from the illuminated object, which would essentially influence the outcome of the processing of the received object's response. Therefore the antennas response needs to be removed.

In sections 2.4.7 and 2.4.8 it was described that the antennas used, should have a flat frequency response from frequency limits f_l =0.7 GHz to f_h=6.7 GHz, which is similar to the spectrum of Figure 2.29. Furthermore a flat frequency response removes the antennas response in the time domain. Therefore the process of equalisation is applied on the antennas frequency response. Once the antennas frequency response

$H_{tr}(f)\times H_{re}(f)$ is known, a waveform $I_{eq}(f)$ is applied, which makes the resultant response $H_{eq}(f)=I_{eq}(f)\times H_{tr}(f)\times H_{re}(f)$ horizontal at the specific level that is defined as $\left|H_{eq}(f)\right|$

$$\left|H_{eq}(f)\right| = \frac{\max[\left|H_{tr}(f)\times H_{re}(f)\right|]+\min[\left|H_{tr}(f)\times H_{re}(f)\right|]}{2} \tag{5.2}$$

The waveform denoted as $I_{eq}(f)$ is referred to as the frequency domain equalising waveform. Thus the equalising signal $I_{eq}(f)$ is equal to

$$I_{eq}(f)=\frac{H_{eq}(f)}{[H_{tr}(f)\times H_{re}(f)]} \tag{5.3}$$

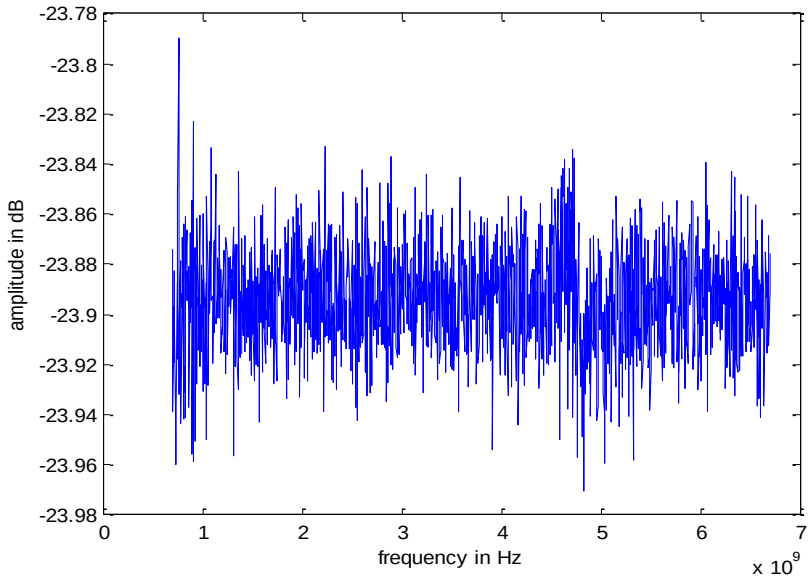

Figure 5.4: Response $\left|H_{eq}(f)\right|$ of two antennas facing each other after frequency domain equalisation has been applied on the measured $\left|H_{tr}(f)\times H_{re}(f)\right|$(antennas response is removed).

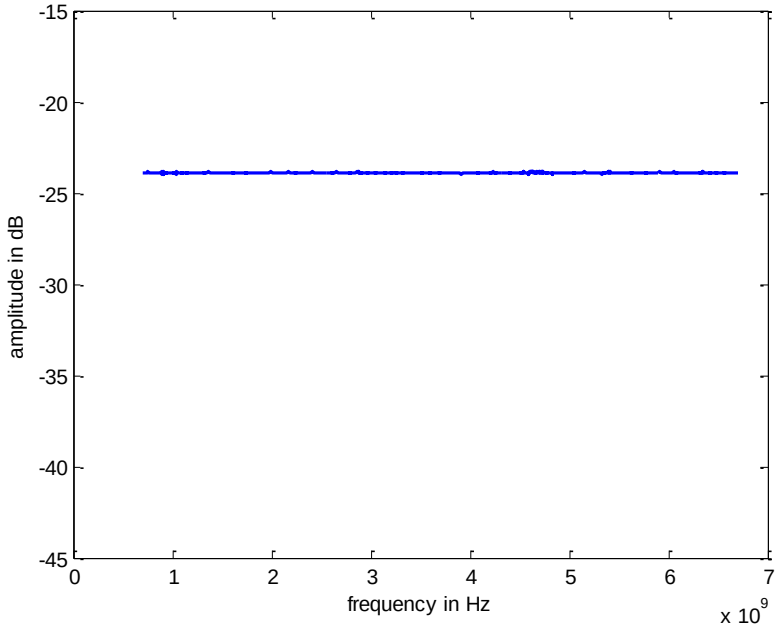

Figure 5.5: Response $|H_{eq}(f)|$ (like Figure 5.4) in the same scale as Figure 5.2.

Consequently the equalisation process is applied to cancel the antennas response and the outcome is the response of Figures 5.4 and 5.5. By application of an IFT on the frequency response shown in Figure 5.4, using the same parameters as in the case of Figure 5.3, the UWB pulse $p_{eq}(t)$ of Figure 5.6 is obtained, and therefore $p_{eq}(t)$=IFT[$H_{eq}(f)$]. The pulse of Figure 5.6 is equivalent to the pulse of Figure 2.28. Furthermore following the method presented in section 2.4.7 in order to remove the sidelobes of the pulse of Figure 5.6 a Gaussian window $W(f)$ is applied in the equalised frequency response of Figure 5.4 and $H_{eq}(f)W(f)$ is obtained. If an IFT is applied on the frequency response $H_{eq}(f)W(f)$, the UWB pulse $p_{in}(t)$ which is shown in Figure 5.7 is obtained, and consequently $p_{in}(t)$=IFT[$H_{eq}(f)W(f)$]. Therefore the driving function or incident field onto an object will be similar to the UWB pulse of Figure 5.7

and the reflected signal from the object will be the object's impulse response. This incident field will be the illuminating UWB pulse used for concealed weapon detection.

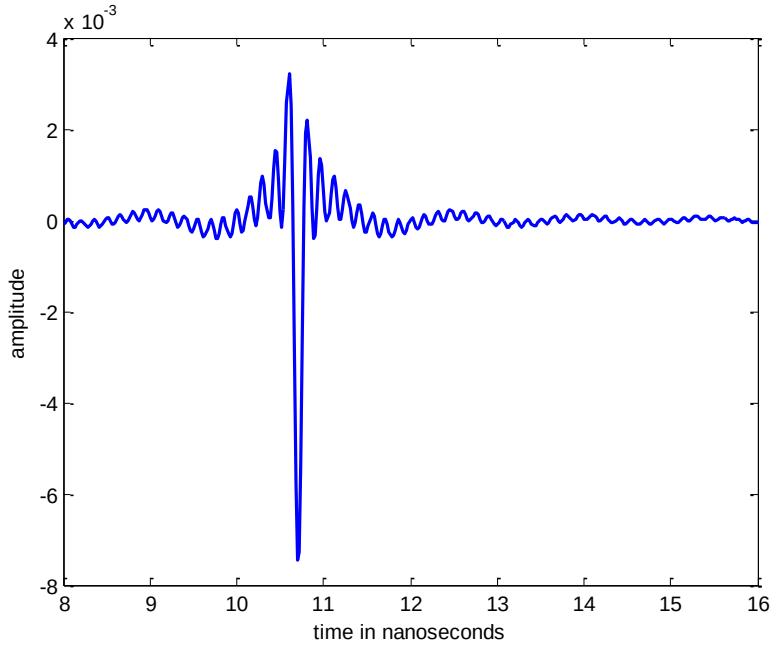

Figure 5.6: Received UWB pulse $p_{eq}(t)$ when two antennas are facing each other after equalisation.

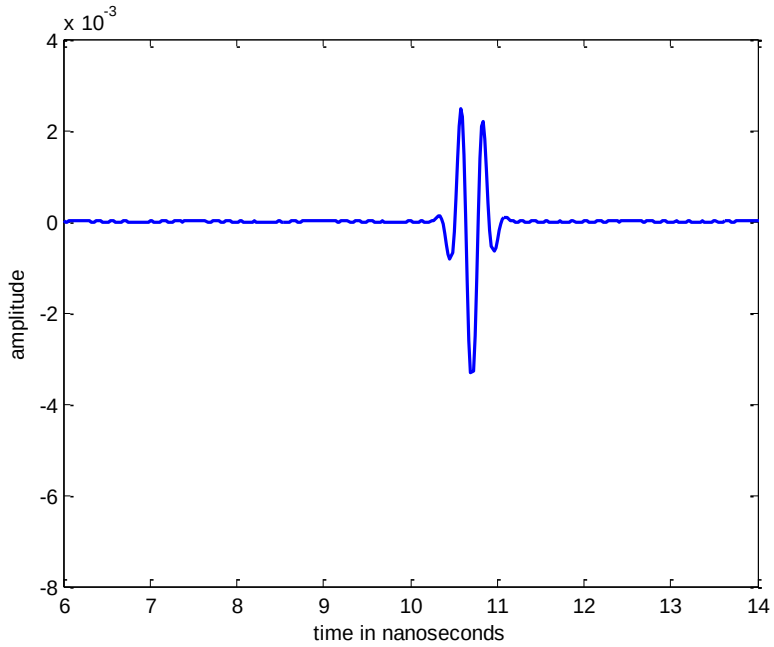

Figure 5.7: Received UWB pulse $p_{in}(t)$ after equalisation and application of Gaussian window.

5.3 Frequency Response Acquisition

After the equalisation procedure, the experimental data are acquired in terms of the frequency responses using the experimental configuration shown in Figure 5.8. This configuration is used to illuminate the target with the UWB pulse and used to obtain the backscattered field from the target-object. In this way the backscattered signals from the various relevant composite objects are obtained.

In this experiment the transmitting antenna and the receiving antenna used in the measurement (antennas set to face each other) in section 5.2 are utilised and the VNA produces the frequency stepped signal. The transmitting antenna with frequency response $H_{tr}(f)$ converts the driving signal into an incident field. Thus backscattered fields from the object and chamber absorber, with respective frequency responses $H_{sc}(f)$ and $H_{abs}(f)$ are created. Multipath scatterings originating from the interaction between the fields of object, antenna and chamber absorber are described by the response $H_{sc-abs}(f)$. The field that is created directly between the transmitting and the adjacent receiving antennas is expressed as the antenna coupling frequency response $H_{cou}(f)$.This field is also known as leakage field. The receiving antenna with frequency response $H_{re}(f)$ converts the sum of the fields into signals and the backscattered field $H_{sc}(f)$ of interest is obtained.

The first object for which the experiment is carried out is the 0.0325 m radius sphere. In order to ensure that the sphere is in the far field, the far field threshold $R \geq \frac{2D^2}{\lambda}$ is used. D in this case is the sphere diameter so $D = 0.065\text{m}$. λ the

wavelength and by considering the minimum wavelength as $\lambda = c / f_h$, for high frequency f_h=6.7 GHz, the wavelength is $\lambda = 0.0448$m. Therefore the range is calculated as $R \geq 0.19$m and the range of 1.55m, where the experiment is performed, is more than adequate.

The modelling for obtaining the reflected signals assumes the case of monostatic radar. However Figure 5.8 depicts a bistatic arrangement with a bistatic angle of 40^o. In [90] it is stated for the RCS in the resonance region of the conducting sphere that, the pseudomonostatic region extends to a bistatic angle of 40^o. For the RCS in the optics region of the conducting sphere, the pseudomonostatic region extends to a bistatic angle of 100^o. In [91] it is stated that except for forward scattering, the bistatic and monostatic conducting sphere RCS in the optics region coincide.

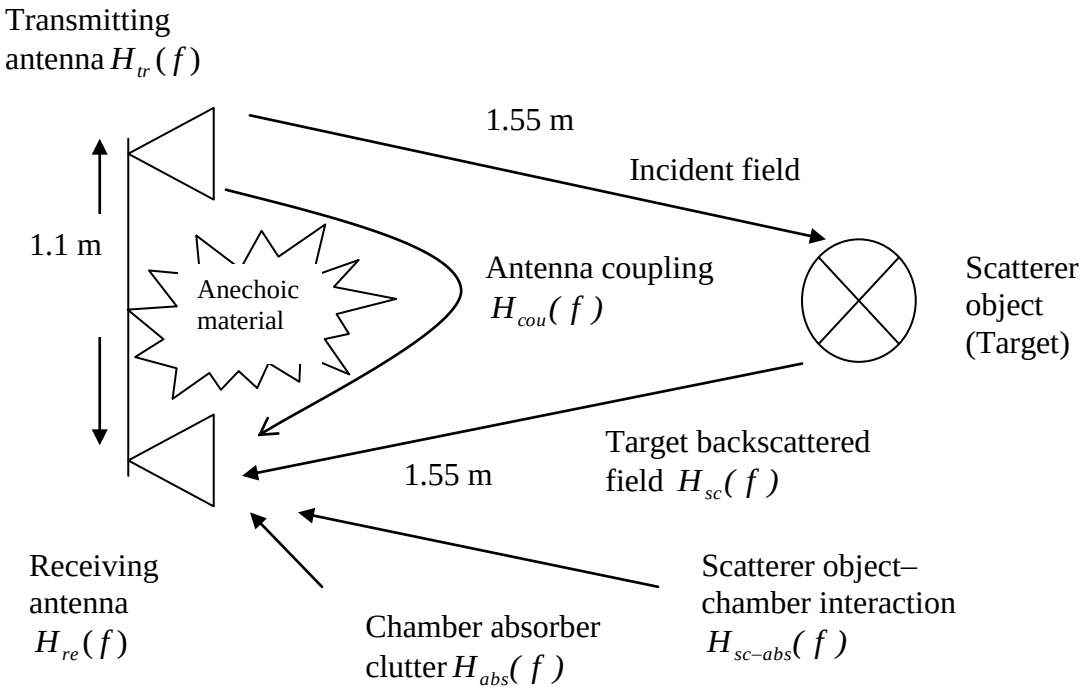

Figure 5.8: General experimental configuration.

In order to acquire the scatterer object backscattered field, the antenna coupling field and the chamber absorber clutter field must be eliminated. Therefore for every target two measurements are made; $S_1(f)$ that describes the response from the sum of fields S21 parameter measurement when the target is present and $S_2(f)$ that describes the response of the background settings i.e. without the target, total fields S21 parameter measurement. In order to eliminate the antenna coupling field and the chamber absorber clutter field, the background fields are subtracted from the target in presence fields, forming the response $S_3(f) = S_1(f) - S_2(f)$. Consequently the object backscattered field is obtained. From Figure 5.8 $S_1(f)$ and $S_2(f)$ can be respectively expressed as

$$S_1(f) = H_{tr}(f)\left[H_{sc}(f) + H_{sc-abs}(f) + H_{abs}(f) + H_{cou}(f)\right]H_{re}(f) + N_1(f) \quad (5.4)$$

$$S_2(f) = H_{tr}(f)\left[H_{abs}(f) + H_{cou}(f)\right]H_{re}(f) + N_2(f) \quad (5.5)$$

Therefore

$$S_3(f) = S_1(f) - S_2(f) = H_{tr}(f)\left[H_{sc}(f) + H_{sc-abs}(f)\right]H_{re}(f) + N_3(f) \quad (5.6)$$

where $N(f)$ is used to denote the noise that affects the measurements. The reduction of the noise effect can be achieved if each response is obtained as the average of 60 measurements. The level of noise or noise floor of the measurements can be established by considering the background fields i.e. without the sphere. Thus two consecutive averages of $S_2(f)$ response are obtained. After the first average is obtained the VNA is restarted, then the second average is obtained. The difference between the two averaged measurements, which is the outcome of subtracting the two averages of $S_2(f)$ responses, is the noise level. Comparison of the level of responses of interest with the noise level can confirm the reliability of the method of experimental data acquisition. The

support of the sphere was completely covered with anechoic material. Additionally the support was present during the measurement of the response $S_2(f)$, so any scattering from the support is subtracted from $S_1(f)$.

The expression of $S_3(f)$ includes the $H_{tr}(f) \times H_{re}(f)$ antennas frequency domain response, which was measured in the previous experiment. Therefore the equalising signal $I_{eq}(f) = \{\frac{H_{eq}(f)}{[H_{tr}(f) \times H_{re}(f)]}\}$ is applied to $S_3(f)$. The various parameters like frequency band limits and frequency step for this experiment are exactly the same as in the measurement (antennas set to face each other) of section 5.2. These parameters are selected on the basis of comparison of the experimentally obtained sphere response to the theoretically obtained sphere response. For this reason this experiment is performed for two objects a 0.0325 m radius sphere and a 0.024 m radius sphere.

Sphere measurement

The first object for which the experiment is carried out is the 0.0325 m radius sphere. Figure 5.9 shows the S21 parameter of the sum of fields of the background settings i.e. without the sphere. This S21 parameter is the response $S_2(f)$ and it is shown in contrast to the noise level of the measurement with mean value of -105 dB. The highest noise level is -88 dB. In this Figure it is observed that $S_2(f)$ has its lowest points at frequencies of 1.7, 1.9, 2, 2.5, 5.1 and 6.7 GHz. At these points the value of $S_2(f)$ is more than 20 dB higher than the highest noise level. Moreover the main part of $S_2(f)$ in all the other different frequencies is 25-55 dB higher than the highest noise level.

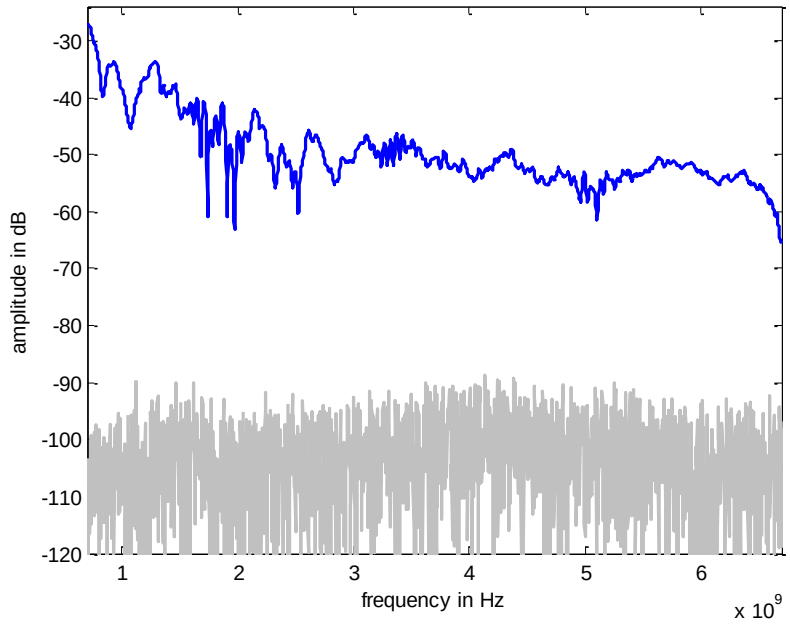

Figure 5.9: The S21 parameter of the sum of fields of the background settings, i.e. without the sphere; this S21 is expressed by the response $S_2(f)$(blue) against the noise level (grey).

Figure 5.10 shows the S21 parameter of the sum of fields that was measured in the frequency domain as the considered sphere was facing the antennas. This S21 parameter is the response $S_1(f)$ and it is shown in contrast to the noise level. In this Figure it is observed that $S_1(f)$ has its lowest points at frequencies of 1.7 and 6.7 GHz. At these points the value of $S_1(f)$ is 15 dB higher than the highest noise level. The main part of $S_1(f)$ in all the other different frequencies is 20-55 dB higher than the highest noise level.

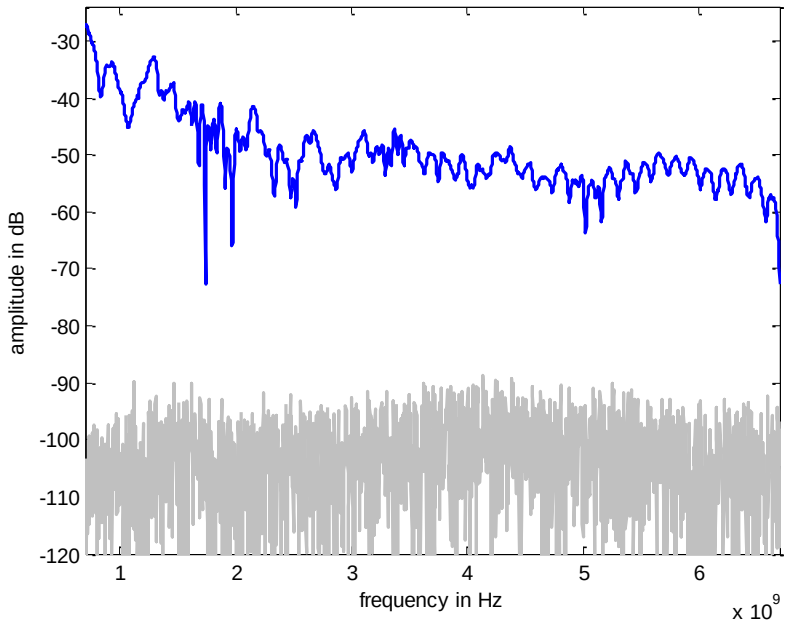

Figure 5.10: The S21 parameter of the sum of fields as the considered 0.0325 m radius sphere is facing the antennas; this S21 is expressed by the response $S_1(f)$ (blue) against the noise level (grey).

Figure 5.11 shows the response resulting from the subtraction of the measured S21 parameter of the background fields $S_2(f)$ from the measured S21 parameter of the sphere in presence fields $S_1(f)$, hence the $S_3(f)$ response is obtained. $S_3(f)$ is shown against the noise level. In this Figure it is observed that at 0.9 GHz $S_3(f)$ is close to the highest noise level while in all the other different frequencies $S_3(f)$ is 10 - 35 dB higher than the highest noise level.

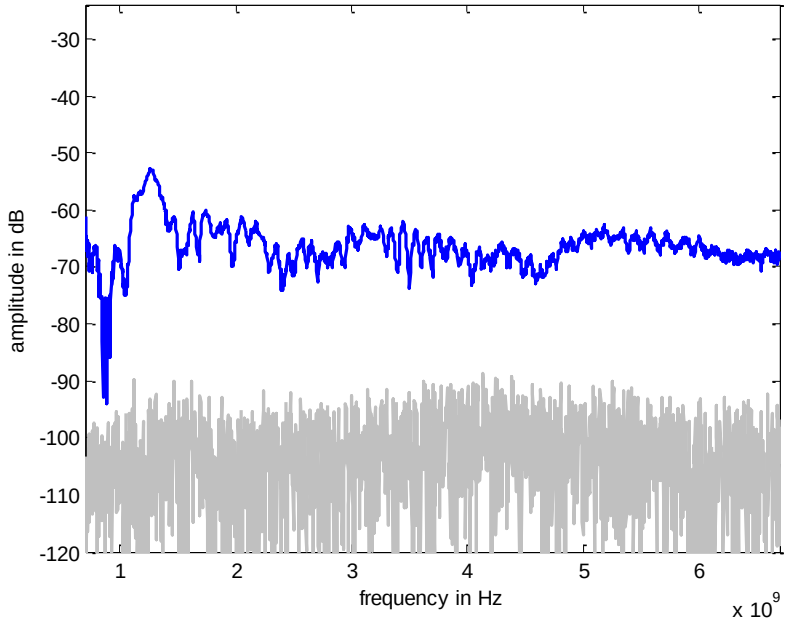

Figure 5.11: Response resulting from the subtraction of the measured S21 parameter of the background fields (Figure 5.9) from the measured S21 parameter of the 0.0325 m radius sphere in presence fields (Figure 5.10). This resulting response is described by $S_3(f)$ (blue) against the noise level (grey).

Additionally Figure 5.12 shows the response created by the application of the equalising signal $I_{eq}(f)$ on the response $S_3(f)$. This response is shown in comparison to the noise level. In this Figure it is observed that at 0.9 GHz $S_3(f)$ is 8 dB higher than the highest noise level and 25 dB higher than the mean noise level. In all the other different frequencies $S_3(f)$ is 20 - 38 dB higher than the highest noise level and 37-55 dB higher than the mean noise level. In addition there is an elevated part of the response, which is in the frequency range 1-1.5 GHz, where the maximum response level is 55 dB higher than the mean noise level. The response in this region is associated with the first resonant peak of 0.0325 m radius sphere RCS.

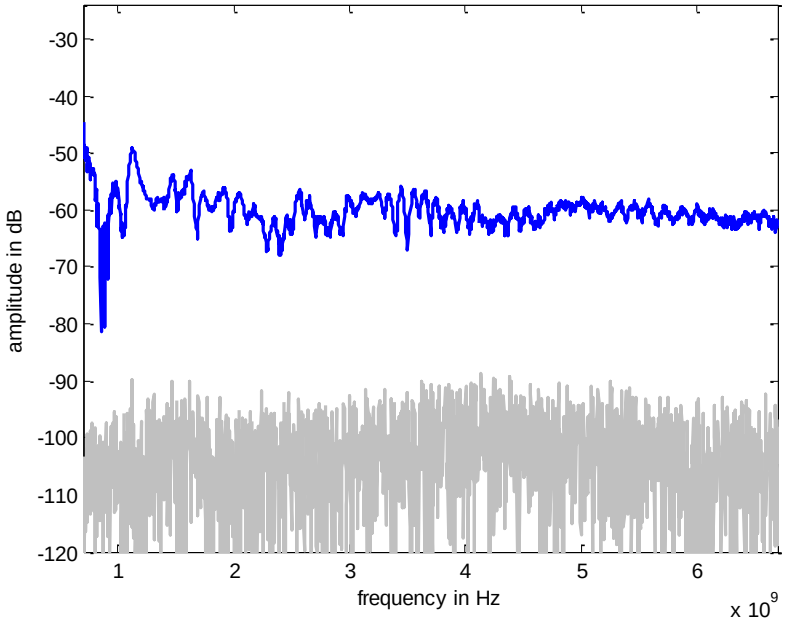

Figure 5.12: The response (blue) created by the application of the equalising signal $I_{eq}(f)$ on the response $S_3(f)$ of Figure 5.11 against the noise level (grey).

Following the response acquisition of the 0.0325 m radius sphere, the 0.024 radius sphere is also considered. Figure 5.13 shows the S21 parameter of the sum of fields that was measured in the frequency domain as the considered sphere was facing the antennas. This S21 parameter is the response $S_1(f)$ and it is shown in contrast to the noise level. In this Figure it is observed that $S_1(f)$ has its lowest points at frequencies of 1.7, 2, 5.1 and 6.7 GHz and at these points the value of $S_1(f)$ is 20 dB higher than the highest noise level. The main part of $S_1(f)$ in all the other different frequencies is 25-55 dB higher than the highest noise level.

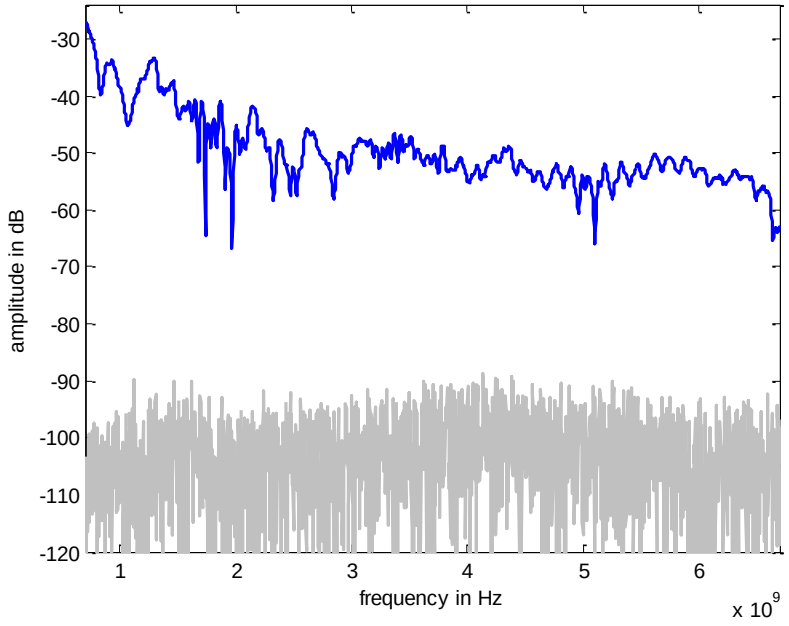

Figure 5.13: The S21 parameter of the sum of fields as the considered 0.024 m radius sphere is facing the antennas; this S21 is expressed by the response $S_1(f)$ (blue) against the noise level (grey).

Figure 5.14 shows the response resulting from the subtraction of the measured S21 parameter of the background fields $S_2(f)$ from the measured S21 parameter of the sphere in presence fields $S_1(f)$, hence the $S_3(f)$ response is obtained. $S_3(f)$ is shown against the noise level. In this Figure it is observed that in the frequency ranges of 0.7-1 GHz and 2.9-3.7 GHz $S_3(f)$ is close to the highest noise level while in all the other different frequencies $S_3(f)$ is 10 - 30 dB higher than the highest noise level.

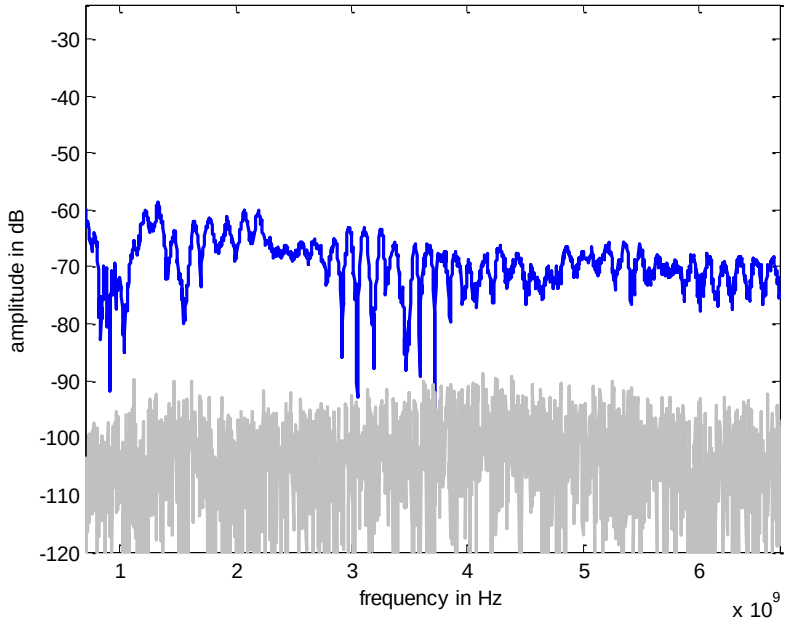

Figure 5.14: Response resulting from the subtraction of the measured S21 parameter of the background fields (Figure 5.9) from the measured S21 parameter of the 0.024 m radius sphere in presence fields (Figure 5.13). This resulting response is described by $S_3(f)$ (blue) against the noise level (grey).

Additionally Figure 5.15 shows the response created by the application of the equalising signal $I_{eq}(f)$ on the response $S_3(f)$. This response is shown in comparison to the noise level. In this Figure it is observed that in the frequency range 2.9-3.7 GHz the response is close to the highest noise level and 15 dB higher than the mean noise level. In all the other different frequencies the response is 10-33 dB higher than the highest noise level and 27-50 dB higher than the mean noise level. Furthermore in the frequency range 1.6-2 GHz the maximum response level is 50 dB higher than the mean noise level. The response in this region is associated with the first resonant peak of 0.024 m radius sphere RCS.

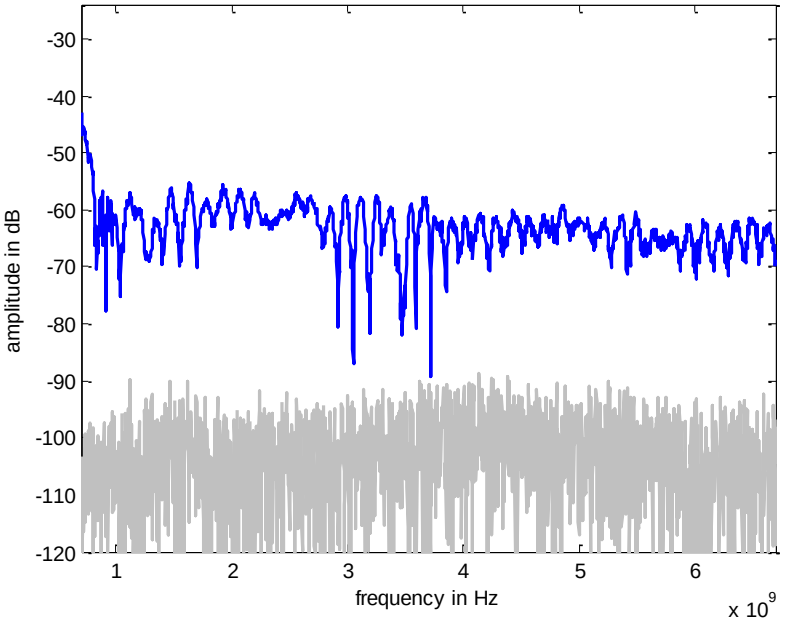

Figure 5.15: The response (blue) created by the application of the equalising signal $I_{eq}(f)$ on the response $S_3(f)$ of Figure 5.14 against the noise level (grey).

Reflector measurement (the 0.5m*0.4m metal sheet)

The main objective as presented in section 5.1 of this chapter is the comparison of the information provided by the response of the reflector-sphere composite object to the information provided by the response of the reflector. Therefore the case of the reflector is considered in order to obtain its frequency response.

Initially Figure 5.16 shows the S21 parameter of the sum of fields of the background settings i.e. without the reflector. This S21 parameter is the response $S_2(f)$. In this Figure the response and the noise level is the same as in Figure 5.9.

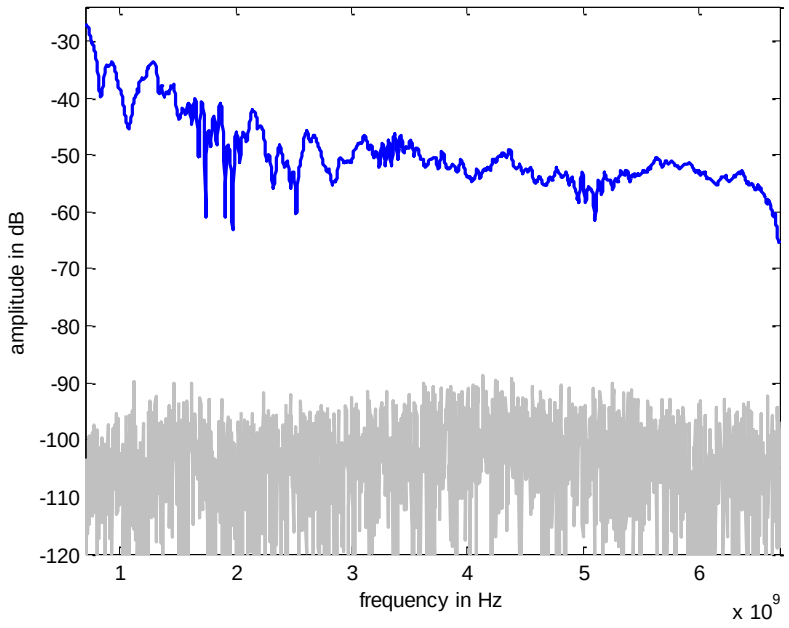

Figure 5.16: The S21 parameter of the sum of fields of the background settings i.e. without the reflector; this S21 is expressed by the response $S_2(f)$(blue) against the noise level (grey).

Figure 5.17 shows the S21 parameter of the sum of fields that was measured in the frequency domain as the reflector was facing the antennas. This S21 parameter is the response $S_1(f)$ and it is shown in contrast to the measurement noise level. $S_1(f)$ is 38 - 63 dB higher than the highest noise level and 55-80 dB higher than the mean noise level. The presence of reflector in this case produces an obvious difference to previous cases. Subtracting the measured S21 parameter of the background fields $S_2(f)$ from the measured S21 parameter of the reflector in presence fields $S_1(f)$, yields the $S_3(f)$ response as presented in Figure 5.18 . $S_3(f)$ is shown against the noise level. $S_3(f)$ is 38 - 60 dB higher than the highest noise level and 55-77 dB higher than the mean noise level.

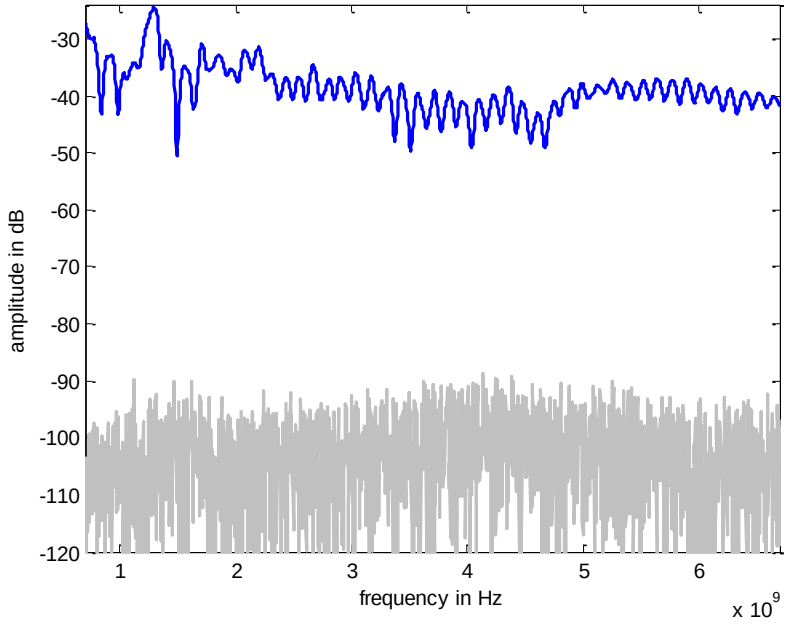

Figure 5.17: The S21 parameter of the sum of fields as the reflector is facing the antennas; this S21 is expressed by the response $S_1(f)$ (blue) against the noise level (grey).

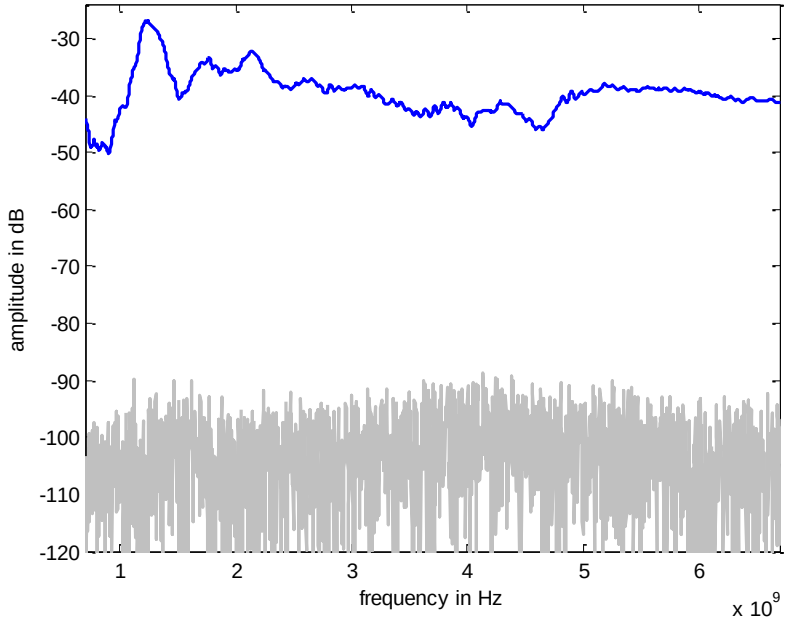

Figure 5.18: Response resulting from the subtraction of the measured S21 parameter of the background fields (Figure 5.16) from the measured S21 parameter of the reflector in presence fields (Figure 5.17). This resulting response is described by $S_3(f)$ (blue) against the noise level (grey).

Figure 5.19 shows the response created by the application of the equalising signal $I_{eq}(f)$ on the response $S_3(f)$. This response is shown in comparison to the noise level. The response is 50 - 60 dB higher than the highest noise level and 67 - 77 dB higher than the mean noise level. This response is 25-30 dB stronger than responses for the sphere in Figures 5.12 and 5.15.

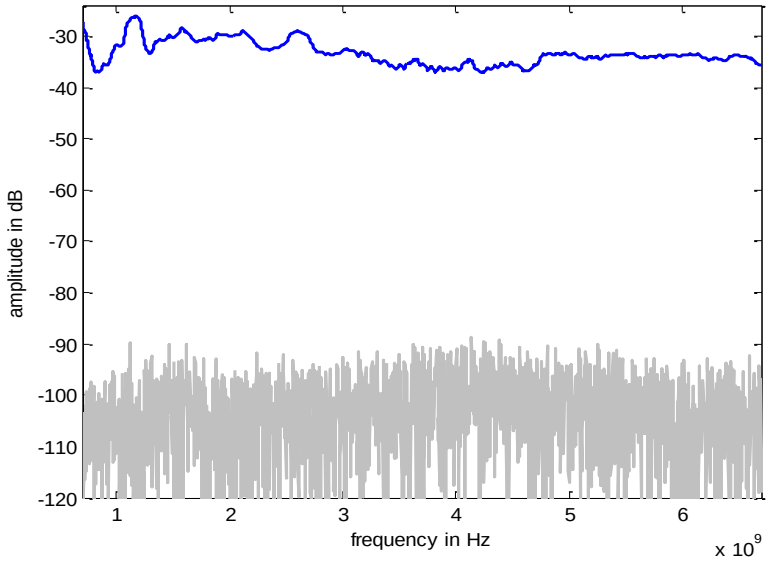

Figure 5.19: The response (blue) created by the application of the equalising signal $I_{eq}(f)$ on the response $S_3(f)$ of Figure 5.18 against the noise level (grey).

In order to achieve the detection of the sphere, the same procedure is utilised for the cases of reflector-sphere composite objects and the following responses are obtained. Figure 5.20 and Figure 5.21 show the response created by the application of the equalising signal $I_{eq}(f)$ on the response $S_3(f)$ for the reflector - 0.024 m radius sphere and the reflector - 0.0325 m radius sphere composite objects respectively. These responses are shown in comparison to the noise level, they are 50 - 60 dB higher than the highest noise level and 67 - 77 dB higher than the mean noise level. The responses of Figures 5.20 and 5.21 are unsurprisingly dominated by the response of reflector.

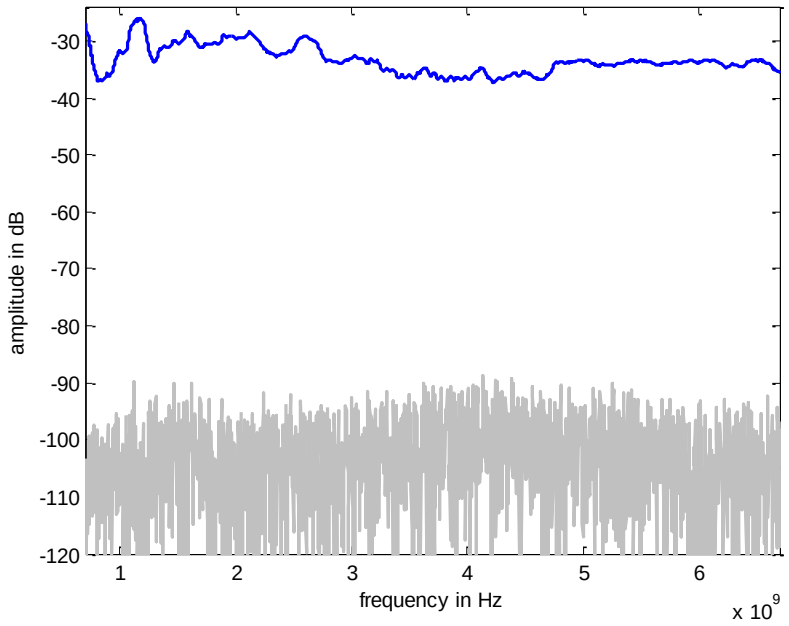

Figure 5.20: The response (blue) created by the application of the equalising signal $I_{eq}(f)$ on the response $S_3(f)$ for the reflector - 0.024 m radius sphere against the noise level (grey).

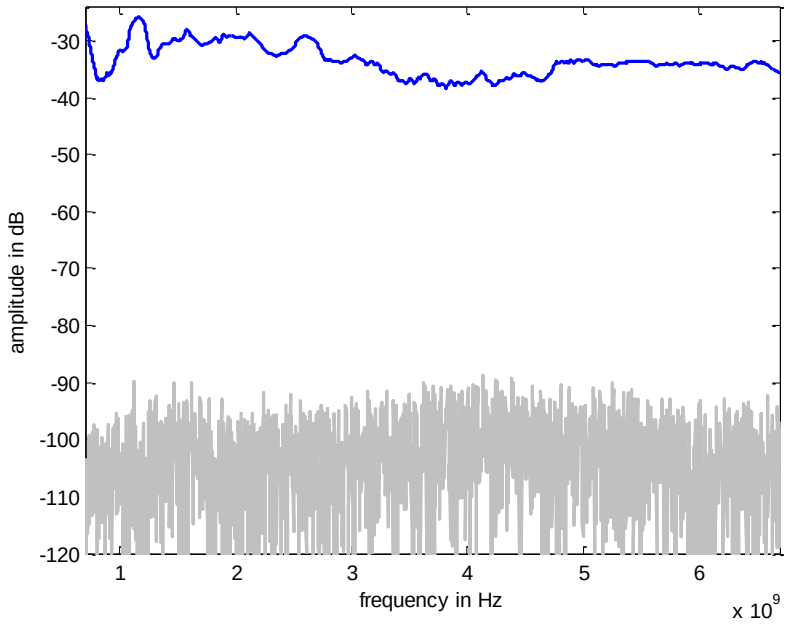

Figure 5.21: The response (blue) created by the application of the equalising signal $I_{eq}(f)$ on the response $S_3(f)$ for the reflector - 0.0325 m radius sphere against the noise level (grey).

In Figures 5.22a and Figure 5.22b the responses of reflector, reflector-0.024 m radius sphere and reflector-0.0325 m radius sphere from the respective Figures 5.19, 5.20, 5.21 are gathered. As the responses are 67 - 77 dB higher than the mean noise level, the effect noise on these responses is minimal. As it can be observed in Figure 5.22b the existence and the type of sphere affects the response. However since the amplitude of sphere response is much lower than the amplitude of response of reflector the more critical difference between the responses are observed at levels between -34 to -38 dB and between 3.2 to 4.5 GHz. In general the resolution of a target which is overwhelmed by a large clutter signal is a classic problem. This problem has also been considered in [92] through the use of matched illumination waveforms. In order to extract the natural resonant frequencies of the objects from these responses in the next section these responses will be converted and studied in the time domain.

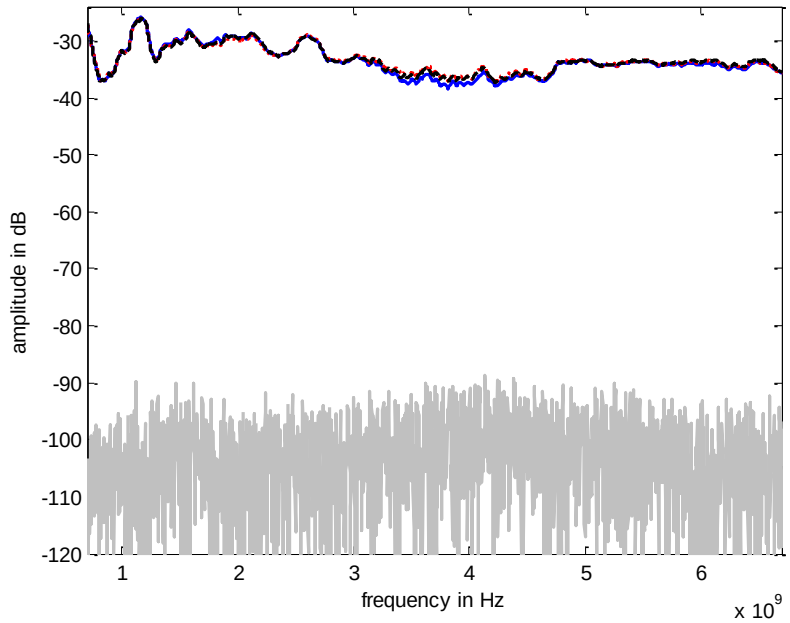

Figure 5.22a: The responses of reflector (red), reflector - 0.024 m radius sphere (black) and reflector -0.0325 m radius sphere (blue) from the respective Figures 5.19, 5.20, 5.21 against the noise level (grey).

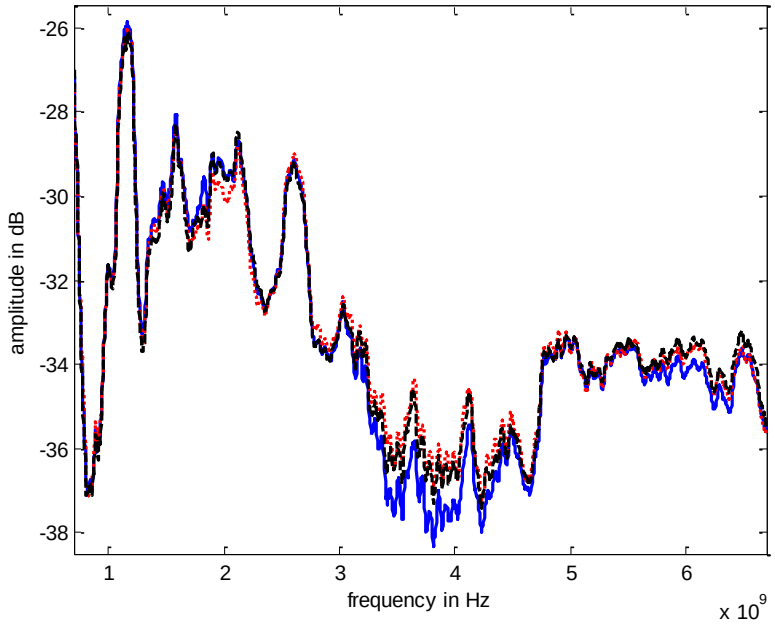

Figure 5.22b: The responses of Figure 5.22a in different scale.

5.4 Sphere ETR and LTR

This section presents the study of the experimentally obtained IR of the sphere. The main objective of this study is the selection of the Late Time Response (LTR) of the sphere from the overall sphere experimental IR and the confirmation that the experimental LTR corresponds to the theoretically obtained sphere LTR as presented in section 4.3. At first the LTR is selected from the IR, then the poles and residues of the sphere experimental LTR are extracted. These poles and residues are compared with the ones obtained from the sphere theoretical LTR. An investigation can be performed on the different parameters that are used for the processing of the frequency domain measurement. Some of these parameters, which are referred in section 5.2 and 5.3, are frequency band limits, frequency step, sampling frequency of the time domain field and type of window for this experiment. Additionally, important conclusions can be drawn on

the physical duration of the IR and the LTR. Furthermore the level of the sphere LTR against the noise level is also compared for the experimental settings used.

This experiment was performed for two spheres of radius 0.0325 m and 0.024 m respectively, so as to evaluate the experimental procedure. In this way through the accuracy of the experimental results in relation to the theoretical results, the methodology and the experimental configuration and frequency domain processing that was shown in section 5.2 and 5.3 is examined.

In order to obtain the sphere IR, the S21 parameter of the measured fields of the sphere, as shown in Figure 5.10, is considered. In appendix section 5.a this response is presented in the time domain. In this response the antennas coupling field and the chamber absorber clutter field in addition to the antennas response are present. The elimination of these fields from the measured sphere S21 parameter as it was shown in section 5.3, is succeeded via the formulation of $S_3(f)\times I_{eq}(f)$. Additionally before converting into time domain a window is applied as it was described in section 5.2, so $S_3(f)\times I_{eq}(f)\times W(f)$ is formulated. The response $S_3(f)\times I_{eq}(f)\times W(f)$ can be converted into the time domain via zero padding and estimation of the IFT. Therefore estimation of $h_y(t) = IFFT[S_3(f)\times I_{eq}(f)\times W(f)]$ will yield the sphere backscattered time domain field which is the sphere IR. The experimentally obtained IRs of the 0.035 and 0.024 radius spheres are shown in Figure 5.23 and Figure 5.24 respectively against the noise in time domain which has been obtained via estimation of the IFT of the frequency domain noise data. The IRs of Figures 5.23 and 5.24 are obtained by IFT of the responses in Figures 5.12 and 5.15. In Figures 5.23 and 5.24, for both cases of sphere's sizes the levels of IRs are 20-55 dB higher than the noise level depending on the time

instant that the IRs are considered. This is due to the difference between the levels of the responses and mean noise level in frequency domain in Figures 5.12 and 5.15.

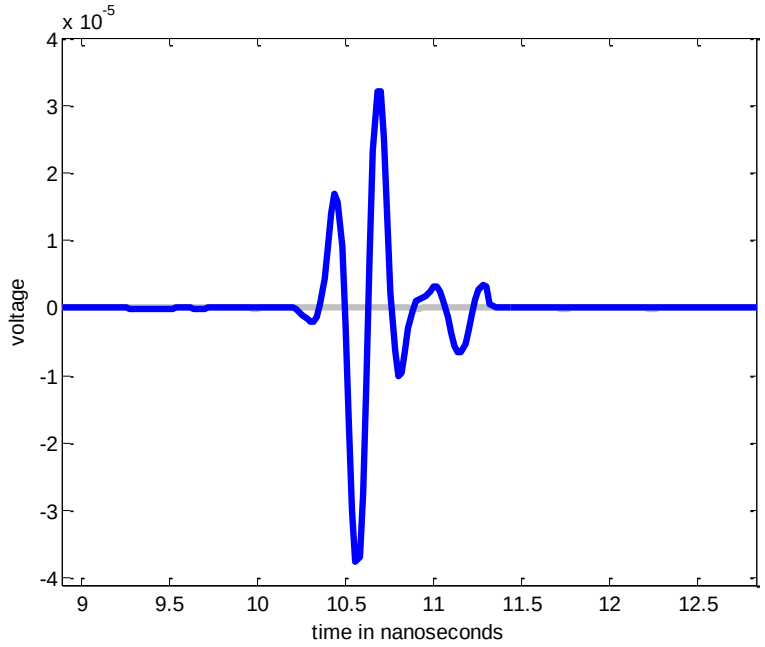

Figure 5.23: Experimentally obtained IR of 0.0325m sphere (blue) against the noise (grey).

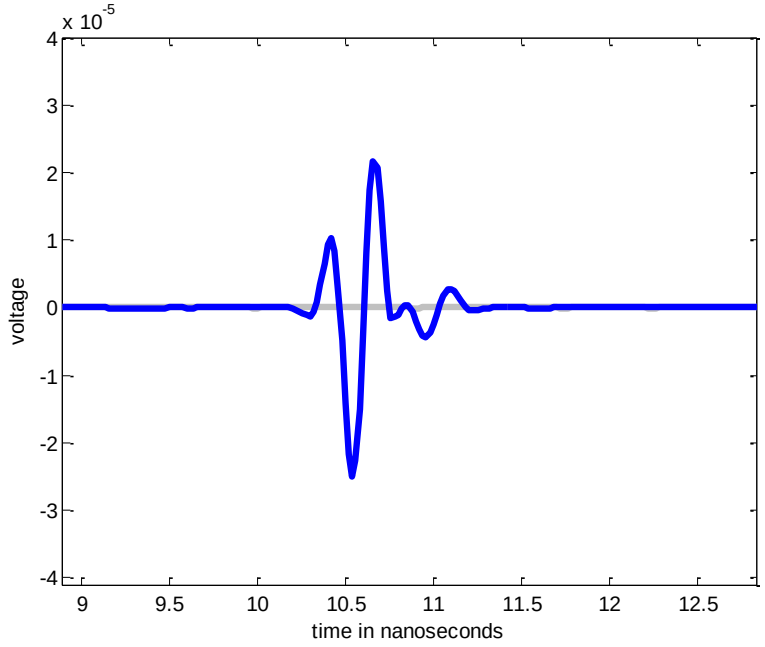

Figure 5.24: Experimentally obtained IR of 0.024m sphere (blue) against the noise (grey).

In section 3.4 it was stated that the IR of the sphere consists of the short duration Early Time Response (ETR) and LTR. Additionally it was described that the duration of the ETR T_L is twice the time the incident field takes to pass over the line of sight extent or diameter of the sphere , so the duration T_L for sphere of radius α is equal to $T_L = 4\left(\frac{\alpha}{c}\right)$, where c is the velocity of light.

This definition of T_L is described as the time the incident field interacts with the sphere in case that this field has the form of an impulse waveform. In case that the incident field is a UWB pulse of width (length) τ and $\tau = \frac{1}{B}$ where B is the measurement bandwidth, the interval of interaction T_L should also contain the width so T_L is expressed as

$$T_L = 4\left(\frac{\alpha}{c}\right) + \tau \tag{5.7}$$

Therefore if the measurement bandwidth is equal to $B=6\times10^9$ Hz the pulse width is equal to $\tau = 0.167$ *nanoseconds (ns)*. So for the sphere of radius $\alpha = 0.0325$ m since $c = 3\times10^8$ the duration is $T_L \cong 0.6\,ns$ and for the sphere of radius $\alpha = 0.024$m the duration is $T_L = 0.487$ *ns*. So the ETR durations can be considered approximately equal to $T_L \cong 0.6\,ns$ and $T_L \cong 0.49\,ns$ for the spheres of radius 0.0325m and 0.024m respectively.

Therefore as it is observed in the 0.0325 m radius sphere IR shown in Figure 5.23 if the ETR starts at approximately $10.3\,ns$ the LTR which follows should start at approximately $10.9\,ns$. By observation of the 0.024 m radius sphere IR shown in Figure

5.24, if the ETR starts at approximately 10.31*ns* the LTR which follows should start at approximately 10.8*ns*. Therefore focusing on the LTRs from the ETRs, Figures 5.25 and 5.26 present the experimentally obtained LTRs of the spheres of radius 0.0325 m and 0.024 m respectively against the noise.

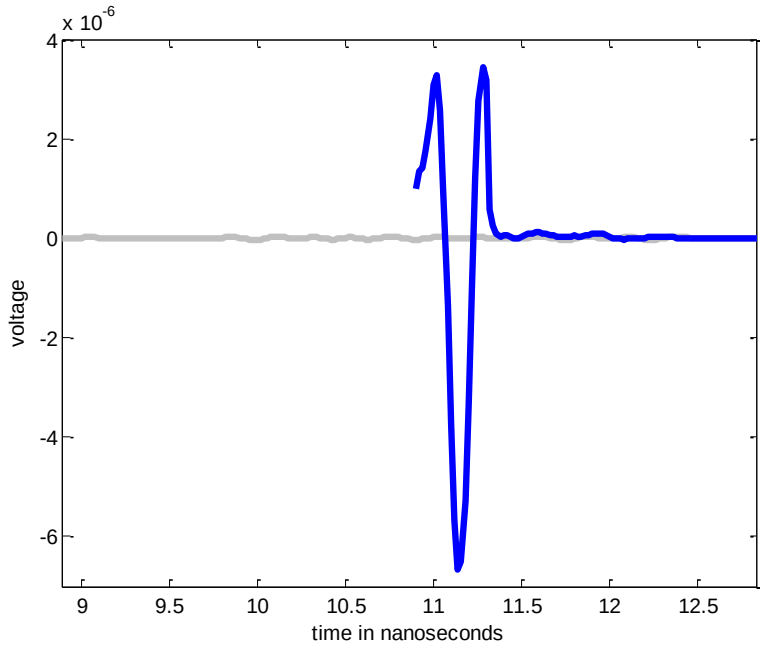

Figure 5.25: Experimentally obtained (blue) LTR of 0.0325 m radius sphere against the noise (grey).

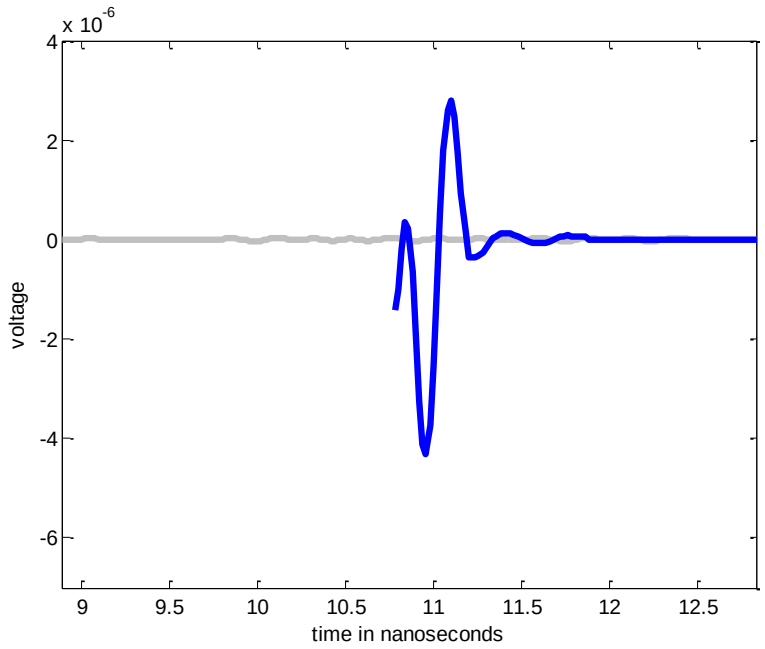

Figure 5.26: Experimentally obtained (blue) LTR of 0.024 m radius sphere against the noise (grey).

In chapter 4 the theoretical model of sphere IR was described and the theoretical sphere LTR was obtained, as a result Figure 5.27 and Figure 5.28 show the theoretical and reconstructed LTRs of spheres of radius 0.0325 m and 0.024 m respectively. By observing the theoretical LTR of the sphere of radius 0.0325m it is shown that at 1.5 *ns* after the beginning of the LTR the signal has converged to zero. For the sphere of radius 0.024 m it is shown that at 1.1 *ns* after the beginning of the LTR, the signal has converged to zero. However from the theoretical LTRs, it is observed that 0.5 *ns* after the beginning of the LTRs, the amplitude of the signals are significantly reduced.

Consequently for the 0.0325 m radius sphere if the beginning of the experimentally obtained LTR is at approximately 10.9 *ns* as shown in Figure 5.25, the signal data should be assumed approximately until 11.4 *ns*. In Figure 5.25 it is observed that after 11.4 *ns* the level of signal is closer to the noise level, so the previous

assumption on the considered time interval is valid. So, in the 10.9-11.4 *ns* time interval the sphere LTR is in the order of 20-44 dB higher than the noise level and the SVD-Prony method is used for processing the LTRs. Similarly and by using the same analysis, considering the experimental LTR of 0.024 m radius sphere shown in Figure 5.26, the time interval for which the LTR is considered is from 10.8 *ns* to 11.3 *ns*. The experimental and reconstructed LTRs of 0.0325 m and 0.024 m radius sphere are shown in Figures 5.29 and 5.30 respectively.

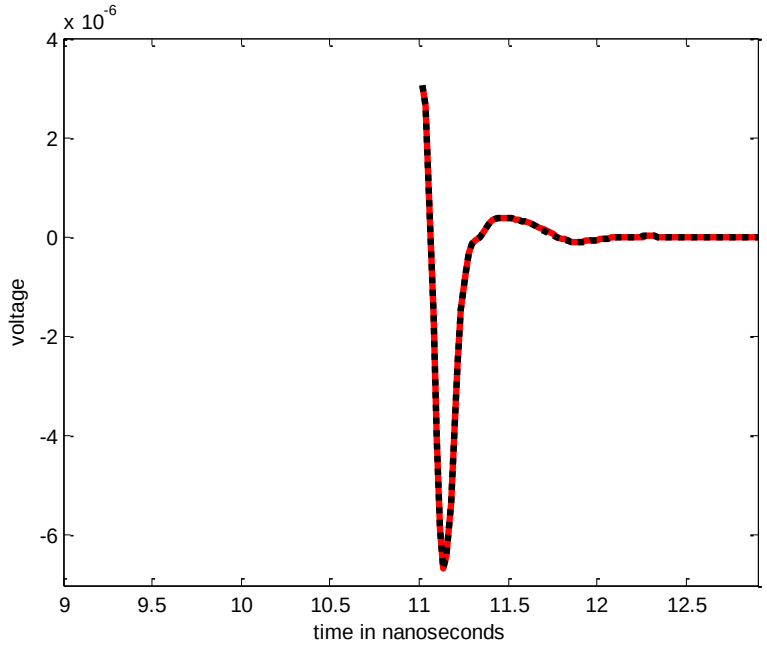

Figure 5.27: The theoretical (red) and reconstructed (black) LTR of 0.0325 m radius sphere.

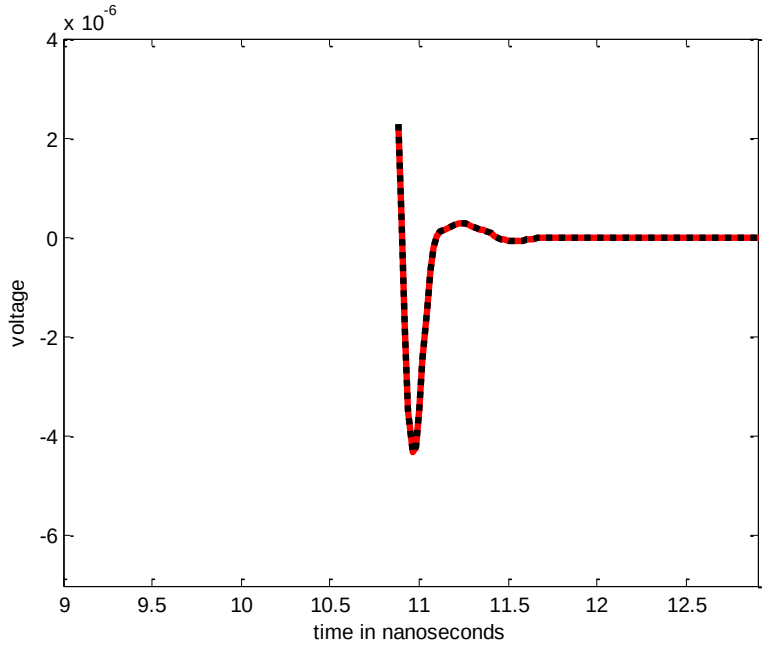

Figure 5.28: The theoretical (red) and reconstructed (black) LTR of 0.024 m radius sphere.

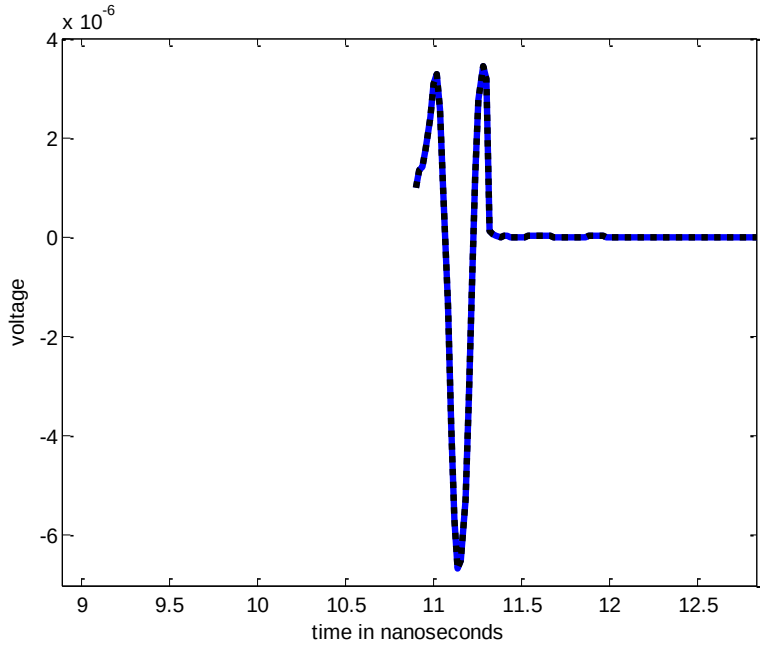

Figure 5.29: Experimentally obtained (blue) and reconstructed (black) LTR of 0.0325 m radius sphere.

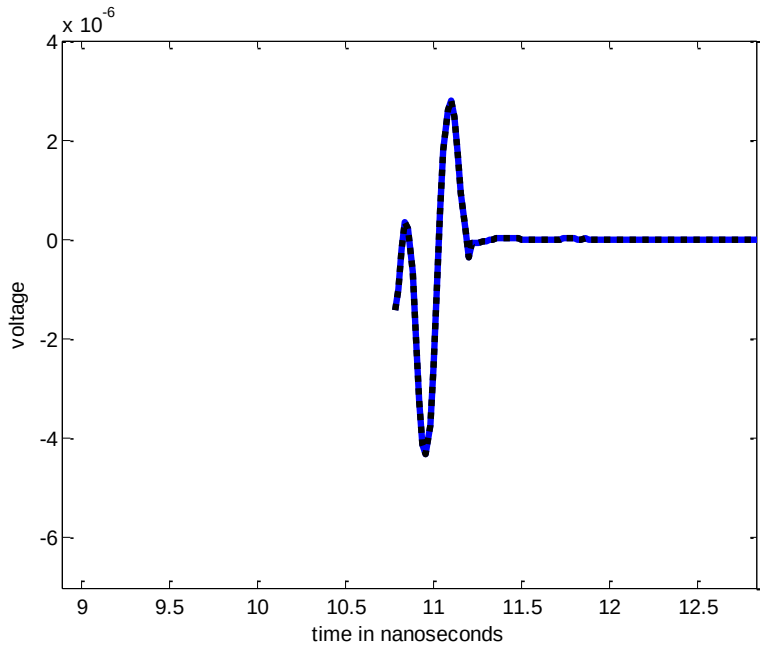

Figure 5.30: Experimentally obtained (blue) and reconstructed (black) LTR of 0.024 m radius sphere.

In order to obtain the signal information of the sphere LTR, the poles or resonant frequencies with their amplitudes have to be calculated. The experimental 0.0325 m radius sphere LTR extracted poles with their amplitudes are shown in Figure 5.31 and Figure 5.32 respectively. These poles and amplitudes are plotted alongside with the extracted poles of theoretical LTR of 0.0325 m radius sphere and their amplitudes.

From Figure 5.31 and Figure 5.32 it is deduced that for the 0.0325 m radius sphere, for the particular set of parameters chosen, the experimental LTR extracted and theoretical LTR extracted poles nearly coincide at the frequency of 1.3 GHz. Additionally the experimental LTR extracted poles at 2.6 GHz, 4.1 GHz and 5.4 GHz are similar to the theoretical LTR extracted ones in terms of frequency. Although there are small differences in the damping coefficients the experimentally extracted poles are in the vicinity of the theoretically extracted ones. Considering Figure 5.31, apart from the

similarities in frequencies, the overall clustering of the theoretically extracted poles has a comparable shape to the clustering of the experimentally extracted ones. Consequently the 5.4 GHz experimental pole has the largest damping coefficient. From Figure 5.32 among the poles the 1.3 GHz experimental pole has the largest amplitude; this is verified from the theoretical poles. This pole is the principal pole of the 0.0325 m radius sphere LTR.

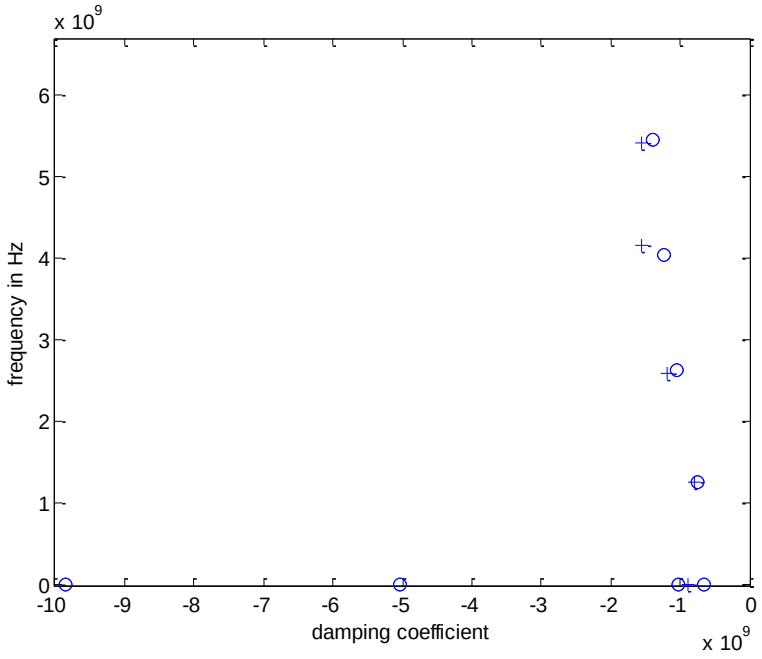

Figure 5.31: Experimental LTR extracted (+), and theoretical LTR extracted (o) poles of the 0.0325 m sphere.

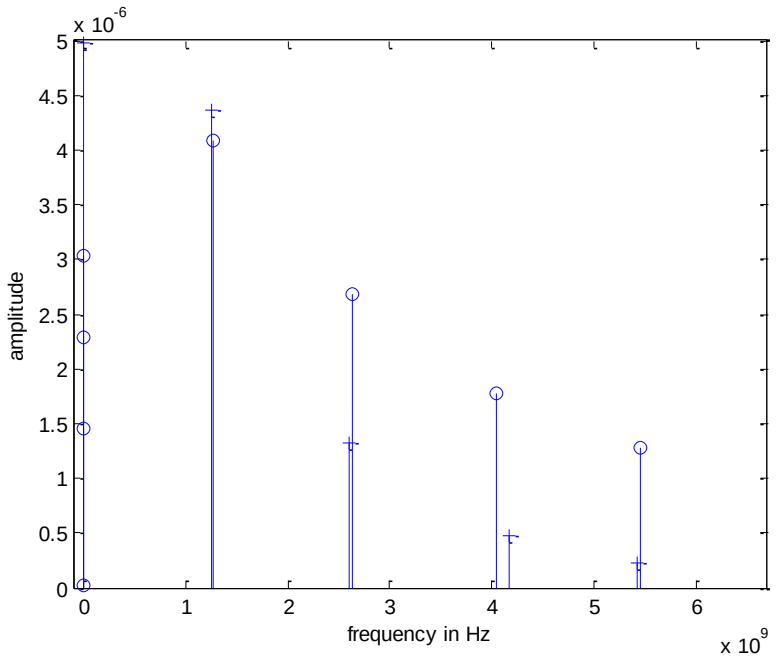

Figure 5.32: Amplitudes of experimental LTR extracted (+), and theoretical LTR extracted (o) poles of 0.0325 m sphere against frequencies of poles.

The experimental 0.024 m radius sphere LTR extracted poles with their amplitudes are shown in Figure 5.33 and Figure 5.34 respectively. These poles and amplitudes are plotted alongside with the extracted poles of theoretical LTR of 0.024 m radius sphere and their amplitudes.

From Figure 5.33 and Figure 5.34 for the 0.024 m radius sphere, it is realised that the experimental LTR extracted, and theoretical LTR extracted poles nearly coincide at frequency of 1.8 GHz. Additionally the experimental LTR extracted poles at 3.7 GHz and 5.3GHz are similar to the theoretical LTR extracted ones in terms of frequency. Additionally the respective poles are in the same vicinity and the overall clustering of the theoretically extracted poles has a comparable shape to the clustering of the experimentally extracted ones. Consequently the 5.3 GHz experimental pole has the largest damping coefficient. From Figure 5.34 among the poles the 1.8 GHz experimental

pole has the largest amplitude; this is verified from the theoretical poles. This pole is the principal pole of the 0.024 radius sphere LTR.

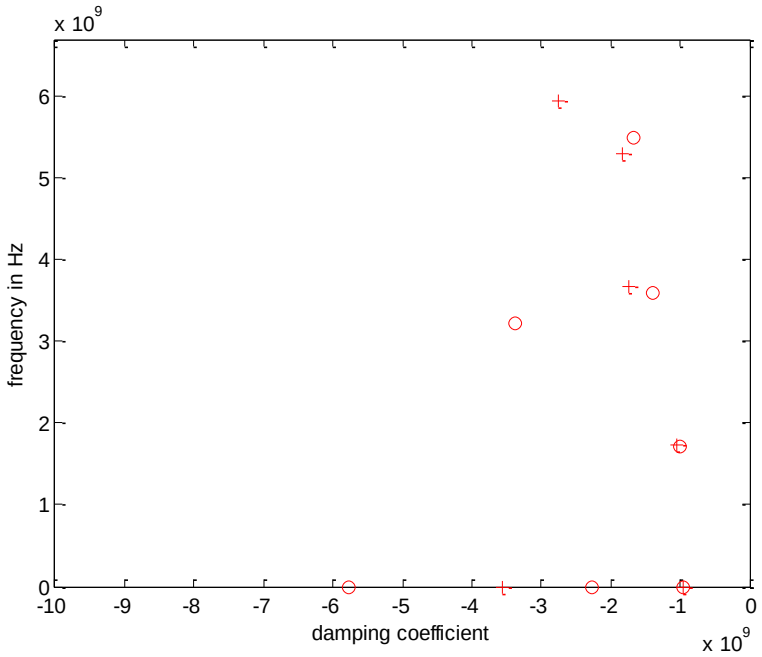

Figure 5.33: Experimental LTR extracted (+), and theoretical LTR extracted (o) poles of the 0.024 m sphere.

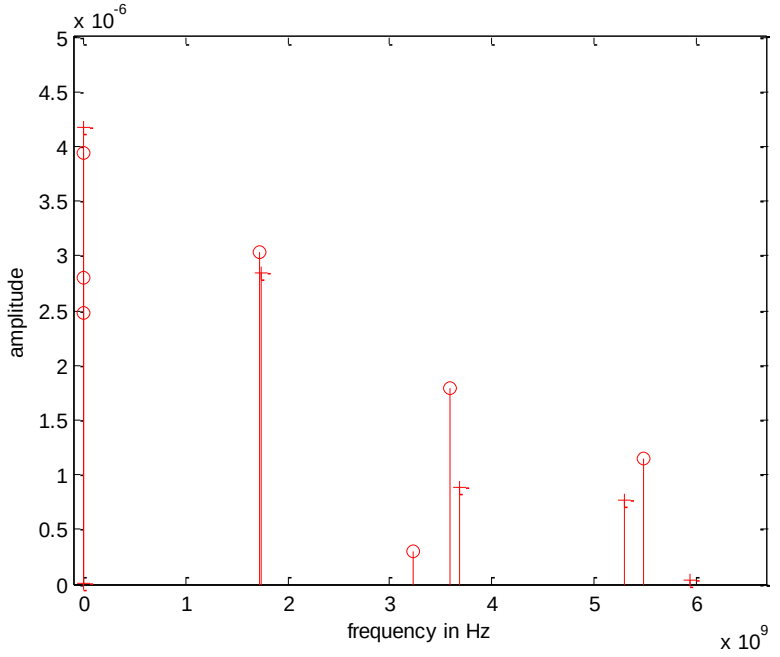

Figure 5.34: Amplitudes of experimental LTR extracted (+), and theoretical LTR extracted (o) poles of 0.024 m sphere against frequencies of poles.

Any differences between damping coefficients between experimental and theoretical poles are primarily due to the finite conductivity of the sphere used for the measurements, and secondarily due to the overall response of the measuring system. The finite conductivity of the sphere introduces resistive losses, this means that only a fraction of the power of the incident wave on the sphere is reflected back. As a result the extracted poles of the experimental LTR at frequencies 4.1 GHz and 5.4 GHz in Figures 5.31 and 5.32 have a higher damping coefficient and smaller amplitudes than the poles of the theoretical LTR. A similar trend can be observed in Figures 5.33 and 5.34 for the poles of the experimental LTR at frequencies 3.7 GHz and 5.3 GHz.

In this section the experimental configuration and methodology were tested via comparison of the theoretical and experimental results. This set of parameters used in this section is also used for the processing of all experimental data throughout the experiment as presented in the following sections, since for these parameters the experimental results proved to be in accordance with the theoretical results. The results agreement corroborates the correctness of the methodology followed in the Thesis. Furthermore it is also proved that the system noise has insignificant effect on the experimental data.

5.5 Reflector and Reflector-Sphere ETR and LTR

In this section the viability of detection of the sphere attached to the background conducting metal sheet or reflector is examined. Therefore the main objective is to compare the information provided by the LTR of the reflector-sphere composite object with the information provided by the LTR of the reflector.

This experiment is carried out for the reflector and for the sphere of radius 0.0325 and the sphere of radius 0.024 which are appended on the reflector. The S21 parameter of the backscattered fields is measured in the frequency domain as the considered object i.e. reflector or reflector sphere is facing the antennas.

In order to process these frequency domain measurements the methodology, experimental configuration and parameters of section 5.3 are used in order to obtain the frequency response of the considered object. Moreover, the estimation of Inverse Fast Fourier Transform (IFFT) of the response yields the IR of the object. After the experimental IR of the considered object is obtained, the LTR is selected in order to extract the object LTR poles and amplitudes. For the selected LTR, the number of poles is not known beforehand. Additionally the number of LTR poles is most likely to be different depending on the objects since in this section simple object i.e. reflector and composite object i.e. reflector-sphere are considered. Additionally as it is explained in appendix section 5.b the poles extraction algorithm requires the number of poles to be previously determined. So the number of poles can be realized by application of the information theoretic criteria as shown in [86, 93-97]. In this approach the estimate for the number of poles is determined by the number which minimizes the Minimum Description Length (MDL) criterion. In appendix section 5.b The MDL is shown for the cases of reflector LTR, reflector -0.024 m radius sphere and reflector -0.0325 m radius sphere LTR. As it can be observed and was predicted both cases of reflector-sphere LTRs involve a larger number of poles than the reflector LTR.

The most important objective of the experiment is to examine the reflector-sphere LTR poles and amplitudes, and compare them with the reflector LTR poles and

amplitudes. In this way conclusions can be drawn as to whether there is a difference in the observed poles (reflector poles and reflector-sphere poles), or a difference in the amplitudes of the respective poles, i.e. amplitude modulation at the specific poles of interest, when the sphere is present. Any difference in the clustering of the poles at natural resonant frequencies of sphere or any amplitude modulation due to the existence of sphere will signify that the detection of the sphere attached to the reflector is feasible. The reflector experimental IR i.e. ETR and LTR is shown in Figure 5.35 against the noise.

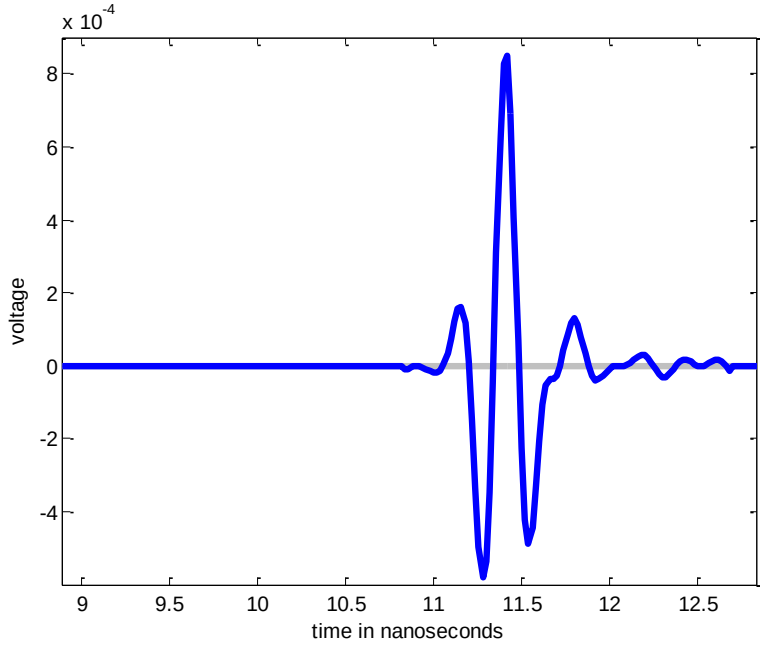

Figure 5.35: Reflector (blue) IR (ETR and LTR) against the noise (grey).

As it was described in section 3.3 the duration of the ETR T_L for the reflector with line of sight extent or width *L*, is equal to $T_L = 2\frac{L}{c}$. This definition of T_L is the time the incident field interacts with the object in case that this field has the shape of impulse

waveform. In case that this field is a UWB pulse of length τ and $\tau = \frac{1}{B}$ if B is the measurement bandwidth, the duration of interaction of the incident field with the reflector T_L is defined as

$$T_L = 2\frac{L}{c} + \tau \tag{5.8}$$

Therefore if the measurement bandwidth is equal to $B=6\times10^9$ the pulse width is equal to $\tau = 0.167\,ns$, so if the considered reflector has a base with width (thickness) L=0.06 m the duration of the ETR from equation (5.8) is $T_L \cong 0.57\,ns$.

Consider the reflector - 0.024 m radius sphere composite object where there is a conducting joint between reflector and sphere; the sphere is attached to the metal thin sheet on the metal base, so it does not alter the overall line of sight extent (width) L of the composite object, since the diameter of the sphere which is equal to 0.048m is smaller than the reflector base width. Therefore it can be assumed that the duration of ETR, $T_L \cong 0.57\,ns$, is still adequate for the reflector - sphere composite object. For the case of the reflector - 0.0325 m radius sphere, if the sphere is attached to the metal thin sheet, the diameter of sphere which is 0.065 m is marginally larger than the reflector base width. Therefore the overall line of sight extent L of the composite object is around 0.065 m and the duration of the ETR from equation (5.8) should be $T_L \cong 0.6\ ns$. Since the duration of ETR should include all cases of composite objects a selection is made that $T_L \cong 0.6\ ns$. The IR of reflector – 0.024 m radius sphere object is shown in Figure 5.36 against the noise. The IR of the reflector – 0.0325 m radius sphere is shown in Figure 5.37 against the noise. It must be mentioned that throughout the measurement the place of the reflector is not altered.

By observation of experimental IRs of reflector, reflector–0.024 m radius sphere and reflector–0.0325 m radius sphere, which are shown in Figures 5.35, 5.36 and 5.37 respectively, it is realised that since $T_L \cong 0.6$ *ns*, if the ETRs starts at approximately $10.9\,ns$ the LTRs should start at approximately $11.5\,ns$. The end of the LTRs is at approximately 12.7 *ns*, since beyond this time instant the LTRs rapidly decay. In Figures 5.35, 5.36 and 5.37 the levels of IRs are approximately 20-85 dB higher than the noise level. This is due to the difference between the responses levels and mean noise level in frequency domain in Figure 5.22. Additionally in appendix section 5.c the LTRs of the considered objects are shown against the noise. The levels of object's LTRs are in the order of 20-80 dB higher than the noise level.

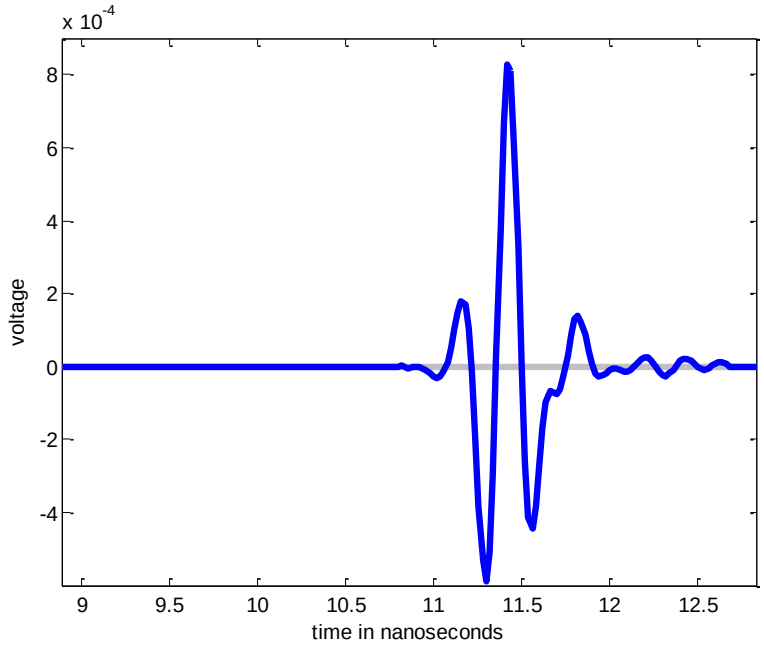

Figure 5.36: Reflector-0.024m sphere (blue) IR (ETR and LTR) against the noise (grey).

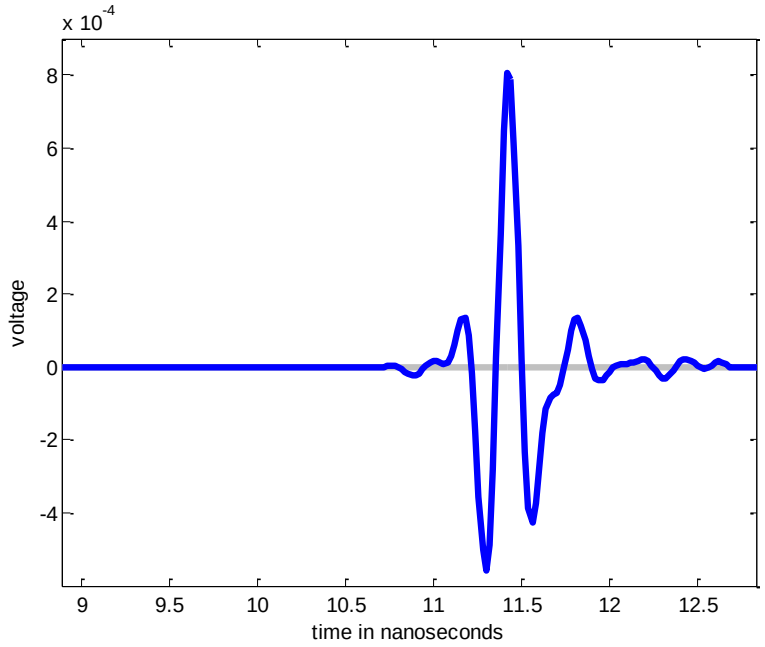

Figure 5.37: Reflector-0.0325m sphere (blue) IR (ETR and LTR) against the noise (grey).

From the reflector IR of Figure 5.35 the LTR is selected and it is presented in Figure 5.38 together with the reconstructed LTR. As it is observed the two LTRs coincide.

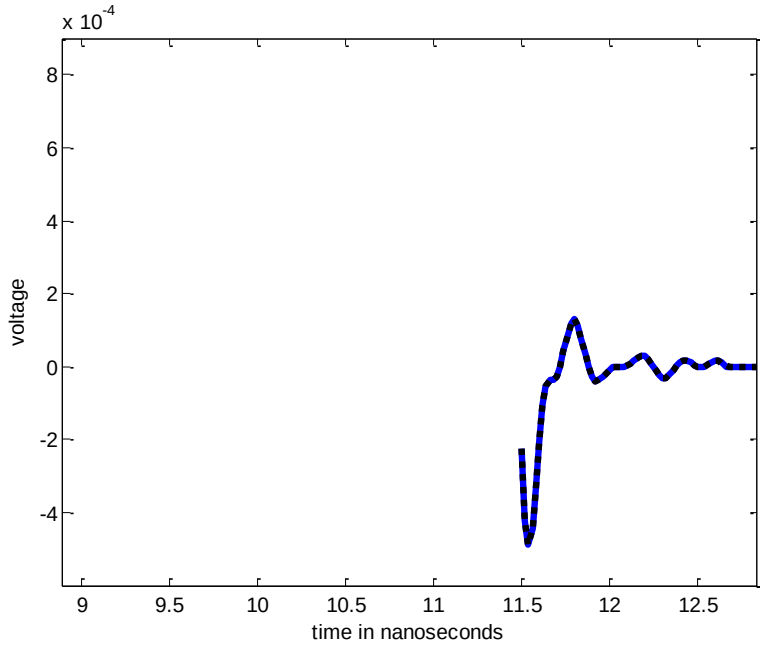

Figure 5.38: Reflector (blue) LTR and reconstructed (black) LTR.

Following the same approach as for the extraction of the sphere LTR information the poles and their amplitudes for the reflector are calculated. The reflector LTR extracted poles and their amplitudes are shown in Figure 5.39 and Figure 5.40 respectively.

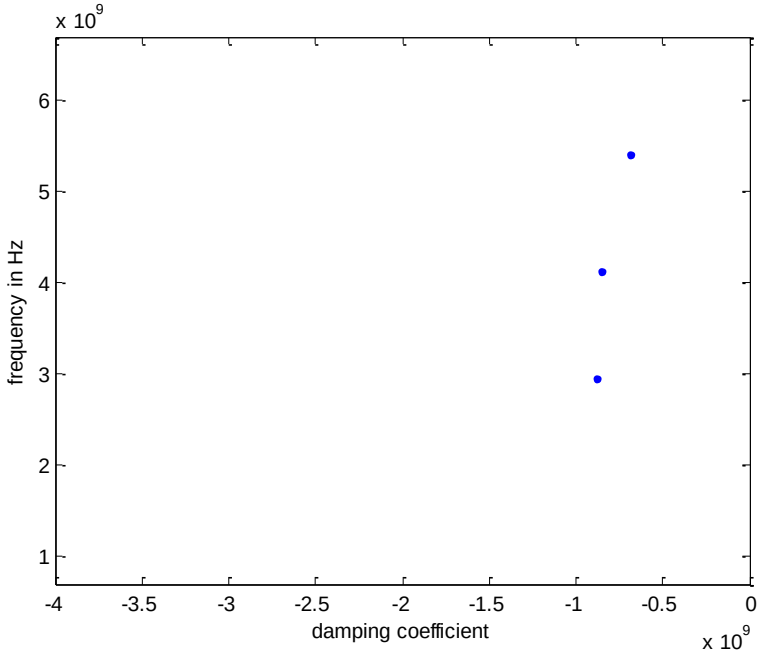

Figure 5.39: Reflector LTR extracted poles.

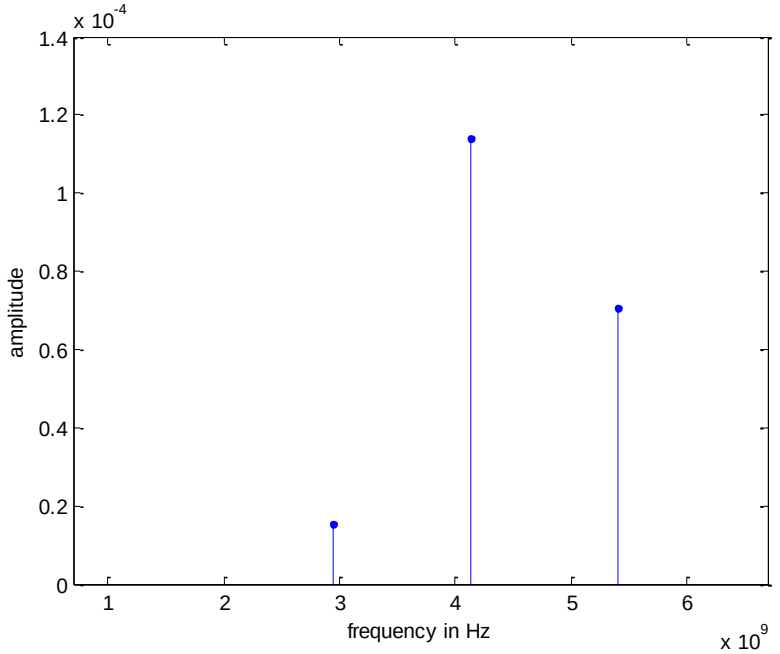

Figure 5.40: Amplitudes of reflector LTR extracted poles.

From the reflector - 0.024m radius sphere IR of Figure 5.36 the LTR is selected, and it is shown in Figure 5.41 together with the reconstructed LTR. As it is observed the two LTRs coincide.

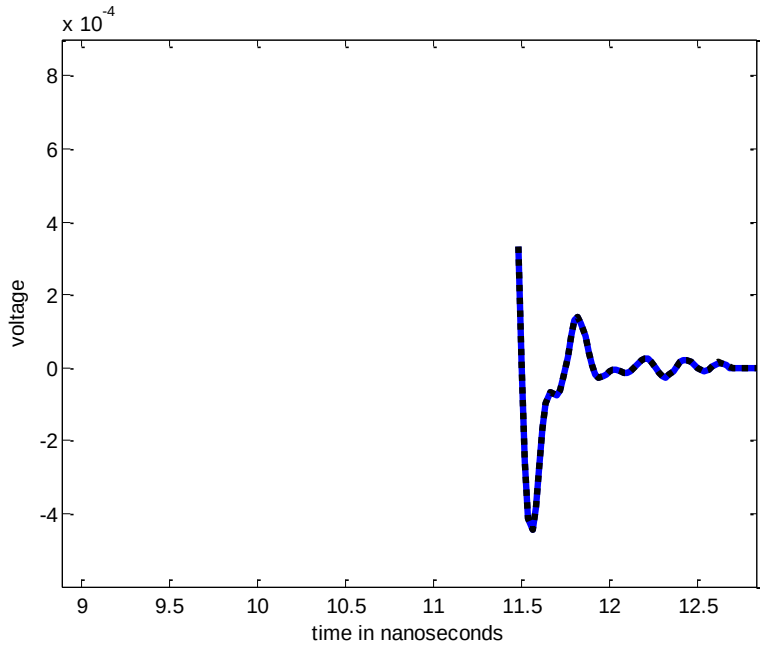

Figure 5.41: Reflector-0.024m radius sphere (blue) LTR and reconstructed (black) LTR.

The extracted poles of the reflector - 0.024m radius sphere LTR with their amplitudes are shown in Figure 5.42 and Figure 5.43 respectively. These poles and their amplitudes are plotted alongside with the poles of reflector LTR (as shown in Figure 5.39), and the poles of experimental 0.024 m radius sphere LTR (as shown in Figure 5.33) and their amplitudes (as shown in Figure 5.40 and Figure 5.34) respectively.

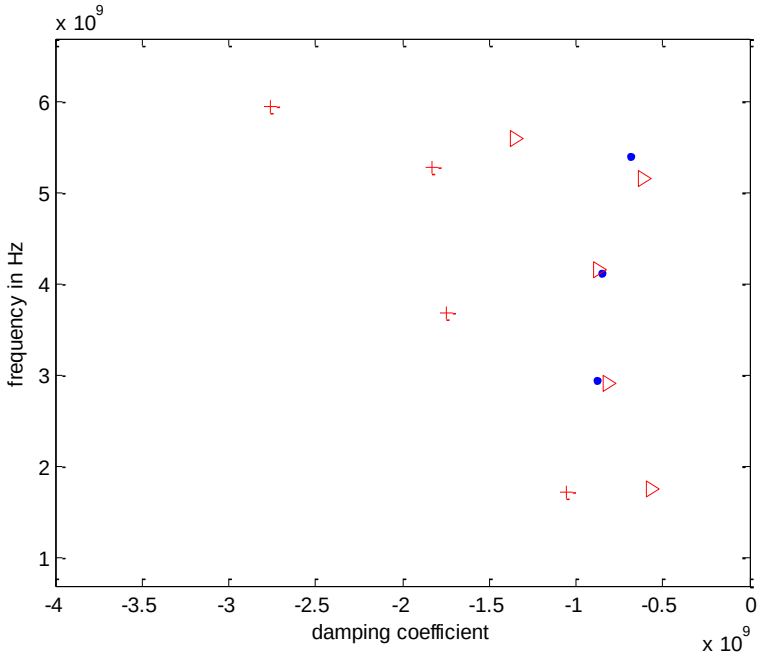

Figure 5.42: Comparison of poles.
(red +) Poles of sphere experimental LTR
(blue .) Poles of reflector LTR
(red >) Poles of reflector-0.024 m radius sphere LTR

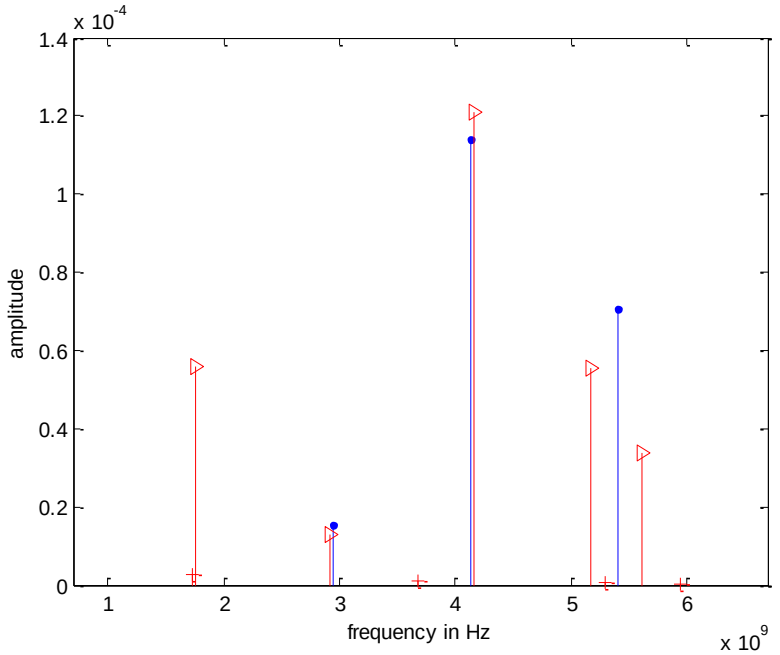

Figure 5.43: All amplitudes of the poles
(red +) Amplitudes of sphere experimental LTR
(blue .) Amplitudes of reflector LTR
(red >) Amplitudes of reflector-0.024 m radius sphere LTR

Comparison of the reflector poles with the reflector - 0.024m radius sphere poles in Figure 5.42 shows that at 2.9 GHz and 4.2 GHz the respective poles almost coincide while the reflector sphere pole is close to the reflector pole at 5.4GHz. However the number and clustering of the reflector LTR poles is different to the number and clustering of the reflector-sphere LTR poles and a pole located at 1.8GHz can be retrieved. This pole is related to the principal pole of the 0.024m radius sphere LTR. Additionally there is amplitude modulation at the respective poles as shown in Figure 5.43 due to the sphere presence. These observations indicate that the detection of the reflector-attached 0.024 m radius sphere is possible. As the reflector–sphere LTR is not a summation between the reflector LTR and sphere LTR, the reflector-sphere poles do not coincide with the reflector poles and the sphere poles.

From the reflector - 0.0325m radius sphere IR of Figure 5.37 the LTR is selected, and it is shown in Figure 5.44 together with the reconstructed LTR. As it is observed the two LTRs coincide.

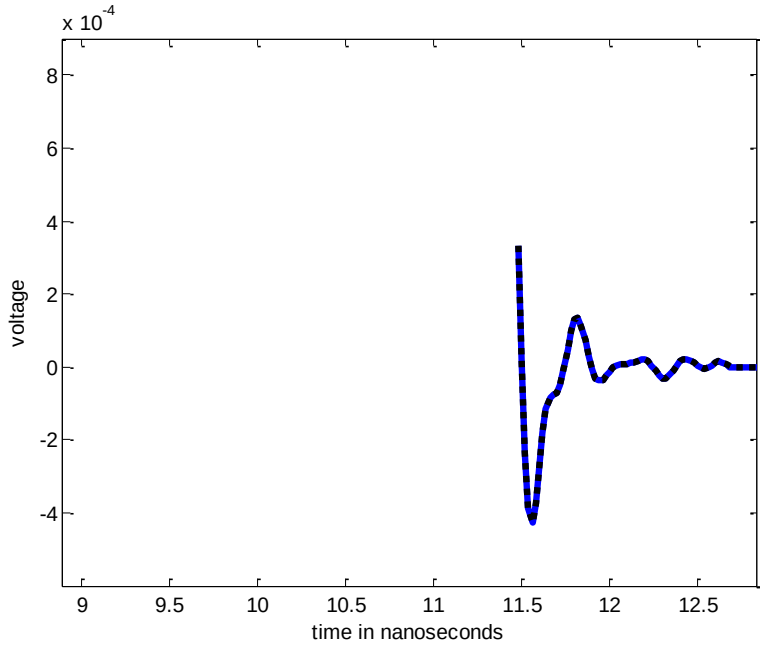

Figure 5.44: Reflector-0.0325m radius sphere (blue) LTR and reconstructed (black) LTR.

The extracted poles of reflector-0.0325 m radius sphere LTR with their amplitudes are shown in Figure 5.45 and Figure 5.46 respectively. These poles and their amplitudes are plotted alongside with the poles of reflector LTR (as shown in Figure 5.39) and the poles of experimental 0.0325 m radius sphere LTR (as shown in Figure 5.31) and their amplitudes (as shown in Figure 5.40 and Figure 5.32) respectively.

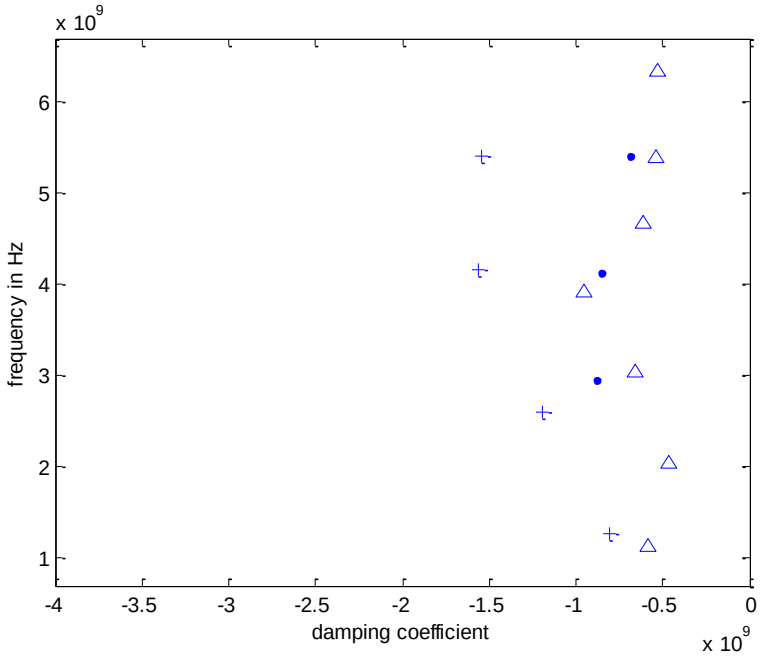

Figure 5.45: Comparison of poles.
(blue +) Poles of sphere experimental LTR
(blue .) Poles of reflector LTR
(blue ^) Poles of reflector-0.0325 m radius sphere LTR

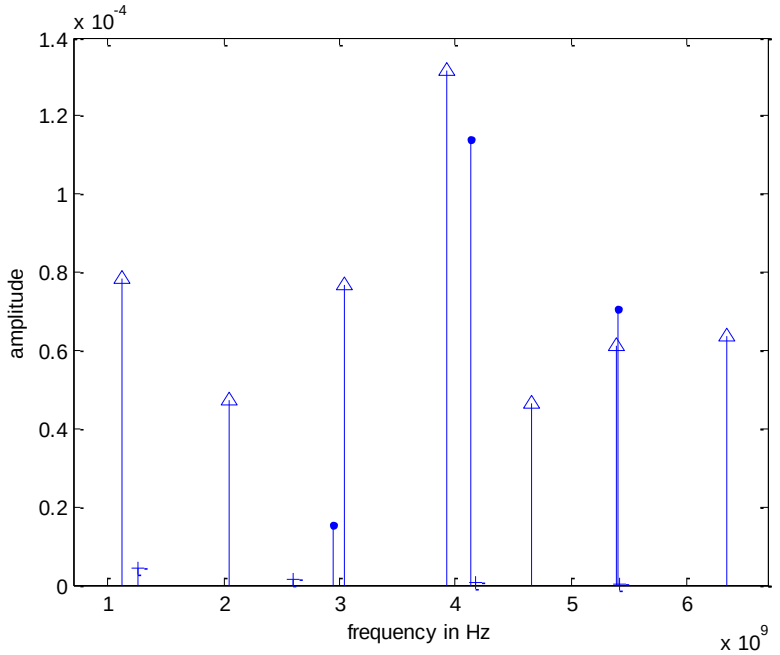

Figure 5.46: All amplitudes of the poles.
(blue +) Amplitudes of sphere experimental LTR
(blue .) Amplitudes of reflector LTR
(blue ^) Amplitudes of reflector-0.0325 m radius sphere LTR

Comparison of the reflector poles with the reflector-0.0325 m radius sphere poles in Figure 5.45 shows the reflector-sphere pole is close to the respective reflector pole at 2.9 GHz, 4.2GHz and 5.4GHz . However the number and clustering of the reflector LTR poles is different to the number and clustering of the reflector-sphere LTR poles and a pole located at 1.2 GHz can be retrieved. This pole is related to the principal pole of the 0.0325m radius sphere LTR. Additionally there is amplitude modulation at the respective poles as shown in Figure 5.46 due to the presence of the sphere. These observations indicate that the detection of the reflector-attached 0.0325 m radius sphere is possible.

5.6 Discussion of Results

In this chapter the feasibility of the detection of the reflector-attached sphere was presented. Comparison of the reflector poles with the reflector-sphere composite object poles in Figures 5.42 and 5.45 shows that the clustering of the reflector LTR poles is different to the clustering of the reflector-sphere LTR poles for both spheres considered. Furthermore from the reflector-sphere poles in Figure 5.45 the existence of a pole at 1.2 GHz frequency is observed, while in Figure 5.42 the existence of a pole is observed at 1.8 GHz frequency. The pole at 1.2 GHz is associated with the principal pole of the 0.0325 m radius sphere experimental LTR which is located at the frequency of 1.3 GHz. The pole at 1.8 GHz is associated with the principal pole of the 0.024 m radius sphere experimental LTR whose location is at the frequency of 1.8 GHz. Additionally in Figures 5.43 and 5.46 where the amplitudes of the 0.024 and 0.0325m spheres are presented, there is amplitude modulation at the respective poles. This difference in clustering of the poles, the amplitude modulation of the poles, the resonant pole at 1.2 GHz and at 1.8

GHz, due to the existence of the spheres, is the information that signifies that the detection of the sphere attached to the reflector is feasible. Otherwise these observations are an alert to the fact that there is something different about the reflector.

5.7 Conclusions

In this chapter the experimental IRs of the objects of interest were obtained via the utilization of the appropriate experimental configuration and methodologies. The validation of the experimental methodology was accomplished through comparison of the experimental LTR and theoretical LTR of sphere. The poles and amplitudes of these LTRs were obtained and showed a lot of similarities. Additionally the detection of a sphere appended on a much larger reflector was investigated and confirmed. From observations of the MDL results it is concluded that complex targets i.e. reflector- sphere require a larger number of poles or higher model order than simple targets i.e. reflector. This was verified for a 0.024 m radius sphere and a 0.0325 m radius sphere. Furthermore the retrieval of the sphere principal pole of sphere from the reflector-sphere complex target poles showed that the sphere can be discerned from the reflector-sphere target.

Chapter 6

HUMAN-ATTACHED SPHERE DETECTION

6.1 Introduction

In this chapter a similar experiment as in chapter 5 is repeated replacing the reflector by a human body recreating the realistic scenario of a concealed explosive on a human's body. Hence a human is inserted in the anechoic chamber and the experiment is performed while the approximated grenade or sphere is attached to the human. This is a reasonable approximation as the shape of the grenade is similar to the shape of the sphere. As a result this chapter presents the analysis of the procedure involving the experimental configuration and the methodology for processing of the experimental measurements when the human is engaged. Fundamentally three positions of the sphere are taken into account: front of human, side of human, back (behind) of human. In this way the feasibility of remote detection of a sphere appended on the human is investigated as the position of the sphere on the body is altered.

In principle the human-sphere composite object reflected field presumably includes information on both the resonant frequencies of the human and the resonant frequencies of the sphere similar to the case of the reflector-sphere object as studied in chapter 5. Consequently analysis of the Late Time Response (LTR) of the complex human-sphere object and the LTR of the human yields their different resonant frequencies. Examination of the way the resonant frequencies of the sphere LTR affect the resonant frequencies of the human–sphere object LTR should confirm the existence of the sphere. In this way the main objective of the Thesis, which is the body-worn sphere detection is realised. In sections 5.3 and 5.4 it is shown that the use of LTR for detection requires the selection of the LTR from the IR through accurate estimation of the points in time domain or timings. In this chapter the same timings will be used for LTR

analysis of both composite objects i.e. human-sphere or simple objects i.e. human. So the effect of existence and position of sphere on the human–sphere object LTR frequencies is investigated using the same timings for LTR analysis. In this way any ambiguity on the outcome of analysis due to choice of different timing points is avoided. In order to use the same timings the large background object, which is the human, faces the radar and retains a single placement throughout the experiment while the small object, which is the sphere takes three positions on the human i.e. front, side and back of human. In this way the stance and orientation of the human remain unchanged during the experiment.

. In this chapter, two methods are utilised in order to obtain the information related to the resonant frequencies. These are the SVD-Prony [82-89] method which yields the poles and residues of the object's LTR and the MUltiple SIgnal Classification (MUSIC) [98] method, which yields the Power Spectral Density (PSD) of the LTR of the object. Both methods are the most appropriate for extracting damped sinusoids in the presence of noise. As these methods are independent of each other, the information extracted from their analysis is compared in order to verify the feasibility of the body-worn sphere detection. As the range resolution depends on the bandwidth considered in this chapter the bandwidth B of 8 GHz is chosen. Additionally from the analysis of the sphere Radar Cross Section (RCS) as shown in chapter 2 it is known that the first resonant frequency of the sphere is located at approximately 1.46 GHz. This knowledge enables us to select the frequency band at which the reflected fields measurements are made. So for this measurement the 1-9 GHz frequency band is considered.

In the following sections a detailed analysis is presented on the various aspects involved in the procedure in order to detect the human-attached sphere. Initially the

appropriate experimental measurements are shown and the reflected fields from the illuminated objects are acquired in terms of the object's frequency responses. Then the main objective of the experiment, which is obtaining and analysing the LTR of the various objects is described. The remainder of this chapter is organised as follows. Section 6.2 presents the acquired fields in terms of the objects' frequency responses while section 6.3 presents the sphere Impulse Response (IR). Section 6.4 presents the human IR and section 6.5 presents the human-sphere composite object IR. Finally section 6.6 concludes the chapter.

6.2 Frequency Response Acquisition

This section presents all the measurements in terms of frequency responses in a similar approach as in sections 5.2 and 5.3. Initially Figure 6.1 shows the radiated electric field between the two antennas which are facing each other in terms of the amplitude of the S_{21} parameter measurement expressed as $\left|H_{tr}(f)\times H_{re}(f)\right|$. This measurement was made by taking N_1=1601 frequency steps in the 1-9 GHz frequency band, i.e. the frequency step is equal to $\Delta f = 5000000$Hz. Therefore for this measurement the fractional bandwidth was equal to 1.6. Figure 6.2 and Figure 6.3 show the $\left|H_{eq}(f)\right|$ response occurring after frequency domain equalisation has been applied on measured $\left|H_{tr}(f)\times H_{re}(f)\right|$ as explained in section 5.2.

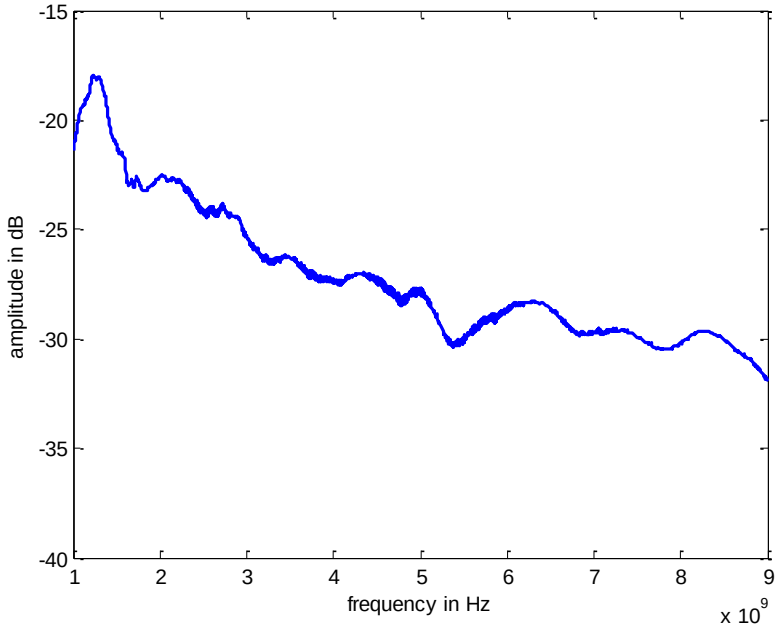

Figure 6.1: $\left|H_{tr}(f)\times H_{re}(f)\right|$ response via S21 measurement when two antennas are facing each other.

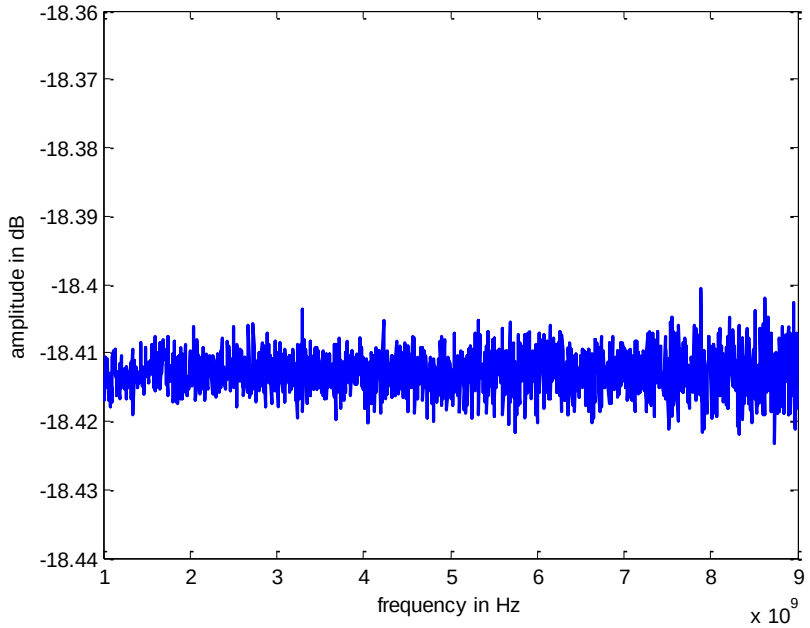

Figure 6.2: Response $\left|H_{eq}(f)\right|$ of two antennas facing each other after frequency domain equalisation has been applied on measured $\left|H_{tr}(f)\times H_{re}(f)\right|$ (antennas response is removed).

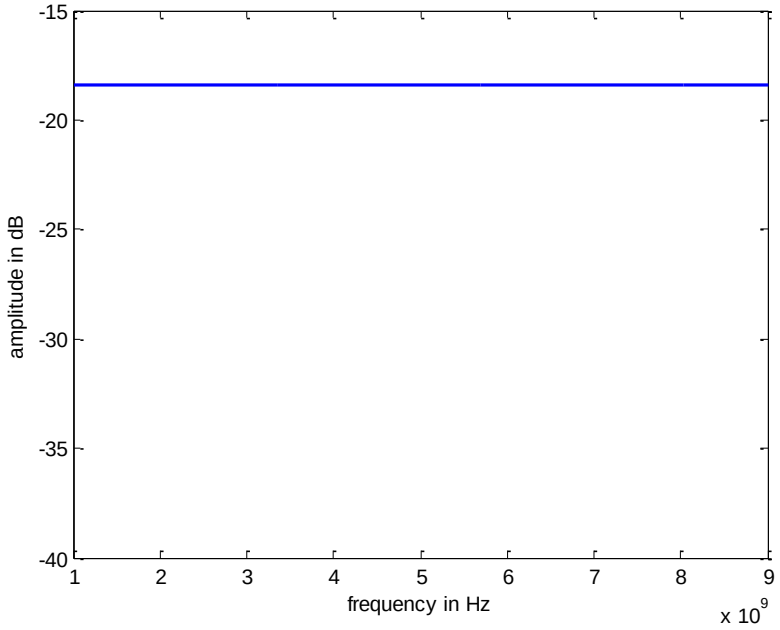

Figure 6.3: Response $\left|H_{eq}(f)\right|$ (like Figure 6.2) in the same scale as Figure 6.1.

After the equalisation procedure, the experimental data was acquired by means of the experimental configuration shown in Figure 6.4. From the utilised experimental radar configuration a UWB pulse is transmitted, which is incident on a target and the reflected field from the target-object is obtained. In this way the reflected fields from the various composite objects of interest are acquired.

In this experiment, the frequency stepped pulse compression is realised via the VNA and the transmitting and receiving horn antennas that were also used in the previous measurement (antennas set to face each other) are deployed. From Figure 6.4 the following frequency responses of the system are discerned. The transmitting horn antenna with frequency response $H_{tr}(f)$ is driven via the VNA and converts the frequency stepped signal into incident field. The frequency responses $H_{sc}(f)$ and $H_{abs}(f)$ are used to describe the reflected fields from the object and chamber absorber respectively. The response $H_{sc-abs}(f)$ describes multipath scattering fields that are due to the

interaction between the fields of object, antenna and chamber absorber. $H_{cou}(f)$ is used to express the antenna coupling frequency response, which is the field that is created directly between the transmitting and the adjacent receiving antenna, this field is also referred as leakage field. $H_{re}(f)$ describes the frequency response of the receiving antenna that converts the sum of the fields into signals. In this way the backscattered field of interest $H_{sc}(f)$ is obtained.

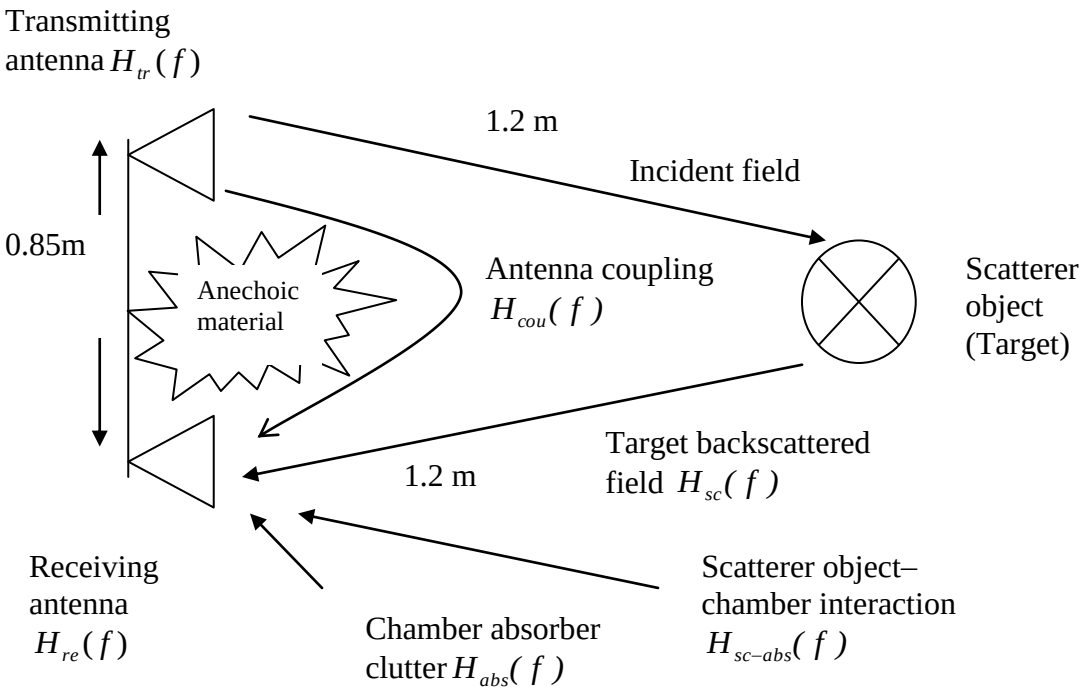

Figure 6.4: General experimental configuration.

In order to obtain the scatterer object backscattered field, the elimination of the chamber absorber clutter field and the antenna coupling field is necessary. Therefore for every target two measurements are made. During the first measurement the target is present, and the response is obtained from the sum of fields S21 parameter measurement. This response is described by $S_1(f)$. For the second measurement, the response is obtained only from the total fields S21 parameter measurement of the background

settings i.e. without the target. This response is described by $S_2(f)$. The elimination of the antenna coupling field and the chamber absorber clutter field is realised via the subtraction of the background fields from the target in presence fields, hence the response $S_3(f) = S_1(f) - S_2(f)$ is formed. Consequently the considered object backscattered field is obtained. From Figure 6.4 S_1 and S_2 can be respectively described as

$$S_1(f) = H_{tr}(f)\left[H_{sc}(f) + H_{sc-abs}(f) + H_{abs}(f) + H_{cou}(f)\right]H_{re}(f) + N_1(f) \quad (6.1)$$

$$S_2(f) = H_{tr}(f)\left[H_{abs}(f) + H_{cou}(f)\right]H_{re}(f) + N_2(f) \quad (6.2)$$

Therefore

$$S_3(f) = S_1(f) - S_2(f) = H_{tr}(f)\left[H_{sc}(f) + H_{sc-abs}(f)\right]H_{re}(f) + N_3(f) \quad (6.3)$$

where $N(f)$ is used to denote the noise that affects the measurements. In order to reduce the effect of noise each response is obtained as the average of 120 measurements. As it is mentioned in section 5.3 the level of noise or noise floor of the measurements can be established by considering the background fields i.e. without the sphere. Thus two consecutive averages of $S_2(f)$ response are obtained and subtracted. After the first average is obtained the VNA is restarted, then the second average is obtained. The difference between the two averaged measurements is the noise level. Comparison of the level of responses of interest with the noise level can confirm the reliability of the method of experimental data acquisition .The expression of $S_3(f)$ includes the $H_{tr}(f) \times H_{re}(f)$ frequency domain signal which was measured in the previous experiment. Therefore the equalising signal $I_{eq}(f) = \{\frac{H_{eq}(f)}{[H_{tr}(f) \times H_{re}(f)]}\}$ is applied in $S_3(f)$. The parameters for this measurement are exactly the same as in the previous measurement (antennas set to

face each other) and they are determined through comparing the experimentally obtained 0.0325 m radius sphere response to the theoretically obtained 0.0325 m radius sphere response.

Sphere measurement

The first object for which the experiment is carried out is the 0.0325 m radius sphere. Figure 6.5 shows the S21 parameter of the sum of fields of the background settings i.e. without the sphere. This S21 parameter is the response $S_2(f)$ and it is shown in contrast to the noise level of the measurement with mean value of -104 dB. The highest noise level is -85 dB. In this Figure it is observed that $S_2(f)$ has its lowest points at frequencies of 3.6, 4.7 and 8.8 GHz. At these points the value of $S_2(f)$ is close to the highest noise level. Moreover the main part of $S_2(f)$ in all the other different frequencies is 20- 55 dB higher than the highest noise level.

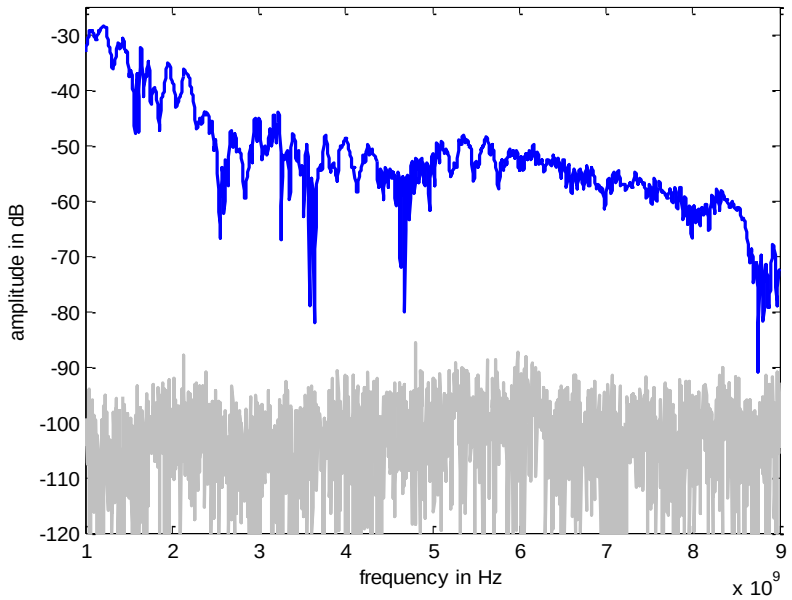

Figure 6.5: The S21 parameter of the sum of fields of the background settings, i.e. without the sphere; this S21 is expressed by the response $S_2(f)$ (blue) against the noise level (grey).

Figure 6.6 shows the S21 parameter of the sum of fields that was measured in the frequency domain as the considered sphere was facing the antennas. This S21 parameter is the response $S_1(f)$ and it is shown in contrast to the noise level. In this Figure it is observed that $S_1(f)$ has its lowest points at frequencies of 2.6, 3.6, 4.9 and 8.6 GHz. At 3.6, 4.9 and 8.6 GHz the value of $S_1(f)$ is close to the highest noise level while at 2.6 GHz $S_1(f)$ is 10 dB higher than the highest noise level. The main part of $S_1(f)$ in all the other different frequencies is 20-55 dB higher than the highest noise level.

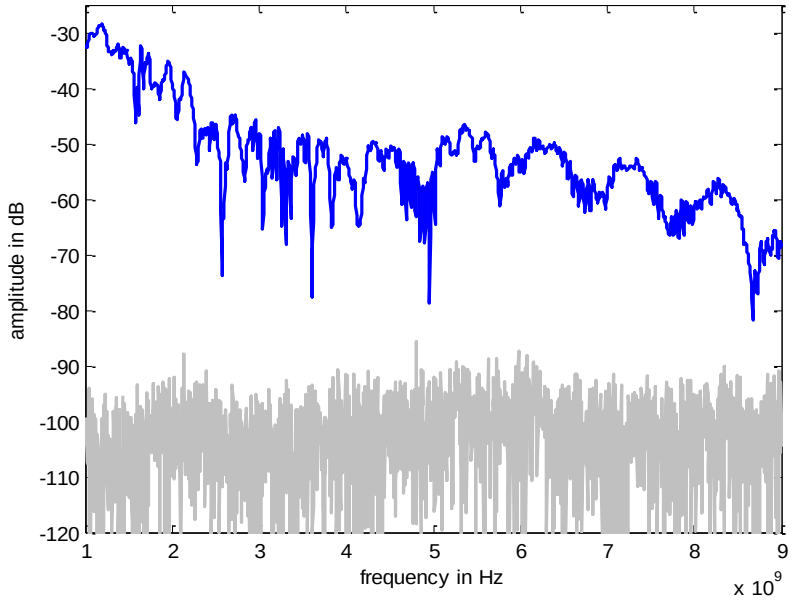

Figure 6.6: The S21 parameter of the sum of fields as the considered 0.0325 m radius sphere is facing the antennas; this S21 is expressed by the response $S_1(f)$ (blue) against the noise level (grey).

Figure 6.7 shows the response resulting from the subtraction of the measured S21 parameter of the background fields $S_2(f)$ from the measured S21 parameter of the sphere in presence fields $S_1(f)$, hence the $S_3(f)$ response is obtained. $S_3(f)$ is shown against the noise level. In this Figure it is observed that at 9 GHz $S_3(f)$ is 10 dB higher

than the highest noise level while in all the other different frequencies $S_3(f)$ is 20-40 dB higher than the highest noise level.

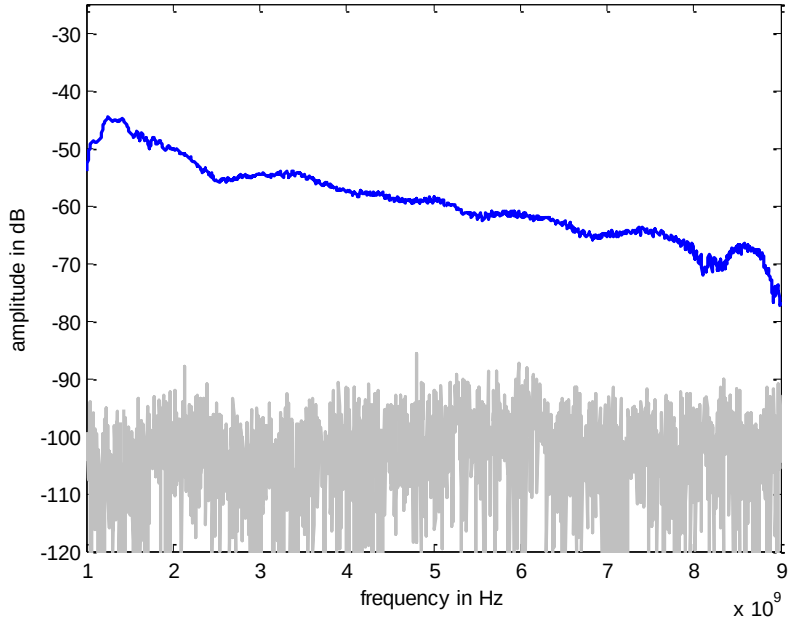

Figure 6.7: Response resulting from the subtraction of the measured S21 parameter of the background fields (Figure 6.5) from the measured S21 parameter of the 0.0325 m radius sphere in presence fields (Figure 6.6); this resulting response is described by $S_3(f)$ (blue) against the noise level (grey).

Additionally Figure 6.8 shows the response created by the application of the equalising signal $I_{eq}(f)$ on the response $S_3(f)$. This response is shown in comparison to the noise level. In this Figure it is observed that this response is 20-40dB higher than the highest noise level, and 39-59 higher than the mean noise level. In addition there is an elevated part of the response, which is in the frequency range 1-1.6 GHz, where the maximum response level is 59 dB higher than the mean noise level. The response in this region is associated with the first resonant peak of 0.0325 m radius sphere RCS.

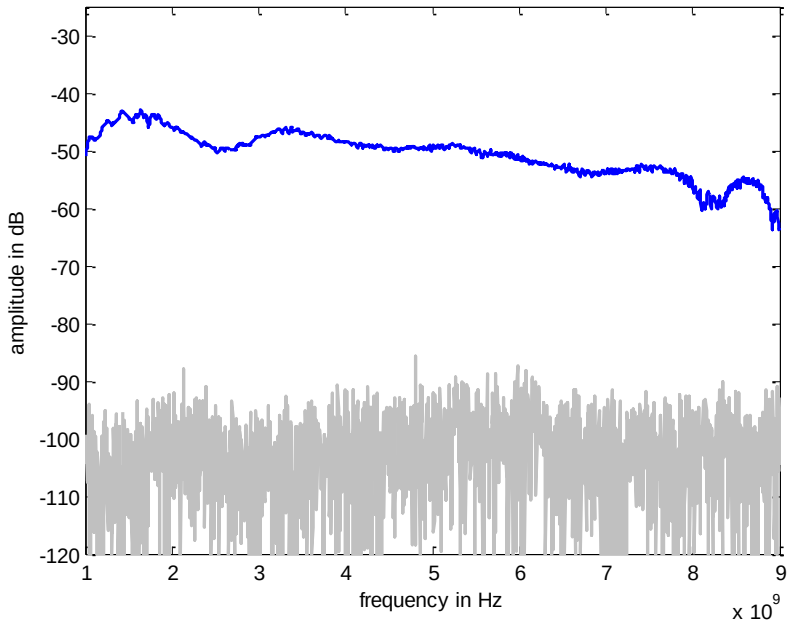

Figure 6.8: The response (blue) created by the application of the equalising signal $I_{eq}(f)$ on the response $S_3(f)$ of Figure 6.7 against the noise level (grey).

Human measurement

The main objective as declared in section 6.1 of this chapter is the comparison of the information provided by the response of the human-sphere composite object with the information provided by the response of the human. First the case of the human is considered in order to obtain its frequency response.

Initially Figure 6.9 shows the S21 parameter of the sum of fields of the background settings i.e. without the human. This S21 parameter is the response $S_2(f)$ and it is shown in contrast to the measurement noise level. In this Figure it is observed that the lowest points of $S_2(f)$ are in the frequency range of 7.7- 8.6 GHz. At these points the value of $S_2(f)$ is close to the highest noise level, while in the frequency range of 3-4 GHz and at 5.2 , 7.1 GHz $S_2(f)$ is approximately 10 dB higher than the highest

noise level. The main part of $S_2(f)$ in all the other different frequencies is 20-60 dB higher than the highest noise level.

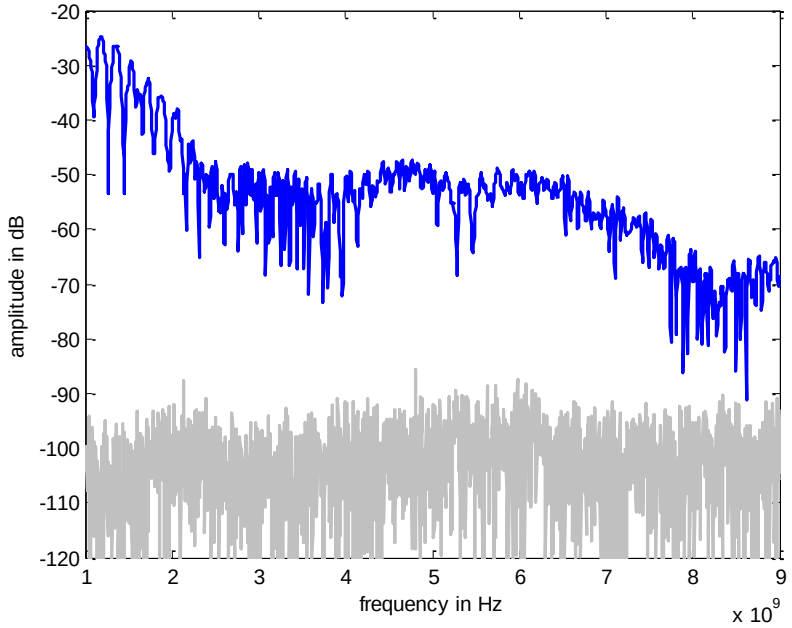

Figure 6.9: The S21 parameter of the sum of fields of the background settings i.e. without the human; this S21 is expressed by the response $S_2(f)$(blue) against the noise level (grey).

Figure 6.10 shows the S21 parameter of the sum of fields that was measured in the frequency domain as the human was facing the antennas. This S21 parameter is the response $S_1(f)$ and it is shown in contrast to the measurement noise level. In this Figure it is observed that the lowest points of $S_1(f)$ are at frequencies of 2.1, 2.3 and 9 GHz where $S_1(f)$ is approximately 20 dB higher than the highest noise level and 39 dB higher than the mean noise level. The main part of $S_1(f)$ in all the other different frequencies is 25-60 dB higher than the highest noise level and 44-79 higher than the mean noise level. Subtracting the measured S21 parameter of the background fields $S_2(f)$from the measured S21 parameter of the human in presence fields $S_1(f)$, yields

the $S_3(f)$ response as presented in Figure 6.11 . $S_3(f)$ is shown against the measurement noise level. In this Figure it is observed that the lowest points of $S_3(f)$ are in the frequency range of 5-5.4 GHz where the value of $S_3(f)$ is close to the highest noise level and 20 dB higher than the mean noise level. The main part of $S_3(f)$ in all the other different frequencies is 15-60 dB higher than the highest noise level and 34-79 higher than the mean noise level.

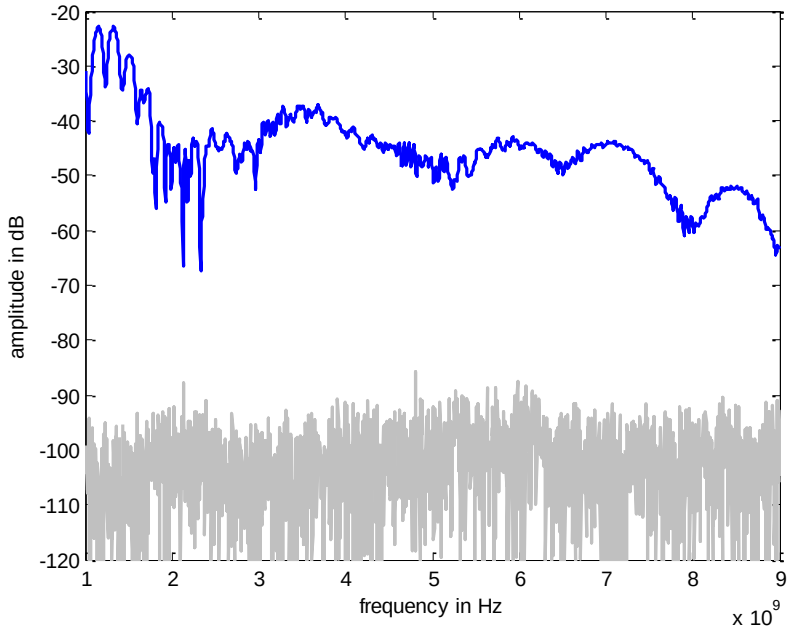

Figure 6.10: The S21 parameter of the sum of fields as the human is facing the antennas; this S21 is expressed by the response $S_1(f)$ (blue) against the noise level (grey).

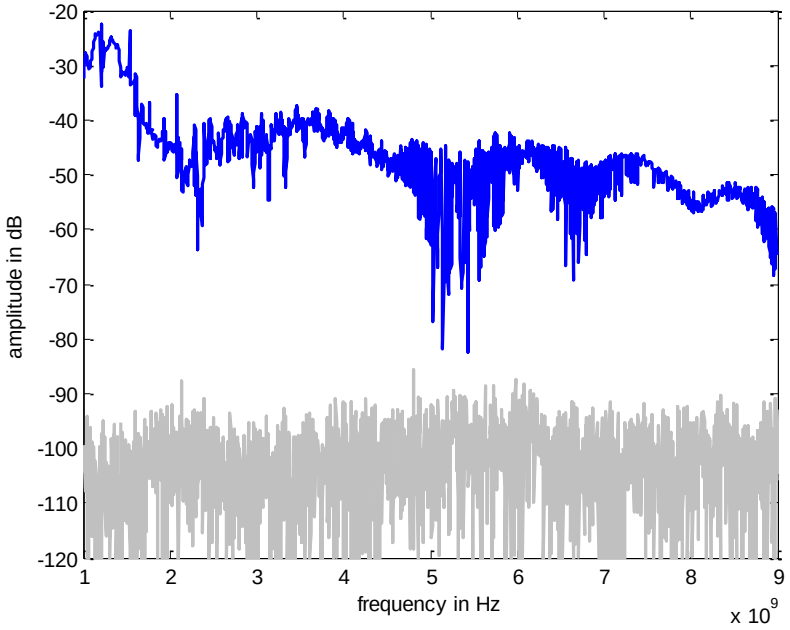

Figure 6.11: Response resulting from the subtraction of the measured S21 parameter of the background fields (Figure 6.9) from the measured S21 parameter of the human in presence fields (Figure 6.10) ; this resulting response is described by $S_3(f)$ (blue) against the noise level (grey).

Figure 6.12 shows the response created by the application of the equalising signal $I_{eq}(f)$ on the response $S_3(f)$. This response is shown in comparison with the noise level. It is observed that the response is 25-60 dB higher than the highest noise level and 44-79 higher than the mean noise level. However at the lowest points of the response that are in the frequency range of 5-5.4 GHz, the value of the response is 10 dB higher than the highest noise level and 29 dB higher than the mean noise level.

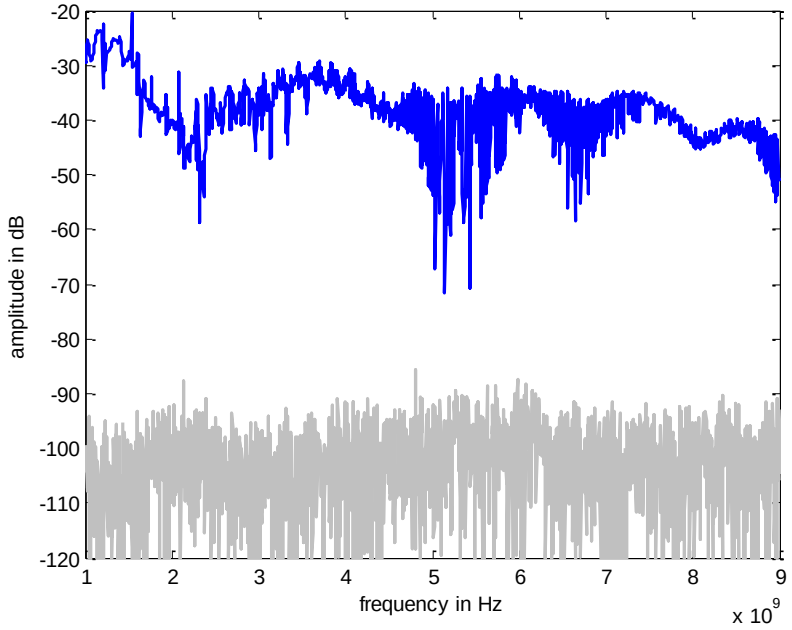

Figure 6.12: The response (blue) created by the application of the equalising signal $I_{eq}(f)$ on the response $S_3(f)$ of Figure 6.11 against the noise level (grey).

Human-sphere (the human is facing the radar and the sphere is attached to the front side illuminated by the radar.)

As the main objective of the experiment is to identify the sphere appended on the human body naturally the case of the human-sphere composite object is also considered. In this case the sphere is appended to the front of the human illuminated by the radar. Initially Figure 6.13 shows the S21 parameter of the sum of fields of the background settings i.e. without the composite object. This S21 parameter is the response $S_2(f)$. In this Figure the response and the noise level is the same as in Figure 6.9.

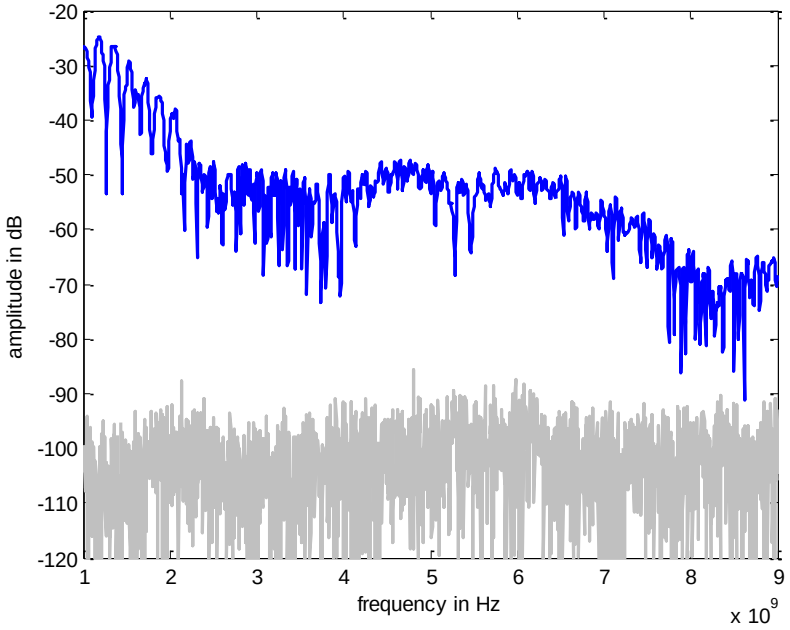

Figure 6.13: The S21 parameter of the sum of fields of the background settings i.e. without the composite object; this S21 is expressed by the response $S_2(f)$(blue) against the noise level (grey). It can be observed that this figure is the same as Figure 6.9

Figure 6.14 shows the S21 parameter of the sum of fields that was measured in the frequency domain as the human-sphere was facing the antennas. This S21 parameter is the response $S_1(f)$ and it is shown in contrast to the measurement noise level. In this Figure it is observed that the lowest points of $S_1(f)$ are at frequencies of 2.5 and 2.7 GHz where $S_1(f)$ is approximately 10 dB higher than the highest noise level and 29 dB higher than the mean noise level. The main part of $S_1(f)$ in all the other different frequencies is 15-60 dB higher than the highest noise level and 34-79 dB higher than the mean noise level. Subtracting the measured S21 parameter of the background fields $S_2(f)$ from the measured S21 parameter of the human-sphere in presence fields $S_1(f)$, yields the $S_3(f)$ response as presented in Figure 6.15 . $S_3(f)$ is shown against the measurement noise level. In this Figure it is observed that the lowest points of $S_3(f)$ are

in the frequency range of 5-5.3 GHz where the value of $S_3(f)$ is close to the highest noise level and 19 dB higher than the mean noise level. The main part of $S_3(f)$ in all the other different frequencies is 15-60 dB higher than the highest noise level and 34-79 dB higher than the mean noise level.

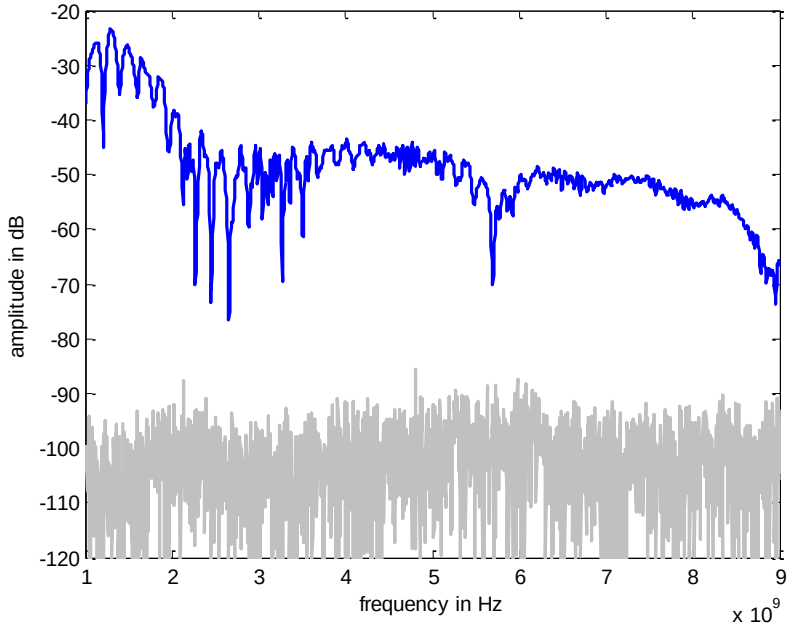

Figure 6.14: The S21 parameter of the sum of fields as the human-sphere object (sphere in front of the human) is facing the antennas; this S21 is expressed by the response $S_1(f)$ (blue) against the noise level (grey).

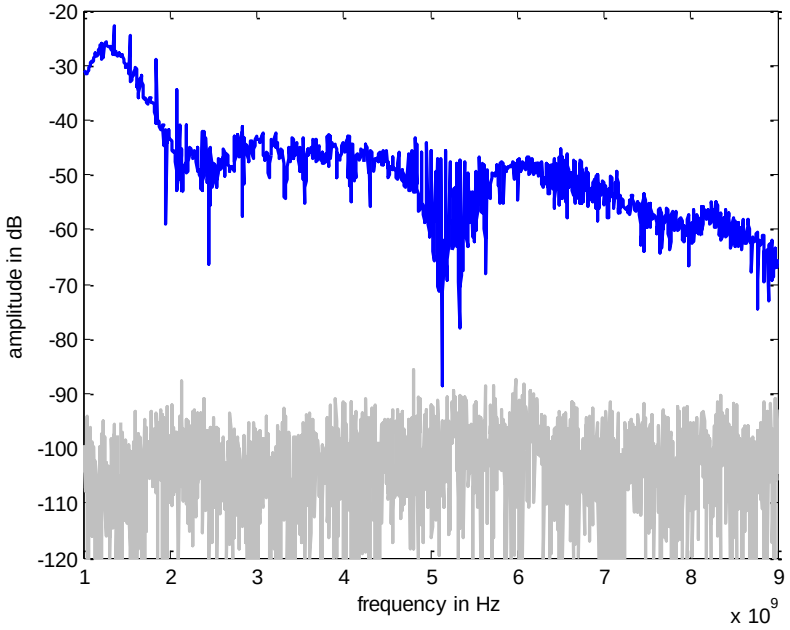

Figure 6.15: Response resulting from the subtraction of the measured S21 parameter of the background fields (Figure 6.13) from the measured S21 parameter of the human - sphere in presence fields (Figure 6.14) ; this resulting response is described by $S_3(f)$ (blue) against the noise level (grey).

Figure 6.16 shows the response created by the application of the equalising signal $I_{eq}(f)$ on the response $S_3(f)$. This response is shown in comparison to the noise level. It is observed that the response is 25-60 dB higher than the highest noise level and 44-79 dB higher than the mean noise level. However at the lowest points of the response that are in the frequency range of 5-5.3 GHz, the value of the response is approximately 8 dB higher than the highest noise level and 27 higher than the mean noise level.

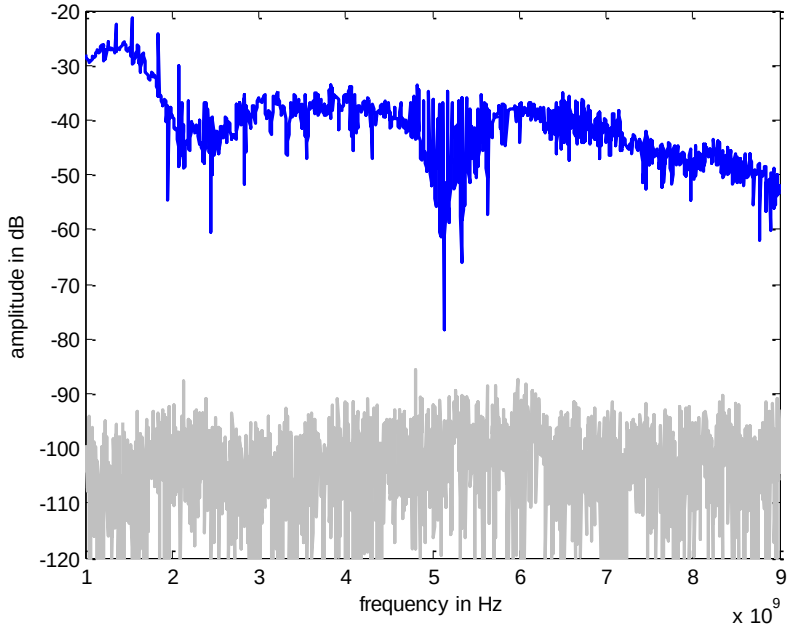

Figure 6.16: The response (blue) created by the application of the equalising signal $I_{eq}(f)$ on the response $S_3(f)$ of Figure 6.15 against the noise level (grey).

Applying the same methodology and processing to the cases of the remaining two different positions of sphere on the human the following results are obtained. Figure 6.17 and Figure 6.18 show the response created by the application of the equalising signal $I_{eq}(f)$ on the response $S_3(f)$ for two cases of human-sphere composite objects against the noise level. In the first case the human is facing the radar and the sphere is by the side of the human. In the second case and the human is facing the radar and the sphere is in the radar shadow of human. In Figure 6.17 the response is 39-79 dB higher than the mean noise level except from the frequency of 8.8 GHz where the value of the response is 20 dB higher than the mean noise level. In Figure 6.18 the response is 44-79 dB higher than the mean noise level apart from the frequency of 3.1 GHz where the value of the response is 27 dB higher than the mean noise level.

Human-sphere (the human is facing the radar and the sphere is by the side of the human**)**

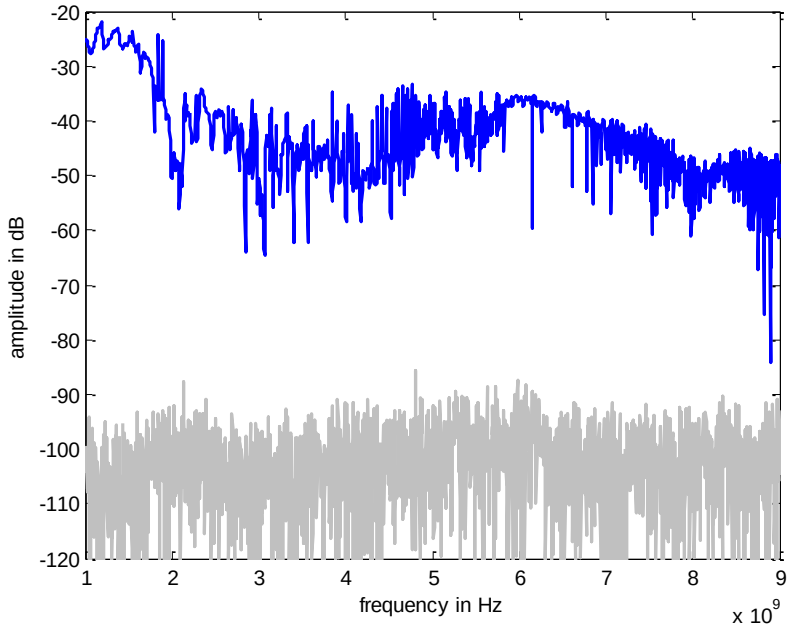

Figure 6.17: The response (blue) created by the application of the equalising signal $I_{eq}(f)$on the response $S_3(f)$ for the human-sphere (sphere by the side of the human) against the noise level (grey).

Human-sphere (the human is facing the radar and the sphere is radar shadow of human**)**

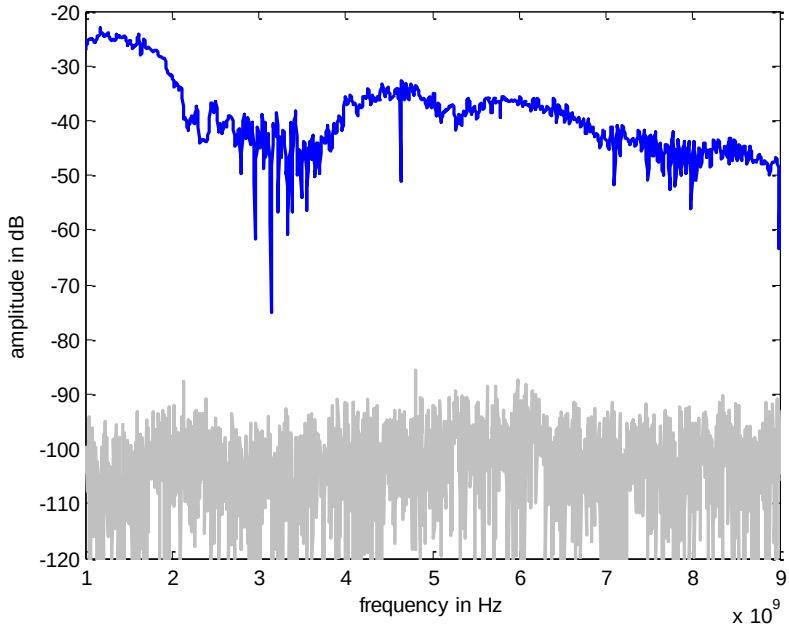

Figure 6.18: The response (blue) created by the application of the equalising signal $I_{eq}(f)$on the response $S_3(f)$ for the human-sphere (sphere attached to the back of the human) against the noise level (grey).

In Figures 6.19a and 6.19.b the responses of human and human-sphere composite objects for all cases of the positions of the sphere on the human body from the respective Figures 6.12, 6.16, 6.17 and 6.18 are gathered.

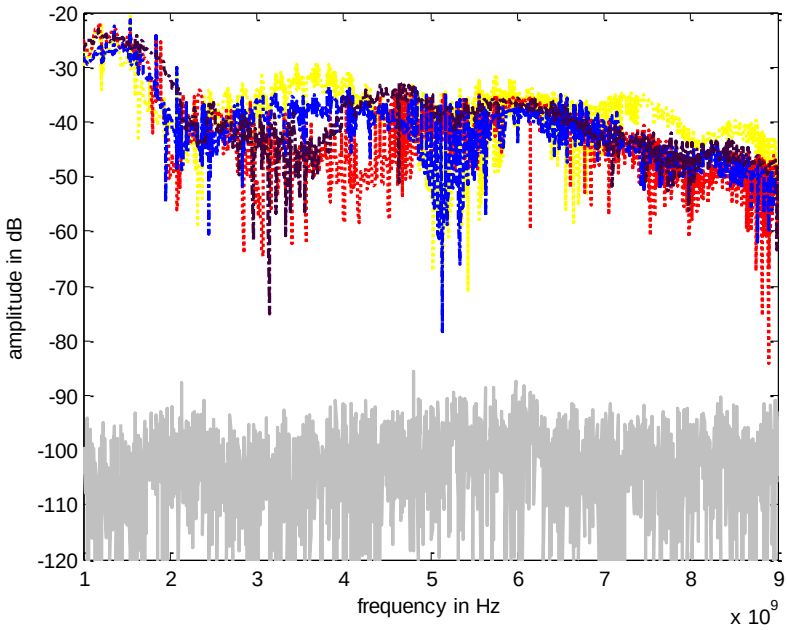

Figure 6.19.a: All the frequency responses against the noise level (grey).
Response of human (yellow)
Response of human-sphere (blue) (sphere in front).
Response of human-sphere (red) (sphere by the side of the human).
Response of human-sphere (black) (sphere attached to the back of the human).

In Figure 6.19.a it is observed that the responses are 40-79 dB higher than the mean noise level except from the frequencies of 3.1 GHz, 5.1 GHz and 8.8 GHz where the responses are 28dB, 24dB and 20 dB respectively higher than the mean noise level. The difference in levels between the responses and the noise yields that the effect of noise on these responses is diminished. Comparison of the responses in Figure 6.19 and Figure 5.22 yields that the response of the human is less than the response of the conducting plate. This was expected as the RCS of conducting plate (11 m^2) and the RCS

of human (1 m^2) were estimated. However the IR of human is likely to be much more complex than that of the plate.

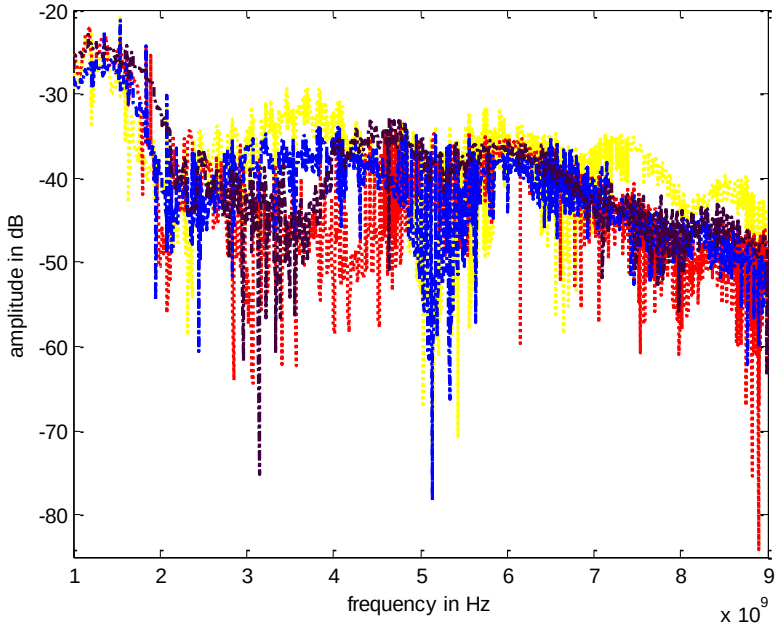

Figure 6.19.b: All the frequency responses of Figure 6.19.a in different scale

As it is observed in Figure 6.19.b the response is affected by both the existence and the position of the sphere. However since the amplitude of the sphere response is much lower than the amplitude of response of the human the more critical difference between the responses are observed below the -30 dB levels. The extraction of the natural resonant frequencies of the objects from these responses requires converting these responses in the time domain. This is accomplished in the next section.

6.3 Sphere ETR and LTR

In this section the experimentally obtained impulse response (IR) of the sphere is considered and studied for the case that broadband horn antennas are used for the reflected fields acquisition. Therefore from the overall sphere experimental IR the LTR is

selected in order to verify that the experimental LTR corresponds to the theoretical sphere LTR as presented in section 4.3. Initially the LTR is selected from the IR, and then the experimental LTR poles and residues of the sphere are extracted. These poles and residues are compared with the ones obtained from the sphere theoretical LTR. The result of this examination is the determination of the different parameters that are used for the processing of the frequency domain measurement. These parameters, which are referred to in section 6.2, are frequency band limits and frequency step. Additionally different parameters presented in section 5.2 like sampling frequency of the time domain field and type of window used for this measurement are determined. Moreover the level of the sphere LTR against the noise level is also compared for the experimental settings used. Essential conclusions can also be drawn on the physical duration of the IR and the LTR.

In order to assess the experimental procedure, this experiment is carried out for a sphere of radius 0.0325 m. In this way through the accuracy of the experimental results in relation to the theoretical results, the methodology, the experimental configuration and frequency domain processing that is shown in section 6.2 is investigated.

The sphere IR can be obtained via consideration of the S21 parameter of the measured fields of the sphere, as shown in Figure 6.6. In appendix section 5.a this response is presented in the time domain. In this response the antennas coupling field and the chamber absorber clutter field in addition to the antennas response are present. These fields are removed from the measured S21 parameter, via the formulation of $S_3(f)\times I_{eq}(f)$ as it was shown in section 6.2. Moreover before the time domain conversion a window is applied for the similar reason explained in section 5.2, so

$S_3(f)\times I_{eq}(f)\times W(f)$ is created. Subsequently in order to convert $S_3(f)\times I_{eq}(f)\times W(f)$ into time domain an IFT is estimated after zero padding. So estimation of $h_y(t) = IFFT[S_3(f)\times I_{eq}(f)\times W(f)]$ will yield the sphere backscattered time domain field which is the sphere IR. Figure 6.20 shows the experimentally obtained IR i.e. Early Time Response (ETR) and LTR of the 0.0325 m radius sphere respectively against the noise in time domain which has been obtained via estimation of the IFT of the frequency domain noise data.

In Figure 6.20, the level of IR is 20-62 dB higher than the noise level depending on the time instant that the IRs are considered. This is due to the difference between the level of the response and mean noise level in frequency domain in Figure 6.8.

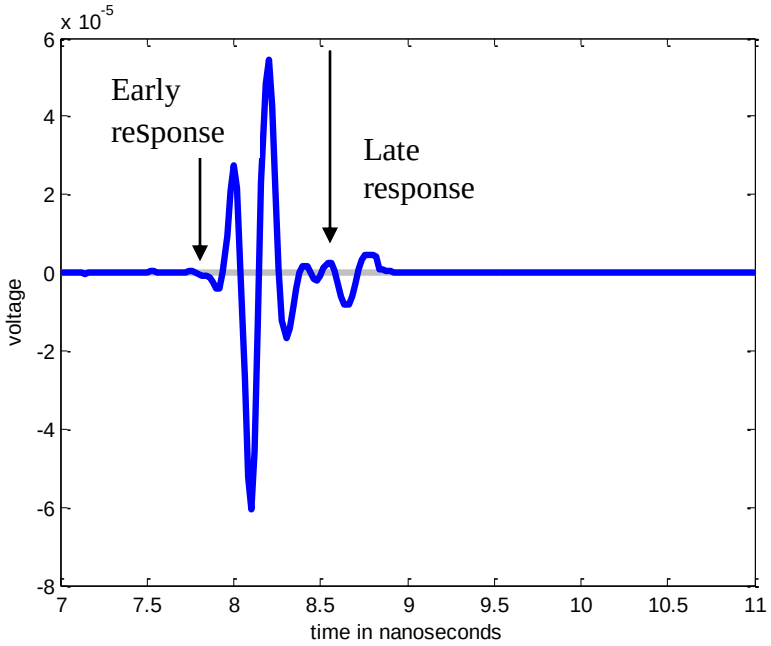

Figure 6.20: Experimentally obtained IR of the 0.0325m sphere (blue) against the noise (grey).

In section 5.4 it was described that the ETR duration T_L is the time the incident field interacts with the sphere of radius α and $T_L = 4\left(\frac{\alpha}{c}\right) + \tau$. Where τ is the UWB pulse length (pulse width), which is utilised as incident field. Additionally τ is defined as $\tau = \frac{1}{B}$ where B is the measurement bandwidth. Therefore if the measurement bandwidth is equal to $B = 8 \times 10^9$ Hz the pulse width is equal to $\tau = 0.125$ *nanoseconds (ns)*. So for the sphere of radius $\alpha = 0.0325$m and since $c = 3 \times 10^8$, which is the speed of light $T_L = 0.5583$ *ns*. Thus the ETR duration can be considered approximately equal to $T_L \cong 0.56\,ns$. Therefore by observation of Figure 6.20 if the ETR starts at approximately $7.94\,ns$ the LTR which follows should start at approximately $8.5\,ns$. Therefore focusing on the LTR from the ETR, Figure 6.21 presents the experimentally obtained LTR of the sphere of radius 0.0325 m against the noise.

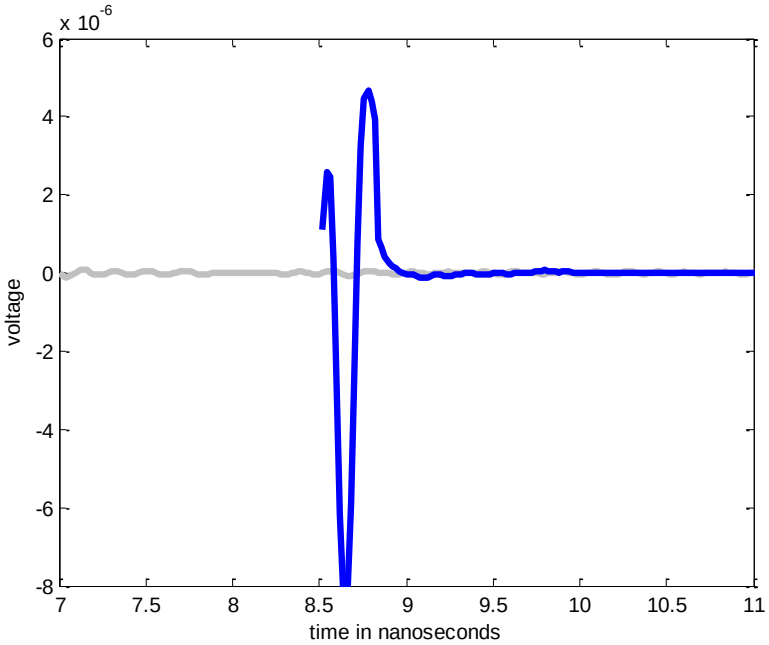

Figure 6.21: Experimentally obtained (blue) LTR of 0.0325 m radius sphere against the noise (grey).

As the theoretical sphere LTR was obtained in chapter 4, Figure 6.22 shows the theoretical and reconstructed LTR of the sphere of radius 0.0325 m. By observation of the theoretical LTR of the sphere of radius 0.0325m it can be seen that at 1.5 *ns* after the beginning of the LTR, the signal has converged to zero. However from the theoretical IR, it is observed that 0.5 *ns* after the beginning of the LTR, the signal amplitude is significantly reduced. So if the beginning of the experimentally obtained LTR is at approximately 8.5 *ns* as shown in Figure 6.21, the end of signal data should be at an earlier time instant than 9.0 *ns*. In Figure 6.21 it is observed that after 8.9 *ns* the level of signal is closer to the noise level, consequently the previous assumption on the considered time interval is valid. So, in the 8.5-8.9 *ns* time interval the sphere LTR is in the order of 20-44 dB higher than the noise level and the SVD-Prony method is used for processing the LTR. The experimental and reconstructed LTR of 0.0325 m radius sphere are shown in Figure 6.23.

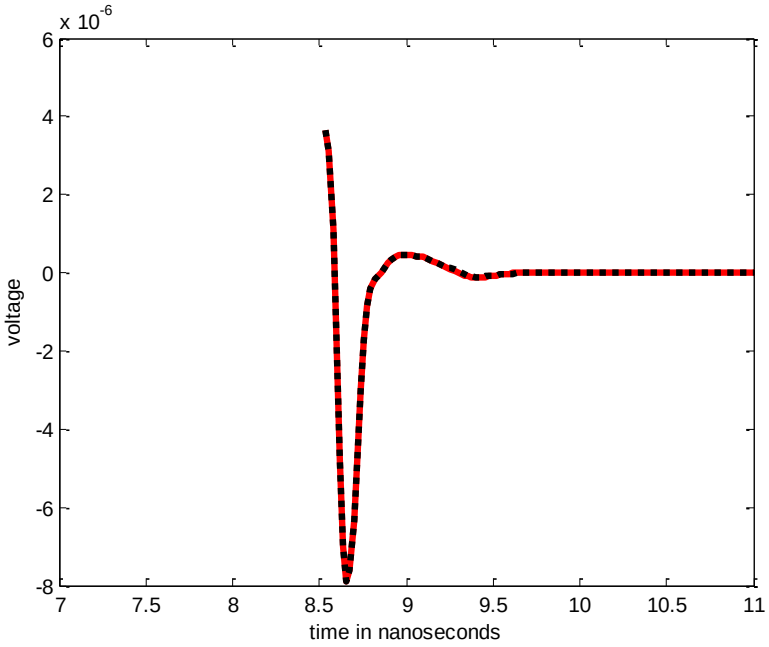

Figure 6.22: The theoretical (red) and reconstructed (black) LTR of 0.0325 m sphere.

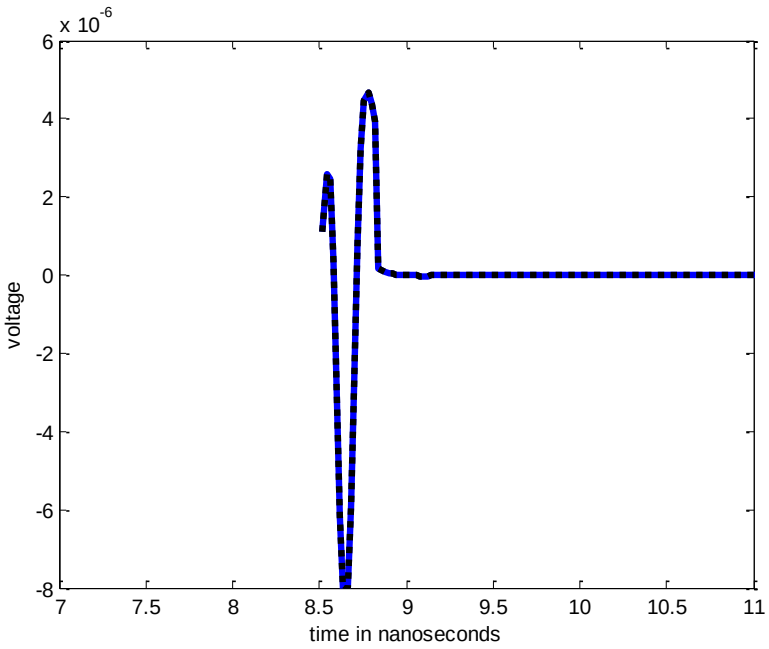

Figure 6.23: Experimentally obtained (blue) and reconstructed (black) LTR of the sphere of radius 0.0325 m.

As explained in section 6.1 in order to obtain the signal information of the sphere LTR, the PSD has to be calculated along with the poles or resonant frequencies and their amplitudes. The PSD of the experimental LTR of 0.0325 m radius sphere is shown in Figure 6.24 next to the PSD of the theoretical LTR of the 0.0325 m radius sphere. The experimental sphere LTR extracted poles with their amplitudes are shown in Figure 6.25 and Figure 6.26 respectively. These poles and amplitudes are plotted alongside with the extracted poles of the theoretical LTR of 0.0325 m radius sphere and their amplitudes.

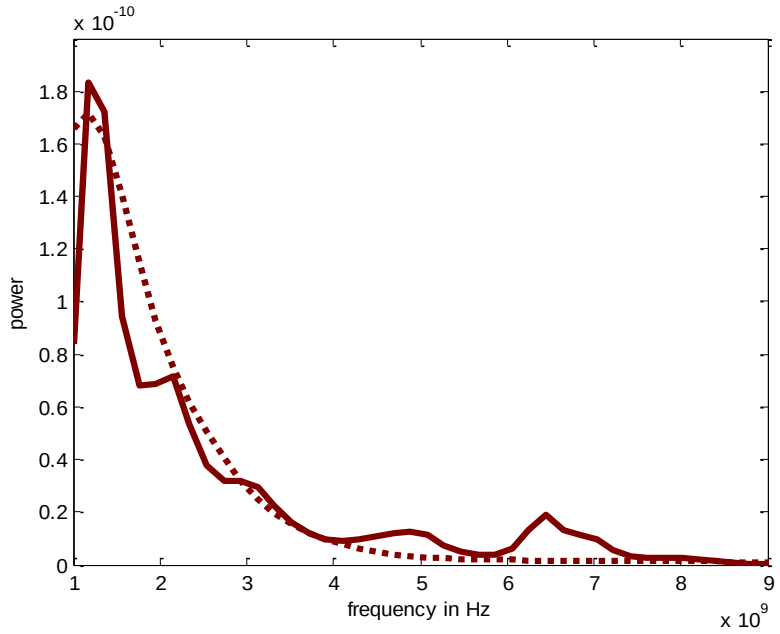

Figure 6.24: The PSD (solid line) of experimental LTR of 0.0325 m radius sphere and the PSD (dotted line) of theoretical LTR of 0.0325 m radius sphere.

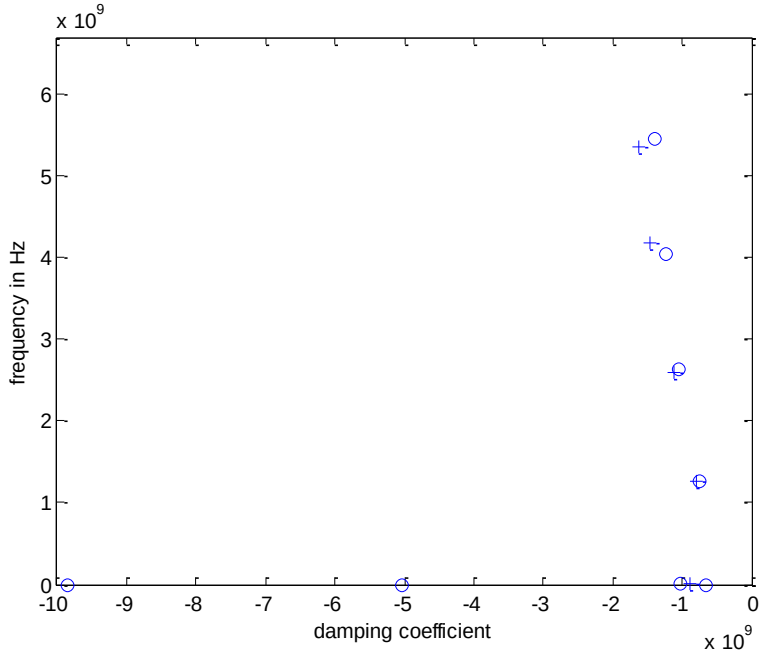

Figure 6.25: Experimental LTR extracted (+), and theoretical LTR extracted (o) poles of the 0.0325 m sphere.

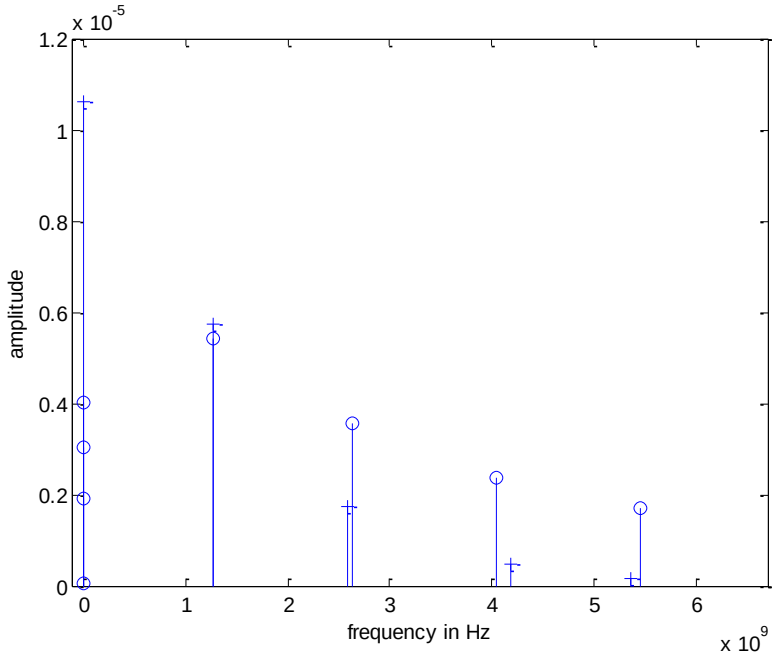

Figure 6.26: Amplitudes of experimental LTR extracted (+), and theoretical LTR extracted (o) poles of 0.0325 m sphere against frequencies of poles.

In Figure 6.24 it is shown that the PSD of the theoretical LTR has the highest peak location at the same frequency as the PSD of the experimental LTR i.e. at approximately 1.3 GHz. Furthermore the two PSDs have similar shapes and their critical power levels appear in the 1-5.5 GHz band. From Figure 6.25 and Figure 6.26 it is deduced that for the 0.0325 radius sphere for the particular set of parameters chosen, the experimental LTR extracted, and theoretical LTR extracted poles almost coincide at the frequency of 1.3 GHz and 2.8 GHz. Additionally the experimental LTR extracted poles at 4.1 GHz and 5.4 GHz are similar to the theoretical LTR extracted ones in terms of frequency. Moreover the experimentally extracted poles are in the vicinity of the theoretically extracted ones, even though there are small differences in the damping coefficients. Another strong indication of the correctness of the approach, apart from the similarities in frequencies, is that as shown in Figure 6.25 the overall clustering of the theoretically extracted poles has similar shape to the clustering of the experimentally

extracted ones, which results in the 5.4 GHz pole having the largest damping coefficient. From Figure 6.26 it is shown that among the poles the 1.3 GHz experimental pole has the largest amplitude; this is also verified from the theoretical poles. This pole is the most significant pole of the 0.0325 radius sphere LTR and it will be referred to as the principal pole. It must be mentioned that any differences on the damping coefficients in Figure 6.25 and the amplitudes in Figure 6.26 between experimental and theoretical poles are mainly due to the finite conductivity of the sphere used for the measurements. Some slight discrepancy between experimental and theoretical results may be due to the overall response of the measuring system, which cannot be completely isolated. As it was also mentioned in section 5.4 the finite conductivity of the sphere results in the sphere reflecting back only a fraction of the power of the incident wave. As a result the extracted poles of the experimental LTR at frequencies 4.1 GHz and 5.4 GHz have a higher damping coefficient and smaller amplitudes than the poles of the theoretical LTR.

In this section the experimental configuration and methodologies were tested via comparison of the theoretical and experimental results. The set of parameters used in this section is also used for the processing of all experimental data throughout the experiment as presented in the following sections, since for these parameters the experimental results proved to be in accordance with the theoretical results.

6.4 Human ETR and LTR

This section describes the analysis of the backscattered field from the human in terms of the human's IR. Knowing the response of the sphere, as shown above, the frequency response of the human can be acquired. The S21 parameter of the

backscattered fields is measured in the frequency domain as the human is facing the antennas. For the processing of this frequency domain measurement the methodology, experimental configuration and parameters of section 6.2 are used so as to obtain the frequency response of the human. Additionally, the estimation of the IFFT of the human's response yields the human's IR.

Subsequently the LTR of the human from the overall human IR is selected in order to obtain the PSD and extract the human LTR poles and amplitudes. For the selected human LTR the number of poles is not known beforehand. Furthermore as it was explained in section 5.5 the poles extraction algorithm requires the number of poles to be previously determined, so the estimate for the number of poles is determined by the number which minimizes the Minimum Description Length (MDL) criterion. In appendix section 5.b the MDL is shown for the case of human LTR.

The human experimental IR i.e. ETR and LTR is shown in Figure 6.27 against the noise. As it was explained in section 5.5 the ETR duration T_L is the time of interaction of the incident field with the human with line of sight extent L and $T_L = 2\left(\frac{L}{c}\right) + \tau$. Where τ is the UWB pulse width, which is utilised as the incident field. Since the measurement bandwidth for the human was the same as in the case of the sphere, the width of the UWB pulse is $\tau = 0.125\,ns$.

In Figure 6.27 the start of the LTR is found by taking into account the duration T_L. For the human used in the experiments the line of sight extent of the body is $L \cong 0.22$ m therefore $T_L = 1.6\,ns$. So the ETR duration is equal to approximately 1.6 *ns*. Hence by observation of Figure 6.27 since the ETR starts at approximately $7.5\,ns$ the LTR should

start at approximately 9.1*ns*. The end of the LTR is at approximately 10.6 *ns* and in this experiment for all targets the time interval of 1.5 *ns* is considered. The end of the LTR is at approximately 10.6 *ns*, since beyond this time instant the LTR rapidly decays. In all cases where the human is present the human is almost motionless so the human position does not change. Therefore whenever the human is present only the 9.1-10.6 *ns* time interval is considered as the LTR. In Figures 6.27, the level of IR is approximately 20-78 dB higher than the noise level. This is due to the difference between the response level and mean noise level in frequency domain in Figure 6.12. Additionally in appendix section 5.d the human LTR is shown against the noise. The level of human LTR is in the order of 20-66 dB higher than the noise level.

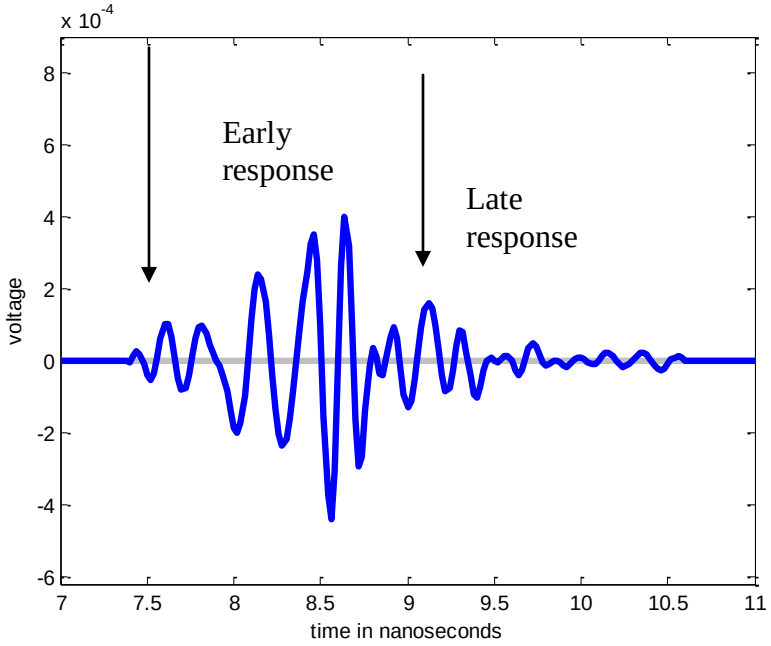

Figure 6.27: Human (blue) IR (ETR and LTR) against the noise (grey).

From the human IR of Figure 6.27 the LTR is selected, and it is presented in Figure 6.28 together with the reconstructed LTR. As it is observed the two LTRs coincide. Following the same approach as the approach of the extraction of the sphere

LTR information, the PSD and the poles with their amplitudes for the human body are calculated. Figure 6.29 presents the PSD of the human LTR.

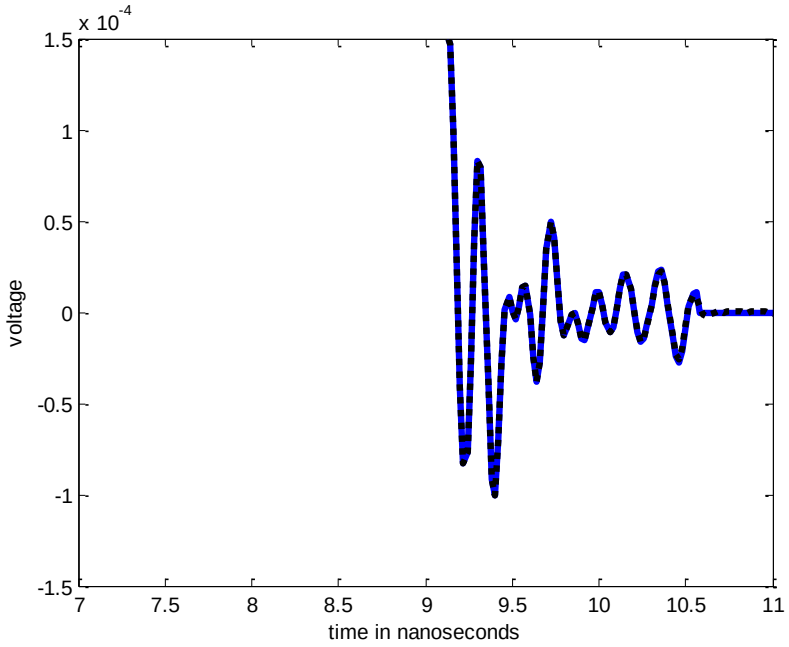

Figure 6.28: Human (blue) LTR and reconstructed (black) LTR.

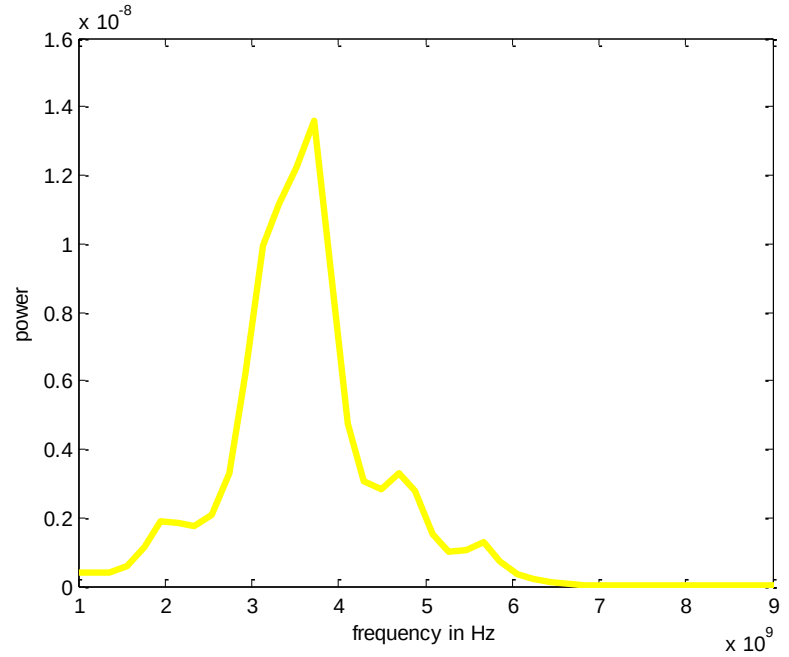

Figure 6.29: PSD of the human LTR.

The human LTR extracted poles with their amplitudes are shown in Figure 6.30 and Figure 6.31 respectively.

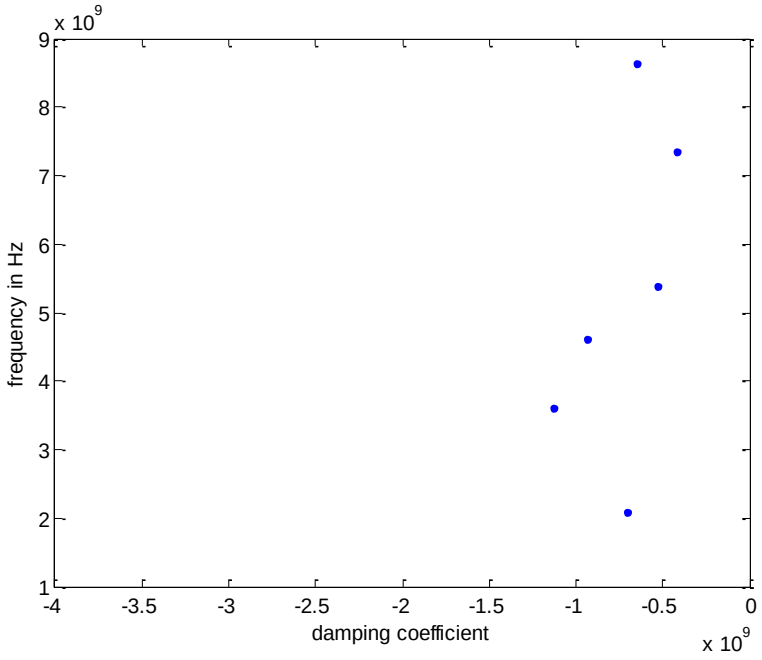

Figure 6.30: Human LTR extracted poles.

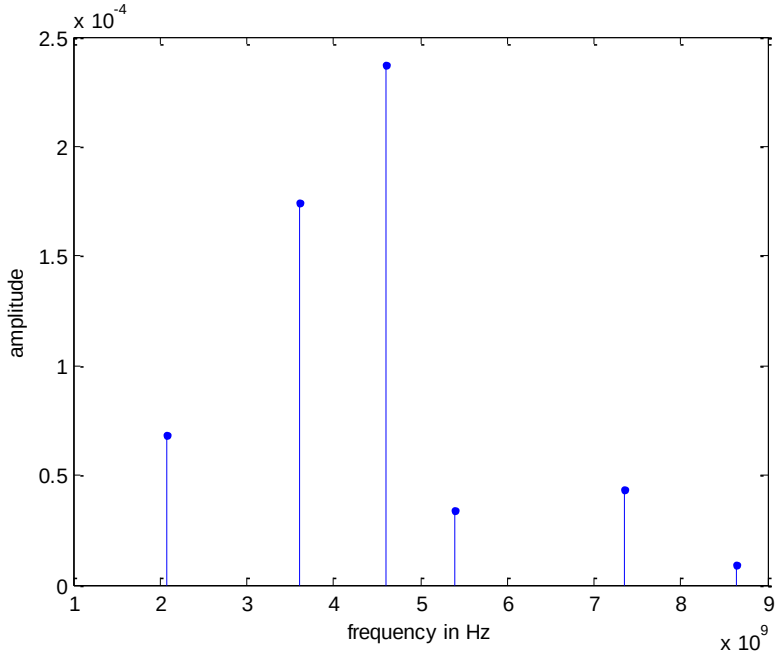

Figure 6.31: Amplitudes of the human LTR extracted poles.

As it was mentioned in section 6.2, in order to reduce the effect of noise each measured response is the average of 120 measurements. Therefore for the human's response 4 frequency domain measured responses were considered and each response was the average of 30 measurements. This averaging process for 30 measurements was performed by the network analyser and lasted for about 30 seconds. During the time needed to perform all the measurements the human was kept still. However it is impossible for the human to be completely motionless, so in order to test the effect of the human normal motion on the measurement the 4 frequency domain measured responses are combined by 2 each time and then the total of 6 combinations of responses are processed and compared. So each response resulting from each combination is an average of 60 measurements and the combined responses are considered in terms of LTR, PSD and poles with their amplitudes.

Subsequently in order to achieve the highest possible signal to noise ratio the 4 measured responses are averaged and in this way a response which is the average of 120 measurements is obtained. The average of 120 measurements has been processed and its LTR, PSD and obtained poles are shown in Figures 6.28-6.31. In appendix section 5.e these quantities are compared with the respective quantities of each of the other averages of 60 measurements. While in this section the PSD and obtained poles of the response derived from the average of 120 measurements are compared with the respective quantities of the average of 60 measurements.

The PSD of the human LTR originating from averaging 60 frequency domain measurements is shown in Figure 6.32 together with the PSD (shown in Figure 6.29) of the human LTR derived via processing of the average of 120 measurements.

The extracted poles of the human LTR created from averaging 60 frequency domain measurements is shown in Figure 6.33 and their amplitudes are shown in Figure 6.34 respectively. These poles and their amplitudes are plotted alongside with the poles of the human LTR (as shown in Figure 6.30) derived via processing of the average of 120 measurements and their amplitudes respectively (as shown in Figure 6.31).

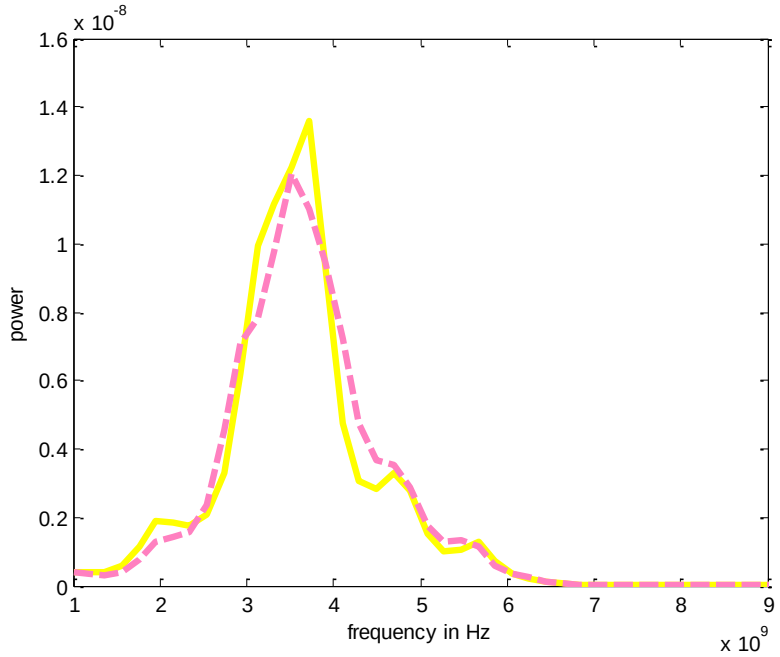

Figure 6.32: PSDs of human LTR.
(solid) average of 120 measurements
(dashed) average of 60 measurements

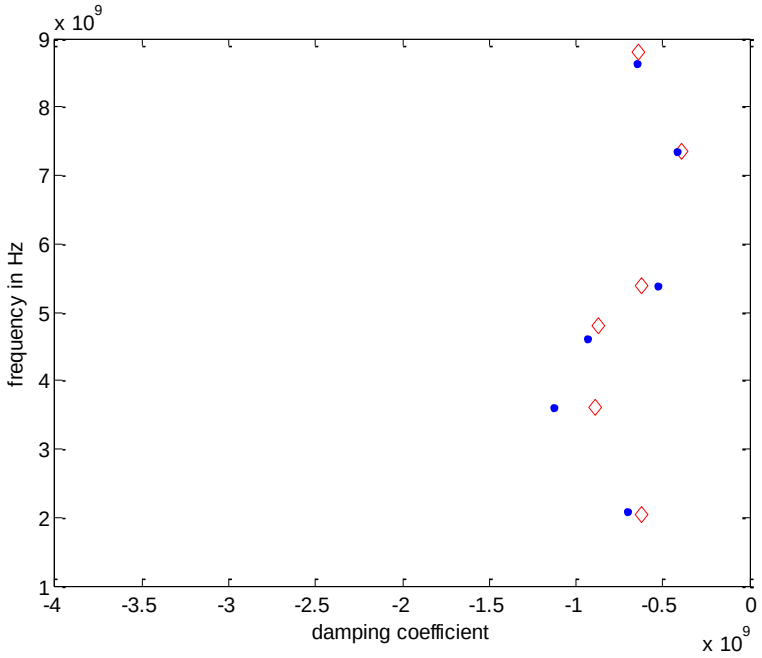

Figure 6.33: Comparison of human LTR poles.
(.) average of 120 measurements
(◊)average of 60 measurements

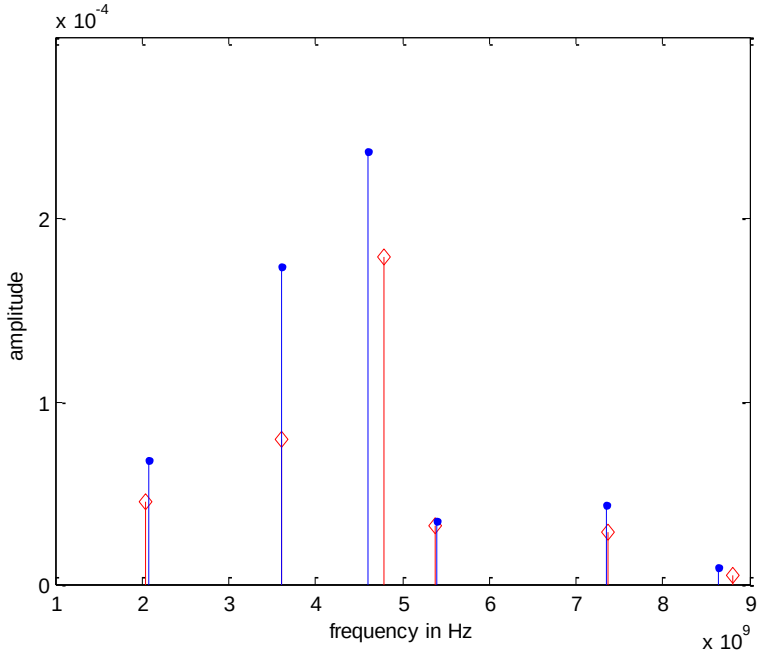

Figure 6.34: Amplitudes of the human LTR poles.
(.) average of 120 measurements
(◊)average of 60 measurements

By consideration and comparison of the PSDs of the human LTR in Figures 6.32 and the respective Figures of appendix section 5.e it is concluded that for the responses

which are the result of averaging of 60 frequency domain measurements the critical power levels exist in the 2-5.5 GHz band. The higher power levels for the PSD of the human LTR resulting from averaging of 120 frequency domain measurements also exist in the 2-5.5 GHz band. Observing Figures 6.33 and 6.34 and the respective Figures of appendix section 5.e, a conclusion is drawn that the LTR poles and their amplitudes from averaging of 120 measurements are similar to the LTR poles and their amplitudes from averaging 60 measurements in terms of frequency. Some differences can only be observed in terms of damping coefficients and amplitudes of poles in the 3.5–4.5 GHz interval. So the lack of absolute stillness for human affects the human response and its poles, however no new poles are created and all the human LTR poles are located in the 2-5.5 GHz band.

The specific results of the PSD, the poles and amplitudes of poles of the human LTR will be analysed in relation to the human-appended sphere composite object results, as presented in the following section. This comparison is performed in order to acquire the quantitative and qualitative differences between the results that can lead to the detection of the sphere appended on the human body.

6.5 Human-Sphere ETR and LTR

6.5.1Human-Sphere (in Front)

The feasibility of detection of the sphere appended to the human is investigated in this section, as it is the main objective of this Thesis. Therefore the main goal is the comparison of the information provided by the LTR of the human-sphere composite object with the information provided by the human LTR.

This experiment is carried out with a sphere of radius 0.0325 m which is appended on the human and which imitates the body-attached grenade. This measurement is repeated as the position of the sphere on the body is altered. Three different positions of the sphere location are taken into account: front of human, side of human, back (behind) of human. The S21 parameter of the backscattered fields is measured in the frequency domain as the human-sphere object is facing the antennas.

In order to process this frequency domain measurement the methodology, experimental configuration and parameters of section 6.2 are used in order to obtain the frequency response of the human-sphere composite object. Moreover, the estimation of IFFT of the human-sphere's response yields the IR of the human-sphere. After the experimental IR of the considered object is obtained, the LTR is selected in order to obtain the PSD and extract the human-sphere LTR poles and amplitudes. For the selected human-sphere LTR the number of poles is not known beforehand and it is most likely to be different to the number of poles for the human LTR. This is because the human i.e simpler object LTR has presumably less poles than the human-sphere i.e. a more complex object LTR. Furthermore as it was explained in section 5.5 the poles extraction algorithm requires the number of poles to be previously determined, so the estimate for the number of poles is determined by the number which minimizes the Minimum Description Length (MDL) criterion. In appendix section 5.b the MDL is shown for the cases of human LTR, and human-0.0325 m radius sphere LTR for all cases of sphere position on the body. As it can be observed the human-sphere LTRs involve a larger number of poles than the human LTR.

The most significant objective of the experiment is to examine the PSD of the human-sphere LTR and compare it with the PSD of the human LTR. An analogous comparison is carried out between the human-sphere LTR poles and amplitudes and the human LTR poles and amplitudes. In this way conclusions can be drawn as to whether there is a difference in the observed PSDs or the clustering of poles related to the human LTR or human-sphere LTR due to the sphere's presence. The presence of sphere appended on the human could yield the human-sphere LTR clustering to be quantified due to a bigger number of poles and due to the existence of the sphere most significant pole. Conclusions can also be drawn from the difference in the amplitudes of the respective poles, i.e. amplitude modulation at the specific poles of interest, when the sphere is present. Any difference in the PSDs or clustering of the poles at natural resonant frequencies of the sphere or any amplitude modulation due to the existence of the sphere will signify that the detection of the sphere attached to the human is feasible.

The human-sphere (in front) experimental IR, which is shown in Figure 6.35 against the noise, is approximately 20-78 dB higher than the noise level. This is due to the difference between the response level and mean noise level in frequency domain in Figure 6.16.

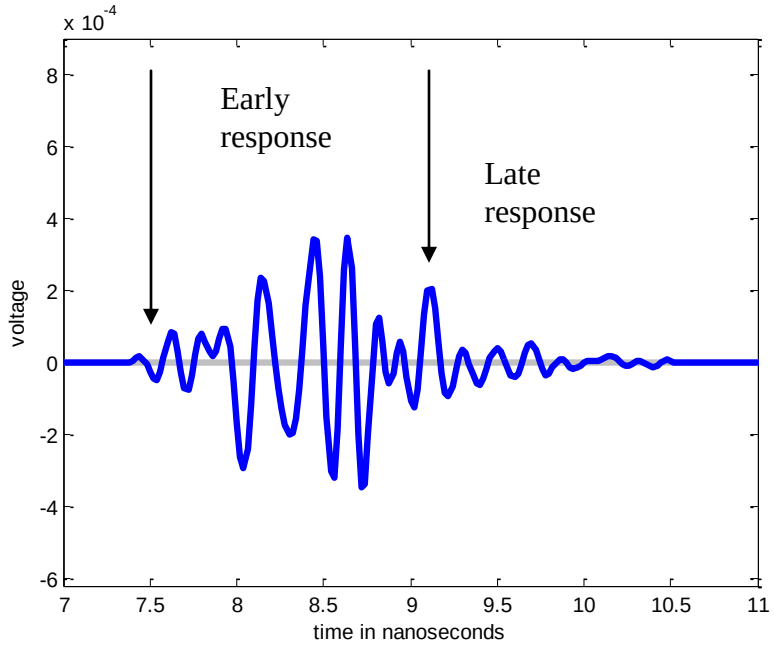

Figure 6.35: Human-sphere (sphere in front of the human) (blue) IR against the noise (grey).

Similar to the human LTR, as shown in appendix section 5.d the human-sphere (in front) LTR is in the order of 20-66 dB higher than the noise level. From the human-sphere (in front) IR of Figure 6.35 the LTR is selected and it is shown in Figure 6.36 together with the reconstructed LTR. As it is observed the two LTRs coincide. The PSD of the human-sphere (in front) LTR is shown in Figure 6.37 together with the PSD (shown in Figure 6.29) of the human LTR.

The extracted poles of the human-sphere (in front) LTR with their amplitudes are shown in Figure 6.38 and Figure 6.39 respectively. These poles and their amplitudes are plotted alongside with the poles of the human LTR (as shown in Figure 6.30) and the poles of the experimental sphere LTR (as shown in Figure 6.25) and their amplitudes (as shown in Figure 6.31 and Figure 6.26) respectively.

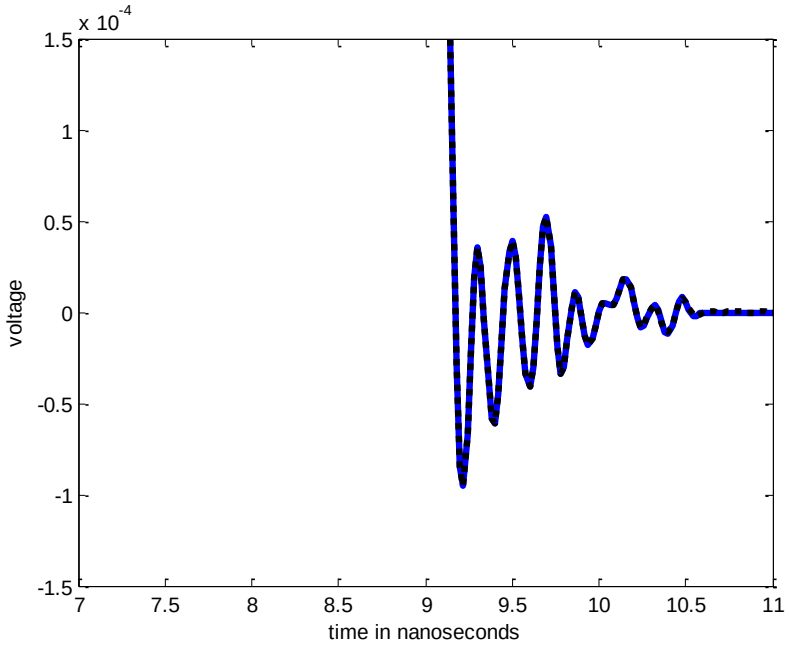

Figure 6.36: Human-sphere (in front) (blue) LTR and reconstructed (black) LTR.

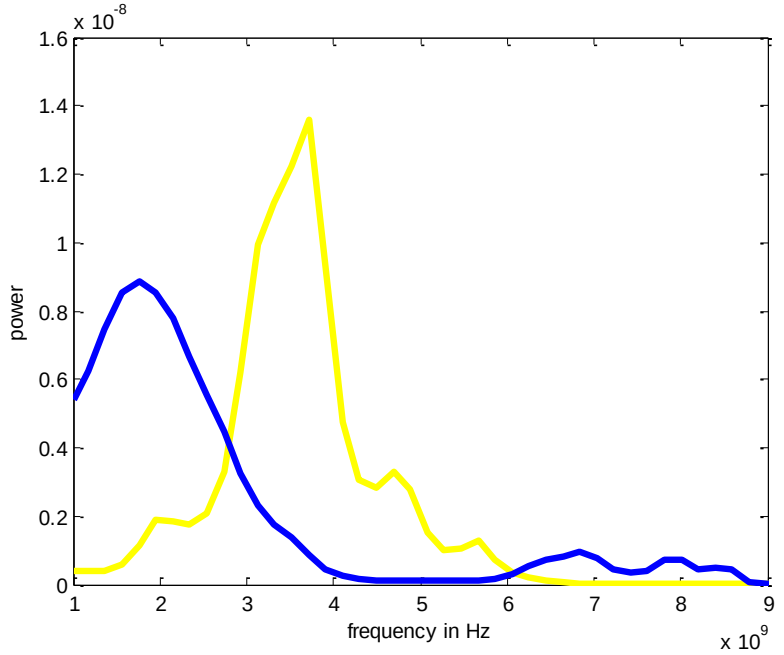

Figure 6.37: PSD of human-sphere (in front) (blue) LTR, PSD of human (yellow) LTR.

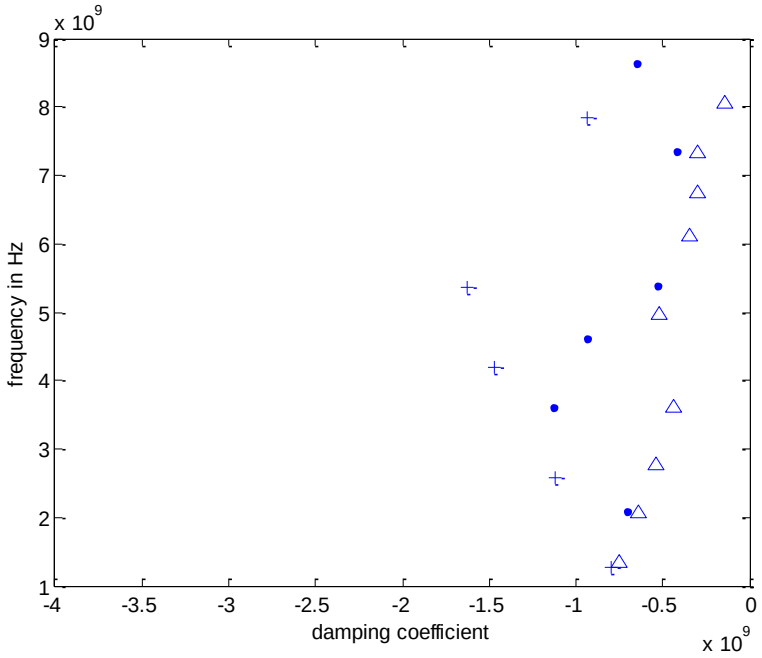

Figure 6.38: Comparison of poles.
(blue +) Poles of sphere experimental LTR
(blue .) Poles of human LTR
(blue ^) Poles of human with sphere (in front) LTR

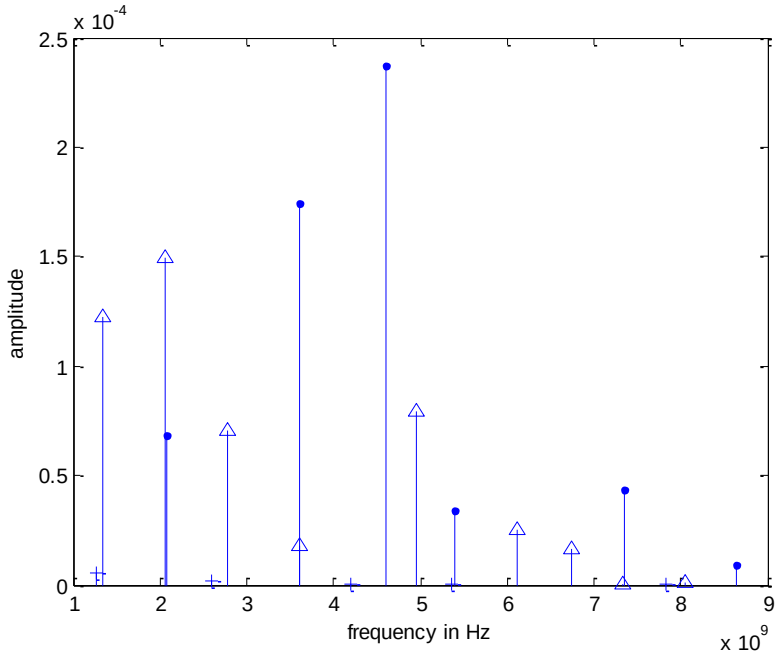

Figure 6.39: All amplitudes of the poles.
(blue +) Amplitudes of sphere experimental LTR.
(blue .) Amplitudes of human LTR.
(blue ^) Amplitudes of human with sphere (in front) LTR.

Observing Figure 6.37 it is understood that the critical power levels of the PSD of the human LTR exist in the 2-5.5 GHz band while the highest peak of the PSD is at the 3.8 GHz frequency. On the contrary the critical power levels of the PSD of human-sphere (in front) LTR appear in the 1-4 GHz band and in the 6.5-8.5 GHz band. Thus it is concluded that the existence of the sphere creates a wider band which starts from the 1 GHz band limit. Furthermore the PSD of the human-sphere (in front) LTR has the highest peak location at 1.8 GHz frequency, which is close to the peak of the PSD (Figure 6.24) of the sphere experimental LTR that was located at the frequency of 1.3 GHz. This indicates that the sphere affects the overall response therefore the detection of the sphere appended to the front of the human is possible.

Comparison of the human's poles with the human-sphere composite object's poles, as presented in Figure 6.38 shows that the number and the clustering of the human LTR poles is different to the number and the clustering of the human-sphere LTR poles and a pole located at 1.3 GHz can be retrieved. This pole is related to the principal pole of the 0.0325m radius sphere LTR. So the overall clustering is quantified due to the sphere LTR pole. This is caused by the existence of the body-appended sphere. Additionally amplitude modulation is observed at the respective poles, when the sphere is present as shown in Figure 6.39. For example the 2 GHz frequency the human LTR amplitude is 0.6×10^{-4} and the human sphere (in front) is 1.5×10^{-4}. This difference in clustering and the amplitude modulation due to the existence of the sphere signify that the detection of the sphere attached to the front of the human is feasible.

In section 6.1 it was stated that during the measurements the human retained a single placement throughout the experiment. Therefore there is a necessity of further

experimentation of multiple measurements from multiple placements of the human body inside the anechoic chamber. Resonant frequencies of the experimental LTRs of human-CWE complex objects regarding different orientation and stances with respect to the measuring system should be obtained. The range of experimental circumstances could be expanded to involve people of different age, shape and heights as the human subject. In case that the pole of the human-sphere object that is closely related to the principal pole of sphere would remain the same or be within certain limits; then the approach presented in the Thesis would guarantee the repeatability of detection. Also the robustness of the proposed method for the sphere detection in relation to subject movement and measurement conditions would be established. Another important issue that should be addressed is whether the approximated grenade or sphere and other CWEs could be identified on the human. One possible way to address this issue would be to test for a variety of CWEs like the ones that were considered in chapter 2. Such CWEs have a different shape than the sphere or approximated grenade studied in this Thesis hence they would have different signature poles. This assumption should be verified by using the experimental procedure described. It would also be very important to experimentally evaluate if signature poles for the CWE appended on the human body could be extracted from the human-CWE object LTR. If this is possible then the identification of approximated grenade or sphere and other CWEs appended on the human would be realised, and the classification of human-appended CWEs would be established. Additionally the detection of multiple CWEs appended on the human body should be considered.

6.5.2Human-Sphere (Side)

Following a similar procedure for obtaining the human-sphere (front) IR, the human-sphere (side) experimental IR is presented. The human-sphere (side) experimental IR, which is shown in Figure 6.40 against the noise, is approximately 20-78 dB higher than the noise level. This is due to the difference between the response level and mean noise level in frequency domain in Figure 6.17.

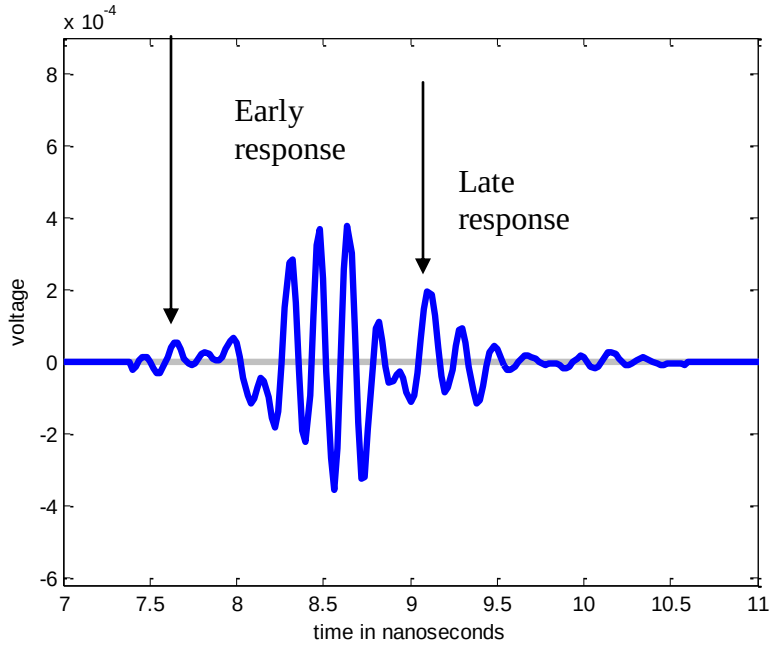

Figure 6.40: Human-sphere (sphere by the side of the human) (blue) IR against the noise (grey).

Similar to the human LTR, as shown in appendix section 5.d the human-sphere (side) LTR is in the order of 20-66 dB higher than the noise level. From the human-sphere (side) IR of Figure 6.40, the LTR is selected and it is shown in Figure 6.41 together with the reconstructed LTR. As it is observed the two LTRs coincide. The PSD of the human-sphere (side) LTR is shown in Figure 6.42 together with the PSD (shown in Figure 6.29) of the human LTR.

The extracted poles of the human-sphere (side) LTR with their amplitudes are shown in Figure 6.43 and Figure 6.44 respectively. These poles and their amplitudes are plotted alongside with the poles of the human LTR (as shown in Figure 6.30) and the poles of experimental sphere LTR (as shown in Figure 6.25) and their amplitudes (as shown in Figure 6.31 and Figure 6.26) respectively.

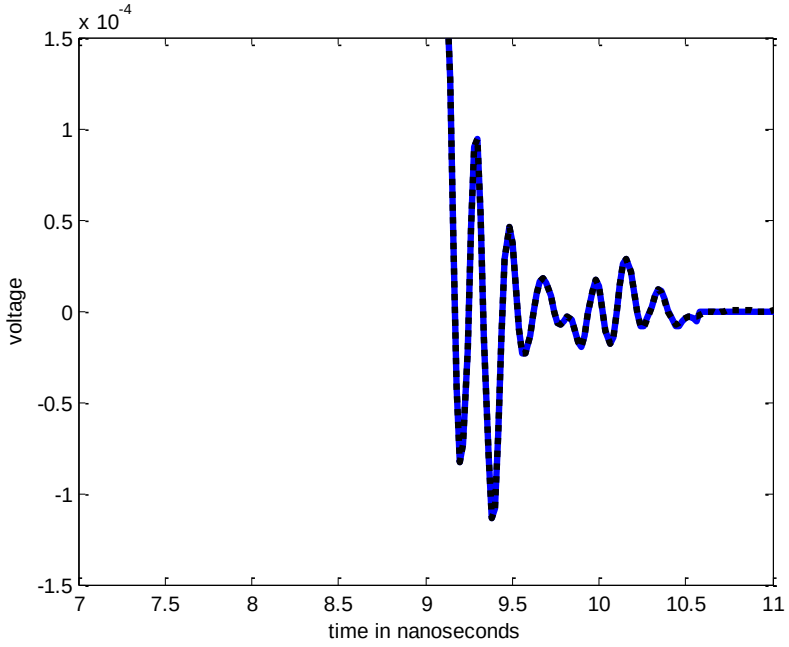

Figure 6.41: Human-sphere (by the side) (blue) LTR and reconstructed (black) LTR.

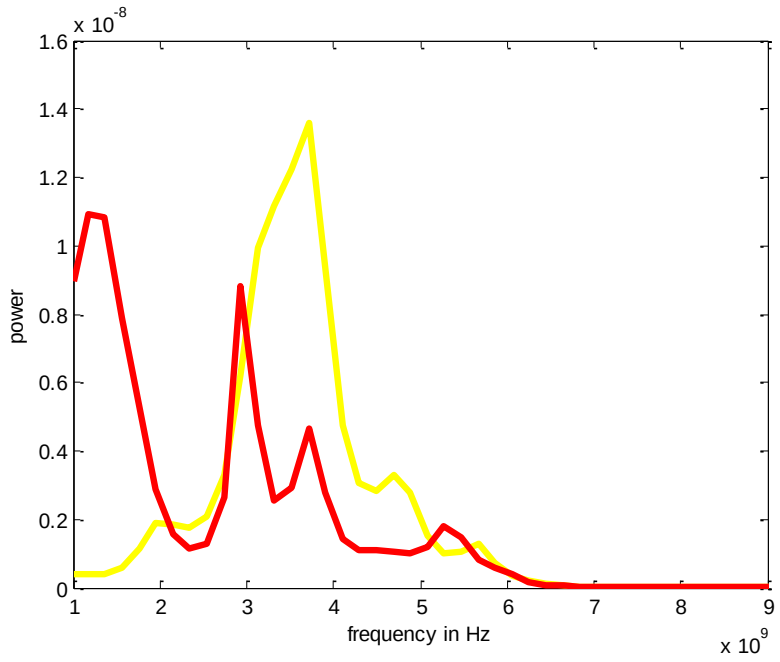

Figure 6.42: PSD of human-sphere (side) (red) LTR, PSD of human (yellow) LTR.

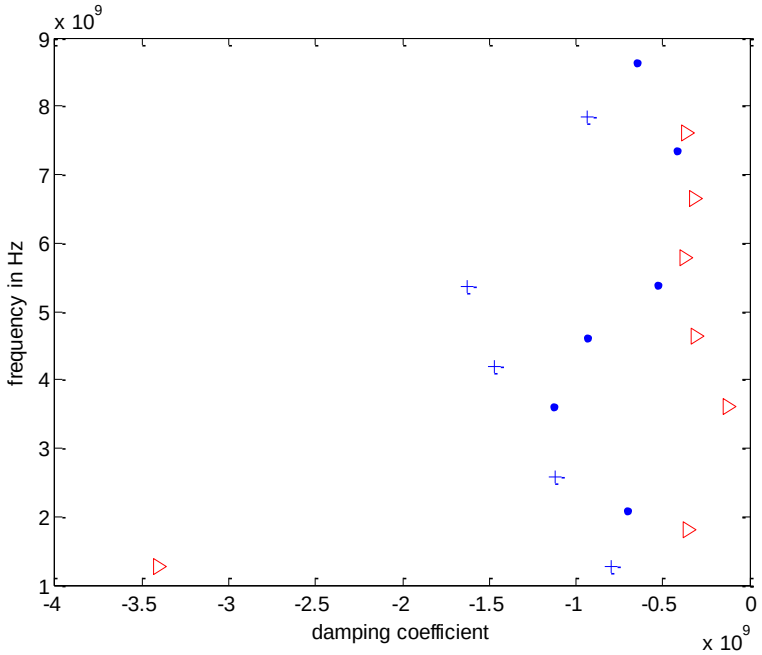

Figure 6.43: Comparison of poles.
(blue +) Poles of sphere experimental LTR
(blue .) Poles of human LTR
(red >) Poles of human with sphere (side) LTR

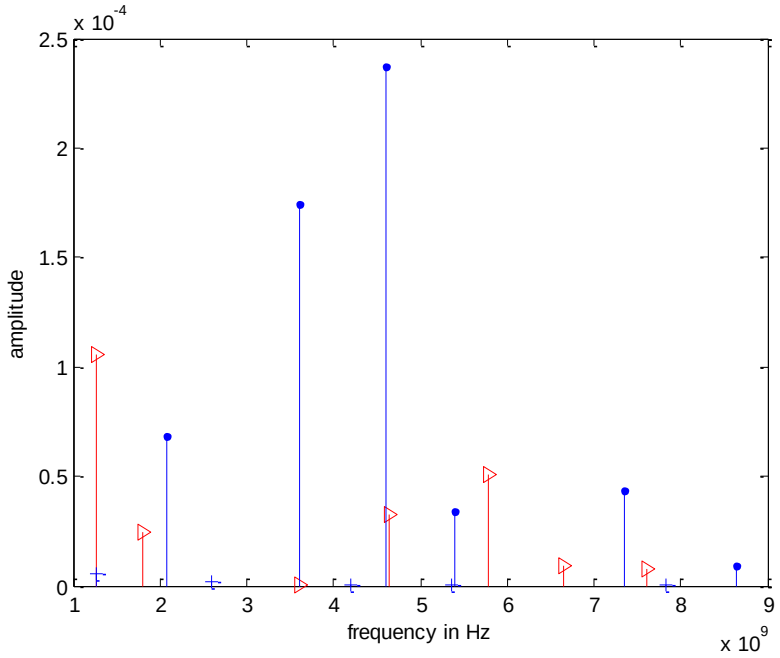

Figure 6.44: All amplitudes of the poles.
(blue +) Amplitudes of sphere experimental LTR
(blue .) Amplitudes of human LTR
(red >) Amplitudes of human with sphere (side) LTR

Similar to the analysis of the human-sphere (in front), it is observed in Figure 6.42 that the critical power levels of the PSD of the human-sphere (side) LTR appear in the 1-6 GHz band. Thus the existence of the sphere creates a wide band starting from the 1 GHz band limit. Furthermore the PSD of the human-sphere (side) LTR has the highest peak location at 1.2 GHz frequency, which is close to the peak of the PSD (Figure 6.24) of the sphere experimental LTR located at around 1.3 GHz frequency. Conversely as it has been mentioned the critical power levels of the PSD of human LTR exist in the 2-5.5 GHz band while the highest peak of the PSD is at 3.8 GHz. This indicates that the sphere affects the overall response therefore the detection of the sphere appended to the side of the human is possible.

Comparison of human poles with the human-sphere composite object poles in Figure 6.43 shows that the clustering of the human LTR poles is different to the

clustering of the human-sphere LTR poles and a pole located at 1.2 GHz can be retrieved. This pole is related to the principal pole of the 0.0325m radius sphere LTR. This is caused by the existence of the body-appended sphere. Additionally there is amplitude modulation at the respective poles as shown in Figure 6.44. This difference in clustering and the amplitude modulation due to the existence of sphere signify that the detection of the sphere attached to the side of the human is feasible. Similar to the case of the human-sphere (in front), in this case some issues for further consideration arise. The first issue is that the robustness of the sphere detection to subject movement and measurement conditions must be established. The second issue that should be addressed is whether the approximated grenade or sphere and other CWEs could be identified on the human.

6.5.3Human-Sphere (Back)

Finally the detection of the sphere hidden at the back of the human body is presented. The human-sphere (back) experimental IR, which is presented in Figure 6.45 against the noise, is approximately 20-84 dB higher than the noise level. This is due to the difference between the response level and mean noise level in frequency domain in Figure 6.18.

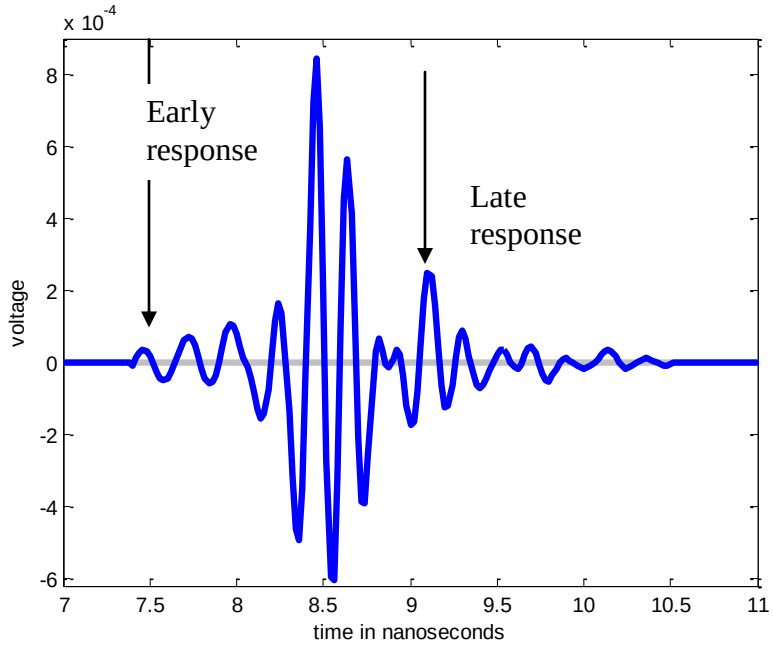

Figure 6.45: Human-sphere (sphere attached to the back of the human) (blue) IR against the noise (grey).

Similar to the human LTR, as shown in appendix section 5.d the human-sphere (back) LTR is in the order of 20-66 dB higher than the noise level. From the human-sphere (back) IR of Figure 6.45 the LTR is selected and it is shown in Figure 6.46 together with the reconstructed LTR. As it is observed the two LTRs coincide. The PSD of human-sphere (back) LTR is shown in Figure 6.47 together with the PSD (shown in Figure 6.29) of the human LTR.

The extracted poles of the human-sphere (back) LTR with their amplitudes are shown in Figure 6.48 and Figure 6.49 respectively. These poles and their amplitudes are plotted alongside with the poles of human LTR (as shown in Figure 6.30) and the poles of experimental sphere LTR (as shown in Figure 6.25) and their amplitudes (as shown in Figure 6.31 and Figure 6.26) respectively.

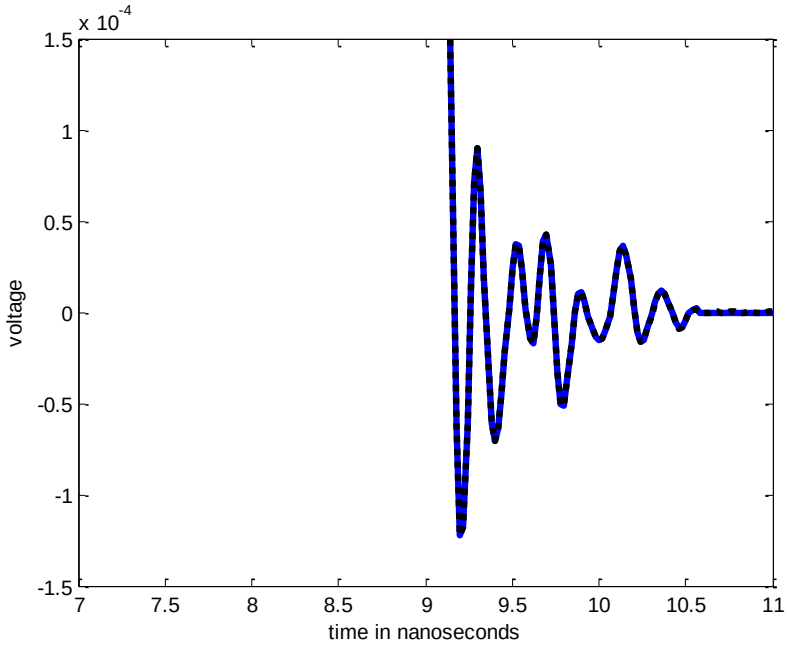

Figure 6.46: Human-sphere (back) (blue) LTR and reconstructed (black) LTR.

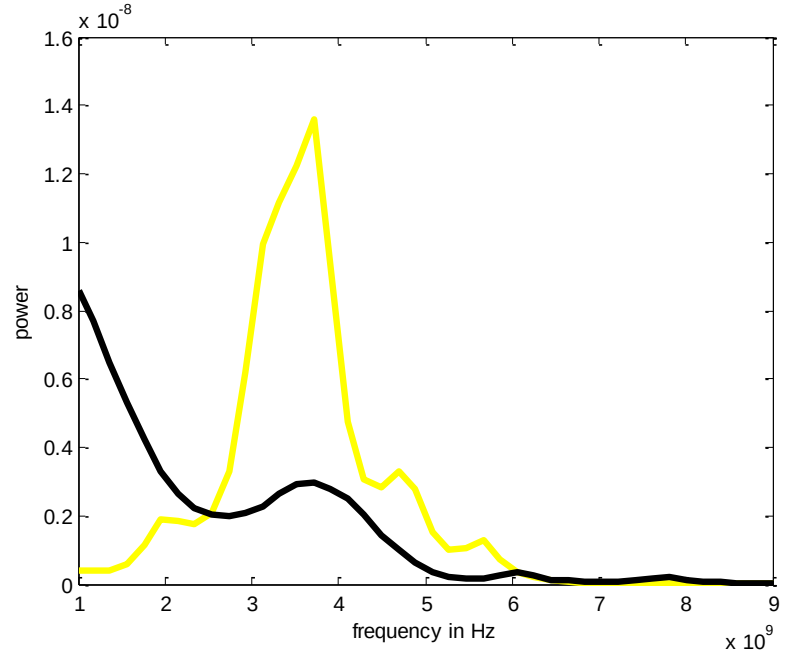

Figure 6.47: PSD of human-sphere (back) (black)LTR, PSD of human (yellow) LTR.

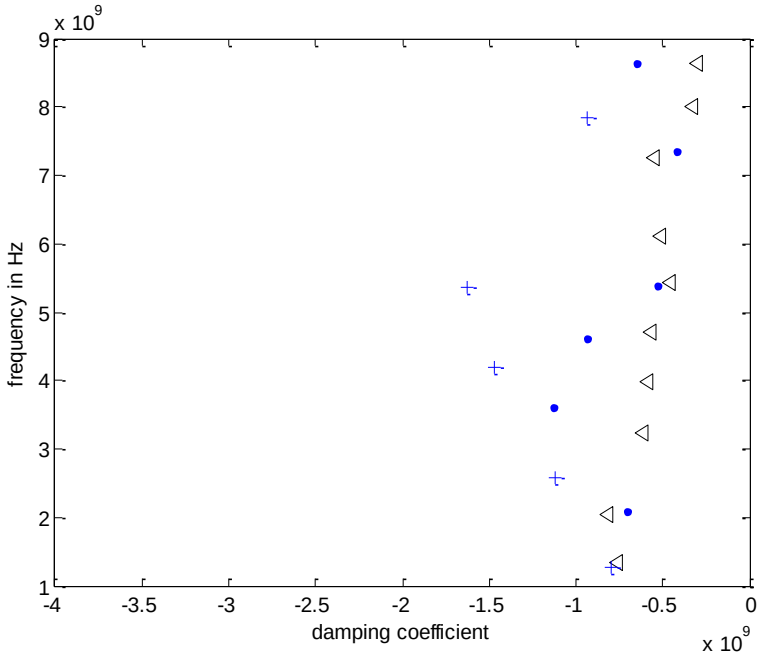

Figure 6.48: Comparison of poles.
(blue +) Poles of sphere experimental LTR
(blue .) Poles of human LTR
(black <) Poles of human with sphere (back) LTR

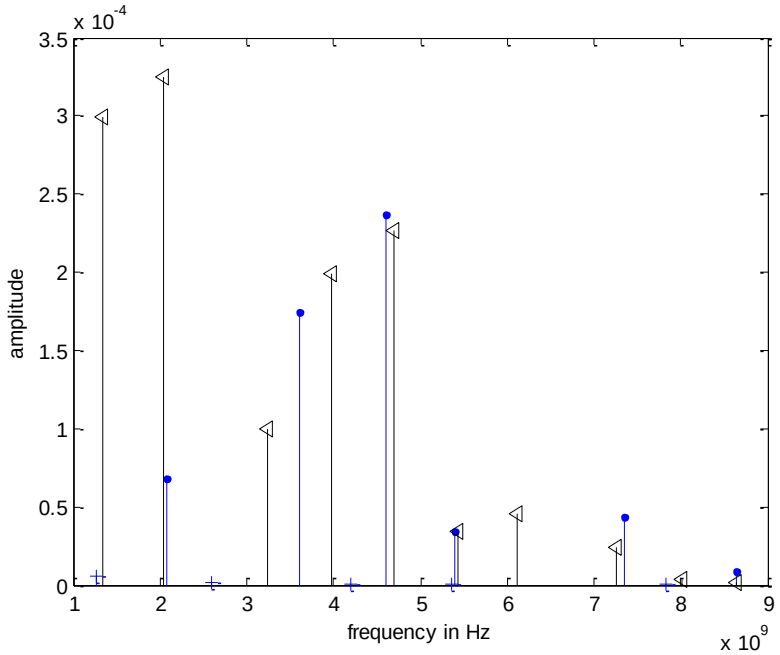

Figure 6.49: All amplitudes of the poles.
(blue +) Amplitudes of sphere experimental LTR
(blue .) Amplitudes of human LTR
(black <) Amplitudes of human with sphere (back) LTR

Similar to the two different positions of the hidden sphere as presented above, by observation of Figure 6.47, it is shown that the critical power levels of the PSD of the human-sphere (back) LTR appear in the 1-5.5 GHz band. Thus the existence of the sphere creates a wide band. Furthermore the PSD of the human-sphere (back) LTR has the highest peak location at 1 GHz frequency, which is close to the peak of the PSD (Figure 6.24) of the sphere experimental LTR located at around 1.3 GHz frequency. Conversely as it has been mentioned the critical power levels of the PSD of the human LTR exist in the 2-5.5 GHz band while the highest peak of the PSD is at around 3.8 GHz. This indicates that the sphere affects the overall response therefore the detection of the sphere appended to the back of the human is possible.

Comparison of the human poles with the human-sphere composite object poles in Figure 6.48 shows that the clustering of the human LTR poles is different to the number and the clustering of the human-sphere LTR poles and a pole located at 1.3 GHz can be retrieved. This pole is related to the principal pole of the 0.0325m radius sphere LTR. This is caused by the existence of the body-appended sphere. Additionally there is amplitude modulation at the respective poles as shown in Figure 6.49. This difference in clustering and the amplitude modulation due to the existence of sphere signify that the detection of the sphere attached to the back of the human is feasible. Similar to the case of the human-sphere (in front), some issues for further consideration arise. One issue is the establishment of the robustness of the sphere detection to subject movement and measurement conditions. The second issue to address is whether the approximated grenade or sphere and other CWEs could be identified on the human.

6.6 Discussion of Results

In this chapter the theoretical and experimental methodology for the detection of a concealed weapon (CWE) has been presented. The choice of CWE is the grenade as the weapon utilised by terrorists as it is easy to carry and easy to hide. At this stage of the research the hidden weapon has been approximated by a sphere, which is a rational choice as the shape of the grenade naturally resembles to the shape of the sphere. The CWE detection is based on the observation and analysis of the LTR of the backscattered signal from the UWB Radar. The LTR is analysed using the well documented and highly used MUSIC and SVD-Prony algorithms for signal processing that respectively produce the object's PSD and the poles and their amplitudes. Observation of the IRs of Figures 6.27, 6.35, 6.40, 6.45 and LTRs of Figures 6.28, 6.36, 6.41, 6.46 shows that both the presence and the position of the sphere affects the shapes of the time domain responses. Observation of the PSDs of Figures 6.29, 6.37, 6.42. 6.47 shows that whenever the sphere is present the highest peak of the PSD is located in the 1-2 GHz frequency interval and the more critical power levels start appearing closer to the 1 GHz band limit. This behaviour is in accordance with the peak of the PSD (Figure 6.24) of the sphere experimental LTR which is located at the 1.3 GHz frequency. On the contrary as it has been mentioned the critical power levels of the PSD of human LTR exist in the 2-5.5 GHz band while the PSD of human LTR has the highest peak at around 3.8 GHz.

Comparison of human poles with the human-sphere composite object poles in Figures 6.38, 6.43 and 6.48 shows that the clustering of the human LTR poles is different to the clustering of the human-sphere LTR poles. Furthermore from the human-sphere poles in Figures 6.38, 6.43 and 6.48 the existence of a pole at 1.3 GHz frequency is

observed. This specific pole is associated with the principal pole of the sphere experimental LTR which is located at the frequency of 1.3 GHz. Additionally in Figures 6.39, 6.44, 6.49 there is amplitude modulation at the respective poles. Moreover there is modulation of the amplitudes of the principal pole due to the position of the sphere on the human. So the location of the sphere on the human affects the human-sphere LTR. This difference in clustering of the poles, the amplitude modulation of the poles, the resonant pole at 1.3 GHz, and the observations from the PSDs due to the existence of the sphere, is the information resulting from two autonomous methods i.e. MUSIC and SVD – Prony. This information signifies that the sphere influences the overall human-sphere reflection and that the detection of the sphere attached to either the front, the side, or to the back of the human is realised. Another issue for further consideration that arises is whether there is sufficient separability in the various sphere positions that would yield the determination of the location of the sphere on the human. This issue can be addressed if the human-sphere pole that is related to the sphere principal pole shows specific characteristics like particular amplitude for specific position of sphere on the human. Additionally the robustness of this statement for repeated measurements must be verified.

6.7 Conclusions

In this chapter the detection of a 0.0325 m radius sphere appended on the human was confirmed. Three positions of the sphere were taken into account: front of human, side of human, back (behind) of human. The detection was achieved by the comparison of the information of the human resonant frequencies with the information of the human-sphere composite object resonant frequencies. From the MDL results it is observed that

composite objects i.e. human-sphere involve a larger number of poles or higher model order than simple objects i.e. human in order to correctly model the objects. Additionally, the resemblance in frequency of the sphere principal pole with the pole of lowest frequency of human-sphere composite target was confirmed.

Hence, through the existence of the sphere LTR principal pole in the human-sphere reflection the effect of the sphere on the overall human-sphere reflection is established. In this way the sphere is detected.

Chapter 7

DISCUSSION of RESULTS and CONCLUSIONS

7.1 Discussion of Results

In this Thesis a thorough study of the detection of a concealed weapon or explosive (CWE) on a human's body using LTR analysis in UWB radar has been presented using theoretical analysis, theoretical modeling and real laboratory experimentation. The main contribution of this work is the research on the concept of the LTR analysis for remote detection of human body-worn concealed weapons and explosives (CWEs). As it is discussed in the introduction of the Thesis in chapter 1 other hidden object detection solutions have already being considered such as millimetre wave sensors and imaging sensors. The most critical weaknesses of these solutions are the relatively short distances in which these sensors operate, since the scanned object must be within the focal plane of the sensor; the long scanning time period needed for these sensors; and the vulnerability of some sensors to weather or other environmental conditions. Hence the UWB radar approach fills the gap for the study of detection sensors able to robustly operate at extended stand-off distances and under harsh weather conditions. Such an approach could be used as a standalone system or as a part of a hybrid system that includes two or more CWE detection solutions for better data fusion. In this way success in the detection of CWEs that can potentially cause a threat when used for terrorist and malicious attacks can be achieved.

As it is presented in chapter 1, on the problem statement and methodology section, the first issue for consideration in any radar design is the selection of the appropriate waveform that will be transmitted, since the radar performance is essentially dependent upon the transmitted waveform. So in chapter 2, where the fundamental radar

properties are presented, the pulse radar is analyzed and its basic principles related are defined. Additionally the various methods are also presented in order to maintain a high average power and adequate range resolution for a specific transmitter output peak power. These methods that are also referred as pulse compression techniques are, phase modulation of pulse, frequency modulation of pulse and frequency stepped pulse compression. Considering all these methods the frequency stepped pulse compression is selected for use in the transmitted waveform. In this method the range resolution depends on the number of frequency steps considered and therefore by arranging the number of frequency steps the appropriate range resolution for the radar application is selected. For any specific object, adjusting the specific range resolution the pulse radar can create the object's radar image since the overall reflected field from the illuminated complex object depends on the spatial relationship among all reflectors of which the composite object consists. Therefore the range resolution is very important for detection or recognition applications of pulse radar.

Apart from the adjustment of the range resolution the method of frequency stepping is used in order to create the UWB pulse. If frequency steeping is considered, as the number of frequency steps of the transmitted signal increases, the frequency spectrum or bandwidth of the pulse waveform becomes wider until it theoretically reaches the frequency spectrum of an impulse. Therefore frequency stepped pulse compression leaded us into the transmission of a UWB pulse depending on the utilised signal fractional bandwidth as explained in the UWB radar fundamentals in chapter 2.

Since the settings of the UWB radar functional frequency bands are individual for each specific target for detection, in chapter 2 an attempt is made to derive the resonant

frequency bands of the radar operation for the weapons that were considered for detection. Among all the considered weapons, the grenade detection is the most difficult task, due to the grenade smaller size and therefore smaller reflected field amplitude. Additionally the grenade is the most probable weapon to be carried by a terrorist due to its small size and destruction capabilities. Therefore the research for weapon detection is focused on the grenade.

In order to derive the grenade resonant frequency band, the grenade is approximated as a conducting sphere of 0.0325 m radius since the sphere and the grenade have similar shapes and most importantly since the conducting sphere is one of the objects whose reflected field or Impulse Response (IR) is theoretically known. In the following chapters it is straightforward to obtain the expected theoretical impulse response of the approximated grenade or sphere and compare it with the experimental response acquired from the laboratory experiments.

From the Radar Cross Section (RCS) of the sphere in chapter 2 it is known that the sphere first resonant frequency is located at 1.46 GHz. Consequently in the following chapters the reflected field from the sphere is theoretically obtained at the 0.7-6.7 GHz band or at the 0.7-12 GHz band depending on the number of resonant frequencies that are considered. Furthermore the laboratory experiments are performed in the 0.7 -6.7 or 1-9 GHz band for the Vivaldi and the Horn antennas respectively. These measurement bands depend on the required bandwidth of the measurement which influences the range resolution needed and the frequency response of the antennas used. For example the minimum limit of the band for the horn antennas is 1 GHz. In the case of the 0.7 -6.7 GHz band the fractional bandwidth is equal to 1.62 and in the case of the 0.7-12 GHz

band the fractional bandwidth is equal to 1.78, while for the 1-9 GHz band the fractional bandwidth is equal to 1.6. So the reflected fields in all cases are classified as UWB signals. Finally in order to acquire the response of the illuminated object, the UWB radar's antennas frequency response that is used for experimental purposes is investigated in chapter 2. As it is shown the antennas that are used to transmit the UWB pulse and receive the reflected field from the illuminated object should have a flat frequency response between the frequency limits of the band.

Having established the required UWB radar characteristics the next fundamental issue for investigation, as it is presented in the methodology section in chapter 1, is the appreciation of how the natural resonant frequencies are involved in the reflected signal of the object. As it is shown in chapter 3 the role of the resonant frequencies can be realised if the backscattered field from the object is considered in the time domain which is equivalent to the acquisition of the object's IR. Most importantly it is presented in chapter 3 that the time invariant parameters of the delayed part of the impulse response i.e. Late Time Response (LTR), which are the natural resonant frequencies, and which are only dependent on the object's particular geometry, dimensions, and its electrical properties, will facilitate the detection of the hidden object. This is the fundamental principle that research in this Thesis is based and it is used to extract a unique signature for the object and therefore detect the object.

Another issue for research as presented in chapter 1 is the means of extraction of the resonant frequencies from the response of the considered object as the essential process for the object's detection. In order to extract the resonant frequencies from the considered object response, in chapter 4 the theoretical backscattered far field of the

sphere was considered since the sphere is one of the few objects whose reflected field can be theoretically obtained. Knowledge and expansion of the backscattered field of the sphere in terms of singularities yields the derivation of the theoretical IR of the sphere. Furthermore a computer simulation algorithm is developed and programmed which produces the IR. The outcome of the computer simulation is the theoretical IR of the sphere. For the obtained IR, algorithms for signal modelling are applied on the LTR in order to extract the poles of the sphere simulated LTR and their residues.

Since the numerically extracted poles coincided with the most important sphere poles obtained via analytical solution, both in the 0.7-6.7 GHz band and the 0.7-12 GHz band, the algorithms for pole extraction were considered as trustworthy. Therefore these algorithms were applied as the basis for processing experimental IRs of composite objects for pole extraction, as it is presented at the remaining chapters of the Thesis.

Having established all the theoretical fundamentals for the hidden object detection via the UWB radar, research in Chapters 5 and 6 is focused on the actual laboratory experimentation and the signal processing methodology used for the detection of the concealed object. Initially the determination of the different parameters that are used for the processing of the measurements related to the experimental procedure is developed. The parameters were determined for 2 sets of measuring antennas, in chapter 5 the Vivaldi antennas in the 0.7-6.7 GHz frequency band and in chapter 6 the Horn antennas in the 1-9 GHz frequency band. The determination of the parameters was decided after comparison between the experimental sphere LTR poles and the theoretical sphere LTR poles and their amplitudes. These poles were extracted by means of the SVD-PRONY algorithm. In chapter 5 this comparison was accomplished for a sphere of

radius 0.024 m and a sphere of radius 0.0325 m. While in chapter 6 the comparison was performed for a sphere of 0.0325 m. In both chapters the poles clustering and general characteristics were similar for theoretical LTR resonant frequencies and experimental LTR resonant frequencies. In this way the experimental configuration and methodologies were tested and confirmed for the determined set of parameters. Since for these parameters the experimental results were in agreement with the theoretical results, these parameters were used for the processing of all experimental data throughout the experiment of each chapter.

The most important issue of the research was the execution of an experiment with the human and the sphere as a composite target. As the sphere has much smaller dimensions than the human the reflection from the sphere is much smaller than the human's reflection. Therefore the sphere detection was performed via comparison of the qualitative information of the human-sphere resonant frequencies with the information of the resonant frequencies of the human. As this investigation occurs at the resonant frequencies of the sphere reflected field, conclusion can be drawn on the effect of the sphere on the overall human-sphere complex target reflection. In chapter 5 the human was approximated as a 50 cm x 40 cm conducting metal sheet. Therefore the possibility of the detection of a 0.024 m radius sphere or a 0.0325 m radius sphere appended on the background of a much larger reflector was investigated. In chapter 6 the analogous investigation occurred for the detection of a 0.0325 m radius sphere appended on the human as the position of the sphere on the body was altered. Three positions of the sphere were taken into account: front of human, side of human, back (behind) of human. In chapter 5 analysis of LTR was realised by extracting the LTR poles and amplitudes.

The extraction was completed through the SVD-PRONY algorithm. In chapter 6 apart from the pole amplitudes extraction the Power Spectral Density (PSD) was obtained by means of the MUltiple SIgnal Classification (MUSIC) algorithm. In this way the outcome of the two independent algorithms is evaluated.

Comparison of simple objects poles i.e. reflector or human poles with composite objects poles i.e. reflector–sphere or human-sphere poles in Chapters 5 and 6 respectively, showed that the clustering of the reflector or human LTR poles is different to the clustering of the reflector-sphere or human-sphere LTR poles. In addition the existence of a pole at specifically: 1.2 GHz frequency is observed in the reflector-0.0325 m radius sphere LTR poles and 1.3 GHz frequency is observed in the human-0.0325 m radius sphere LTR poles. This pole is mainly related to the principal pole of the 0.0325 m radius sphere experimental LTR which is located at the frequency of 1.3 GHz. A similar observation is made for a 0.024 m radius sphere in chapter 5. Additionally there is amplitude modulation at the respective poles when the sphere is present.

Finally from the MUSIC algorithm in chapter 6 the existence of the sphere results in the highest peak of the PSD of each LTR being located in the 1-2 GHz frequency interval and the critical power levels emerge closer to the 1 GHz band limit. This result is in agreement with the peak of the PSD of the sphere experimental LTR which is located at the 1.3 GHz frequency. In contrast as it was shown in chapter 6 the critical power levels of the PSD of the human LTR are resident in the 2-5.5 GHz band while the PSD of the human LTR has the highest peak at approximately 3.8 GHz. All the conclusions drawn from the two autonomous methods i.e. MUSIC and SVD – PRONY about the

influence of the sphere on the overall human-sphere reflection, signified that the detection of the sphere attached to the reflector or the human is feasible.

7.2 Conclusions

This Thesis presented the feasibility of CWE detection using UWB radar via analysis of the LTR of the target. The appropriate radar waveform was synthesized with the aim of exciting the resonant frequencies of the CWE. So the consideration of resonant frequencies of the CWE yields the frequency band of the transmitted waveform of the radar. In this research the grenade was considered as the CWE as it is a weapon that could be easily used during a terrorist attack. Throughout the thesis, the grenade was approximated as a conducting sphere of 0.0325 m radius since the sphere and the grenade have similar shapes and since the resonant frequencies and IR of sphere are theoretically known. So the detection of sphere is the basic objective that the work in the Thesis was focused.

The resonant frequencies extraction from the LTR was accomplished. A specific signal modelling algorithm was deployed so as to extract the resonant frequencies from the LTR of the considered object. This is an essential process for the object's detection. The algorithm for pole-amplitude extraction was validated through comparison of the numerical extraction of the simulated LTR poles with the analytical solution for the poles of the conducting sphere. Consequently this algorithm was used for the processing of the considered objects' LTRs which were experimentally obtained.

Subsequently, obtaining the objects' experimental IRs was achieved. So the appropriate experimental configuration and methodologies were deployed in order to

obtain the IRs of the objects of interest. The experimental methodology was validated through the IR of sphere. First the experimental IR of sphere was obtained, next through comparison of the experimental LTR and theoretical LTR of sphere the experimental procedure was verified. The association between the two LTRs was accomplished through comparison between the experimental sphere LTR poles and the theoretical sphere LTR poles and their amplitudes. This comparison demonstrated that the respective quantities (poles-amplitudes) were in accordance for specific parameters used for processing the measured frequency domain responses.

Detection of a sphere attached to the background of a much larger reflector was investigated and confirmed. This detection was verified for two spheres of different radius: specifically a 0.024 m radius sphere and a 0.0325 m radius sphere. The pole-amplitude extraction algorithms were utilized. The sphere detection was performed via comparison of the information related to the reflector-sphere resonant frequencies with the information of the resonant frequencies of the reflector. The resemblance in frequency of the sphere principal pole with the pole of lowest frequency of reflector-sphere complex target showed that the sphere can be discerned from the reflector-sphere complex target. Hence the reflector-attached sphere detection is achieved

The analogous case of detection of a 0.0325 m radius sphere appended on the human was also confirmed. In order to investigate the detection for the various positions that the CWE could be appended on the human body, three positions of the sphere were taken into account: front of human, side of human, back (behind) of human. Hence the effect of the sphere on the overall human-sphere reflection was verified with the use of two independent methods that modelled the LTRs of human and human-CWE object.

The first method extracts the LTR poles and amplitudes while the other estimates the frequency spectrum. These methods yielded the comparison of the information of the human resonant frequencies with the information of the human-sphere composite object resonant frequencies. From the comparison, the similarity in frequency of the sphere principal pole with the pole of lowest frequency of human-sphere composite target was confirmed. Hence the existence of the sphere LTR principal pole in the human-sphere reflection was demonstrated. In this way it is concluded that the body-worn sphere LTR is not overwhelmed by the human reflection and it affects the human-sphere reflection. Thus the detection of the human-attached sphere can be achieved.

Additionally composite objects i.e. reflector- sphere or human-sphere depicted a higher requirement in terms of number of LTR poles or model order than simple targets i.e. reflector or human in order to be model each LTR. This was concluded from observations of the MDL results. This reinforces the previous conclusion that body-worn sphere LTR has an important effect on the human-sphere reflection.

7.3 Suggestions for Future Work and Self Critique

During the development of the work discussed in this thesis, several questions and ideas of possible further study and future research have been raised. These ideas constitute the missing research milestones in order to characterise the proposed method of the Thesis as a generalised method for automatic CWE detection. A generalised method for CWE detection should consider all possible detection scenarios with a variety of weapons concealed on a variety of body types. The ideas considered for

further study were not addressed, as the core objective of this research was to resolve the differences in the LTR of a human with and without a sphere. From these differences it was realised that the sphere has an important effect on the overall human-sphere reflection, hence detection of the body-worn sphere can be attained under the experimental conditions presented in chapters 5 and 6. This statement is supported from the conclusions of sections 5.7, 6.7 and 7.2. Consequently, having reached this fundamental milestone, for the continuation of the research for CWE detection, the following significant ideas are considered.

The first of these ideas considers that, as it was stated in chapter 6 during the development of the experimental work the human retained a single placement throughout the experiment and remained motionless. Therefore there is a requirement of further experimentation of multiple measurements from multiple different placements of the human body inside the anechoic chamber. It would be of great interest to acquire a greater span of data and the extracted resonant frequencies of the experimental LTRs of human-CWE complex objects regarding different stances and orientation with respect to the UWB radar. Additionally the range of experimental scenarios could naturally be expanded to include people of different age, shape and heights as the human subject. In case that the poles of the human-CWE object that are closely related to the signature poles of CWE would remain the same or would be located within certain bounds; such an approach would guarantee the repeatability of detection. Additionally the robustness of the proposed method for the CWE detection to measurement conditions and subject movement would be confirmed. Such research

would be inherently easier using as a framework the work presented in this Thesis that the sphere appended on the various positions on the human body can be detected.

Moreover it would also be of great interest to test for a variety of CWEs that could potentially be used from terrorists during an attack. Such weapons include the pistols, Uzi and riffle also considered in chapter 2. Such CWEs have a different shape than the grenade studied in this Thesis hence they would have different signature poles. This assumption should be verified with the experimental procedure. It would be very important to evaluate with experimental procedure if signature poles for the CWE appended on the human body can be extracted from the human-CWE composite object LTR. In case a robust conclusion could be reached about the signature poles of the different CWEs, identification and classification of grenade and different CWEs appended on the human body could be established. Additionally the case of detection of multiple CWEs appended on the body should be considered. Moreover whether the determination of the location of the CWE on the human is possible should be investigated. In case that sufficient separability would exist in the amplitudes of the poles for the various CWE positions then the location of the sphere on the human could be determined. Furthermore it is important that the detection method is automated in producing an algorithmic measure of similarity between measured and signature CWE poles. This could be realised by introducing a normalised distance vector for the respective poles of interest. Hence the distance vector could be a measure of similarity between measured and signature CWE poles.

Finally the detection method could be automated in terms of finding the ETR/LTR boundary. As it was shown both theoretically and experimentally, the LTR

is a series of damped sinusoids. The MUSIC algorithm is used for processing both damped and undamped sinusoids. Therefore consideration and processing of different time segments of unknown object IR with the MUSIC and root MUSIC [98] algorithm can determine the nature of the time segment i.e. whether the segment is made of damped or undamped sinusoids and extract the frequency information. The segment of IR which will be made of damped sinusoids is the LTR that can be analysed with the methods that are shown in this Thesis.

APPENDIX Chapter 2

2.a Theoretical Background of Frequency Stepping

This section provides the theoretical proof of how a periodic signal $k_p[n\Delta t]$ with period τ_T yields a frequency domain spectrum $K_p(e^{j\omega})$ which is discrete (frequency stepped), and describes the relation between the period τ_T and the frequency step Δf .

Consider a finite length signal $k[n\Delta t]$, that has been sampled with the time spacing $\Delta t = \frac{1}{f_s}$. $k[n\Delta t]$ is nonzero for $0 \le n \le N-1$ and $k[n\Delta t] = 0$ otherwise.

If $k[n\Delta t]$ is convolved with the periodic impulse train $l_p[n\Delta t] = \sum_{r_1=-\infty}^{\infty} \delta[n\Delta t - r_1 N\Delta t]$,

where $\delta[n\Delta t]$ is the discrete impulse or Dirac function then

$$k_p[n\Delta t] = k[n\Delta t] \otimes \sum_{r_1=-\infty}^{\infty} \delta[n\Delta t - r_1 N\Delta t] = \sum_{r_1=-\infty}^{\infty} k[n\Delta t - r_1 N\Delta t] \qquad (2.a.1)$$

$k_p[n\Delta t]$ is periodic and consists of a set of periodically repeated replicas of the finite length sequence $k[n\Delta t]$ and the period is $\tau_T = N\Delta t$. Therefore

$$k[n\Delta t] = \begin{cases} k_p[n\Delta t] & 0 \le n \le N-1 \\ 0 & n < 0, n > N-1 \end{cases} \qquad (2.a.2)$$

If the Discrete Time Fourier Transform (DTFT) of $k[n\Delta t]$ is $K(e^{j\omega})$

$$K(e^{j\omega}) = \sum_{n=0}^{N-1} k[n\Delta t] e^{-j\omega n\Delta t} \qquad (2.a.3)$$

and the DTFT of $l_p[n\Delta t]$ is $L_p(e^{j\omega}) = \sum_{r_2=-\infty}^{\infty} \frac{2\pi}{N\Delta t} \delta\left(\omega - \frac{2\pi r_2}{N\Delta t}\right)$ [38], then the DTFT of $k_p[n\Delta t]$ which is $K_p(e^{j\omega})$ is equal to

$$K_p(e^{j\omega}) = K(e^{j\omega}) L_p(e^{j\omega})$$

$$K_p\left(e^{j\omega}\right)= K\left(e^{j\omega}\right)\sum_{r_2=-\infty}^{\infty}\frac{2\pi}{N\Delta t}\delta\left(\omega-\frac{2\pi r_2}{N\Delta t}\right)$$

$$K_p\left(e^{j\omega}\right)= \sum_{r_2=-\infty}^{\infty}\frac{2\pi}{N\Delta t}K\left(e^{j\left(\frac{2\pi}{N\Delta t}\right)r_2}\right)\delta\left(\omega-\frac{2\pi r_2}{N\Delta t}\right) \quad (2.a.4)$$

Equation (2.a.4) shows that $K_p\left(e^{j\omega}\right)$ is periodic. If $K_p\left(e^{j\omega}\right)$ is considered in the interval between $\omega=0$ and $\omega=\omega_s=\frac{2\pi}{\Delta t}=2\pi f_s$, which is one period in the frequency domain, then the corresponding values for r_2 are $r_2=0,1,...,N-1$ therefore

$$K_p\left(e^{j\omega}\right)= \sum_{r_2=0}^{N-1}\frac{2\pi}{N\Delta t}K\left(e^{j\left(\frac{2\pi}{N\Delta t}\right)r_2}\right)\delta\left(\omega-\frac{2\pi r_2}{N\Delta t}\right) \quad (2.a.5)$$

Equation (2.a.4 or 2.a.5) means that $K_p\left(e^{j\omega}\right)= K\left(e^{j\left(\frac{2\pi}{N\Delta t}\right)r_2}\right)= K\left(e^{j\omega}\right)$ when $\omega=\frac{2\pi}{N\Delta t}r_2$.

Consequently $K_p\left(e^{j\omega}\right)$ can be obtained by sampling $K\left(e^{j\omega}\right)$ at N equally spaced frequencies between $\omega=0$ and $\omega=\omega_s=\frac{2\pi}{\Delta t}=2\pi f_s$ with frequency spacing or step

$$\Delta\omega=\frac{2\pi}{N\Delta t} \quad (2.a.6)$$

$$\text{or } \Delta f=\frac{1}{N\Delta t}=\frac{1}{\tau_T}=\frac{f_s}{N} \quad (2.a.7)$$

If $K_p\left(e^{j\omega}\right)=\sum_{n=0}^{N-1}k_p\left[n\Delta t\right]e^{-j\omega n\Delta t}$ is the Discrete Fourier Series (DFS) [38] for $k_p\left[n\Delta t\right]$ in the interval $0\le n\le N-1$, considering equation (2.a2) and (2.a.3)

$$K\left(e^{j\omega}\right)=\sum_{n=0}^{N-1}k\left[n\Delta t\right]e^{-j\omega n\Delta t}=\sum_{n=0}^{N-1}k_p\left[n\Delta t\right]e^{-j\omega n\Delta t}=K_p\left(e^{j\omega}\right)=K\left(e^{j\left(\frac{2\pi}{N\Delta t}\right)r_2}\right) \quad (2.a.8)$$

For $\omega = \frac{2\pi}{N\Delta t} r_2$, equation (2.a.8) gives rise to the Discrete Fourier Transform (DFT) [41]

$K_p\left(e^{j\omega}\right) = \sum_{n=0}^{N-1} k_p[n\Delta t] e^{-j\frac{2\pi r_2}{N\Delta t} n\Delta t}$ by cancellation of Δt the DFT is given by

$$K_p\left(e^{j\omega}\right) = \sum_{n=0}^{N-1} k_p[n\Delta t] e^{-j\frac{2\pi r_2}{N} n} \tag{2.a.9}$$

Therefore a frequency domain spectrum $K_p\left(e^{j\omega}\right)$ which is frequency stepped or sampled, yields a time domain signal $k_p[n\Delta t]$ which is periodic. The periodicity in the time domain is due to the fact that, the sampling or multiplication in the frequency domain is equivalent to convolution in the time domain. In this way from equation 2.a.7 the frequency step is defined as $\Delta f = \frac{1}{\tau_T}$ where τ_T is the period of $k_p[n\Delta t]$.

2.b Frequency Stepping in Relation with Carrier Signal

This section shows that the frequency domain shift or delay of $K_p\left(e^{j\omega}\right)$ by a frequency ω_{ca} is equivalent to the modulation of $k_p[n\Delta t]$ with the carrier signal $\cos(\omega_{ca} n\Delta t)$.

Supposing $K_p\left(e^{j\omega}\right)$ is the Discrete Fourier Transform (DFT) of $k_p[n\Delta t]$ and from equation (2.a.9) of the appendix for variable $\omega = \frac{2\pi}{N\Delta t} r_2$

$$K_p\left(e^{j\omega}\right) = \sum_{n=0}^{N-1} k_p[n\Delta t] e^{-j\frac{2\pi r_2}{N} n} \tag{2.b.1}$$

If $k_p[n\Delta t]$ is a real signal then its DFT can be written as

$$K_p(e^{j\omega}) = \frac{1}{2}K_p(e^{j\omega}) + \frac{1}{2}K_p{}^*(e^{-j\omega}) \qquad (2.b.2)$$

Considering the case of Figure 2.29 where the frequency spectrum is delayed by a frequency $\omega_{ca} = \frac{2\pi}{N\Delta t} r_{ca}$, then the spectrum is given by

$$K_{mp}(e^{j(\omega)}) = K_p(e^{j(\omega-\omega_{ca})}) = \frac{1}{2}K_p(e^{j(\omega-\omega_{ca})}) + \frac{1}{2}K_p{}^*(e^{-j(\omega-\omega_{ca})}) \qquad (2.b.3)$$

Taking the Inverse Discrete Fourier Transform (IDFT) of $K_{mp}(e^{j(\omega)})$ yields

$$k_{mp}[n\Delta t] = \frac{1}{2}k_p[n\Delta t]e^{j(\omega_{ca})n\Delta t} + \frac{1}{2}k_p[n\Delta t]e^{j(-\omega_{ca})n\Delta t} \qquad (2.b.4)$$

therefore $$k_{mp}[n\Delta t] = k_p[n\Delta t]\cos(\omega_{ca} n\Delta t) \qquad (2.b.5)$$

since $$\cos(\omega_{ca} n\Delta t) = \frac{1}{2}e^{j(\omega_{ca})n\Delta t} + \frac{1}{2}e^{j(-\omega_{ca})n\Delta t} \qquad (2.b.6)$$

Therefore the pulse $k_p[n\Delta t]$ is modulated with the carrier signal $\cos(\omega_{ca} n\Delta t)$.

APPENDIX Chapter 3

3.a Laplace Transform of LTR Theoretical Derivation

This section provides the theoretical proof of the Laplace Transform (LT) of the LTR. Considering equation (3.10)

$$\overline{h}_{LTR}(t) = u(t - T_L)\sum_{i=1}^{\frac{I}{2}} \frac{R_i}{2}\left[e^{s_i t}e^{j\phi_i} + e^{s_i^* t}e^{-j\phi_i}\right] \tag{3.a.1}$$

Obtaining the LT of (3.a.1) yields

$$\overline{H}_{LTR}(s) = \text{LT}\left[\overline{h}_{LTR}(t)\right] = \int_0^{\infty}\left[u(t - T_L)\sum_{i=1}^{\frac{I}{2}} \frac{R_i}{2}\left[e^{s_i t}e^{j\phi_i} + e^{s_i^* t}e^{-j\phi_i}\right]\right]e^{-st}dt \tag{3.a.2}$$

$$\overline{H}_{LTR}(s) = \sum_{i=1}^{\frac{I}{2}} \frac{R_i}{2} e^{j\phi_i}\int_0^{\infty}\left[u(t - T_L)e^{s_i t}\right]e^{-st}dt + \sum_{i=1}^{\frac{I}{2}} \frac{R_i}{2} e^{-j\phi_i}\int_0^{\infty}\left[u(t - T_L)e^{s_i^* t}\right]e^{-st}dt \tag{3.a.3}$$

Suppose the integral is calculated

$$\int_0^{\infty}\left[u(t - T_L)e^{s_i t}\right]e^{-st}dt$$

With a change of variable the integral will become

$\tau = t - T_L \qquad t = \tau + T_L$

$$\int_0^{\infty} u(t - T_L)e^{s_i t}e^{-st}dt = \int_{-T_L}^{\infty} u(\tau)e^{s_i(\tau + T_L)}e^{-s(\tau + T_L)}d\tau$$

Since the unit step function $u(\tau) = 1$ for $\tau > 0$, which shows causality

$$\int_{-T_L}^{\infty} u(\tau)e^{s_i(\tau + T_L)}e^{-s(\tau + T_L)}d\tau = \int_0^{\infty} u(\tau)e^{s_i(\tau + T_L)}e^{-s(\tau + T_L)}d\tau = \int_0^{\infty} e^{s_i(\tau + T_L)}e^{-s(\tau + T_L)}d\tau$$

And can be written as $\int_0^{\infty} e^{-(s - s_i)(\tau + T_L)}d\tau$

Therefore $\int_0^\infty e^{-(s-s_i)(\tau+T_L)}d\tau = e^{-(s-s_i)(T_L)}\int_0^\infty e^{-(s-s_i)(\tau)}d\tau$

Evaluation of the integral yields $e^{-(s-s_i)(T_L)}\int_0^\infty e^{-(s-s_i)(\tau)}d\tau = e^{-(s-s_i)(T_L)}\frac{1}{s-s_i}$

Therefore from (3.a.3)

$$\sum_{i=1}^{\frac{I}{2}} \frac{R_i}{2} e^{j\phi_i} \int_0^\infty \left[u(t-T_L)e^{s_i t}\right]e^{-st}dt = e^{-(s-s_i)(T_L)}\sum_{i=1}^{\frac{I}{2}} \frac{R_i}{2} e^{j\phi_i}\frac{1}{s-s_i} \qquad (3.a.4)$$

And in the same way

$$\sum_{i=1}^{\frac{I}{2}} \frac{R_i}{2} e^{-j\phi_i} \int_0^\infty \left[u(t-T_L)e^{s_i^* t}\right]e^{-st}dt = e^{-(s-s_i^*)(T_L)}\sum_{i=1}^{\frac{I}{2}} \frac{R_i}{2} e^{-j\phi_i}\frac{1}{s-s_i^*} \qquad (3.a.5)$$

So from (3.a.3) (3.a.4) (3.a.5)

$$\overline{H}_{LTR}(s) = \int_0^\infty \left[u(t-T_L)\sum_{i=1}^{\frac{I}{2}} \frac{R_i}{2}\left[e^{s_i t}e^{j\phi_i} + e^{s_i^* t}e^{-j\phi_i}\right]\right]e^{-st}dt =$$

$$\overline{H}_{LTR}(s) = e^{-(s-s_i)(T_L)}\sum_{i=1}^{\frac{I}{2}} \frac{R_i}{2} e^{j\phi_i}\frac{1}{s-s_i} + e^{-(s-s_i^*)(T_L)}\sum_{i=1}^{\frac{I}{2}} \frac{R_i}{2} e^{-j\phi_i}\frac{1}{s-s_i^*} \qquad (3.a.6)$$

APPENDIX Chapter 4

4.a Squared Error Minimisation

This part of the appendix describes how the squared error minimisation leads into the formation of the *covariance normal equations.*

If $h_e(n)$ is real, the minimisation of $E_p = \sum_{n=p}^{N}[e(n)]^2$ in equation (4.20) can be accomplished by solving $\frac{\partial E_p}{\partial a_p(i)} = 0$ for $i = 1,...,p$, which will yield the coefficients $a_p(i)$ of the poles of the signal $h_e(n)$.

If in equation (4.20), $e(n) = h_e(n) + \sum_{k=1}^{p} a_p(k) h_e(n-k)$ (4.a.1)

$$\frac{\partial E_p}{\partial a_p(i)} = \frac{\partial[e(n)^2]}{\partial a_p(i)} = \frac{\partial\left[\sum_{n=p}^{N}\left[h_e(n) + \sum_{k=1}^{p} a_p(k) h_e(n-k)\right]^2\right]}{\partial a_p(i)} = 0 \qquad (4.a.2) \Leftrightarrow$$

$$\frac{\partial E_p}{\partial a_p(i)} = 2\sum_{n=p}^{N}\left[\left[h_e(n) + \sum_{k=1}^{p} a_p(k) h_e(n-k)\right]\frac{\partial\left[h_e(n) + \sum_{k=1}^{p} a_p(k) h_e(n-k)\right]}{\partial a_p(i)}\right] = 0 \quad (4.a.3) \Leftrightarrow$$

since the partial derivative of $h_e(n) + \sum_{k=1}^{p} a_p(k) h_e(n-k)$ with respect to $a_p(i)$ is $h_e(n-i)$ equation (4.a.3) becomes

$$\frac{\partial E_p}{\partial a_p(i)} = 2\sum_{n=p}^{N}\left[\left[h_e(n) + \sum_{k=1}^{p} a_p(k) h_e(n-k)\right] h_e(n-i)\right] = 0 \text{ for } i = 1,...,p \qquad (4.a.4) \Leftrightarrow$$

or $$2\sum_{n=p}^{N}\left[\left[h_e(n) + \sum_{k=1}^{p} a_p(k) h_e(n-k)\right] h_e(n-i)\right] = 0 \text{ for } i = 1,...,p \qquad (4.a.5) \Leftrightarrow$$

$$\sum_{n=p}^{N}\left[\left[\sum_{k=1}^{p} a_p(k) h_e(n-k)\right] h_e(n-i)\right] = -\sum_{n=p}^{N}[h_e(n) h_e(n-i)] \text{ for } i = 1,...,p \qquad (4.a.6) \Leftrightarrow$$

$$\sum_{k=1}^{p} a_p(k)\left[\sum_{n=p}^{N}\left[h_e(n-k)h_e(n-i)\right]\right] = -\sum_{n=p}^{N}\left[h_e(n)h_e(n-i)\right] \text{ for } i=1,...,p \qquad (4.a.7) \Leftrightarrow$$

If $h_e(n)$ is complex, the minimisation of $E_p = \sum_{n=p}^{N}|e(n)|^2$ can be accomplished by solving

$\frac{\partial E_p}{\partial a_p^*(i)} = 0$ for $i=1,...,p$, which will yield the coefficients $a_p(i)$ of the poles of the signal $h_e(n)$.

$$\frac{\partial E_p}{\partial a_p^*(i)} = \sum_{n=p}^{N}\frac{\partial|e(n)|^2}{\partial a_p^*(i)} = \sum_{n=p}^{N}\frac{\partial\left[e(n)e^*(n)\right]}{\partial a_p^*(i)} = \sum_{n=p}^{N} e(n)\frac{\partial\left[e^*(n)\right]}{\partial a_p^*(i)} = 0 \text{ for } i=1,...,p \qquad (4.a.8)$$

since the partial derivative of $e^*(n)$ with respect to $a_p^*(i)$ is $h_e^*(n-i)$ equation (4.a.8) becomes

$$\sum_{n=p}^{N} e(n)h_e^*(n-i) = 0 \text{ for } i=1,...,p \qquad (4.a.9)$$

From equation (4.a.9) and (4.a.1)

$$\sum_{n=p}^{N}\left[\left[h_e(n)+\sum_{k=1}^{p}a_p(k)h_e(n-k)\right]h_e^*(n-i)\right] = 0 \qquad (4.a.10)$$

Or equivalently equation (4.a.10) becomes

$$\sum_{k=1}^{p} a_p(k)\left[\sum_{n=p}^{N}\left[h_e(n-k)h_e^*(n-i)\right]\right] = -\sum_{n=p}^{N}\left[h_e(n)h_e^*(n-i)\right], \text{ for } i=1,...,p \qquad (4.a.11)$$

If the definition is made that for real $h_e(n)$

$$r_{h_e h_e}(i,k) = \sum_{n=p}^{N} h_e(n-k)h_e(n-i) \qquad (4.a.12)$$

and for complex $h_e(n)$

$$r_{h_e h_e}(i,k) = \sum_{n=p}^{N} h_e(n-k) h_e^*(n-i) \qquad (4.a.13)$$

Considering equations (4.a.12) and (4.a.13), equations (4.a.7) and (4.a.11) are converted into

$$\sum_{k=1}^{p} a_p(k) r_{h_e h_e}(i,k) = -r_{h_e h_e}(i,0), \text{ for } i = 1,..., p \qquad (4.a.14)$$

Equation (4.a.14) is a collection of *p* linear equations with *p* unknowns which are the coefficients $a_p(1),\ldots, a_p(p)$, and they are also referred to as the *covariance normal equations*.

4.b Evaluation of the Minimum Modelling Squared Error

This part of the appendix estimates the minimum modelling squared error. Considering equations (4.a.5) and (4.a10) of the appendix, it can be realised that if $h_e(n)$ is real

$$\sum_{n=p}^{N} \left[\left[h_e(n) + \sum_{k=1}^{p} a_p(k) h_e(n-k) \right] h_e(n-i) \right] = 0 \text{ for } i = 1,..., p \qquad (4.a.15)$$

and if $h_e(n)$ is complex

$$\sum_{n=p}^{N} \left[\left[h_e(n) + \sum_{k=1}^{p} a_p(k) h_e(n-k) \right] h_e^*(n-i) \right] = 0 \text{ for } i = 1,..., p \qquad (4.a.16)$$

since $e(n) = h_e(n) + \sum_{k=1}^{p} a_p(k) h_e(n-k)$, then (4.a.15) and (4.a.16) can be respectively written as

$$\sum_{n=p}^{N}\left[e(n)h_e(n-i)\right]=0 \qquad \text{for } i=1,...,p \tag{4.a.17}$$

$$\text{or} \quad \sum_{n=p}^{N}\left[e(n)h_e^*(n-i)\right]=0 \qquad \text{for } i=1,...,p \tag{4.a.18}$$

if $\mathbf{e}_p$ is the column vector

$$\mathbf{e}_p=\left[e(p) \quad e(p+1) \quad . \quad . \quad . \quad e(N-1) \quad e(N)\right]^T \tag{4.a.19}$$

in terms of (4.38) and (4.a.19) equations (4.a.17) and (4.a.18) can be written as

$$\mathbf{X}_p^H\mathbf{e}_p=\mathbf{0} \tag{4.a.20}$$

which means that each row vector of $\mathbf{X}_p^H$ is orthogonal to $\mathbf{e}_p$

For real $h_e(n)$

$$E_p=\sum_{n=p}^{N}\left[e(n)\right]^2=\sum_{n=p}^{N}\left[e(n)\left[h_e(n)+\sum_{i=1}^{p}a_p(i)h_e(n-i)\right]\right]=$$

$$\sum_{n=p}^{N}\left[e(n)h_e(n)\right]+\sum_{n=p}^{N}\left[e(n)\sum_{i=1}^{p}a_p(i)h_e(n-i)\right] \tag{4.a.21}$$

For complex $h_e(n)$

$$E_p=\left|e(n)\right|^2=\sum_{n=p}^{N}\left[e(n)\left[h_e(n)+\sum_{i=1}^{p}a_p(i)h_e(n-i)\right]^*\right]=$$

$$\sum_{n=p}^{N}\left[e(n)h_e^*(n)\right]+\sum_{n=p}^{N}\left[e(n)\left[\sum_{i=1}^{p}a_p(i)h_e(n-i)\right]^*\right] \tag{4.a.22}$$

Equation $\sum_{n=p}^{N}\left[e(n)\sum_{i=1}^{p}a_p(i)h_e(n-i)\right]$, can be written as $\sum_{i=1}^{p}a_p(i)\sum_{n=p}^{N}\left[e(n)h_e(n-i)\right]$ however

from equation (4.a.17) $\sum_{n=p}^{N}\left[e(n)h_e(n-i)\right]=0$ for $i=1,...,p$ therefore

$$\sum_{n=p}^{N}\left[e(n)\sum_{i=1}^{p}a_p(i)h_e(n-i)\right]=\sum_{i=1}^{p}a_p(i)\sum_{n=p}^{N}\left[e(n)h_e(n-i)\right]=0 \qquad (4.a.23)$$

In the same way $\sum_{n=p}^{N}\left[e(n)\left[\sum_{i=1}^{p}a_p(i)h_e(n-i)\right]^*\right]$, can be written as $\sum_{i=1}^{p}a_p^*(i)\sum_{n=p}^{N}\left[e(n)h_e^*(n-i)\right]$,

however from equation (4.a.18) $\sum_{n=p}^{N}\left[e(n)h_e^*(n-i)\right]=0$ for $i=1,...,p$ therefore

$$\sum_{n=p}^{N}\left[e(n)\left[\sum_{i=1}^{p}a_p(i)h_e(n-i)\right]^*\right]=\sum_{i=1}^{p}a_p^*(i)\sum_{n=p}^{N}\left[e(n)h_e^*(n-i)\right]=0 \qquad (4.a.24)$$

Consequently in terms of equation (4.a.23) and using the autocorrelation sequence $r_{h_eh_e}(i,k)$ in equation (4.a.12), equation (4.a.21) is written as

$$E_p=\left[e(n)\right]^2=\sum_{n=p}^{N}\left[e(n)h_e(n)\right]+\sum_{n=p}^{N}\left[e(n)\sum_{i=1}^{p}a_p(i)h_e(n-i)\right]=\sum_{n=p}^{N}\left[e(n)h_e(n)\right]=$$

$$\sum_{n=p}^{N}\left[h_e(n)+\sum_{i=1}^{p}a_p(i)h_e(n-i)\right]h_e(n)=r_{h_eh_e}(0,0)+\sum_{k=1}^{p}a_p(k)r_{h_eh_e}(0,i)$$

Accordingly in terms equation of (4.a.24) and the autocorrelation sequence $r_{h_eh_e}(i,k)$ in equation (4.a.13), equation (4.a.22) is written as

$$E_p=\left|e(n)\right|^2=\sum_{n=p}^{N}\left[e(n)h_e^*(n)\right]+\sum_{n=p}^{N}\left[e(n)\left[\sum_{i=1}^{p}a_p(i)h_e(n-i)\right]^*\right]=\sum_{n=p}^{N}\left[e(n)h_e^*(n)\right]=$$

$$\sum_{n=p}^{N}\left[h_e(n)+\sum_{i=1}^{p}a_p(i)h_e(n-i)\right]h_e^*(n)=r_{h_eh_e}(0,0)+\sum_{i=1}^{p}a_p(i)r_{h_eh_e}(0,i)$$

Therefore the minimum value for the square error E_p can be expressed as

$$E_p=r_{h_eh_e}(0,0)+\sum_{k=1}^{p}a_p(k)r_{h_eh_e}(0,i) \qquad (4.a.25)$$

Therefore equation (4.31) can be augmented to include E_p as

$$\begin{bmatrix} r_{h_e h_e}(0,0) & r_{h_e h_e}(0,1) & r_{h_e h_e}(0,2) & r_{h_e h_e}(0,3) & \cdots & r_{h_e h_e}(0,p-1) & r_{h_e h_e}(0,p) \\ r_{h_e h_e}(1,0) & r_{h_e h_e}(1,1) & r_{h_e h_e}(1,2) & r_{h_e h_e}(1,3) & \cdots & r_{h_e h_e}(1,p-1) & r_{h_e h_e}(1,p) \\ r_{h_e h_e}(2,0) & r_{h_e h_e}(2,1) & r_{h_e h_e}(2,2) & r_{h_e h_e}(2,3) & \cdots & r_{h_e h_e}(2,p-1) & r_{h_e h_e}(2,p) \\ r_{h_e h_e}(3,0) & r_{h_e h_e}(3,1) & r_{h_e h_e}(3,2) & r_{h_e h_e}(3,3) & \cdots & r_{h_e h_e}(3,p-1) & r_{h_e h_e}(3,p) \\ \vdots & \vdots & \vdots & \vdots & & \vdots & \vdots \\ r_{h_e h_e}(p-1,0) & r_{h_e h_e}(p-1,1) & r_{h_e h_e}(p-1,2) & r_{h_e h_e}(p-1,3) & \cdots & r_{h_e h_e}(p-1,p-1) & r_{h_e h_e}(p-1,p) \\ r_{h_e h_e}(p,0) & r_{h_e h_e}(p,1) & r_{h_e h_e}(p,2) & r_{h_e h_e}(p,3) & \cdots & r_{h_e h_e}(p,p-1) & r_{h_e h_e}(p,p) \end{bmatrix} \begin{bmatrix} 1 \\ a_p(1) \\ a_p(2) \\ a_p(3) \\ \vdots \\ a_p(p-1) \\ a_p(p) \end{bmatrix} = \begin{bmatrix} E_p \\ 0 \\ 0 \\ 0 \\ 0 \\ 0 \\ 0 \\ 0 \end{bmatrix}$$

APPENDIX Chapters 5 & 6

5.a Time domain representations of measured reflections from sphere.

In this section the unprocessed reflections of the sphere are shown in time domain. Figure 5.a1 shows the sphere response, which is obtained by direct estimation of the IFT of the S21 parameter of the measured fields for sphere, which as shown in Figure 5.10. This was obtained using Vivaldi antennas. The sphere response shown in Figure 5.a2 is obtained by estimation of the IFT of the S21 parameter of the sphere measured fields, which is shown in Figure 6.6. This was obtained using broadband horn antennas. Therefore in these responses the antennas coupling field and the chamber absorber clutter field in addition to the antennas response are present.

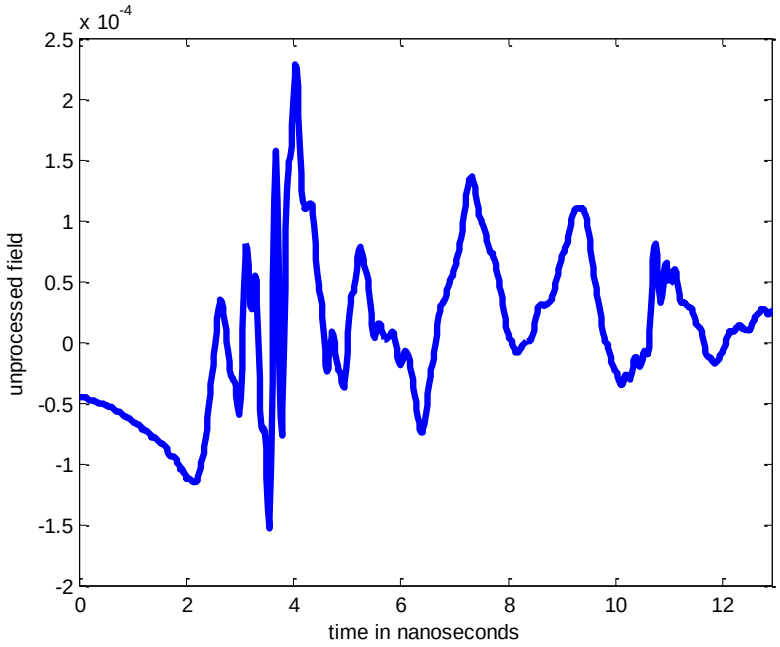

Figure 5.a1: Unprocessed signal in the time domain with the use of Vivaldi antennas.

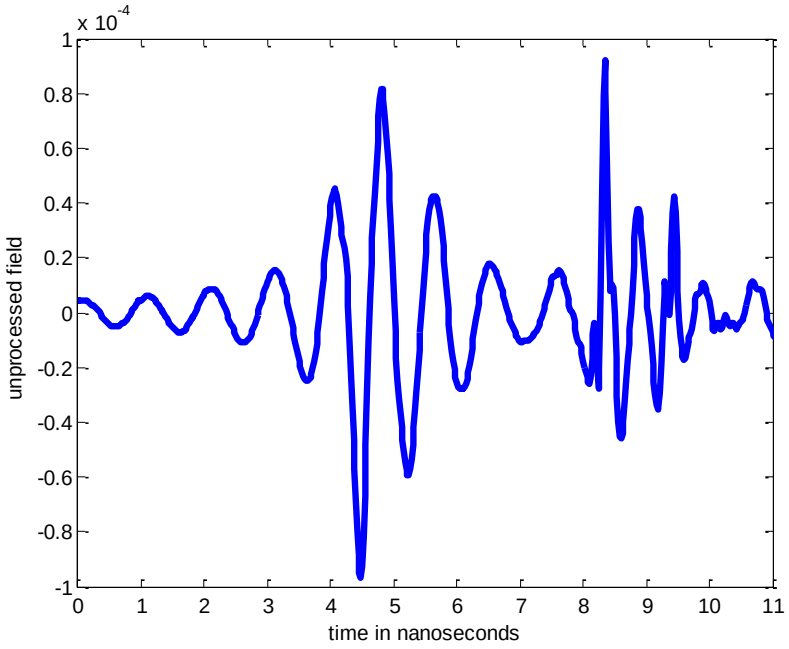

Figure 5.a2: Unprocessed field in the time domain with the use of horn antennas.

5.b MUltiple SIgnal Classification (MUSIC) and Information Theoretic Criterion

The MUSIC [98] algorithm and the Singular Value Decomposition (SVD) - Prony algorithm [82-89] are widely recognised techniques which are used to acquire the components and estimate the frequency content of signals that are sum of damped complex exponentials in the presence of noise, since noise and signal components remain uncorrelated. Other algorithms capable of obtaining components of damped complex exponentials in noise involve SVD or linear prediction methods [99-101]. The algorithm described in [102] assumes an autoregressive moving average model for frequency estimation while the algorithm in [85-86] employs an autoregressive signal model.

The MUSIC algorithm considers the impulse response, and it estimates the pseudo-spectrum or power spectral density (PSD) using the eigenvalue analysis method of the autocorrelation matrix of the impulse response. The eigenvalue decomposition of the autocorrelation matrix leads to the estimation of the frequency content of the impulse response. The SVD-Prony algorithm is a least squares method estimating the coefficients of an Infinite Impulse Response (IIR) filter whose impulse response is previously described. Therefore these algorithms are used for exponential signal modelling of signals which are perturbed by noise.

In both algorithms the LTR is considered as the input signal. Then by means of the MUSIC algorithm the PSD of the LTR is obtained. Using the SVD-Prony the filter coefficients are calculated, then from these coefficients the poles and the residues of LTR are extracted. In both algorithms the basic idea is the study of the autocorrelation of the LTR, so here the LTR autocorrelation is briefly presented and how it is affected by additive noise.

From equation (4.1) if the LTR is expressed as a sum of damped complex exponentials

$$h_e(n) = \sum_{i=1}^{I} \frac{R_i}{2} e^{s_i n\Delta t} e^{j\phi_i} \quad \text{for } n = 0,1,..,N \tag{5.b.1}$$

S_i denote both the complex poles and their conjugates. If

$$\mathbf{h}_e(n) = \begin{bmatrix} h_e(n) \\ h_e(n+1) \\ h_e(n+2) \\ . \\ . \\ . \\ h_e(n+p-1) \end{bmatrix} \quad \text{where } I < p < N/2$$

The $p \times p$ autocorrelation matrix $\mathbf{R}_{h_e h_e}$ of $h_e(n)$ can be written [70, 86] as

$$\mathbf{R}_{h_e h_e} = E\left[\mathbf{h}_e(n)\mathbf{h}_e(n)^H\right] = \sum_{i=1}^{I} \left(\frac{R_i}{2}\right)^2 \mathbf{e}_i \mathbf{e}_i^H \tag{5.b.2}$$

Where

$$\mathbf{e}_i = \begin{bmatrix} 1 \\ e^{j\omega_i} \\ e^{j2\omega_i} \\ . \\ . \\ . \\ e^{j(p-1)\omega_i} \end{bmatrix} \qquad \text{for } i = 1,2,...I$$

$\mathbf{e}_i$ is a set of I linearly independent vectors, $\text{span}\{\mathbf{e}_1 \quad \mathbf{e}_2 \quad \mathbf{e}_3 \quad . \quad . \quad . \quad \mathbf{e}_{I-1} \quad \mathbf{e}_I\}$ is referred to as the signal subspace of the signal $h_e(n)$.

If λ denote the eigenvalues of $\mathbf{R}_{h_e h_e}$ which are ordered so that $\lambda_1 > \lambda_2 > \lambda_3 > ... > \lambda_{p-1} > \lambda_p$ and if $\mathbf{v}_1, \mathbf{v}_2, \mathbf{v}_3, ..., \mathbf{v}_{p-1}, \mathbf{v}_p$ are the corresponding eigenvectors, which are normalised so that $\mathbf{v}_{i_1}{}^H \mathbf{v}_{i_2} = \delta[i_1 - i_2]$ then

$$\mathbf{R}_{h_e h_e} \mathbf{v}_i = \lambda_i \mathbf{v}_i \tag{5.b.3}$$

If $\mathbf{R}_{h_e h_e}$ has rank I then $\lambda_{I+1} = 0$, $\lambda_{I+2} = 0, ..., \lambda_p = 0$ so $\mathbf{R}_{h_e h_e}$ can be expressed as

$$\mathbf{R}_{h_e h_e} = \sum_{i=1}^{I} \lambda_i \mathbf{v}_i \mathbf{v}_i{}^H \tag{5.b.4}$$

The eigenvectors $\mathbf{v}_1, \mathbf{v}_2, \mathbf{v}_3, ..., \mathbf{v}_{I-1}, \mathbf{v}_I$ are referred as the principal eigenvectors of $\mathbf{R}_{h_e h_e}$

If the LTR $h_y(n)$ which is obtained from experiments is the result of addition of the discrete signal $h_e(n)$ with noise $w(n)$, then $h_y(n)$ can be expressed as

$$h_y(n) = h_e(n) + w(n) \tag{5.b.4}$$

where $w(n)$ is a stationary white-noise signal, which is independent of $h_e(n)$ and it has zero-mean, and its variance is denoted as $\sigma_w^2 = E[w(n)w(n)^*]$. If

$$\mathbf{h}_y = \begin{bmatrix} h_y(n) \\ h_y(n+1) \\ h_y(n+2) \\ . \\ . \\ . \\ h_y(n+p-1) \end{bmatrix} \text{ and } \mathbf{w}_y = \begin{bmatrix} w(n) \\ w(n+1) \\ w(n+2) \\ . \\ . \\ . \\ w(n+p-1) \end{bmatrix}$$

The $p \times p$ autocorrelation matrix $\mathbf{R}_{h_y h_y}$ of $h_y(n)$ can be expressed as

$$\mathbf{R}_{h_y h_y} = E[\mathbf{h}_y(n)\mathbf{h}_y(n)^H] = \mathbf{R}_{h_e h_e} + \sigma_w^2 \mathbf{I} \tag{5.b.5}$$

The autocorrelation matrix $\mathbf{R}_{h_y h_y}$ is full rank since $\sigma_w^2\mathbf{I}$ is full rank. If $\mathbf{R}_{h_y h_y}\ \mathbf{v}_i = \mu_i\ \mathbf{v}_i$ is the eigenvalue equation of $\mathbf{R}_{h_y h_y}$ and its eigenvalues are sorted as $\mu_1 > \mu_2 > \mu_3 > ... > \mu_{p-1} > \mu_p$, the first *I* eigenvalues of $\mathbf{R}_{h_y h_y}$ are associated to the first *I* eigenvalues of $\mathbf{R}_{h_e h_e}$ by

$$\mu_i = \lambda_i + \sigma_w^2 \tag{5.b.6}$$

the eigenvectors corresponding to μ_i and λ_i are equal.

Additionally p-*I* eigenvalues $\mu_{I+1} > \mu_{I+2} > \mu_{I+3} > ... > \mu_{p-1} > \mu_p$ are equal to σ_w^2 .

As it is explained in [70] since $\mathbf{R}_{h_e h_e}$ has rank *I* then $\mathbf{R}_{h_e h_e}$ is rank deficient.

In this way $\mathbf{R}_{h_y h_y}$ can be expressed as

$$\mathbf{R}_{h_y h_y} = \mathbf{V}\mathbf{M}\mathbf{V}^H \tag{5.b.7}$$

where $\mathbf{M} = \text{diag}(\mu_1, \mu_2, \mu_3, ..., \mu_{p-1}, \mu_p)$ is a diagonal matrix consisting of the eigenvalues μ_i arranged in a decreasing order . $\mathbf{V}$ is a $p \times p$ orthogonal matrix consisting of the common eigenvectors of $\mathbf{R}_{h_y h_y}$ and $\mathbf{R}_{h_e h_e}$

$\mathbf{V} = [\mathbf{v}_1 \quad \mathbf{v}_2 \quad \mathbf{v}_3 \quad . \quad . \quad . \quad \mathbf{v}_{p-1} \quad \mathbf{v}_p]$

$\mathbf{R}_{h_y h_y}$ is also expressed as

$$\mathbf{R}_{h_y h_y} = \sum_{i=1}^{I} \left(\lambda_i + \sigma_w^2\right) \mathbf{v}_i \mathbf{v}_i^H + \sum_{i=I+1}^{p} \sigma_w^2 \mathbf{v}_i \mathbf{v}_i^H \tag{5.b.8}$$

Since $\mathbf{V}$ is the matrix consisting of the eigenvectors of $\mathbf{R}_{h_y h_y}$ the eigenvectors $\mathbf{v}_1 \quad \mathbf{v}_2 \quad \mathbf{v}_3 \quad . \quad . \quad . \quad \mathbf{v}_{I-1} \quad \mathbf{v}_I$ are referred to as signal eigenvectors since they are associated to the first *I* signal eigenvalues and they span the signal

subspace. $\mathrm{span}\{\mathbf{v}_{I+1} \quad \mathbf{v}_{I+2} \quad \mathbf{v}_{I+3} \quad . \quad . \quad . \quad \mathbf{v}_{p-1} \quad \mathbf{v}_{p}\}$ is referred to as the noise subspace since the $\mathbf{v}_{I+1}$, $\mathbf{v}_{I+2}, \mathbf{v}_{I+3}$, ..., $\mathbf{v}_{p-1}, \mathbf{v}_{p}$ eigenvectors are related to the last *p-I* noise eigenvalues.

The data matrix $\tilde{\mathbf{X}}_{p}$ which is involved in the formation of the autocorrelation matrix since $\mathbf{R}_{h_y h_y} = \tilde{\mathbf{X}}_{p}^{H} \tilde{\mathbf{X}}_{p}$, can be decomposed by means of the singular value decomposition SVD. The signal matrix component in $\tilde{\mathbf{X}}_{p}$ has the same rank as the rank of signal autocorrelation matrix ($\mathbf{R}_{h_e h_e}$) i.e rank *I.* Therefore for an adequate signal to noise ratio the SVD of $\tilde{\mathbf{X}}_{p}$ allows us to separate the signal subspace from the noise subspace and thus the *I* signal singular values and the *p-I* noise singular values of $\tilde{\mathbf{X}}_{p}$ can be obtained.

In the case of the LTR, the number of exponentials or poles of the LTR or model order I is not known a-priori. Additionally the model order I is most probable to differ depending on the examined object since in this section simpler objects i.e. reflector or human and more composite objects i.e. reflector-sphere or human-sphere are considered. Knowledge of *I* is pre-required for effective pole extraction in order to separate the signal subspace form the noise subspace. Therefore the model selection can be realized by application of the information theoretic criteria as shown in [93-97]. In this approach the estimate for the number of exponentials is determined by the integer between 1and p -1 which minimizes the Minimum Description Length (MDL) criterion. This integer represents the rank I of signal autocorrelation matrix $\mathbf{R}_{h_e h_e}$ shown in equation (5.b.8) and the model order or number of exponentials in equation (5.b.1). In this study, in all

cases of objects considered (sphere , reflector, reflector-sphere , human, human-sphere composite object) the same dimension of autocorrelation matrix $\mathbf{R}_{h_y h_y} = \tilde{\mathbf{X}}_p^H \tilde{\mathbf{X}}_p$ was used i.e $p = 55$

Considering the Prony algorithm $\tilde{\mathbf{X}}_p$ appears in the least squares solution to a set of overdetermined linear equations [83]. Once the precise model order of LTR is known, the singular values of $\tilde{\mathbf{X}}_p$ are obtained, and as it is explained [83] the substitution of the noise singular values with zeros, results in obtaining less noisy estimates of signal parameters. In this way the SVD-Prony method results in the extraction of the exact LTR poles and residues and in accurate numbers. Otherwise the use of simple Prony method may generate poles which are due to noise.

Additionally the Power Spectral Density (PSD) of LTR is estimated by the MUSIC algorithm as

$$P(e^{j\omega}) = \frac{1}{\sum_{i=I+1}^{p} \left| \mathbf{e}^H \mathbf{v}_i \right|^2} \tag{5.b.11}$$

Where for each input frequency

$$\mathbf{e} = \begin{bmatrix} 1 \\ e^{j\omega} \\ e^{j2\omega} \\ . \\ . \\ . \\ e^{j(p-1)\omega} \end{bmatrix}$$

In Figure 5.b.1 the MDL of reflector LTR is shown. The MDL of reflector -0.024 m radius sphere LTR is shown in Figure 5.b.2 alongside with the MDL of reflector LTR.

The MDL of reflector -0.0325 m radius sphere LTR is shown in Figure 5.b.3 alongside with the MDL of reflector LTR.

From Figure 5.b.1 it is observed that the order of reflector LTR is 15, while in Figure 5.b.2 and Figure 5.b.3 the order of reflector-sphere LTR is 24 for both cases of spheres.

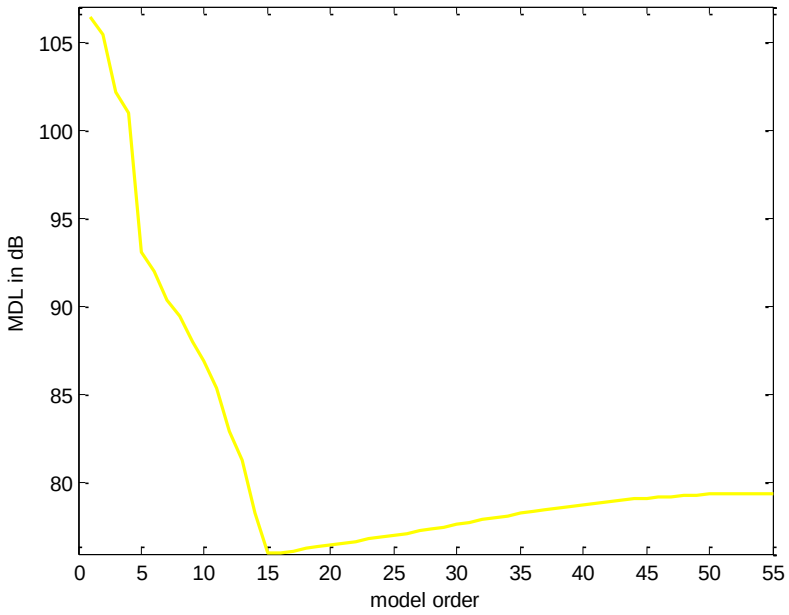

Figure 5.b.1: Reflector MDL.

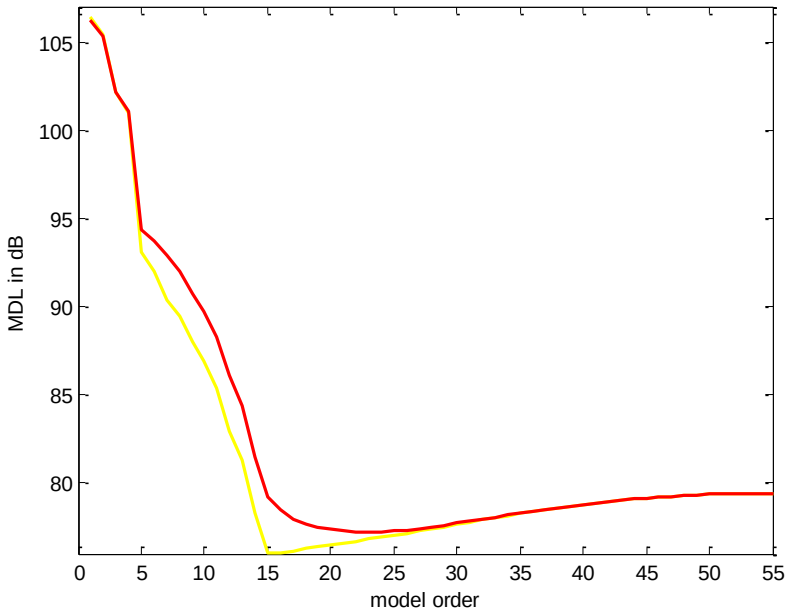

Figure 5.b.2: Reflector-0.024 m radius sphere (red) MDL and reflector (yellow) MDL.

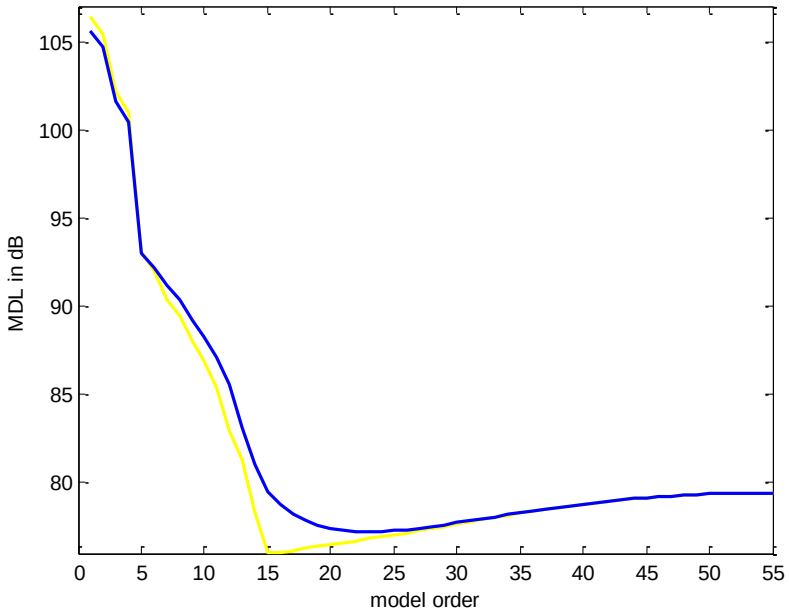

Figure 5.b.3: Reflector-0.0325 m radius sphere (blue) MDL and reflector (yellow) MDL.

In Figure 5.b.4 the MDL of human LTR is shown. The MDL of human- 0.0325 m radius sphere (in front) LTR is shown in Figure 5.b.5 alongside with the MDL of human

LTR. From Figure 5.b.4 and 5.b.5 it is observed that the order of human LTR is 23, while from Figure 5.b.5 the order of human-sphere LTR is 36.

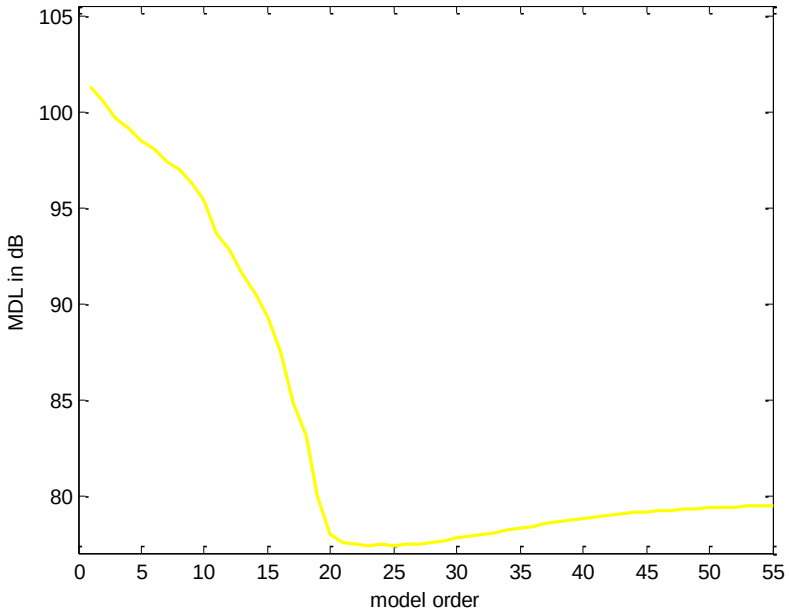

Figure 5.b.4: Human (yellow) MDL.

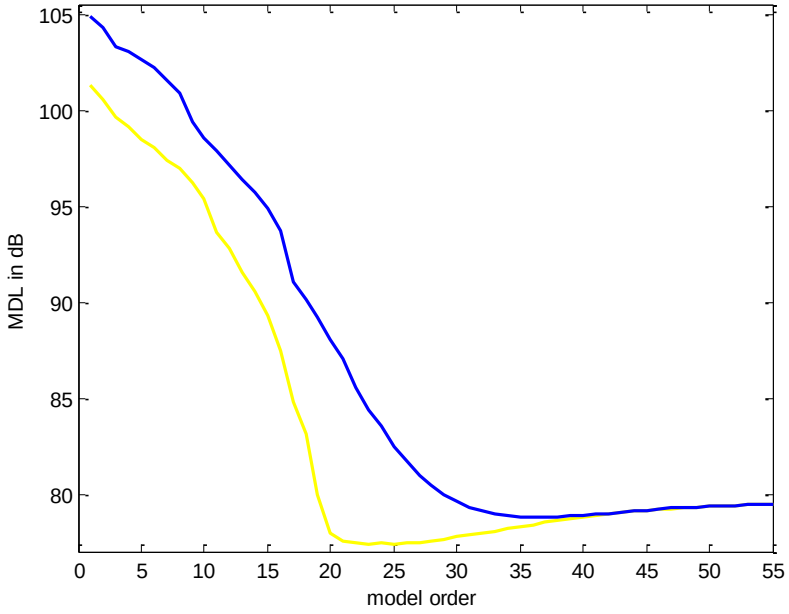

Figure 5.b.5: Human-sphere (in front) (blue) MDL and human (yellow) MDL.

The MDL of human- 0.0325 m radius sphere (side) LTR is shown in Figure 5.b.6 alongside with the MDL of human LTR. From Figure 5.b.6 it is observed that the order of human LTR is 23, while the order of human-sphere (side) LTR is 27.

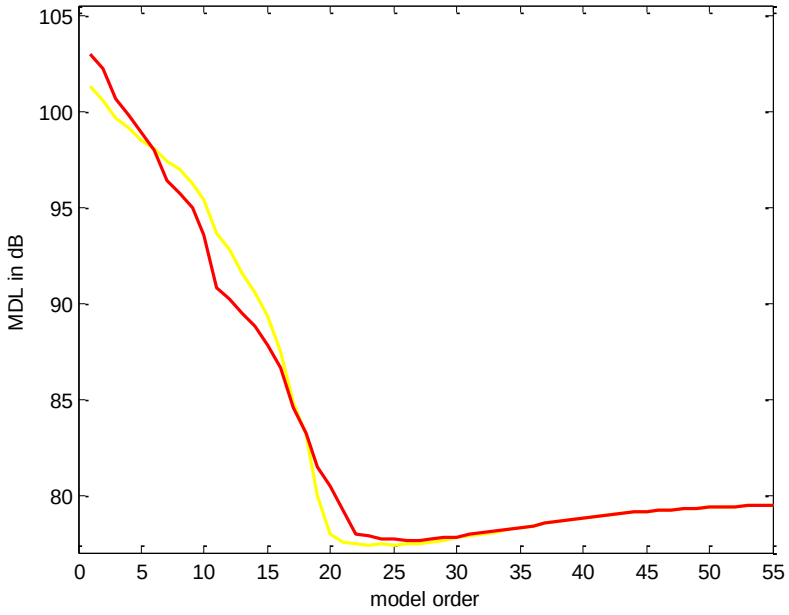

Figure 5.b.6: Human-sphere (side)(red) MDL and human (yellow) MDL.

The MDL of human- 0.0325 m radius sphere (back) LTR is shown in Figure 5.b.7 alongside with the MDL of human LTR. From Figure 5.b.7 it is observed that the order of human LTR is 23, while the order of human-sphere (back) LTR is 34.

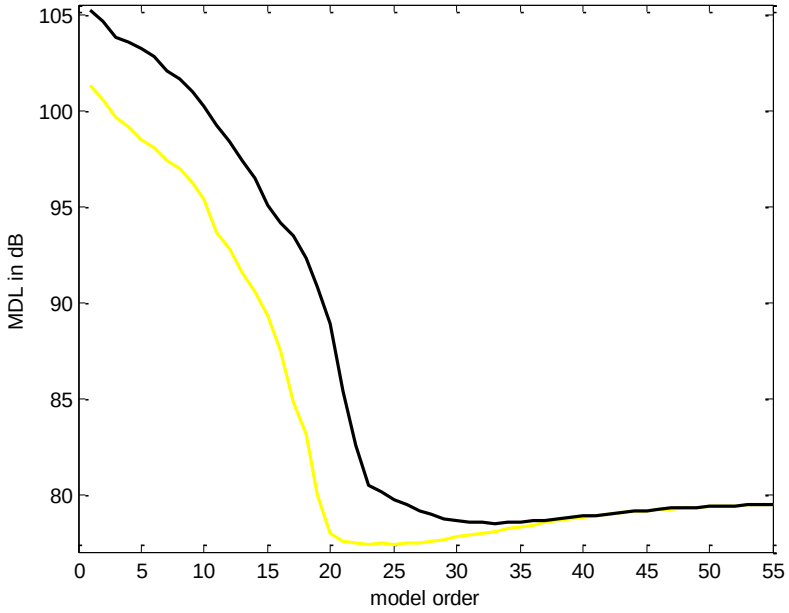

Figure 5.b.7: Human-sphere (back) MDL and human (yellow) MDL.

From observations on MDL it can be concluded that complex targets i.e. reflector-sphere or human-sphere objects require a larger number of poles than simple targets i.e. reflector or human. This justifies the number of LTR poles which is extracted for each object in the previous sections.

5.c LTRs of reflector and reflector-sphere against the noise

In this section the reflector, reflector-0.024m radius sphere, reflector-0.0325m radius sphere LTRs are shown in Figure 5.c.1, 5.c.2 and 5.c.3 respectively against the noise.

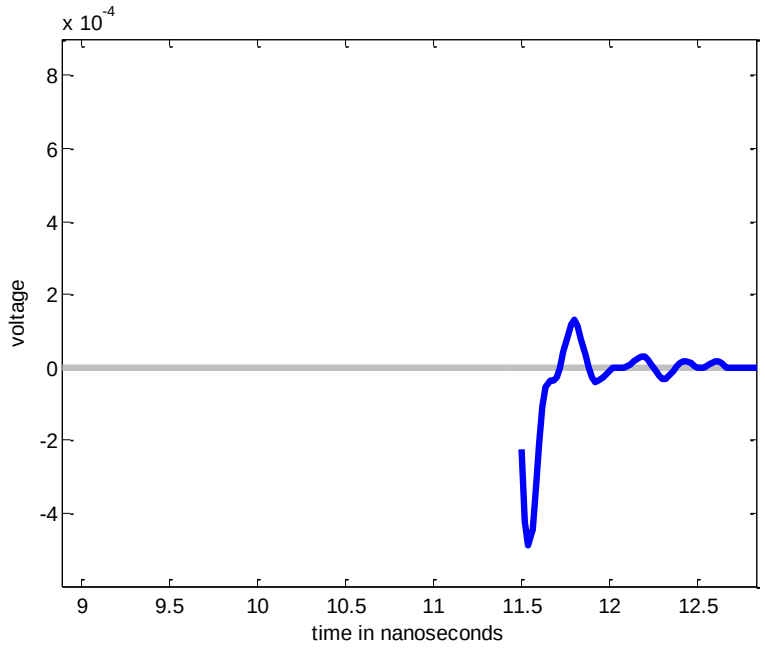

Figure 5.c.1: Reflector (blue) LTR against the noise (grey).

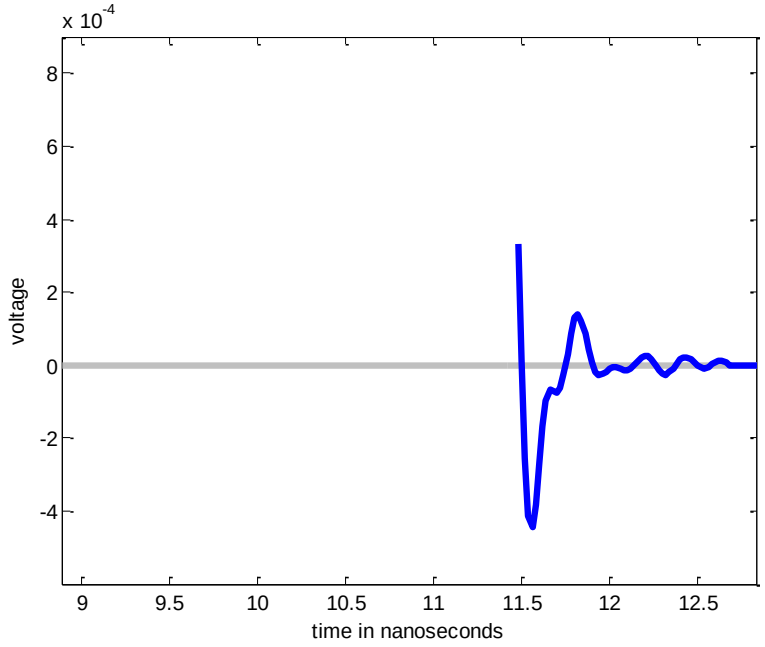

Figure 5.c.2: Reflector-0.024m radius sphere (blue) LTR against the noise (grey).

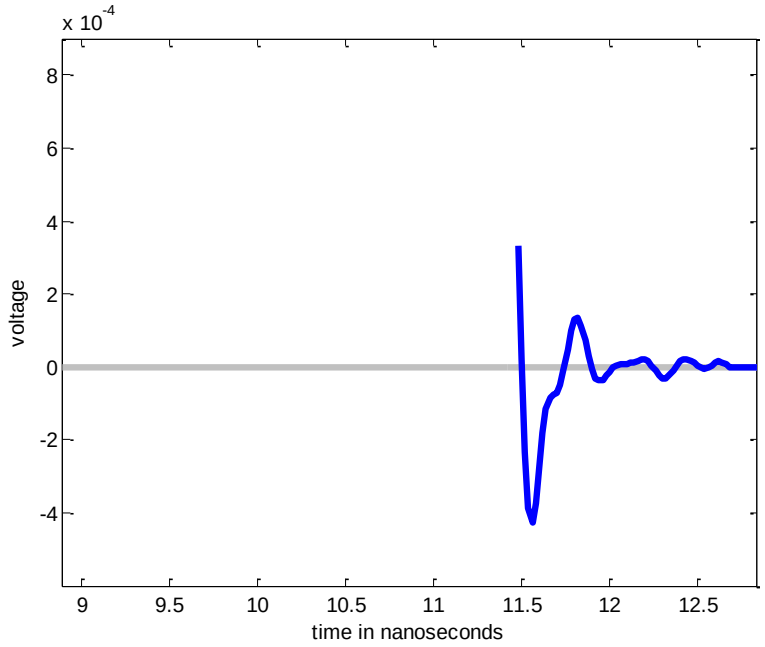

Figure 5.c.3: Reflector-0.0325 m radius sphere (blue) LTR against the noise (grey).

5.d LTRs of human and human-sphere against the noise

In this section the human, human-sphere (in front), human-sphere (side) and human-sphere (back) LTRs are shown in Figure 5.d.1, 5.d.2 and 5.d.3 and 5.d.4 respectively against the noise.

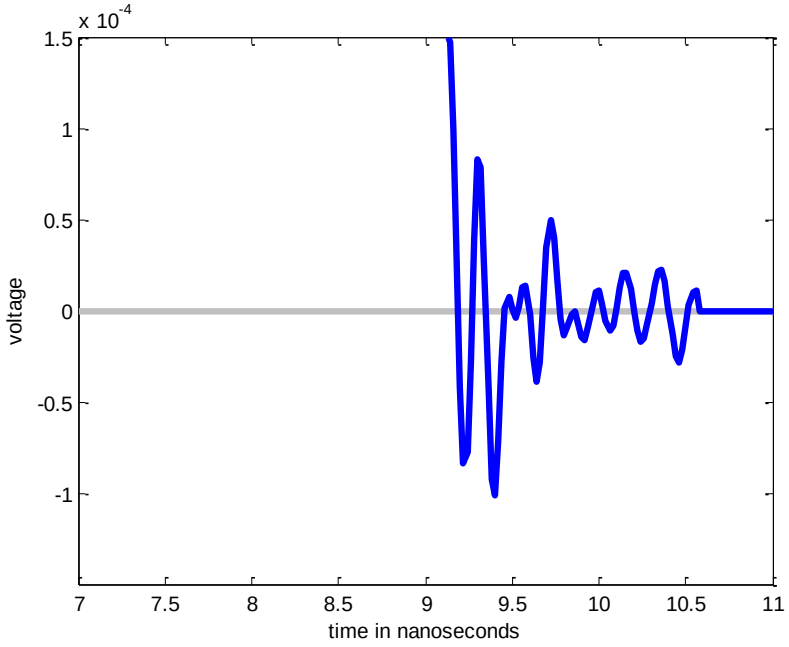

Figure 5.d.1: Human (blue) LTR against the noise (grey).

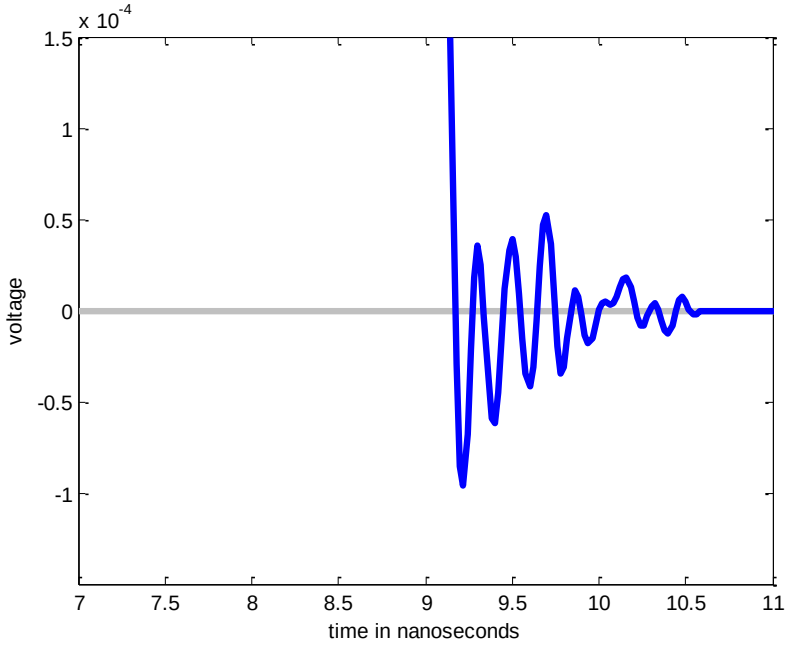

Figure 5.d.2: Human-sphere (in front) (blue) LTR against the noise (grey).

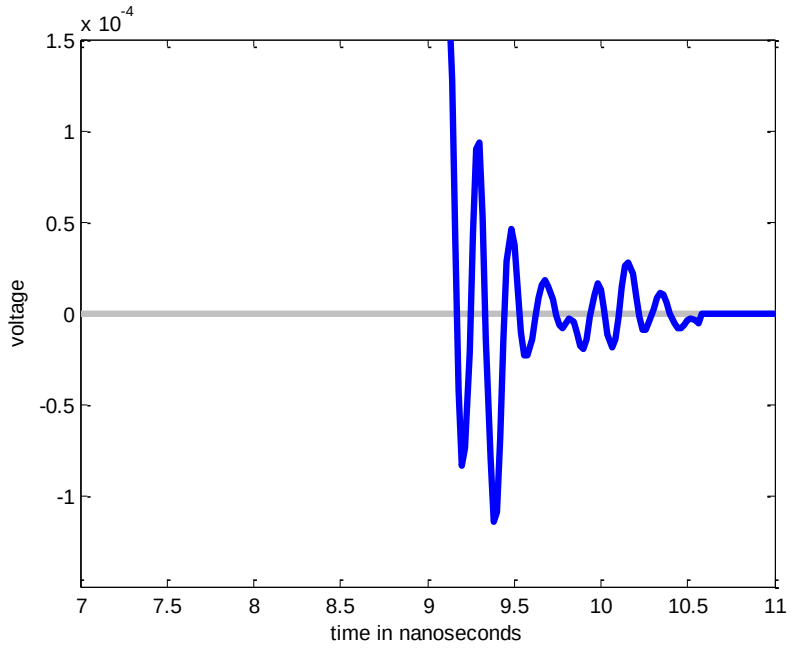

Figure 5.d.3: Human-sphere (by the side) (blue) LTR against the noise (grey).

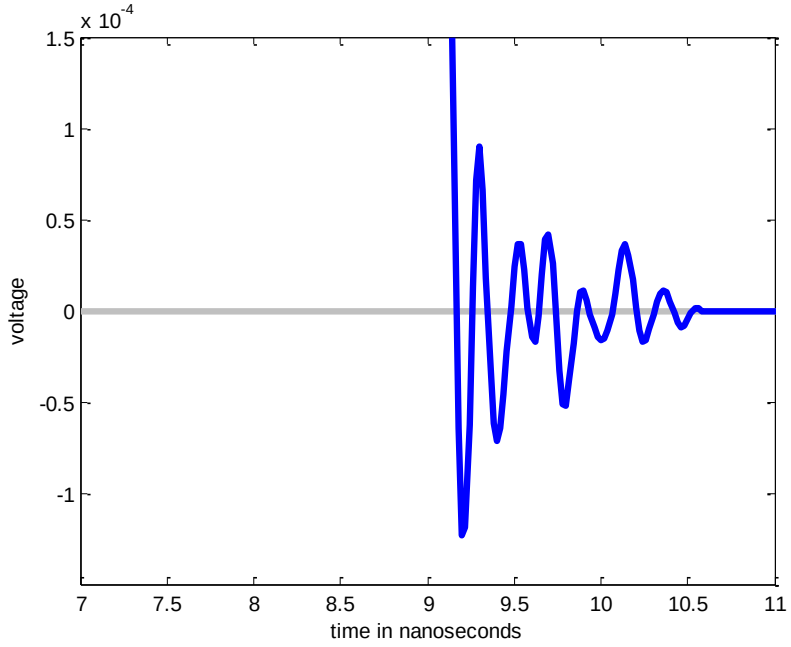

Figure 5.d.4: Human-sphere (back) (blue) LTR against the noise (grey).

5.e Comparison of averages of measurements

In this section the LTR, PSD and obtained poles of the response which is the average of 120 measurements are compared with the respective quantities of each of the other averages of 60 measurements. Figures 5.e.1 and Figure 5.e 2 show the human LTRs, each LTR is the result of processing a combined response which is an average of 60 frequency domain measurements. So Figure 5.e.1 shows the combinations of: 1st and 2nd measured responses, 1st and 3rd measured responses, 1st and 4rth measured responses. Figure 5.e.2 shows the combinations of: 2nd and 3rd measured responses, 2nd and 4th measured responses, 3rd and 4rth measured responses. The human LTR after processing the average of 120 measurements is shown in Figure 5.e.3 and it was also shown in Figure 6.28 with different time scale.

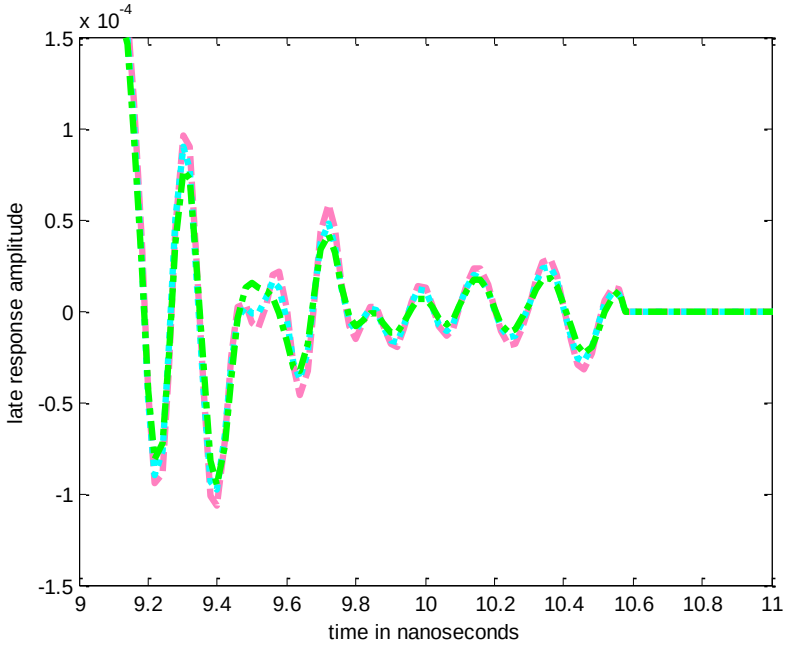

Figure 5.e.1: Combinations of human LTR.
(dashed)1st and 2nd measured responses.
(dotted)1st and 3rd measured responses.
(dashed-dotted)1st and 4rth measured responses.

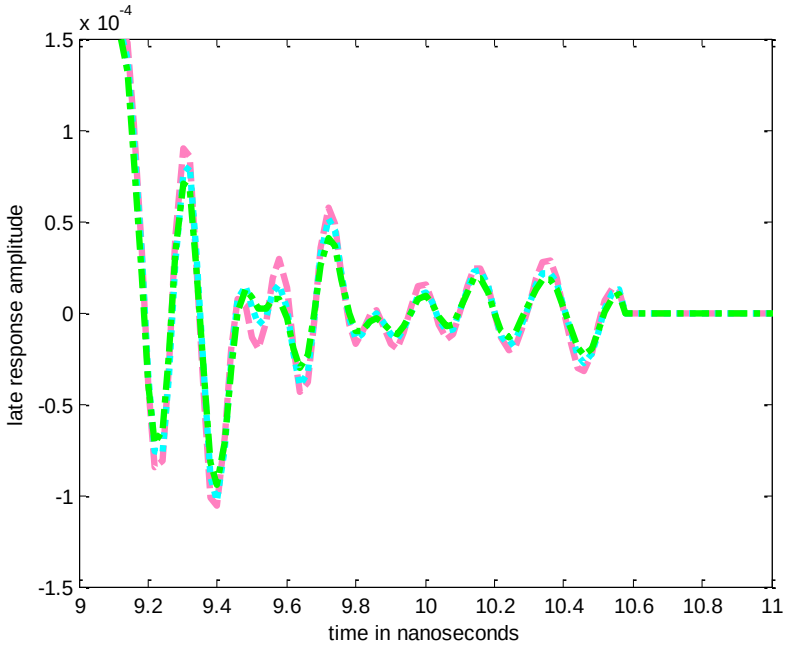

Figure 5.e.2: Combinations of human LTR.
(dashed) 2nd and 3rd measured responses
(dotted) 2nd and 4rth measured responses
(dashed-dotted) 3rd and 4rth measured responses

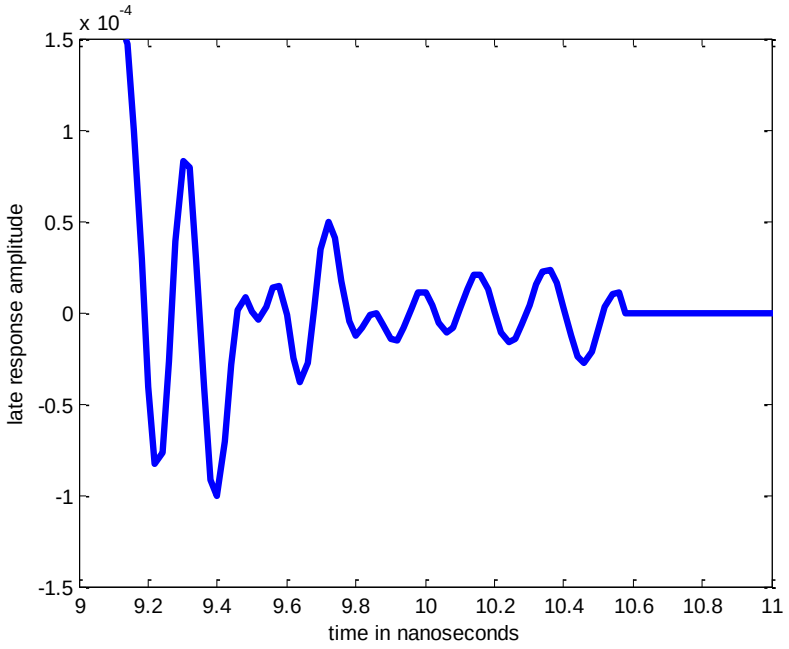

Figure 5.e.3: Human LTR from Figure 6.29 in different time scale.

The PSD of the human LTRs originating from averaging 60 frequency domain measurements are shown in Figure 5.e.4 and in Figure 5.e.5 together with the PSD

(shown in Figure 6.29) of the human LTR derived via processing of the average of 120 measurements.

The extracted poles of the human LTR created from averaging 60 frequency domain measurements are shown in Figure 5.e.6 and Figure 5.e.7 and their amplitudes are shown in Figure 5.e.8 and Figure 5.e.9 respectively. These poles and their amplitudes are plotted alongside with the poles of the human LTR (as shown in Figure 6.30) derived via processing of the average of 120 measurements and their amplitudes respectively (as shown in Figure 6.31).

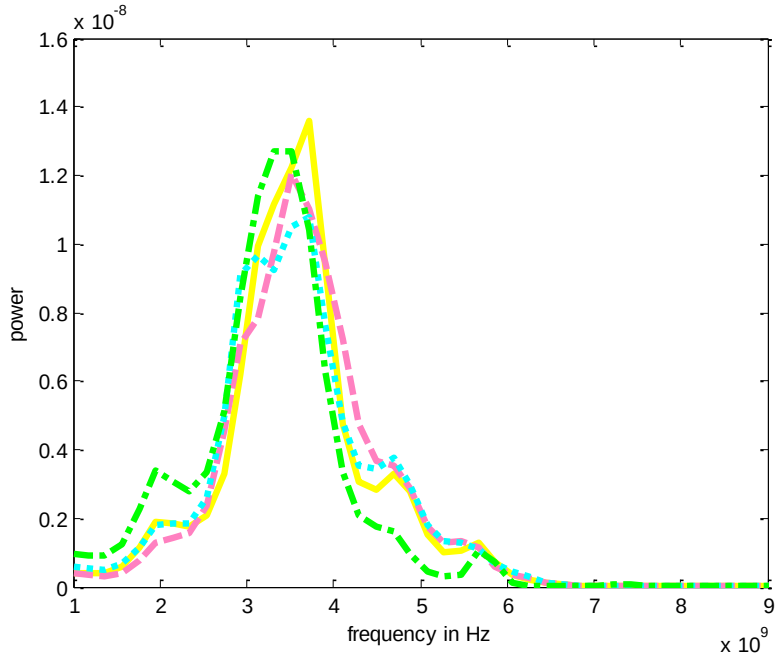

Figure 5.e.4: PSDs of human LTR.
(solid) average of 120 measurements
(dashed)1st and 2nd measured responses
(dotted)1st and 3rd measured responses
(dashed-dotted)1st and 4rth measured responses

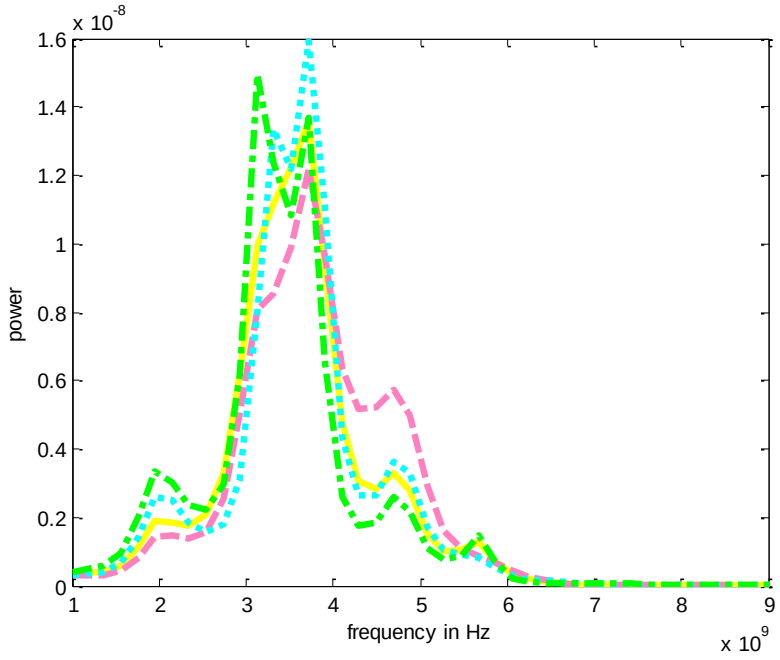

Figure 5.e.5: PSDs of human LTR.
(solid) average of 120 measurements
(dashed) 2nd and 3rd measured responses
(dotted) 2nd and 4rth measured responses
(dashed-dotted) 3rd and 4rth measured responses

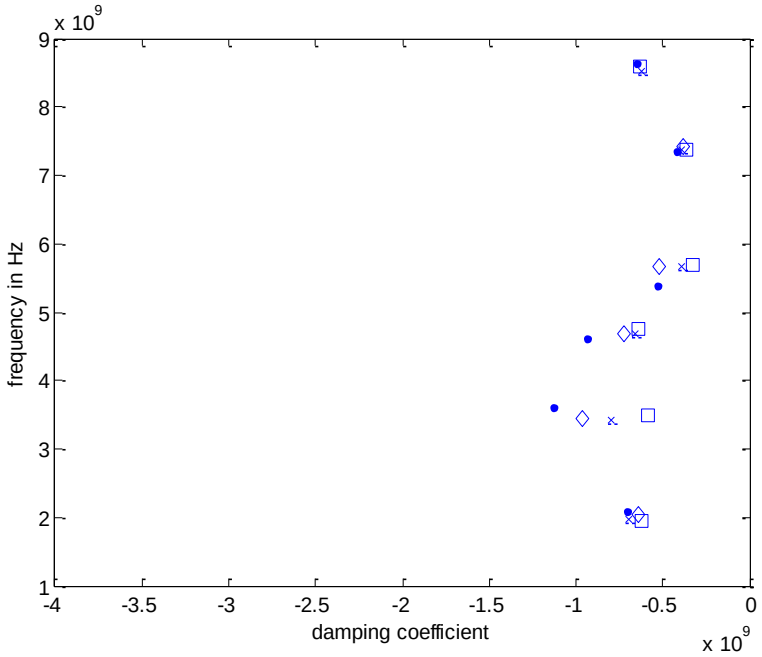

Figure 5.e.6: Comparison of human LTR poles.
(.) average of 120 measurements
(×) 1st and 2nd measured responses
(◊) 1st and 3rd measured responses
(□) 1st and 4rth measured responses

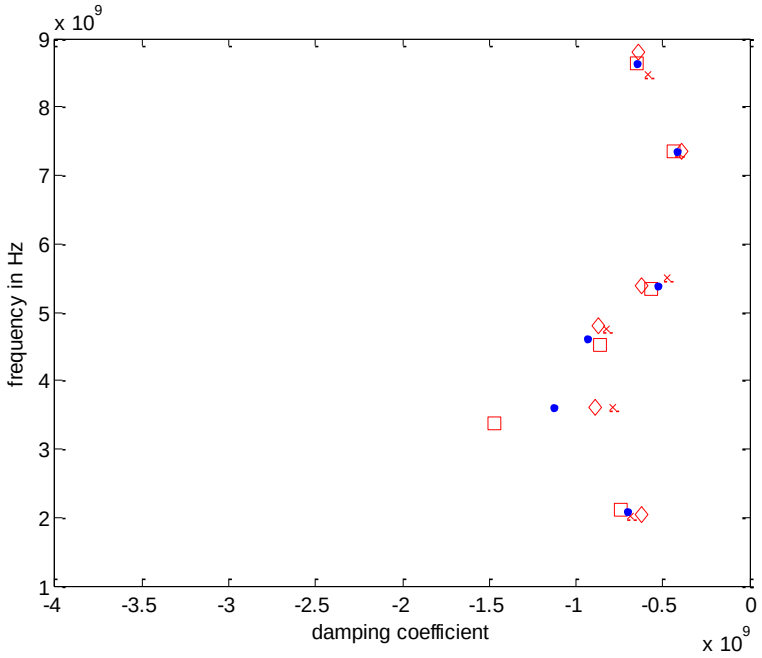

Figure 5.e.7: Comparison of human LTR poles.
(.) average of 120 measurements
(×) 2nd and 3rd measured responses
(◊) 2nd and 4rth measured responses
(□) 3rd and 4rth measured responses

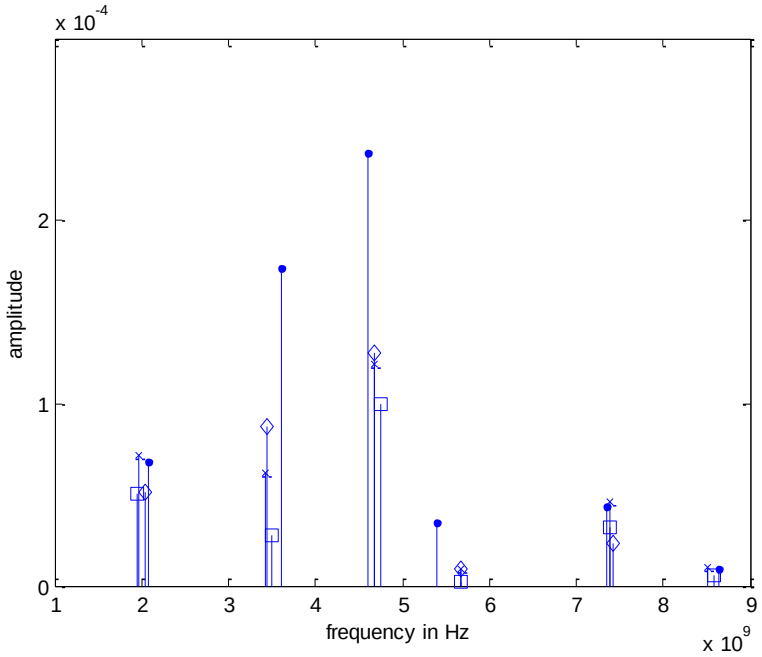

Figure 5.e.8: Amplitudes of the human LTR poles.
(.) average of 120 measurements
(×)1st and 2nd measured responses
(◊) 1st and 3rd measured responses
(□)1st and 4rth measured responses

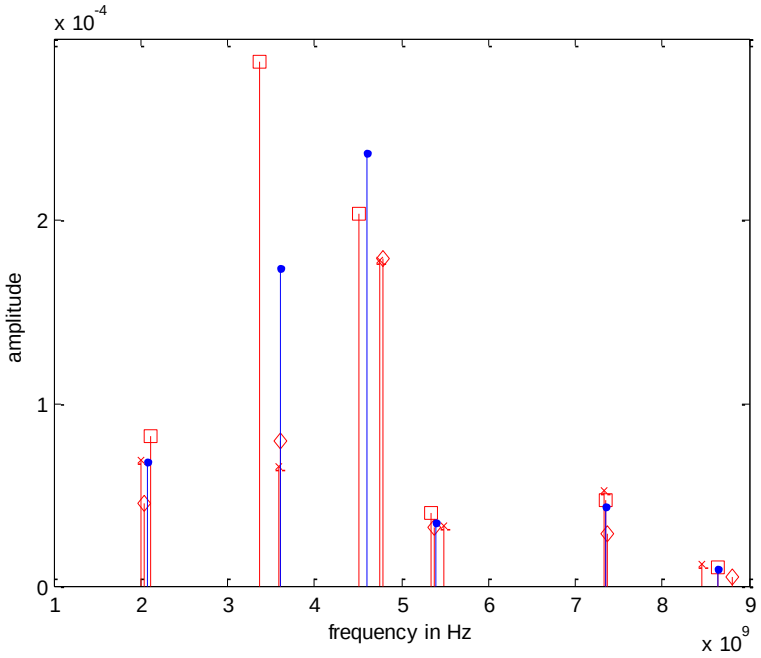

Figure 5.e.9: Amplitudes of the human LTR poles.
(.) average of 120 measurements
(×) 2nd and 3rd measured responses
(◊) 2nd and 4rth measured responses
(□) 3rd and 4rth measured responses

References

[1] C. L. Bennett, G. F. Ross, “Time-domain electromagnetics and its applications,” *Proc. IEEE,* vol. 66, Mar. 1978, pages: 299–318.

[2] http://www.fcc.gov/Bureaus/Engineering_Technology/Orders/2002/fcc02048.pdf

[3] R. J. Fontana “Recent System Applications of Short-Pulse Ultra-Wideband (UWB) Technology (Invited Paper)”, IEEE Microwave Theory and Techniques, vol. 52, no. 9, September 2004, pages: 2087-2104.

[4] D M. Sheen, D L. McMakin, and T E. Hall, “Three-Dimensional Millimeter-Wave Imaging for Concealed Weapon Detection” IEEE Transactions on Microwave Theory and Techniques, vol. 49, no. 9, Sept.2001, pages:1581-1592.

[5] A Agurto, Li Yong, Y T Gui, N Bowring, S. Lockwood, ”A review of concealed weapon detection and research in perspective” IEEE International Conference on Networking, Sensing and Control, April 2007, pages: 443 – 448.

[6] N. G. Paulter, "Guide to the Technologies of Concealed Weapons and Contraband Imaging and Detection", National Institute of Justice Guide 602-00, February 2001, pages: 33-50.

[7] L. G. Roybal, P. M. Rice, and J. M. Manhardt, "A new approach for detecting and classifying concealed weapons," Proceedings of the SPIE, The International Society for Optical 54 Engineering,Conference on Surveillance and Assessment Technologies for Law Enforcement, Vol. 2935, Boston, MA, November 1996, pages: 95-107.

[8] L. Yujiri, “Passive Millimeter Wave Imaging” Microwave Symposium Digest, 2006. IEEE MTT-S International pages: 98 - 101 June 2006.

[9] L. Yujiri, M. Shoucri, and P. Moffa, "Passive Millimeter-Wave Imaging", IEEE microwave magazine, September 2003, pages: 39-50.

[10] R. Appleby, "Passive millimetre-wave imaging and how it differs from terahertz imaging", The Royal Society, 10.1098/rsta.2003.1323, 2003, pages: 379- 394.

[11] R. W. McMillan, N.C. Currie, D.D. Ferris, Jr. Wicks, "Concealed Weapon Detection using Microwave and Millimeter Wave Sensors".US Air Force Res. Lab., Rome, NY.

[12] H.-M. Chen, S. Lee, R. M. Rao, M.-A. Slamani, and P. K. Varshney, "Imaging for concealed weapon detection: a tutorial overview of development in imaging sensors and processing," IEEE Signal Processing Mag., vol. 22, Mar. 2005, pages: 52-61.

[13] J. F. Federici, D. Garya, R. Baratb, D. Zimdarsc, "THz Standoff Detection and Imaging of Explosives and Weapons", Proc. SPIE 5781, 75, 2005.

[14] J. D. Taylor, (Editor) “Introduction to Ultra Wideband Radar systems”, CRC Press 1995.

[15] S. Kingsley, S. Quegan, “Understanding Radar Systems”, McGraw-Hill 1992.

[16] F. Nathanson, “Radar Design Principles”, McGraw-Hill 1991 (second edition).

[17] J. D. Taylor, “Ultra-wideband Radar Technology”, CRC Press 2000, pages: 96.

[18] D. R. Wehner, “High Resolution Radar”, Norwood Mass Artech House 1987 pages 164-166.

[19] C E. Baum, E J. Rothwell, K Chen, D P. Nyquist, ‘‘The singularity expansion method and its application to target identification’’, Proc. IEEE, vol 79, no 10, Oct 1991, pages: 1481-1492.

[20] L.Yu. Astanin, A.A. Kostylev, “Ultra-Wideband Radar Measurements: Analysis and Processing”, IEE, London UK 1997.

[21] I. J. Imoreev, J. D. Taylor, P.E, "Future of Radars", IEEE Conference on Ultra Wideband Systems and Technologies, 2002, pages: 197-199.

[22] A. Yarovoy, "Ultra-Wideband Systems", IEEE 33rd European Microwave Conference, vol.2, Oct.2003, pages: 597- 600.

[23] G. P. Pochanin, "Problems and promising lines of development of UWB ground penetrating radioallocation", IEEE Second International Workshop on Ultra Wideband and Ultra Short Impulse Signals, Sept.2004, pages: 61-66.

[24] A. Nezirovic, A. G. Yarovoy, L. P. Ligthart, "Signal Processing for Improved Detection of Trapped Victims Using UWB Radar", IEEE Transactions on Geoscience and Remote Sensing, Vol. 48, No. 4, April 2010, pages: 2005-2014.

[25] P. Withington, H. Fluhler, S. Nag, "Enhancing homeland security with advanced UWB sensors", IEEE Microwave Magazine, vol.4, issue 3, Sept.2003, pages: 51-58.

[26] C. N. Paulson, J. T. Chang et al, "Ultra Wideband radar methods and techniques of medical sensing and imaging", SPIE International Symposium on Optics East Boston, Oct.2005.

[27] H. Wang, R. M. Narayanan, Z. O. Zhou, "Through-Wall Imaging of Moving Targets Using UWB Random Noise Radar", IEEE Antennas and Wireless Propagation Letters, Vol. 8, 2009, pages: 2002-2005.

[28] M. Arik, O. B. Akan, "Collaborative Mobile Target Imaging in UWB Wireless Radar Sensor Networks", IEEE Journal on Selected Areas in Communications, Vol. 28, No. 6, Aug. 2010, pages: 950-961.

[29] S. Kidera, T. Sakamoto, T. Sato, "High-Resolution 3-D Imaging Algorithm with an Envelope of Modified Spheres for UWB Through-the-Wall Radars", IEEE

Transactions on Antennas and Propagation, Vol. 57, No. 11, Nov. 2009, pages: 3520-3529.

[30] S. K. Davis, B. D. Van Veen et al, "Breast Tumor Characterization based on Ultra Wideband Microwave Backscatter", http://www.engr.wisc.edu/ece/faculty/vanveen_barry/davisVanveenHagness_2007.pdf

[31] S. K. Davis, H. Tandradinata et al, "Ultra-Wideband microwave breast cancer detection: a detection-theoretic approach using the generalized likelihood ratio test", IEEE Transactions on Biomedical Engineering, vol.52, issue 7, Jul.2005 pages: 1237-1250.

[32] K. Shakti, D. Barry, V. Veen, S. C. Hagness, F. Kelcz, "Breast Tumor Characterization Based on Ultrawideband Microwave Backscatter" IEEE Transactions on Biomedical Engineering, Vol. 55, No. 1, Jan, 2008, pages: 237-246.

[33] I. Gresham, A. Jenkins et al, "Ultra-Wideband Radar Sensors for Short-Range Vehicular Applications", IEEE Transactions on Microwave Theory and Techniques, Vol. MTT-52, no. 9, Sept.2004, pages 2105-2122.

[34] A. M. El-Gabaly and C. E. Saavedra, "A Quadrature Pulse Generator for Short-Range UWB Vehicular Radar Applications Using a Pulsed Oscillator and a Variable Attenuator" IEEE Transactions on Circuits and Systems—I: Regular Papers, Vol. 58, No. 10, Oct. 2011, pages: 2285-2295.

[35] A. Sullivan, R. Damarla et al, "Ultra-Wideband Synthetic Aperture Radar for Detection of Unexploded Ordnance: Modelling and Measurements", IEEE Transactions on Antennas and Propagation, Vol. AP-48, no. 9, Sept.2000, pages 1306-1315.

[36] M. Soumekh, “Reconnaissance with Ultra-Wideband UHF Synthetic Aperture Radar”, IEEE Signal Processing Magazine, vol. 12, issue 4, Jul.1995, pages: 21-40.

[37] C. Fowler, J. Entzminger, J. Corum, “Assessment of Ultra-Wideband (UWB) Technology”, IEEE Aerospace and Electronic Systems Magazine, vol.5, issue 11, Nov.1990, pages: 45-49.

[38] A. V. Oppenheim, R. W. Schafer, J. R. Buck. “Discrete-Time Signal Processing ”, Prentice Hall (second edition) 1999, pages :551.

[39] G. T. Ruck , D. E. Barrick, W. D. Stuart, C. K. Krichbaum, “Radar Cross Section Handbook”, vol 1, Plenum, New York 1970.

[40] D. K. Barton, “Modern Radar Systems Analysis”, Norwood Mass Artech House 1988, pages: 108.

[41] B. Mulgrew, Peter M. Grant, J Thompson, “Digital Signal Processing: Concepts and Applications”, Palgrave 1999, pages: 243.

[42] G.B. Arfken, H.J. Weber, “Mathematical Methods for Physicists”, Elsevier Academic Press, sixth edition, 2005, pages: 455-465.

[43] W. R. LePage, “Complex Variables and the Laplace Transform for Engineers”, Dover Publications, 1980, pages: 140-160.

[44] E. Kreyszig, “Advanced Engineering Mathematics”, John Wiley and Sons, 1999, 8th Edition, pages: 777.

[45] M.L. Van Blaricum, Bruce Noel, (Editor) “Ultra-Wideband Radar: Proceedings of the First Los Alamos Symposium”, CRC Press1991, Boca Raton, pages: 191-202.

[46] M.A. Morgan, “Singularity Expansion Representations of Fields and Currents in Transient Scattering”, IEEE Transactions on Antennas and Propagation, Vol AP-32, May 1984, pages: 466-473.

[47] L.W. Pearson “A Note on the Representation of Scattered Fields as a Singularity Expansion”, IEEE Transactions on Antennas and Propagation, Vol AP-32, May 1984, pages: 466-473.

[48] C.E. Baum “The Singularity Expansion Method in Transient Electromagnetic Fields”, L.B. Felsen (Editor), Springer, 1976, chapter 3, pages: 129-179.

[49] M.S. Aly, T.T.Y Wong, “Root Nature of the Transverse Electric Characteristic Equation for a Dissipative Sphere”, IEEE Transactions on Antennas and Propagation, Vol AP-37, January 1989, pages: 71-77.

[50] J.D. Murphy, P.J. Moser, A. Nagl, H. Uberall, “A Surface Wave Interpretation for the Resonances of a Dielectric Sphere”, IEEE Transactions on Antennas and Propagation, Vol AP-28, November 1980, pages: 924-927.

[51] J.V. Subrahmanyam, G.A.H. Cowart M. Keskin, H. Uberall, G.C. Gaunaurd E. Tanglis, “Surface Waves and their Relation to the Eigenfrequencies of a Circular–Cylindrical Cavity”, IEEE Transactions on Microwave Theory and Techniques, Vol MTT-29, October 1981, pages 1066-1072.

[52] H. Uberall et all, “The Physical Content of the Singularity Expansion Method”, Applied Physics Letters, Vol AP-39, August 1981, pages: 362 -364.

[53] P.J. Moser, J.D. Murphy, A. Nagl, H. Uberall, “Resonances and Surface Waves on Conducting Spheres with a dielectric Coating”, Radio Science, Vol-16, May-June 1981, pages: 279-288.

[54] W.E. Howell, H. Uberall, “Complex Frequency poles of Radar Scattering from Coated Conducting Spheres”, IEEE Transactions on Antennas and Propagation, Vol AP-32, June 1984, pages: 624 -627.

[55] H. Uberall, G.C. Gaunaurd, “Relation Between the Ringing of Resonances and Surface Waves in Radar Scattering” IEEE Transactions on Antennas and Propagation, Vol AP-32, October 1984, pages: 1071-1079.

[56] B. L. Merchant, A. Nagl, H. Uberall, “Resonance Frequencies of Conducting and the Phase Matching of Surface Waves” IEEE Transactions on Antennas and Propagation, Vol AP-34, December 1986, pages: 1464-1467.

[57] H. Uberall, C.R. Schumacher, X.L. Bao, “Resonant Attenuation in Electromagnetic Wave Scattering from Conducting Elongated Objects”, IEEE Transactions on Electromagnetic Compatibility –S , Vol EC-35, November 1993, pages: 466-472.

[58] W.E. Howell, H. Uberall, “Selective Observation of resonances via their Ringing in Transient Radar Scattering, as Illustrated for Conducting and Coated Spheres”, IEEE Transactions on Antennas and Propagation, Vol AP-38, March 1990, pages: 293-298.

[59] D.L. Taylor, A.K. Jordan, P.J. Moser, H. Uberall, “Complex Resonances of Conducting Spheres with Lossy Coatings ”, IEEE Transactions on Antennas and Propagation, Vol AP-38, February 1990, pages: 236 -240.

[60] E. J. Rothwell, D. P. Nyquist, K. M. Chen, and B. Drachman, “Radar Target Discrimination Using the Extinction-Pulse Technique”, IEEE Transactions on Antennas and Propagation, Vol. AP-33, Sept. 1985, pages: 929–937.

[61] K. M. Chen, D. P. Nyquist, E. J. Rothwell, L. Webb, and B. Drachman, “Radar Target Discrimination by Convolution of Radar Return with Extinction-Pulse and

Single-Mode Extraction Signals," IEEE Transactions on Antennas and Propagation, Vol. AP-34, July 1986, pages: 896–904.

[62] E. J. Rothwell, K. M. Chen, D. P. Nyquist, and W. Sun, "Frequency Domain E-pulse Synthesis and Target Discrimination," IEEE Transactions on Antennas and Propagation, Vol. AP-35, Apr. 1987 pages: 426–434.

[63] E. J. Rothwell, K. M. Chen, and D. P. Nyquist, "Extraction of the Natural Frequencies of a Radar Target from a Measured Response Using E-pulse techniques," IEEE Transactions on Antennas and Propagation, Vol. AP-35, June 1987, pages: 715–720.

[64] P. Ilavarasan, J. E. Ross, E. J. Rothwell, K. M. Chen, and D. P. Nyquist, "Performance of an Automated Radar Target Discrimination Scheme Using E-pulses and S-pulses," IEEE Transactions on Antennas and Propagation, Vol. AP-41, May 1993, pages: 582–588.

[65] E. J. Rothwell, K. M. Chen, D. P. Nyquist, P. Ilavarasan, J. E. Ross, R. Bebermeyer, and Q. Li, "A General E-pulse Scheme Arising from the Dual Early-time/late-time Behaviour of Radar Scatterers," IEEE Transactions on Antennas and Propagation, Vol. AP- 42, Sept. 1994, pages: 1336–1341.

[66] N. Shuley and D. Longstaff , "Role of Polarisation in Automatic Target Recognition Using Resonance Descriptions" IEE Electronic letters Vol 40 February 2004 .

[67] M. H. Hayes, "Statistical Digital Signal Processing and Modeling", Wiley, 1996, pages: 129-189.

[68] M. H. Hayes, "Schaum's Outline of Digital Signal Processing ", McGraw-Hill, 1998, pages: 376-380.

[69] J. Proakis, C. M. Rader, F Ling, and C. L. Nikias, “Advanced Digital Signal Processing”, Macmillan, 1992, pages: 210-270.

[70] T. K. Moon, W. C. Stirling, “Mathematical Methods and Algorithms for Signal Processing”, Prentice-Hall, 2000, pages: 375-398 .

[71] C.W. Therrien, “Discrete Random Signals and Statistical Signal Processing”, Prentice-Hall, 1992, pages: 555-558.

[72] W. L. Ko, R. Mittra, “A Combination of FDTD and Prony’s Methods Analyzing Microwave Integrated Circuits”, IEEE Transactions on Microwave Theory and Techniques, Vol. MTT-39, no 12, December 1991, pages 2176-2181.

[73] K. Naishadham, X. Lin, “Application of Spectral Domain Prony’s Method to the FDTD Analysis of Planar Microstrip Circuits”, IEEE Transactions on Microwave Theory and Techniques, Vol. MTT-42, no 12, December 1994, pp 2391-2398.

[74] J.-H. Lee, N. Bushyager, M. M. Tentzeris, “Comparative Study of DSP Techniques for the Effective Modeling and Design of Highly Resonant RF-MEMS Structures”, Proc. of the 2005 IEEE CEM-TD Workshop, Atlanta, GA, September 2005, pages: 88-91.

[75] J.D. Markel, A.H. Gray Jr., “Linear Prediction of Speech”, Springer-Verlag, 1976, pages: 8-15.

[76] G. E. Kopec, A. V. Oppenheim, J. M. Tribolet, “Speech analysis by homomorphic prediction”, IEEE Transactions on Acoustics Speech Signal Processing, Vol ASSP-25, no 1, February 1977, pages: 40–49.

[77] J. Chen, et al., “Using Linear and Nonlinear Predictors to Improve the Computational Efficiency of the FDTD Algorithm”, IEEE Transactions on

Microwave Theory and Techniques, Vol. MTT-42, no 10, October 1994, pages: 1992-1997.

[78] A. V. Oppenheim (editor), "Applications of Digital Signal Processing", Prentice-Hall, 1978, pages: 148-159.

[79] T. W. Parks, C. S. Burrus, "Digital Filter Design", John Wiley & Sons, 1987, pages: 226-228.

[80] Y. Hua, T. K. Sarkar, "Matrix Pencil Method for Estimating Parameters of Exponentially Dampled/Undamped Sinusoids in Noise", IEEE Transactions on Acoustics, Speech, and Signal Processing, Vol. ASSP-38, May 1990, pages 814-824.

[81] K. M. Chen, D. Westmoreland, "Impulse Response of a Conducting Sphere based on Singularity Expansion Method", Proc. IEEE, Vol 69, no 6, June 1981, pages : 747-750.

[82] R. Carrière and R. Moses, "High Resolution Radar Target Modelling using a Modified Prony Estimator", IEEE Transactions on Antennas and Propagation, Vol. AP-40, no. 1, Jan. 1992, pages: 13-18.

[83] N. H. Younan, "Radar Targets Identification via a Combined Epulse/SVD-Prony Method", Record of IEEE 2000 International Radar Conference, 2000.

[84] N.H. Younan , C.D. Taylor, "On using the SVD -Prony Method to Extract Poles of an EM System from its Transient Response," Electromagnetics, Vol. 11, No. 2, 1991, pages: 223-233.

[85] R. Kumaresan , D.W. Tufts, "Estimating the Parameters of Exponentially Damped Sinusoids and Pole-Zero Modelling in Noise " IEEE Transactions on Acoustics Speech Signal Processing, Vol. ASSP-30, No. 6, December 1982, pages: 833-840.

[86] A. Vasalos, I. Vasalos, H. G. Ryu, S. E. Fotinea, "LTR Analysis and Signal Processing for Concealed Explosive Detection ", IEEE GEMIC 2010 International conference, Berlin, Germany , 2010, pages: 166-169.

[87] M. Gashinova, M. Cherniakov, A. Vasalos, "UWB signature analysis for detection of body-worn weapons", IEEE Radar 2006 International conference, Shanghai, China, 2006, pages: 1-4.

[88] M. Cherniakov, A. Vasalos, "Pedestrian Recognition via Ultra wideband (UWB) Radar ", International Workshop on Intelligent Transportation – WIT, 2005, Hamburg, Germany, Proceedings pages: 95-99.

[89] M. Cherniakov, A. Vasalos, "Ultra Wideband Radar for Pedestrian Recognition", First International Conference VehCom-2003, Birmingham, UK, June 2003, Proceeding pages: 61-66.

[90]N. J. Willis, "Bistatic Radar", SciTech Publishing 2nd edition, 2005, pages: 145-147.

[91] M. Cherniakov, "Bistatic Radar: Principles and Practice", John Wiley & Sons, 2007.

[92] F. Soldani, C. M. Alabaster "The Benefits of Matched Illumination for Radar Detection of Ground Based Targets", Proc. Waveform Diversity & Design International conference, 2007, pages: 23-27.

[93] H. Akaike, "A New Look at the Statistical Model Identification", IEEE Transactions on Automatic Control, vol. AC-19, December 1974, pages: 716-723.

[94] H. Akaike, "Fitting autoregressive models for prediction", Annals of the Institute of Statistical Mathematics, Vol 21, 1969, pages: 243-247.

[95] J. Rissanen, "Modeling by shortest data description", *Automatica,* Vol. 14, 1978, pages: 465-471

[96] J. Rissanen, "Consistent order estimation of autoregressive processes by shortest description of data", *Analysis and Optimization of Stochastic Systems,* Jacobs *et al.* Eds. New York: Academic, 1980.

[97] M. Wax , T. Kailath, "Detection of Signals by Information Theoretic Criteria", IEEE Transactions on Acoustics Speech Signal Processing, Vol. ASSP-33, No.2 , April 1985, pages: 387-392.

[98] P. Stoica, R. Moses, "Introduction to Spectral Analysis", Prentice Hall, 1997, pages: 155-168.

[99] D. W. Tufts, R. Kumaresan, "Frequency Estimation of Multiple Sinusoids; Making Linear Prediction Perform like Maximum Likelihood," Proc. IEEE, vol. 70, Sept. 1982, pages: 975-989.

[100] D. W. Tufts, R. Kumaresan, "Singular Value Decomposition and Improved Frequency Estimation using Linear Prediction," IEEE Transactions on Acoustics Speech Signal Processing, Vol. ASSP-30, Aug. 1982, pages: 671-675

[101] R. Kumaresan D. W. Tufts, and L.L. Scharf, "A Prony Method for Noisy Data: Choosing the Signal Components and Selecting the Order in Exponential Signal Models", Proc IEEE, VOL. 72, NO. 2., February 1984, pages: 230-233

[102] J.A. Cadzow, O.M. Solomon, "Algebraic Approach to System Identification", IEEE Transactions on Acoustics Speech Signal Processing, ASSP-34, June 1986, pages: 462-469.